Development of Nanostructured Light Emitters in Gallium Nitride

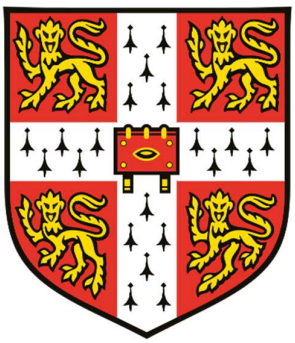

John Jarman

Robinson College

This thesis is submitted for the degree of Doctor of Philosophy

May 2022

Declaration

I hereby declare that except where specific reference is made to the work of others, the contents of this dissertation are original and have not been submitted in whole or in part for consideration for any other degree or qualification in this, or any other university. This dissertation is my own work and contains nothing which is the outcome of work done in collaboration with others, except as specified in the text and Acknowledgements. This dissertation contains fewer than 60,000 words including appendices, bibliography, footnotes, tables and equations.

John Jarman, May 2022

Abstract

Development of Nanostructured Light Emitters in Gallium Nitride

John Jarman

Nanostructured light emitters in gallium nitride (GaN), including quantum wells (QWs) and quantum dots (QDs), are of widespread importance as the key technology enabling high-brightness blue light-emitting diodes (LEDs) and lasers. GaN-based QDs also show promise as novel polarised single-photon sources that can operate at room temperature. This thesis explores methods of structural and optical characterisation of such nanostructures using electron microscopy and in-situ cathodoluminescence, resolving structural features that correlate with cathodoluminescence images, and providing insight into the differences between QD samples grown by quasi-two-temperature and modified droplet epitaxy methods. Refractive index engineering of GaN via the manufacture of porous structures is explored, and the integration of InGaN QWs with porous distributed Bragg reflectors (DBRs) is reported, with a corresponding increase in LED efficiency owing to improved light extraction. Porous DBRs are also integrated with InGaN QDs to create prototype optical cavity structures, combined with a vertical etching process to create nano- and micropillar cavities. Improved light extraction and background suppression from InGaN QDs embedded in such structures is seen, giving a single-photon emission purity of 96%, a record for these QDs. The integration of InGaN QDs into vertical and planar contact geometries also enables the investigation of the behaviour of these QDs under applied electric fields. Finally, the engineering of a full LED structure containing InGaN QDs is reported, leading to the first measurement of electroluminescence from InGaN QDs and the demonstration of electrically-excited single photon emission from this system.

Acknowledgements

There are many people to whom I owe thanks for their endless kindness, support, and (above all) patience during the completion of the PhD work and this thesis. Firstly, to my supervisor Prof. Rachel Oliver for the regularly scheduled meetings, helpful advice and direction throughout the project, infinite patience, and, of course, for welcoming me into to her excellent lab in Cambridge to conduct the work reported here. Specific acknowledgement is owed to Dr Tongtong Zhu, for his guidance, support and for the growth of the samples used in this thesis; Dr James Griffiths for his support with the work in Chapter 3, both for setting up the collaboration with Brunel University that enabled the nano-cathodoluminescence measurements and for his support and friendly company on the long days spent at the microscope; and Dr Peter Griffin for etching many porous DBR samples. I would also like to acknowledge Claudius Kocher, Tim Puchtler and Tong Wang at the University of Oxford for their work measuring the quantum dot devices (specific acknowledgements are placed throughout the thesis), and for their kind and friendly support on visits to Oxford (especially to Claudius for having me to stay!). The work would not have been possible without the smooth running of the cleanrooms in the Cavendish under the watchful eye of Melanie Tribble, who was also very accommodating of the several novel processes I introduced during device development. To Fabien, Helen, An, Boning, Lok Yi, Thomas, Gunnar, Abhiram, Alex, Martin and those mentioned above – thank you for making the office a lovely place to work and my time in the group an enjoyable one. And finally, to all my wonderful friends and family for their support and encouragement through both the good and the hard times of the past few years.

List of Publications

1. C.C. Kocher, **J. C. Jarman**, T. Zhu, G. Kusch, R. A. Oliver, and R. A. Taylor. "Decreased Fast Time Scale Spectral Diffusion of a Nonpolar InGaN Quantum Dot." ACS Photonics (2021)
2. M. J. Holmes, T. Zhu, FC-P. Massabuau, **J.C. Jarman**, R. A. Oliver, and Y. Arakawa. "Pure single-photon emission from an InGaN/GaN quantum dot." APL Materials (2021)
3. FC-P. Massabuau, D. Nicol, F. Adams, **J. C. Jarman**, J. Roberts, A. Kovacs, P. Chalker, and R. A. Oliver. "Study of Ti contacts to corundum α-Ga2O3." Journal of Physics D: Applied Physics (2021)
4. B. Ding, **J. C. Jarman**, M. J. Kappers, and R. A. Oliver. "Combined SEM-CL and STEM investigation of green InGaN quantum wells." Journal of Physics D: Applied Physics (2021)
5. **J. C. Jarman**, T. Zhu, P. H. Griffin, and R. A. Oliver. "Light-output enhancement of InGaN light emitting diodes regrown on nanoporous distributed Bragg reflector substrates." Japanese Journal of Applied Physics (2019)
6. Roberts, J. W., **J. C. Jarman**, D. N. Johnstone, P. A. Midgley, P. R. Chalker, R. A. Oliver, and FC-P. Massabuau. "α-Ga2O3 grown by low temperature atomic layer deposition on sapphire." Journal of Crystal Growth (2018)
7. T. Zhu, **J. C. Jarman**, C. X. Ren, F. Tang, C. C. Kocher, T. J. Puchtler, B. P. Reid, T. Wang, S. K. Patra, S. Schulz and R.A. Taylor. "Nitride single photon sources". Institute of Electrical and Electronics Engineers (2018)
8. H. P. Springbett, K. Gao, **J. C. Jarman**, T. Zhu, M. Holmes, Y. Arakawa, and R. A. Oliver. "Improvement of single photon emission from InGaN QDs embedded in porous micropillars." Applied Physics Letters (2018)
9. C. C. Kocher, T. J. Puchtler, **J. C. Jarman**, T. Zhu, T. Wang, L. Nuttall, R. A. Oliver, and R. A. Taylor. "Highly polarized electrically driven single-photon emission from a non-polar InGaN quantum dot." Applied Physics Letters (2017)

10. T. Wang, T. J. Puchtler, S. K. Patra, T. Zhu, **J. C. Jarman**, R. A. Oliver, S. Schulz, and R. A. Taylor. "Deterministic optical polarisation in nitride quantum dots at thermoelectrically cooled temperatures." Scientific Reports (2017)
11. T. Wang, T. J. Puchtler, T. Zhu, **J. C. Jarman**, R. A. Oliver, and R. A. Taylor. "High-temperature performance of non-polar (11–20) InGaN quantum dots grown by a quasi-two-temperature method." Physica Status Solidi B (2017).
12. T. Zhu, Y. Liu, T. Ding, W. Y. Fu, **J. C. Jarman**, C. X. Ren, R. V. Kumar, and R. A. Oliver. "Wafer-scale fabrication of non-polar mesoporous GaN distributed Bragg reflectors via electrochemical porosification." Scientific Reports (2017)
13. T. Wang, T. J. Puchtler, T. Zhu, **J. C. Jarman**, L. P. Nuttall, R. A. Oliver, and R. A. Taylor. "Polarisation-controlled single photon emission at high temperatures from InGaN quantum dots." Nanoscale (2017)

Contents

Introduction 13

1.1 Single photon sources 13

1.2 Project aims 14

1.3 Gallium nitride 14

1.3.1 Crystallography 15

1.3.2 Growth 16

1.3.3 Doping 17

1.3.4 Bandgap control 17

1.4 Quantum confinement 18

1.4.1 Quantum wells 18

1.4.2 Quantum dots 19

1.5 Excitation of QDs in GaN 22

1.5.1 Photoluminescence (PL) 22

1.5.2 Electroluminescence (EL) 22

1.5.3 Measurement of photon statistics 23

1.5.4 Applications of single-photon sources 24

1.5.5 Single photon emitters in GaN 25

1.6 Photonic structures for single-photon sources 28

1.6.1 Distributed Bragg reflectors 28

1.6.2 Dielectric DBRs 29

1.6.3 Epitaxial DBRs 30

1.6.4 Porous GaN DBRs 31

1.6.5 Air-gap DBRs 33

1.6.6 Optical microcavities 34

1.7 Thesis structure 42

Methods 43

2.1 Sample growth 43

2.2 Sample processing 45

2.2.1 Cleaning 45

2.2.2 Lithography 45

2.2.3 Plasma processes 47

2.2.4 Metal deposition 48

2.2.5 Metal patterning 49

2.2.6 Contact annealing 49

2.2.7 Bonding 50

2.3 Scanning electron microscopy 50

2.3.1 Focused ion beam 51

2.4 Transmission electron microscopy 52

2.4.1 Scanning TEM 53

2.4.2 Sample preparation 54

2.5 Atomic force microscopy (AFM) 54

2.6 Photoluminescence 55

2.6.1 Micro-reflectivity mapping 57

2.7 Electrical characterisation 57

2.7.1 Electroluminescence spectroscopy 58

2.7.2 Transfer length method (TLM) 59

Nano-cathodoluminescence of non-polar InGaN QDs 60

3.1 Introduction 61

3.1.1 STEM-CL of single-photon-emitting nanostructures 61

3.1.2 Structural observations of InGaN quantum dots 64

3.1.3 SEM-CL observations of non-polar InGaN QDs 67
3.2 Aims 68
3.3 Methods 69
3.3.1 Gatan Vulcan STEM-CL system 69
3.3.2 STEM conditions 70
3.3.3 Analysis methodology 70
3.4 Samples 73
3.5 MDE QDs: plan-view 74
3.5.1 Larger features 74
3.5.2 Comparison with structural data 77
3.5.3 STEM-CL of surrounding regions 79
3.5.4 Comparison with PL 80
3.6 Q2T QDs: plan-view 81
3.6.1 HR-STEM 82
3.7 Q2T QDs: cross-section 83
3.7.1 Correlation with STEM and EDX 84
3.8 Single quantum well cross-section 89
3.9 Discussion 92
3.10 Conclusions 94
Regrown LEDs and porous distributed Bragg reflectors 96
4.1 Introduction 97
4.1.1 Distributed Bragg reflectors 97
4.1.2 Quantum-well LEDs 97
4.1.3 Strategies for improving light extraction 108
4.1.4 LED structures incorporating NP-GaN 109
4.2 Aims 112

4.3 Samples 112
4.3.1 Growth 112
4.4 Characterisation of regrown wafers 113
4.4.1 Microscopy 114
4.4.2 Micro-reflectivity 118
4.5 Device processing 121
4.5.1 Device design 121
4.5.2 Cleanroom processing 122
4.6 Device characterisation 123
4.6.1 Contact performance 123
4.6.2 NP-DBR conductivity 127
4.6.3 Electroluminescence 128
4.6.4 Electrical characterisation 130
4.6.5 Efficiency measurements 134
4.6.6 Current-dependent spectroscopy 136
4.6.7 Possible droop mechanisms 139
4.7 Summary 140
Optical microcavities 141
5.1 Introduction 142
5.2 Aims 142
5.3 Porous distributed Bragg reflectors 142
5.3.1 Micro-reflectivity mapping 142
5.3.2 Dry etching of porous DBRs 147
5.4 Processing of optical cavity structures 149
5.4.1 ICP-RIE for high aspect ratio structures 150
5.4.2 Nanosphere lithography 150

5.4.3 Electron-beam lithography 154
5.4.4 Fin-connected pillar structures 167
1.1.1 Porous GaN ICP-RIE grass removal by wet etching 172
5.5 Photoluminescence 175
5.5.1 C-plane lasers 176
5.5.2 A-plane single photon sources 182
5.6 Summary 185
Quantum dots in electrical devices 187
6.1 Introduction 187
6.2 Aims 188
6.3 Quantum dot LEDs 188
6.3.1 SiO_2 deposition and etch 189
6.3.2 Contact deposition and annealing 190
6.3.3 Bonding 190
6.3.4 Device characterisation 190
6.3.5 Origin of leakage 191
6.3.6 Low-temperature measurements 194
6.4 Lateral electric fields 200
6.4.1 Samples 201
6.4.2 Process development 201
6.4.3 Surface passivation 205
6.4.4 Schottky contacts 206
6.4.5 Room-temperature electrical measurements 207
6.4.6 Low-temperature electrical measurements 208
6.4.7 Photoluminescence measurements (early results) 209
6.5 Summary 213

Conclusions 214

7.1 Conclusions and suggestions for future work 214

References 217

Chapter 1

Introduction

1.1 Single photon sources

Devices that emit a single photon on demand have a range of potential applications in quantum cryptography, quantum computing, metrology and random number generation [1]. Streams of single photons can be generated by attenuating the output of a coherent light source (e.g. a laser); by spontaneous parametric down-conversion (SPDC); or by optical transitions in single atoms or quantum dots (QDs). The distribution of photon number states in the first two methods follows Poisson statistics, meaning that very low light intensity is required to ensure a high single-photon purity. However, atom-like systems, particularly semiconductor QDs based on the III-As system [2], can produce streams of single photons with high purity, indistinguishability and brightness (exceeding 50% total system efficiency when integrated into an optical cavity [3]).

This thesis will investigate quantum dots in the Ga(In, Al)-N material system, which, unlike more technologically developed III-As QDs, can potentially operate at room temperature and at wavelengths suited to free-space quantum cryptography [4].

1.2 Project aims

This project aims to investigate ways of using InGaN QDs as single-photon emitters, with a view towards eventual applications in free-space QKD systems. The structure and properties of these emitters will be explored, along with ways of enhancing their photon emission rate and extraction efficiency under optical excitation, and a device will be fabricated that permits electrical excitation of non-polar InGaN QDs.

1.3 Gallium nitride

Gallium nitride is a material of widespread technical importance in optoelectronics and high-frequency power electronics. GaN-based light-emitting diodes are used as highly efficient, high-brightness sources of blue light, forming the basis for the most efficient forms of artificial lighting when the blue emission is partially down-converted using a phosphor to create white light. Blue-emitting GaN-based lasers initially enabled Blu-Ray data storage technology and later ultra-high-brightness white-light sources such as car headlights. High electron mobility transistors based on GaN provide high efficiencies at microwave frequencies, finding applications in powerful and highly efficient switched-mode electrical power converters, and in transmitters for use in wireless communications.

These applications rely on GaN's wide, direct bandgap of 3.4 eV, which may be tuned by alloying with indium and aluminium. This allows the bandgap to be adjusted between 6.2 eV (AlN) and 0.65 eV (InN). This provides a way to engineer heterostructures such as quantum wells (QWs) or quantum dots (QDs). GaN can also be reliably n- and p-doped, allowing these structures to be used in electrical devices.

Commercial light emitters (LEDs and lasers) rely on InGaN QWs to provide 2D confinement of charge carriers for more efficient radiative recombination. Quantum dots can be created by altering growth conditions to form 3D islands of the lower-bandgap material, with potential applications as single-photon sources in quantum encryption and quantum information schemes. The InGaN emission spectrum, emitting towards the green-blue end of the visible range, is of potential interest for free-space quantum key distribution (QKD), for example in inter-satellite and satellite-to-ground communication.

1.3.1 Crystallography

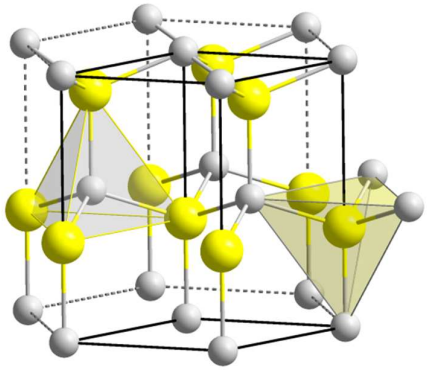

Figure 1: Wurtzite crystal structure, as adopted by GaN. (http://commons.wikimedia.org/wiki/File:Wurtzite_polyhedra.png)

GaN typically adopts the hexagonal wurtzite structure, as illustrated in Figure 1. This structure is non-centrosymmetric, with the Ga and N coordination polyhedra (shaded in Figure 1) arranged such that a strong spontaneous polarisation exists along the [0001] c-axis, perpendicular to the (0001) c-plane. A large intrinsic and strain-induced electric field can, therefore, develop across heterostructures grown on the (0001) c-plane of GaN [5]. This causes a spatial separation of electron and hole wavefunctions in QDs and QWs grown on the c-plane, increasing the radiative lifetime and therefore theoretically lowering the efficiency [6]. Heterostructures grown on a $(11\bar{2}0)$ a-plane or $(10\bar{1}0)$ m-plane, shown in Figure 2, experience a much lower polarisation field [5], which could remove the unwanted effects caused by strong electric field. High-quality films are, however, harder to achieve in the non-polar growth directions, so most commercial devices based on GaN QWs, such as LEDs and lasers, use material grown on the polar c-plane.

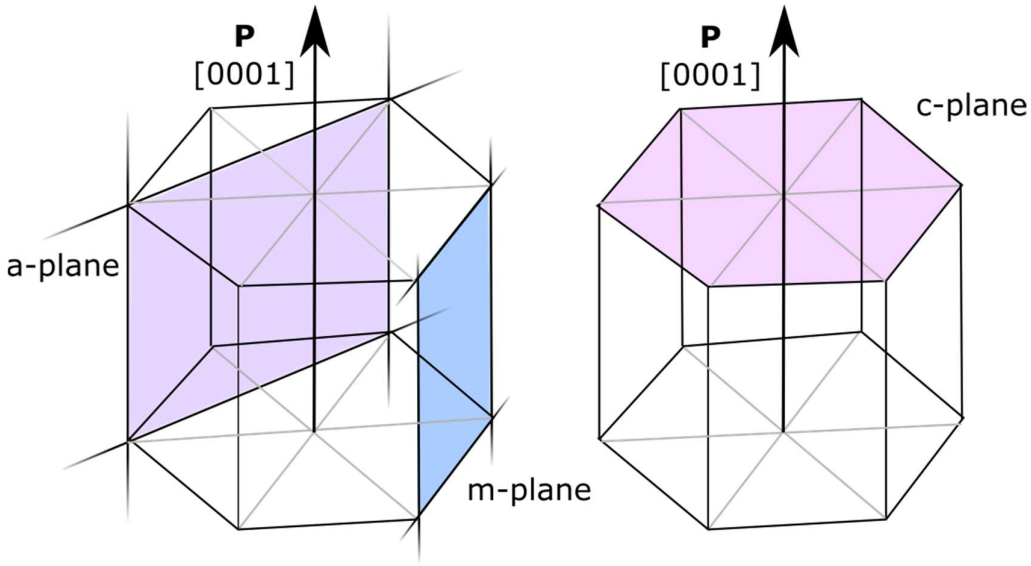

Figure 2: Location of non-polar planes (a- and m-planes, left) and polar c-plane (right) in GaN. The black arrow indicates the direction of the polar [0001] c-axis.

1.3.2 Growth

The GaN epilayers used in this project are grown on sapphire substrates. The crystal orientation of the substrate determines the orientation of the GaN film, with {0001) c-plane sapphire used to grow (0001) c-plane GaN, $(1\bar{1}00)$ m-plane sapphire used for $(1\bar{1}00)$ m-plane GaN and $(1\bar{1}02)$ r-plane sapphire for $(11\bar{2}0)$ a-plane GaN [7].

Growth can be accomplished using metalorganic (MOVPE) or hydride (HVPE) vapour-phase epitaxy, or molecular beam epitaxy (MBE). The samples that will be used in this project will be grown using MOVPE.

There is a large lattice and thermal expansion mismatch between GaN and sapphire. Growth therefore usually begins with a thin layer of GaN or AlN deposited at a low temperature that minimises the lattice mismatch between the film and substrate.

Further defect-reduction techniques can then be employed on this template. For example, epitaxial lateral overgrowth (ELOG) uses lithographically defined stripes of SiO_2 to block vertical growth over the stripes. The film must then grow laterally to coalesce over the stripes, and this leads to annihilation of threading dislocations in the regions over the stripes [8]. A similar technique, using a self-assembled SiN_x mask containing small holes, has been

demonstrated on c- [9] and a-plane GaN [10]. Both techniques have been shown to provide appropriate substrates for the growth of a-plane quantum-dots [11].

1.3.3 Doping

GaN is intentionally n-doped using Si or Ge, which are substitutional impurities that behave as shallow donors when they substitute the Ga atom. Both dopants show ionisation energies below 20 meV for typical dopant concentrations [12, 13], and can give high ($>10^{18}$ cm^{-3}) carrier concentrations and n-type conductivity at room temperature. Higher carrier concentrations can be achieved with Ge doping, as less strain is introduced into the crystal for a given concentration of Ge [14], and concentrations sufficient to move beyond the Mott transition to fully metallic behaviour can be achieved [13].

P-doping is much more difficult, as with other wide-bandgap semiconductors. Mg is used as the p-dopant, and it is also incorporated as a substitutional impurity on the Ga site. The exact nature of the Mg acceptor is complex and poorly understood, but experiments show a relatively high ionisation energy of 200 meV [15], leading to low acceptor ionisation and low hole concentrations. Mg incorporation is also limited by its low solubility in GaN [16]. Another important aspect is the formation of neutral Mg-H complexes during film growth, which means that a high-temperature anneal is required after growth to drive out hydrogen and activate the acceptors [17].

Oxygen is an important impurity, since it acts as a shallow donor (and therefore n-dopant) when substituted for nitrogen and is often unintentionally incorporated during growth [16]. Carbon is a deep acceptor when substituted for nitrogen [18] and is sometimes used to compensate unintentional oxygen doping to produce high-resistivity GaN films [19].

1.3.4 Bandgap control

The bandgap energy of GaN can be increased or decreased by alloying with Al or In respectively. Together, these alloys cover a very wide range of energies, from 0.7 eV for pure InN to 6.28 eV for pure AlN [20, 21], as shown in Figure 3.

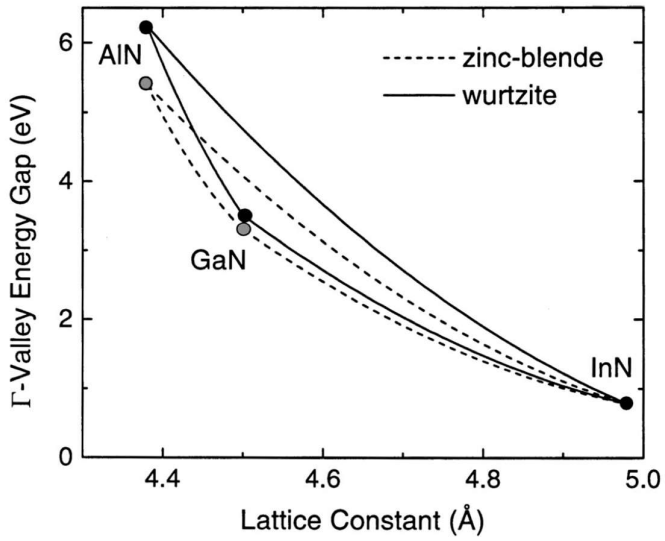

Figure 3: Band-gap energies and lattice constants for III-N semiconductor alloys. Reproduced with permission from [21].

1.4 Quantum confinement

Local band-gap reductions can be engineered to create confined exciton states in GaN devices, using either InGaN inclusions in a GaN matrix, or GaN inclusions in an AlGaN matrix. Structures that confine charge carriers to a 2D sheet are referred to as quantum wells (QWs) while structures that confine charge carriers inside a 3D volume are called quantum dots (QDs).

1.4.1 Quantum wells

Confinement in a QW restricts electrons to movement in a 2D plane and modifies the wavefunction in the confined direction by imposing boundary conditions at the well edges. The boundary conditions give rise to discrete sine-wave solutions to the 1D time-independent Schrodinger equation in the confined direction. While this confinement energy is fixed for a particular well width (and a confined electron cannot have an energy less than this), the electron is still free to move in the 2D plane and can have additional kinetic energy. This means that the energies of confined electrons and holes are split into sub-bands. Generally, only the lowest sub-band is occupied at typical electron densities encountered in photo- or electroluminescence measurements.

The binding energy of excitons is also modified by the confinement in the QW. As the QW width decreases, the binding energy increases up to a maximum value, which occurs when the well width is about the same as the Bohr radius of a free exciton (which, in pure GaN, is about 2.8 nm [22]). Typically, the exciton binding energy is increased by a factor of about 4 at this peak, meaning that excitonic effects are particularly strong in QWs [23].

QWs can increase the efficiency of exciton recombination by increasing the spatial overlap of electrons and holes, leading to their use as the light-emitting element of high-efficiency LEDs.

1.4.1.1 Growth of InGaN QWs

The growth of InGaN QWs in GaN requires some compromises to be made, since the optimum growth temperature of InGaN is lower than that of GaN due to the higher vapour pressure of indium at high temperatures [24]. Typically, the optimum growth temperature is between 800 - 850°C [25], compared to over 1,000°C for GaN.

One approach is to grow the entire QW and barrier structure at the lower InGaN growth temperature (the one-temperature, or 1T, method). However, due to insufficient ammonia cracking at the lower temperature, this has been suggested to degrade the quality of the GaN barriers [26].

To allow the GaN barrier to be grown at a higher temperature, the temperature can be increased after the growth of each InGaN layer. This can happen during a growth interruption just after the InGaN layer is completed (the two-temperature, or 2T, method), in which case some indium can evaporate from the exposed InGaN during the temperature ramp; or a thin GaN cap can be grown at the lower temperature first (the quasi-two-temperature, or Q2T, method). In the Q2T method, a thicker low-temperature cap lowers indium losses but degrades the optical quality of the QW, so a compromise thickness must be found [26]

1.4.2 Quantum dots

Confining electrons in three dimensions limits the allowed energies to a series of discrete values, like those observed in atoms. The spectral linewidth of the observed emission is therefore usually much smaller than that seen for QWs.

The binding energy of excitons also increases when an electron and hole are confined within a QD, to an even greater extent than in a QW. This means that the observed spectral peaks are usually associated with excitons and excitonic complexes rather than free electrons or holes. Specifically, emission lines associated with a single exciton occupying the QD ($|X\rangle$ state), as well as a biexciton comprised of two electrons and two holes ($|XX\rangle$ state) may be observed, along with charged excitons (two electrons and a hole, or two holes and one electron) and higher excited states [27].

The single-exciton $|X\rangle$ state is useful for the generation of single photons, since the decay of a single exciton to the ground state will release exactly one photon. The biexciton state $|XX\rangle$ can be useful for the generation of entangled photons, since the decay chain $|XX\rangle \rightarrow |X\rangle \rightarrow |0\rangle$ can generate two photons with entangled polarisation [28]. The relative energies of the exciton and biexciton decays are controlled by the balance of exchange interactions between electrons and holes confined within the QD, which are usually attractive for electron-hole interactions and repulsive for electron-electron and hole-hole interactions. For InGaN QDs, the $|XX\rangle \rightarrow |X\rangle$ transition is usually blue-shifted by a few tens of meV relative to the $|X\rangle \rightarrow |0\rangle$ transition [29, 30], allowing for each transition to be isolated by spectral filtering. The splitting can also be tuned by adjusting dot shape and size [31], or through the application of external fields [32].

If a single exciton decay is isolated, for example by spectral filtering, a single QD can be used as a single photon source.

1.4.2.1 Energy shifts in response to external fields

The emission energy of transitions in the QD can be shifted by external electric fields due to the quantum-confined Stark effect (QCSE). This is a red-shift in the emission wavelength due to spatial separation of electron and hole wavefunctions in response to an external electric field. The process is shown schematically in Figure 4.

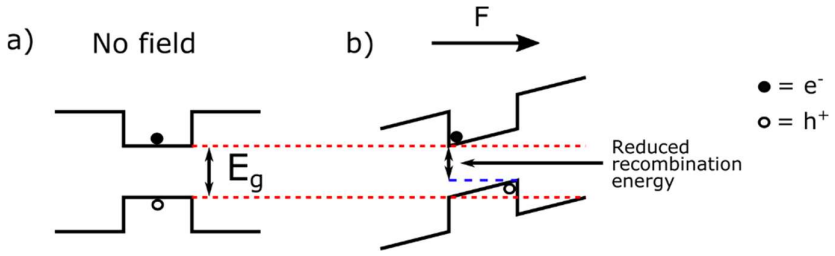

Figure 4: Schematic illustrating the quantum-confined Stark effect, where the emission wavelength and dipole moment of an electronic transition in a QD is modified by application of an electric field F. a) No field; the exciton recombines with energy E. b) With applied electric field F, the electron and hole are spatially separated in the quantum-confined structure and recombination energy is reduced.

The magnitude of the shift is given by [33]:

$$\Delta E = \mu F + \alpha F^2$$

Equation 1

where μ and α are the excited-state dipole moment and its polarisability, respectively, both projected along the direction of the applied field which has magnitude F in that direction.

Such shifts are frequently observed experimentally, including in InGaN QDs, for example by applying voltages to metal contacts patterned on the wafer [34]. Changing the spatial overlap of the electron and hole wavefunctions can also affect the binding energy for excitons, affecting the relative intensity of different excitonic emission peaks [34].

The QCSE also provides a mechanism for nearby defects (such as dislocations) to cause unwanted shifts in the energy and intensity of photon emission from QDs, as stochastic charge trapping at these defect sites can produce electric fields that influence the emission energy of nearby QDs [35, 36]. Additionally, the reduced spatial overlap of electron and hole wavefunctions in the presence of strong electric fields increases the radiative lifetime of the emitter [37], meaning that field-free QDs are desirable for the highest photon generation rates.

In the particular case of wurzite GaN and its alloys, which are piezoelectric, strong electric fields develop across strained heterostructures grown along the polar c-axis, including QDs [36], extending exciton lifetimes [37] and increasing sensitivity to external fluctuations in electric field [35, 38]. This leads to undesirable effects such as intensity fluctuations, linewidth broadening and periodic intensity quenching (blinking) [36].

1.5 Excitation of QDs in GaN

There are two principal ways of exciting electronic transitions in a quantum emitter: either electrons can be injected directly by passing an electrical current through the sample (with the resulting light emission upon exciton recombination being termed electroluminescence), or excitons can be generated in the material by illuminating it with light (with the resulting light emission being termed photoluminescence).

1.5.1 Photoluminescence (PL)

Photoluminescence measurements use a source of light to excite electronic energy-level transitions in the sample. Exciting with a photon energy higher than the energy of the transition is called non-resonant excitation, and typically involves a non-radiative relaxation process where the excess energy is dissipated as heat. Resonant excitation aims to excite a transition with photons carrying an energy nearly equal to the energy of the transition. This is a much more efficient process, and helps to avoid inadvertently pumping other nearby emitters, the fragmented quantum well present in many InGaN QD samples, and charging or discharging nearby defect sites. This means that resonant excitation tends to produce a more stable signal that is less contaminated by background. However, the requirement for highly specialised tunable lasers makes this impractical for on-chip devices.

Multi-photon PL uses multiple-photon absorptions to excite transitions; the energy of the exciting photons is roughly half of the transition energy in two-photon absorption, for example. In the case of InGaN QDs, two-photon excitation is found to strongly suppress emission from surrounding QWs, helping to isolate emission from a single quantum emitter [39, 40].

1.5.2 Electroluminescence (EL)

Electrons and holes can also be injected into samples, where they can recombine in quantum-confined structures and produce light. For example, a sample can be grown with a p-type layer, a nominally undoped (intrinsic) layer, and a n-type layer, forming a diode and allowing electron injection through the n-type layer and hole injection through the p-type layer.

Quantum emitters placed in the intrinsic layer can act as traps for passing charges, which may then recombine and emit light. This is the working principle for QW-based LEDs, and has also been demonstrated for InGaAs [41] , GaAs [42] and InGaN QDs [43], with single photon emission in the latter case observed up to room temperature [43-46].

Electrically injected devices are desirable in on-chip applications, as there is no requirement for a laser, and this provides an advantage for single-photon sources fabricated in a material system such as GaN that can be readily doped.

1.5.3 Measurement of photon statistics

To determine whether a given emitter produces individual single photons, one at a time, a measurement of the joint probability of measuring two photons, one at time t and one at time $t + \tau$ is used. This is called the second-order (intensity) correlation function, $g^{(2)}(\tau)$, written in terms of photon creation and annihilation operators $a^\dagger$ and a in Equation 2 [47]. The probability of measuring two photons at the same time (i.e., when $\tau = 0$) should be zero if the emitter is a single-photon source, i.e. $g^{(2)}(0) = 0$ [48].

$$g^{(2)}(\tau) = \frac{\langle a^\dagger(t)a^\dagger(t+\tau)a(t+\tau)a(t)\rangle}{\langle a^\dagger a\rangle^2}$$

Equation 2

$g^{(2)}(\tau) < 0.5$ indicates a projection on to the single photon Fock state. If values less than 0.5 are observed experimentally, this therefore evidence of the presence of a single quantum emitter, although the excess counts that bring the value above zero indicate that higher photon number states also exist in the emitted light (for example as background light arising from luminescence of surrounding or overlying features, such as a wetting layer) [48]. In many applications, such as QKD, multiple photon events are not desirable and the $g^{(2)}(0)$ becomes an important figure of merit.

One practical setup commonly used for measuring $g^{(2)}(\tau)$ is the Hanbury Brown and Twiss intensity interferometer [1], which is discussed further in Chapter 2 (Methods).

The behaviour of $g^{(2)}(\tau)$ away from $\tau = 0$ can also yield information about the system being examined. The function will rise above 1 at longer times if there are intensity fluctuations (photon bunching) [49], caused by (for example) the existence of a dark state that the emitter

periodically occupies [50]. This bunching will show an exponential decay to a constant value for long τ, providing a means of normalising the correlation function obtained from experimental data.

1.5.3.1 Effect of excitation power

The time delay between successive photons is a function of both the excitation power and the inherent lifetime of the electronic excited state that is responsible for emitting the stream of photons. As the excitation power is increased, the intensity of light collected from the emitter will increase as well due to more frequent excitations of the radiatively-active transition. Eventually, a single quantum emitter will become saturated when the emitter is re-excited as fast as possible after emitting a photon, and further increases in excitation power beyond the saturation point will not produce further increases in counts.

The $g^{(2)}(\tau)$ dip will broaden as the excitation power is reduced, reflecting the increased spacing between photons emitted by the single-photon emitter.

1.5.4 Applications of single-photon sources

Streams of single photons have applications in quantum key distribution (QKD) and quantum random number generators (QRNG) [1], in a variety of quantum computing and simulation schemes [51], and in quantum metrology [52].

1.5.4.1 Requirements of a single-photon emitter

For the applications mentioned in the preceding section, single-photon emitters need to be:

- **Bright**: possessing a fast radiative transition that can be pumped effectively to produce photons on demand
- **Stable**: not showing decay in intensity over time (bleaching) or periodic quenching of the emission (blinking) via (e.g.) interacting with nearby charge traps, and maintaining a narrow linewidth and stable emission energy if the photons need to be indistinguishable
- **Single**: The multiple-photon emission probability needs to be as low as possible.

It is also desirable for a single photon emitter to be electrically excited and able to operate at room temperature, for use in practical on-chip applications. While many applications of

quantum emitters require indistinguishable photons, this is not required for QKD and QRNG, allowing use of emitters with wide linewidths and showing spectral diffusion.

1.5.5 Single photon emitters in GaN

Single photon emitters can be fabricated (Al, In)GaN material system by locally altering the composition to create quantum dots. The large range of bandgap tuning means that quantum dots can be fabricated with a high confinement energy, which allows the creation of room-temperature SPEs [53].

1.5.5.1 InGaN QDs

InGaN quantum dots can be formed by self-assembly on both a- and c-plane GaN. There are two techniques used in this thesis for the self-assembly of QDs by MOCVD, which are called 'modified droplet epitaxy' (MDE) and 'quasi-two-temperature' (Q2T) methods. Site-controlled methods have also been demonstrated, where the QD is formed at the peak of a pyramid [54] or nanowire [55]. The quantum dots used in this project were grown on a-plane substrates by self-assembly using both MDE and Q2T, by Dr. Tongtong Zhu in the Cambridge Centre for Gallium Nitride.

Modified droplet epitaxy (MDE) employs a post-growth anneal of InGaN epilayers in nitrogen [56], as outlined in Figure 6. Indium-rich regions in the InGaN layer decompose to form metallic droplets when annealed at an appropriate temperature. These droplets, which can be imaged using AFM (as shown in Figure 7), react with ammonia to form InGaN quantum dots when a GaN capping layer is grown [56]. This technique works for both c- and a-plane GaN [57], and is qualitatively similar to droplet epitaxy methods used for the self-assembly of III-arsenide QDs [58].

On a-plane wafers, the quasi-two-temperature (Q2T) technique can also be used to form QDs [59]. In this technique, the InGaN layer is grown at a lower growth temperature (selected to grow InGaN of the required composition), followed by a thin cap of GaN at the lower temperature, before the temperature is ramped up for the growth of the rest of the GaN barrier layer at the optimal GaN growth temperature.

The hydrogen used during MOVPE growth stabilises the {0001) c-plane [60, 61], aiding the formation of flat structures on c-plane GaN. Therefore, the Q2T growth sequence produces

planar QWs on c-plane wafers. However, on a-plane wafers, this effect acts to destabilise planar growth, tending to lead to QD formation.

QDs grown by this method tend to show better temperature stability than MDE dots, but also show a stronger background InGaN QW emission, as shown in Figure 5 [59, 62].

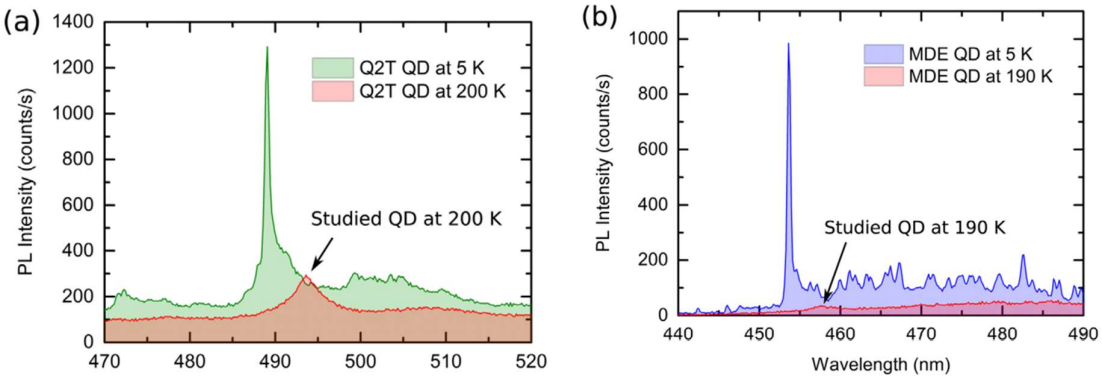

Figure 5: Comparison of μ-PL emission from Q2T (a, left) and MDE (b, right) QDs. Q2T QDs show better high-temperature stability but a higher QW background. Reproduced with permission from [62]

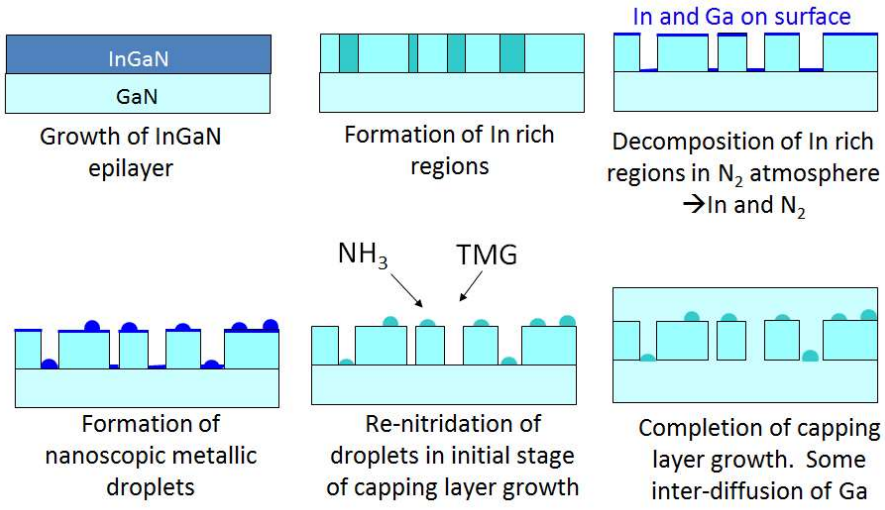

Figure 6: Schematic of modified droplet epitaxy (MDE) growth method for InGaN quantum dots. Figure modified from a presentation by Prof. Rachel Oliver

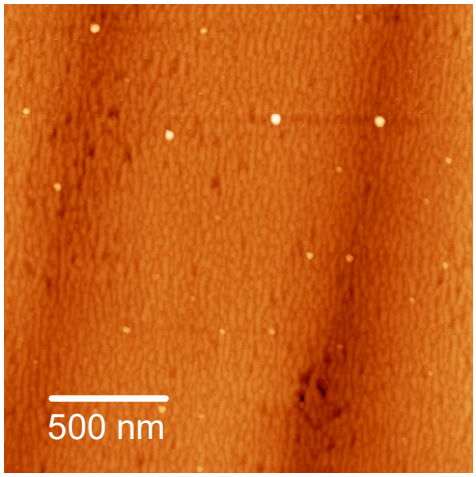

Figure 7: AFM image of an a-plane sample grown without a capping layer, showing nanoscopic InGa droplets (white).

C-plane InGaN QDs have been shown to act as low-temperature single photon emitters, with single-photon emission ($g^{(2)}(0) < 0.5$) shown at temperatures up to 55 K [63] and linear polarisation with random orientation relative to the substrate. The lifetimes are relatively long, generally a few nanoseconds, due to extremely strong polarisation fields across the QDs [64].

Non-polar InGaN QDs have the advantage of lower built-in electric fields across the QDs. This leads to shorter exciton lifetimes of ~300 ps [37], due to improved overlap of the electron and hole wavefunctions in the QD's excited states. A reduced built-in electric dipole should also reduce the sensitivity of the QD emission energy to externally applied fields, such as those arising from nearby defects acting as charge traps [35, 36, 38].

1.5.5.2 GaN QDs

GaN QDs embedded in an AlGaN matrix have shown the highest temperature operation and highest single photon purities in the (Al, In)GaN system. GaN QDs in AlN nanowires have been shown to retain single-photon emission at temperatures even exceeding room temperature [55, 65], with a $g^{(2)}(0)$ value of 0.34 ± 0.14 at 350 K. However, owing to increased difficulty in p-doping Al-rich alloys, and in electrically contacting such nanowire devices, electrically excited single-photon emission has not been demonstrated in GaN QDs.

1.6 Photonic structures for single-photon sources

Some properties of single-photon sources can be enhanced by the use of photonic structures that enhance light extraction or modify the dynamics of the emitter itself to increase radiative rate and achieve indistinguishability of emitted photons.

1.6.1 Distributed Bragg reflectors

Distributed Bragg reflectors (DBRs) form an essential part of many optical cavity and light extraction approaches to improving the performance of SPSs [66]. A DBR consists of a layered structure, with alternating layers of materials with two different refractive indices. A light ray travelling in a DBR therefore encounters regular sharp changes in refractive index, which causes a proportion of the wave power to be reflected from each interface according to Fresnel's law. When the layers are a quarter of a wavelength in thickness, the reflected waves from successive interfaces have an optical path difference of half a wavelength. As the sign of the reflection coefficient is switched at each successive interface by the alternating transitions from low to high n material and vice-versa, there is an additional shift of π radians in the phase of the wave reflected from alternate interfaces. The overall effect is that all the reflected waves are in phase and interfere constructively, creating a structure with high reflectance over a range of wavelengths referred to as the 'stop-band'.

Higher refractive index contrast between the layers increases the stop-band width and the peak reflectance, according to the following relationships for the peak reflection amplitude coefficient r_{peak} and stop-band width Δ [67]:

$$r_{peak} = \frac{\left(\frac{n_1}{n_2}\right)^{2N} - \frac{n_f}{n_o}}{\left(\frac{n_1}{n_2}\right)^{2N} + \frac{n_f}{n_o}}$$

Equation 3

$$\Delta \approx \frac{8c}{\lambda_{peak}} \frac{n_1 - n_2}{n_1 + n_2}$$

Equation 4

where n_1 and n_2 are the refractive indicies of the two materials forming the DBR, N is the number of pairs in the DBR, n_f is the refractive index behind the mirror and n_o is the index in front of the mirror.

1.6.2 Dielectric DBRs

Dielectric DBRs are made from alternating layers of dielectric materials (e.g. SiO_2/TiO_2) and tend to show excellent reflectivity in quite thin (<10 layer) structures, due to high refractive index contrast [68]. For example, a 13-pair ZrO_2/SiO_2 reflector used for a GaN VCSEL showed a 99.9% reflectance and 73 nm wide stopband (>98% reflectance) [69]. The coating technology typically used for creating dielectric DBRs (e.g. evaporation, PECVD or sputtering) is also mature, allowing for deposition of highly uniform and highly reflective DBRs.

Cavities based on these structures have the potential, therefore, for very high Q-factors and small cavity volumes. However, high-quality III-nitride films are grown epitaxially on single-crystalline substrates, and, therefore, dielectric DBRs are unsuitable substrates for growth of the active layers of the semiconductor [70]. For a Fabry-Pérot cavity with both a top and bottom DBR, a significant complication of the device processing is required if dielectric DBRs are used to construct both reflectors. A flip-chip process involving substrate removal and thinning of the active layers is required, using wet chemical substrate removal [71], photoelectrochemical etching (PEC) [72], chemical mechanical polishing (CMP) or laser lift-off [73].

These methods, while requiring complex processing, simplify the growth by reducing the need for strain management. However, the overall quality of the cavity is often compromised by the processing. For CMP or laser lift-off, precise control of the cavity thickness is difficult, and cavities generally have to be thicker than 4μm [74] although photoelectrochemical methods can be used to produce GaN lamellae with sub-micron thickness. These lamellae can then be used to form a cavity by sandwiching between dielectric DBRs [75].

The processing may be simplified if a dielectric DBR is used only for the top mirror, and a different strategy (such as an epitaxial or porous nitride mirror) is used for the bottom DBR of an optical cavity.

1.6.3 Epitaxial DBRs

In the GaN material system, epitaxial DBRs can be constructed from layers of AlGaN or AlInN alternating with GaN, with refractive index contrast achieved by adjusting the composition of the layers. The composition changes also alter the equilibrium lattice parameter of the material, meaning that there is a trade-off between the lattice match and refractive index contrast. For DBRs that use AlGaN as the low-index layer, the lattice parameter decreases as the aluminium content increases, and the same relationship is observed for AlInN-based DBRs. However, AlInN layers may be lattice-matched to pure GaN while still providing an appreciable refractive index contrast. This is shown graphically in Figure 8, which shows the relationship between lattice mismatch and refractive index contrast as the Al content of the layers is varied [76].

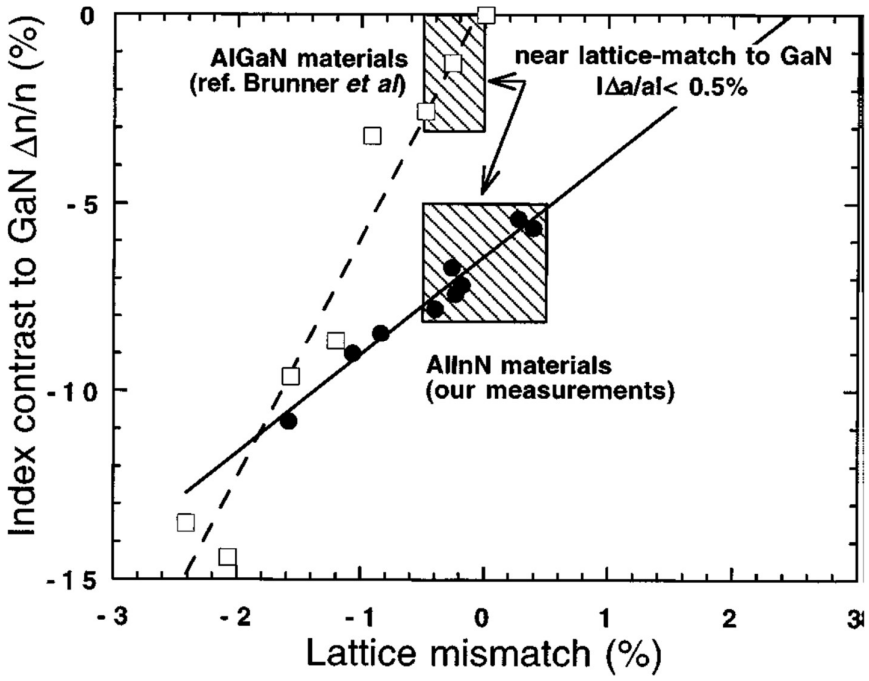

Figure 8: Relationship of lattice mismatch to refractive index contrast as composition is varied for AlInN and AlGaN, for the polar (c-plane) growth direction. Reproduced from Carlin et al., with permission [76]. AlGaN measurements from Brunner et al. [77].

Constructing epitaxial DBRs using layers with mismatched lattice parameters will lead to strain in the DBR that builds up as more layers are added. Eventually this will cause unacceptable wafer bowing or cracking, so there is a practical limit on the reflectance of AlGaN DBRs; even with large differences in composition and additional strain management,

reflectance of about 98% at 410 nm with a 30-pair DBR is reported [78]. Using AlN interlayers to partially relieve strain allows for the growth of the 60 pairs needed to reach 99% reflectance [79]. However, such large DBRs increase the mode volume, directly reducing the Purcell factor, and the narrow stop-band inherent to low-contrast DBRs makes engineering a practical cavity more difficult since the reflector centre wavelength must be matched more precisely to the cavity resonance.

AlInN is theoretically more suitable for DBR applications due to the potential for a close lattice match to GaN. However, the refractive index contrast is only about 7% for lattice-matched DBRs, requiring a large number of repeats to get a sufficiently high reflectance [76], with 99.4% reflectivity reported on a crack-free DBR with 40 repeats [80], and 99.9% with 46 repeats [81]. AlInN also presents growth problems at widely used growth temperatures of ~820ºC. Due to the low temperature, slow growth rates are used to compensate for the lowered surface mobility and avoid surface roughening. Typically, rates of around 0.2-0.5 μm/hour are used, which are substantially lower than the 2-4 μm/hour typically used for GaN growth [82]. This is a particular issue when considered together with requirement for 30-40 repeats to achieve high reflectivity.

1.6.4 Porous GaN DBRs

A more recent approach to forming DBRs in GaN is to introduce porosity into alternating layers of material [83]. If the pores are at least an order of magnitude smaller than the wavelength of light, the porous layer behaves as a homogeneous layer of lower refractive index [84, 85]. In this case, the refractive index of a porous GaN layer can then be estimated by using a simple weighted average of the permittivity of air and GaN; converted to refractive index, this gives, for a porosity fraction φ [86]:

$$n_{porous} = \sqrt{\varphi\, {n_{air}}^2 + (1-\varphi)\, {n_{GaN}}^2}$$

Equation 5

The porosity can be induced using an electrochemical [87] or photoelectrochemical [88] etch that is selective for the conductivity of the material, allowing particular layers (grown with, for example, a high n-dopant concentration) to be selectively porosified. This process is outlined in Figure 9.

The first step in creating a porous GaN DBR therefore involves creating a latent DBR structure during growth, by growing alternating layers of highly n-doped GaN and undoped material.

The n-doped layers are then porosified by electrochemical etching in one of two ways: the electrochemical etch can be made to proceed laterally, etching all the DBR layers simultaneously and proceeding horizontally through the sample; or the sample can be etched vertically, etching the layers sequentially from top to bottom. Surprisingly, the etchant can access layers buried under undoped GaN through dislocation-related channels, leaving the surface largely intact [89].

In both cases, the GaN wafer is immersed in an electrolyte (oxalic [84] and hydrofluoric [90] acids have been demonstrated in the literature, among others). The lateral etching process requires trenches to be etched in the sample to provide the etchant with access to the latent DBR layers, and the top layer is typically protected with a layer of dielectric (e.g. SiO_2) to suppress surface etching. The vertical process requires no pre-processing and can be used to etch full wafers of GaN.

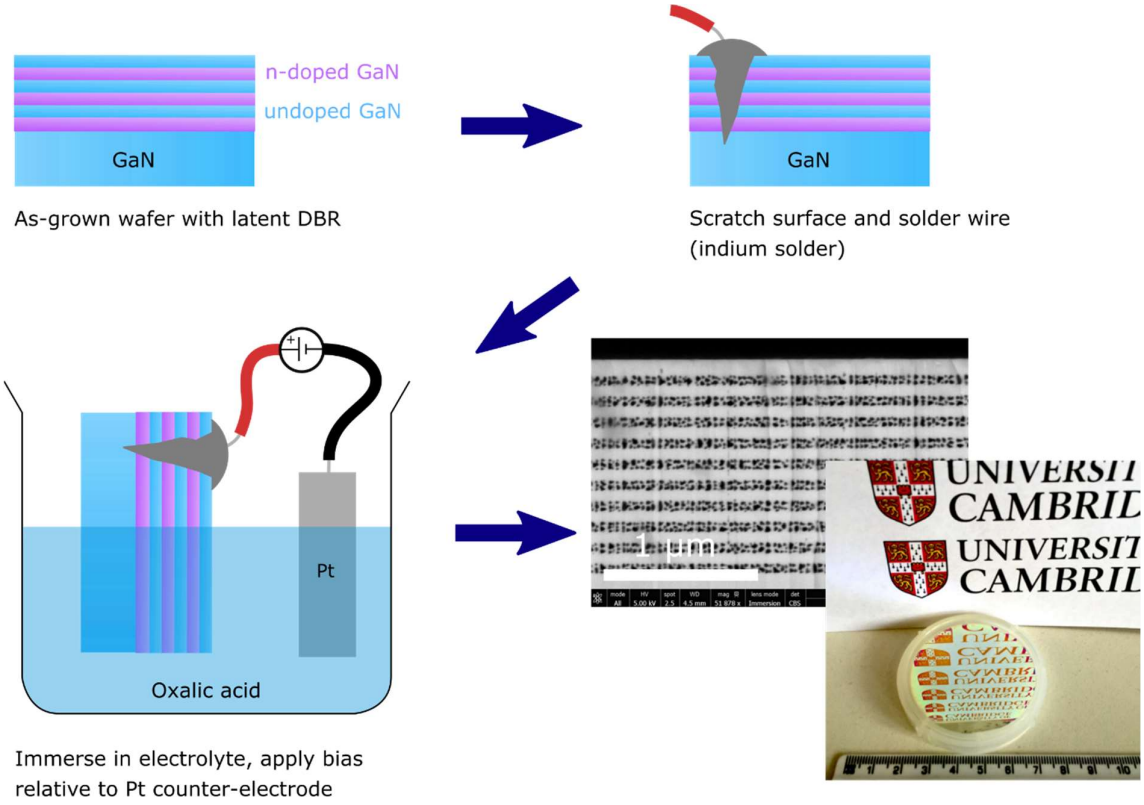

Figure 9: Electrochemical etching procedure. A latent DBR is grown in a GaN wafer, consisting of alternating layers of n-doped and undoped GaN. The layers are contacted by scratching the wafer and connecting a wire with indium solder. The layers are then etched in oxalic acid (or another suitable electrolyte), producing porosity in the n-doped layers and creating a high-reflectivity DBR. The etch can proceed vertically through the top surface, or laterally along the layers. Photograph of wafer by Tongtong Zhu.

Reports of >99% reflectivity at wavelengths around 400 nm exist for both techniques [70, 84], indicating that porous DBRs may be suitable for use in high-Q microcavity applications.

1.6.5 Air-gap DBRs

The highest refractive index contrast can be created by complete etching of the GaN to leave air gaps, creating a DBR from a stack of suspended membranes of solid GaN. Air-gap DBRs can be produced using the electrochemical etching of n-doped GaN layers in hydrofluoric acid, in a similar technique to that used for the creation of porous GaN. This approach can give high reflectivity within a small number of repeats, with >98% reflectivity reported for a 4-pair DBR [91].

Optical microcavities in non-polar m-plane GaN based on air gap/GaN DBRs have also been demonstrated with a quality factor of 1600 [92]. The layers were formed by depositing a few

periods of AlGaN alternating with GaN, patterning with e-beam lithography and RIE, and then a 30 minute anneal at 1070ºC was used to decompose the GaN while leaving the AlGaN in place. While this process produced high-quality cavities, the anneal would be likely to destroy any InGaN active layers present in the sample.

One downside to air-gap DBRs fabricated by any method is that the GaN membranes must have mechanical support, which limits the possible device geometries. Electrical injection vertically through the DBR is also not possible, and the air gaps may also affect heat dissipation. These factors are particularly important for GaN VCSEL applications [70], but is unlikely to be a problem in single-photon sources due to the lower current requirement.

1.6.6 Optical microcavities

Optical microcavities are structures which confine light to a small volume of material, on the order of the wavelength of the confined light [66]. These structures can be used to improve the performance of an SPS by enhancing the radiative rate of optical transitions around a particular photon energy [93].

The quality of an optical cavity depends on the losses from the cavity mode. Typically, either the quality factor (Q) or the finesse ($\mathcal{F}$) is used to express the magnitude of the losses. Finesse is determined by the full width of a resonance peak at half its maximum intensity (FWHM), divided by the free spectral range (the spacing of the cavity modes in frequency space – which is the inverse of the round-trip time for a pulse confined in the cavity). The finesse is related directly to the losses from the cavity, by the relation:

$$\mathcal{F} = \frac{\pi}{2\sin^{-1}\left(\frac{1-\sqrt{\rho}}{2\sqrt[4]{\rho}}\right)} \approx \frac{2\pi}{1-\rho} \text{ (in the limit of low losses, i.e. } \rho > \sim 90\%)$$

Equation 6

where ρ is the fraction of power remaining after one round-trip through the cavity.

The quality factor is defined as 2π multiplied by the fraction of energy lost per cycle of the field, and therefore depends on the round-trip time as well as the frequency of the optical radiation.

$$Q = \nu_0 t_{rt} \frac{2\pi}{1-\rho} \approx \nu_0 t_{rt} \mathcal{F} \approx \frac{\nu_0}{\Delta\nu}$$

Equation 7

where $\Delta\nu$ is the FWHM of the resonant peak in frequency space, ν_0 is the resonant frequency and t_{rt} is the round-trip time of the radiation in the cavity. The relationship between the finesse and the FWHM is exact in the limit of large Q.

The confinement provided by an optical microcavity has the effect of increasing the density of photon states at the resonance wavelength. For a transition between an exciton in a quantum dot to a photon in the cavity, Fermi's golden rule indicates that an increase in the density of final (i.e. photon) states enhances the spontaneous emission rate. This means that embedding a quantum dot in an optical microcavity should increase the emission rate, improving brightness and linewidth, and this increase is given by a quantity called the Purcell factor. For confinement in three dimensions, and assuming that the emitter is a dipole with a linewidth smaller than that of the cavity, positioned at the field maximum and resonant with the cavity mode, the Purcell factor is:

$$F_P = \frac{3}{4\pi^2}\left(\frac{\lambda_c}{n}\right)^3 \frac{Q}{V}$$

Equation 8

where λ_c is the vacuum wavelength of the mode and n is the refractive index of the cavity [66]. The magnitude of cavity enhancement therefore depends on the quality factor Q and the mode volume V (which is related to the physical dimensions of the cavity).

Another advantage of the use of an optical cavity properly tuned to the emission wavelength of a single-photon source is that the density of photon states for off-resonant transitions is reduced, improving the purity of the of the signal by removing contamination by unwanted transitions (such as those associated with the QW or other nearby QDs or defects) and further increasing the efficiency of the desired single-photon emission. This also shows the importance of matching the emission wavelength to the cavity wavelength, since the cavity will have the opposite of the intended effect if the QD emission spectrum is away from the cavity resonance peak. Likewise, if the QD is spatially positioned away from the field maximum of the cavity mode, the cavity will suppress, rather than enhance, its emission [67].

Several types of optical cavity have been demonstrated in GaN: microdisk cavities [94], micropillar cavities [95, 96], and various types of photonic crystal defect cavities [97, 98]. These are discussed in the following sections.

1.6.6.1 Micropillar cavities

Micropillar cavities are an important application of DBRs. The reflectors are inserted above and below an active layer (for example, a layer of quantum dots), forming a planar cavity that confines photons in the direction normal to the plane. The micropillar cavity is then completed by etching a column into the planar structure, confining photons laterally with a semiconductor-air interface. The structure of a finished micropillar cavity is rendered in Figure 10.

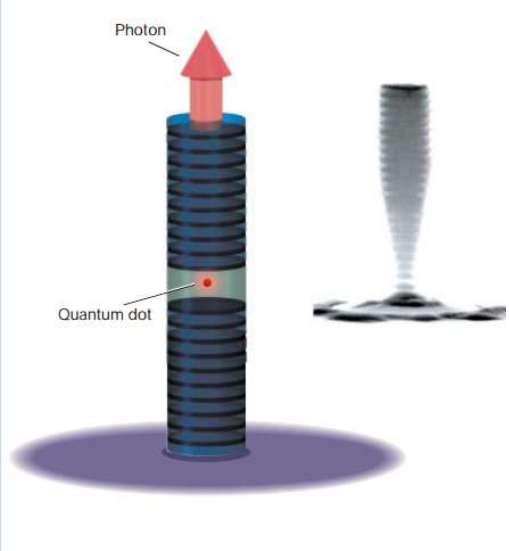

Figure 10: Rendering and SEM image (inset) of a micropillar cavity containing a quantum dot. Reproduced from Vahala et al., with permission [66].

Such cavities, realised in GaAs (and incorporating InAs QDs and AlAs/GaAs DBRs), show high Q-factors of up to 268,000 [99]. These high-Q structures were fabricated in GaAs using e-beam lithography and a nickel hardmask to resist reactive-ion etching, and are shown in Figure 11. This illustrates the smooth sidewalls and deep, anisotropic etch that is required for such high-Q cavities.

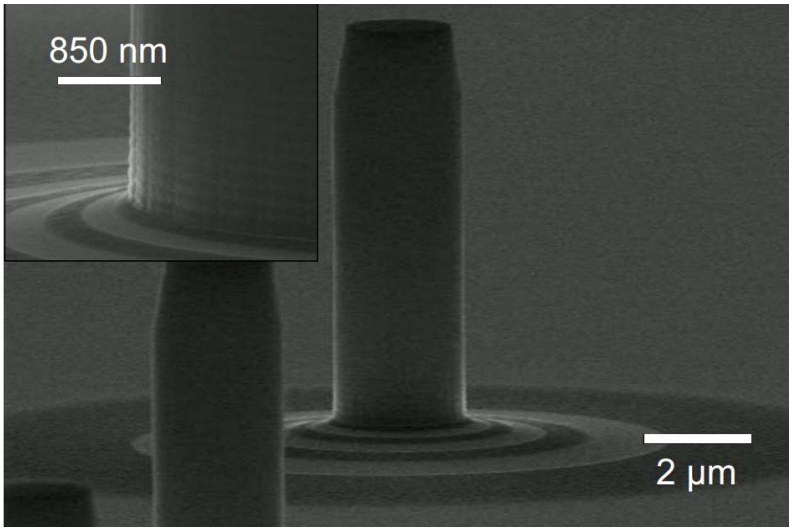

Figure 11: SEM image of high-Q optical micropillar cavities, fabricated in GaAs. From [99]

Another interesting geometry consists of a micropillar cavity connected to a surrounding mesa using fins. This has been demonstrated [100] for InAs QDs in GaAs, using a deterministic method to find QDs and pattern the cavities around them using a patterning laser to expose photoresist [101]. Even without this level of sophistication, this connected-pillar geometry could be useful for connecting electrical contacts to cavities. The Q-factor was determined to be 35,000, showing that micropillars with fins can be used as a functional high-Q cavity, at least at the emission wavelengths of InAs dots. An optical micrograph of one of these cavities is presented in Figure 12.

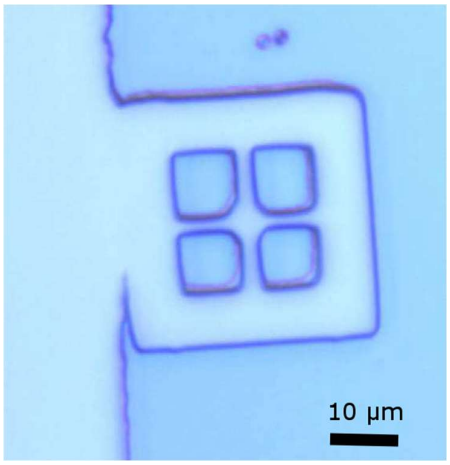

Figure 12: Optical micrograph of a connected micropillar cavity fabricated in GaAs. Reproduced from Nowak et al. [100], under a Creative Commons BY-NC-ND licence (http://creativecommons.org/licenses/by-nc-nd/3.0/).

Another strategy for achieving electrical injection into pillars is to planarise the sample after pillar fabrication, using a flowable material to fill in the gaps between pillars. As this process replaces air at the edge of the cavity, a low refractive index material needs to be used to maintain a high degree of optical confinement in the cavity. For example, benzocylcobutene (BCB) can be used for this purpose [102]. Their planarization process involves spinning BCB to a thickness exceeding the height of the pillars, and then etching the surface of the polymer to expose the tops of the pillars SEM images of Figure 13.

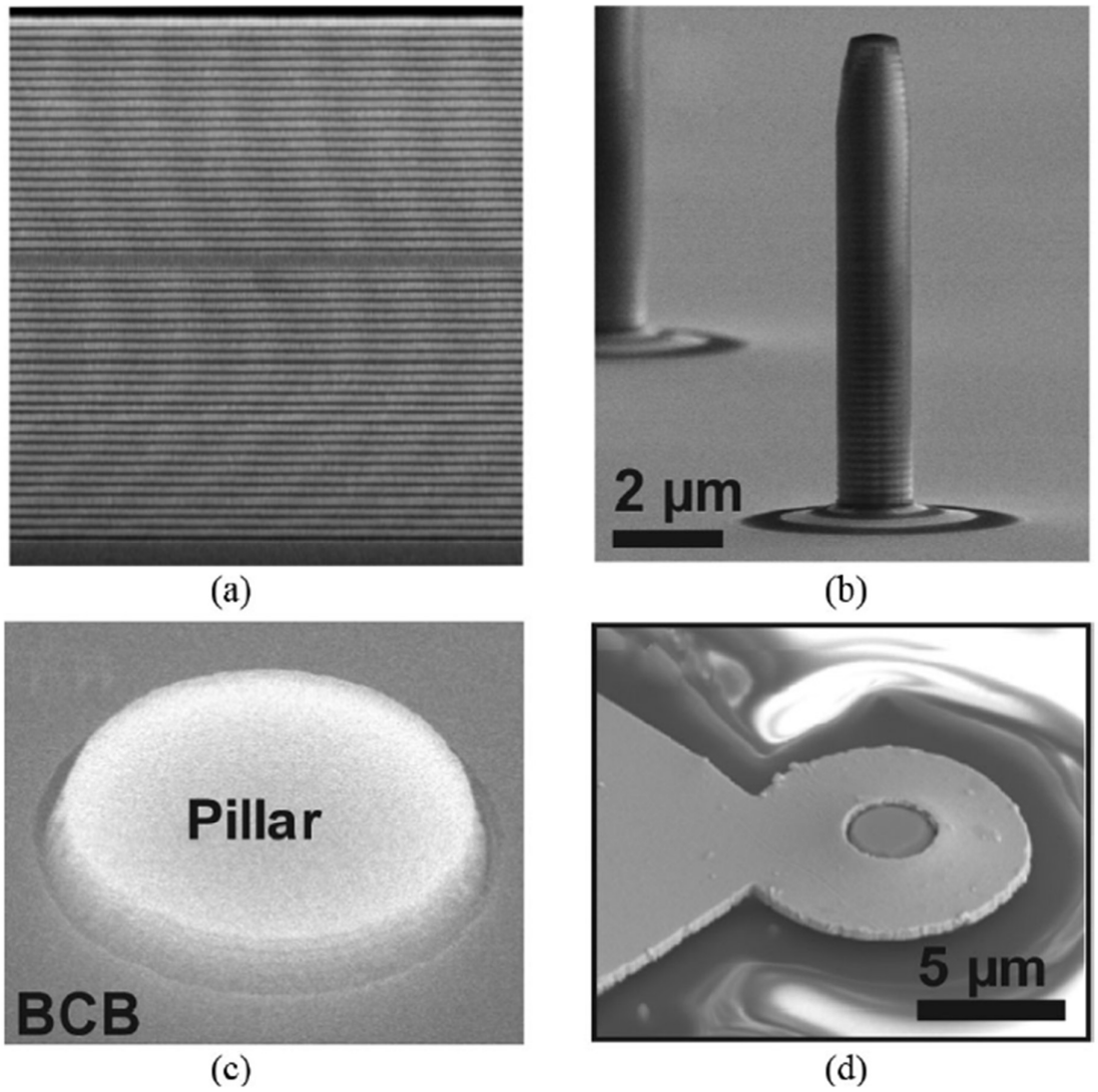

Figure 13: Electrically contacting micropillars using BCB and etch-back planarization. (a) Cross-sectional view of distributed Bragg reflector. (b) Etched pillar containing top and bottom DBRs. (c) BCB coating added and etched back to expose only the end of the pillar. (d) Finished structure including metal top contact. Reproduced with permission from [102].

Micropillars in GaN have been fabricated using focused ion beam patterning [96], reactive-ion etching with metal masks [95], reactive-ion etching with a SiO_2 mask [92] and by bottom-up growth using patterned templates [103].

Micropillars in c-plane GaN fabricated by focused ion beam (FIB) milling were reported by El-Ella *et al.* [96]. These cavities use a 20-period AlN/GaN reflector as the bottom DBR, and a dielectric DBR as the top reflector. These cavities showed quality factors of around 200-450, and backscattered electron diffraction patterns indicated that the FIB produces a layer of amorphous GaN at the edges of the cavities that increases in thickness with milling current. Lower currents produce rougher sidewalls, which also reduce the quality factor of the cavities, and so a compromise was found that gives the best micropillar quality.

Tao *et al.* [92] demonstrate dry-etched micropillar cavities in m-plane GaN with higher Q-factors of around 1600, shown in Figure 14. These were produced using a SiO_2 mask patterned by electron-beam lithography, followed by a dry etch using inductively coupled plasma reactive ion etching (ICP-RIE) with Cl_2 and Ar to pattern the GaN. The distributed Bragg reflector structure was then produced by thermal decomposition of AlGaN layers, described in section 1.6.5. This connected-pillar geometry might also be useful in creating QD-containing micropillar cavities incorporating porous DBRs, if the etch requires the layers to be connected directly to the anode. Thermal decomposition cannot be used for cavities containing QDs, because the active layers would also be decomposed.

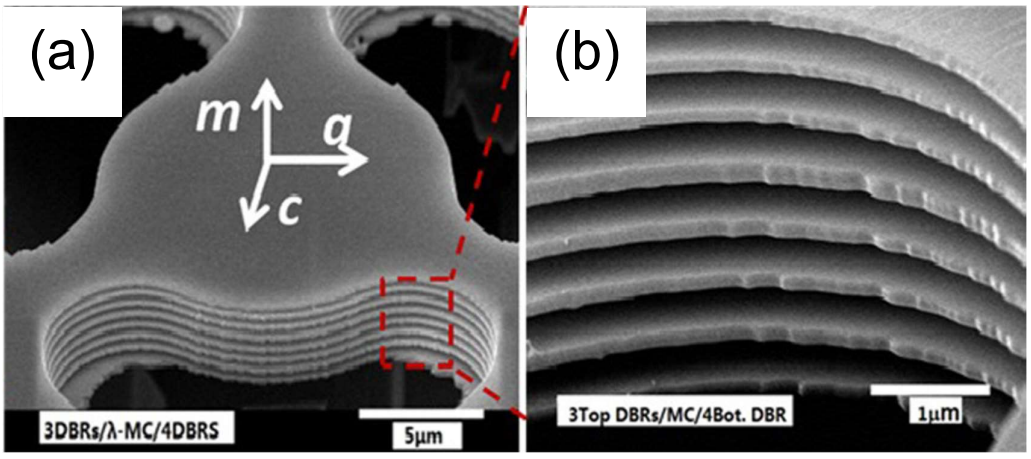

Figure 14: Air-gap DBRs in non-polar GaN reported by Tao et al. (a) Overview of pillar structure with air-gap DBR, indicating c- and a-axis in plane and m-axis out of plane. (b) Detail of air-gap DBR and etched sidewalls. Reproduced with permission from [92].

Debnath *et al.* [95] and Krylyuk *et al.* [104] demonstrate arrays of nanopillars, using a Ti/Ni etch mask patterned by deep-UV lithography to resist ICP-RIE of c-plane GaN. However, these structures were then used for growth of core-shell structures, and there are no data on how well this technique works for optical microcavities. Debnath *et al.* also used a wet etch comprising KOH in ethylene glycol, at 40°C, to attempt to remove plasma-induced etch damage. They observed an increase in photoluminescence intensity from the GaN after etching, coupled with a roughening of the etched surface. It is unclear whether the increased intensity is due to removal of surface damage that could produce a number of non-radiative recombination sites, or if the increase is simply attributable to improved light extraction due to the roughening [95].

1.6.6.2 Microdisk cavities

Microdisk cavities use total internal reflection of light in a disk-shaped structure to create confined photon modes. The modes, termed whispering-gallery modes after their acoustic counterparts, are travelling wave modes that exist around the rim of the disk [66]. They are generally capable of high Q-factors, with experimental values in the range ~10^5 [66].

Such cavities require formation of a pillar, followed by an undercut etch to isolate the disk from the surrounding material (but leaving a central stalk for support). The undercut etch must be both isotropic and selective, which means that wet-chemical etches are usually employed. Low-index layers or DBRs can also be used.

Tamboli *et al.* [105] report a process for making microdisks in c-plane GaN based on a photoelectrochemical (PEC) undercut etch. Electron-beam lithography is used to pattern a SiO_2 hardmask, which is used to resist ICP-RIE etching of GaN to form 300 nm deep micropillars. This is followed by the PEC etch, using illumination from a 1 kW xenon lamp in 0.004 M HCl, which selectively removes a high indium content sacrificial superlattice (consisting of alternating layers of high and low indium content material). Aharonovich *et al.* [106] report a similar process, but one that uses silica microspheres as a mask for ICP-RIE for improved circularity of the disks. These cavities showed a high Q-factor of around 6000, and an example of a cavity is shown in Figure 15.

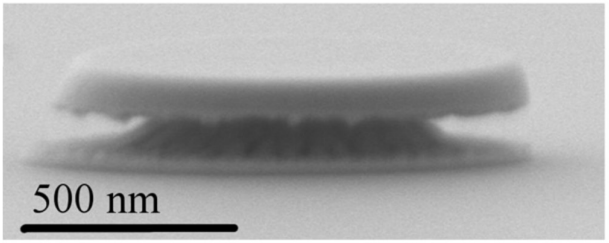

Figure 15: Microdisk cavity in GaN fabricated by ICP-RIE and a photoelectrochemical undercut etch. From Aharonovich et al., with permission [106].

1.6.6.3 Photonic crystal defect cavities

A photonic crystal defect cavity uses Bragg diffraction from a periodic array of holes to provide optical confinement in a defect introduced into this periodic array. Usually, the photonic crystal (PC) is used to provide confinement in two dimensions in a membrane, with a semiconductor-air interface providing confinement in the third dimension. They are capable of similarly high Q-factors to microdisk cavities [66].

One example of a PC structure was fabricated by Lu *et al.* [107] in c-plane GaN, and a PC defect cavity fabricated in the same way was investigated in a-plane GaN by Kao *et al.* [108]. The PC was fabricated using e-beam lithography to first pattern a SiN_x hardmask in one ICP-RIE process, followed by a second ICP-RIE step to pattern the GaN into the periodic array of holes. A FIB was then used to undercut the structure, and form the PC membrane. This structure is shown in Figure 16. These cavities were reported to show quality factors of up to 4,300.

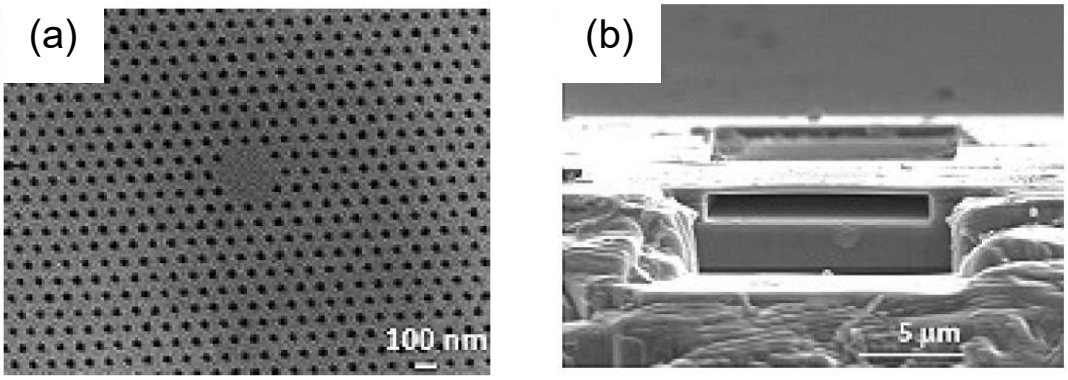

Figure 16: (a) Photonic crystal defect cavity patterned by e-beam lithography and a SiN_x masked ICP-RIE etch into GaN. (b) PC membrane undercut using FIB. Reproduced with permission from Kao et al. [108]. © 2016 IEEE.

Another type of PC-defect cavity is the nanobeam, which uses a 1D PC and GaN-air interfaces to confine light to the small volumes between holes in the beam, shown in Figure 17. The quality factor of these cavities, fabricated by a two-step e-beam lithography process, ICP-RIE and photoelectrochemical undercut etch, ranged from 1300-1900 [98].

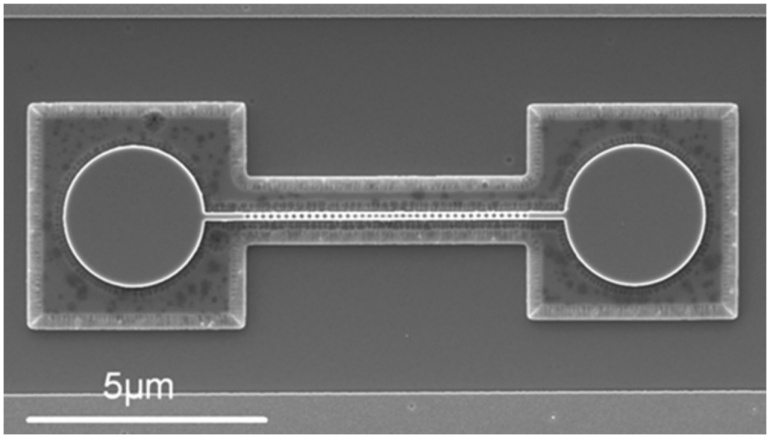

Figure 17: Nanobeam cavity. Reproduced from Niu et al., with permission. [98]

1.7 Thesis structure

This thesis will explore the materials science of InGaN QDs and QWs in a GaN matrix, particularly QDs grown on the non-polar a-plane of GaN due to the potential advantages of such field-free nanostructures for fast single-photon emission. First, the growth, structural and optical properties of a-plane GaN QDs will be investigated with a new technique (cathodoluminescence in the scanning transmission electron microscope, or STEM-CL). Then, electrical injection and extraction efficiency enhancement will be investigated on planar quantum-well samples, with fabrication routes for GaN LEDs investigated and applied to a novel device, a LED overgrown on a porous GaN distributed Bragg reflector (DBR). This QW device is intended to provide a future platform for related QD devices. Potential fabrication strategies for optical microcavities based on porous GaN DBRs will then be explored, and finally electrical injection into a-plane InGaN QDs will be demonstrated for the first time.

Chapter 2

2Methods

2.1 Sample growth

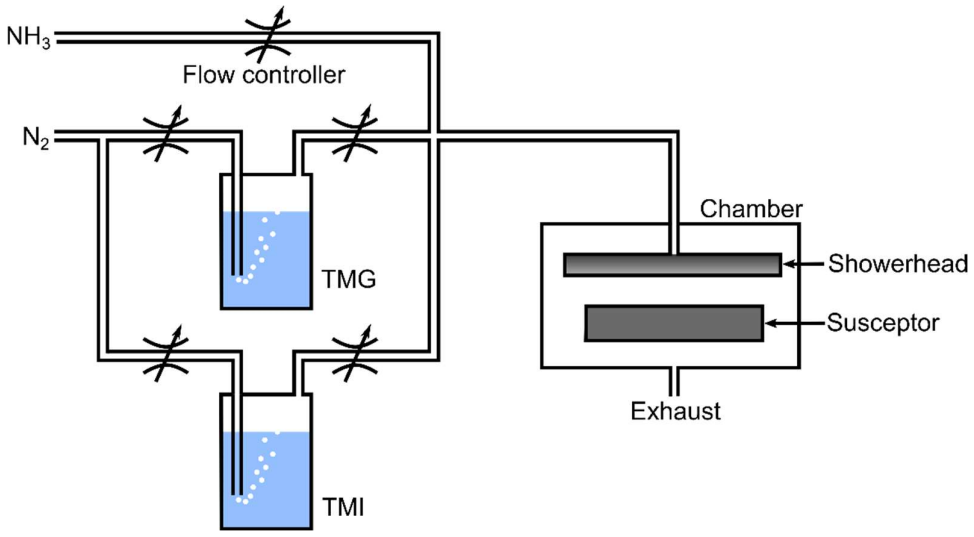

Figure 18: Simplified schematic of MOVPE reactor, showing main gas lines, metalorganic bubblers for trimethylgallum (TMG) and trimethylindium (TMI), the showerhead for gas distribution in the chamber and the heated susceptor that carries the wafers.

GaN samples were grown using metalorganic vapor-phase epitaxy (MOVPE), using a gas phase reactor. This process uses metalorganic precursors that are carried into a reaction chamber by a flow of carrier gas (typically N_2 or H_2). Gas-phase precursors can be mixed

directly into the carrier gas, and metalorganic precursors that are in the liquid phase at room temperature are vaporised using a bubbler.

The growth chamber consists of a cold-wall reactor with a heated susceptor. The process gas mixture is introduced into the chamber via a showerhead that is designed to give uniform flow rates across the entire growth area. The susceptor is also designed to keep the temperature as uniform as possible. Owing to its viscosity, the velocity of the gas is slowed in proximity to the susceptor, forming a boundary layer near to the wafer, and the growth rate is limited by mass transport across this boundary layer [109]. The temperature of precursors moving in the boundary layer rapidly increases as they approach the heated susceptor, causing them to decompose via pyrolysis and react at the substrate to form the desired crystal.

Deposition rates are dependent mostly on the thickness of the boundary layer, while the composition and quality of the resulting film depends on the surface temperature of the wafer and the precursor ratios. Most of the technology of MOVPE reactors is aimed at keeping these parameters well-controlled and as uniform across the growth area as possible. Altering the precursor mixture during growth allows heterostructures to be grown by MOVPE, with monolayer-level control over the thickness of these layers, and atomically sharp interfaces. This is very useful for constructing e.g. quantum wells.

The wafers used in this project were grown by Dr Tongtong Zhu in a Thomas Swan close-coupled showerhead reactor capable of growing on up to six 2″ substrates. The precursors used are given in Table 1.

Material	**Precursor**
Ga	Trimethylgallium (TMG)
N	Ammonia
In	Trimethylindium (TMI)
Si (n-doping)	Silane
Mg (p-doping)	bis-(cyclopentadienyl)magnesium (Cp_2Mg)

Table 1: Precursors used in MOVPE growth processes.

A limited set of substrate materials are suitable for growing GaN by MOVPE; for GaN, these are sapphire, silicon, and 4H- or 6H-SiC.

2.2 Sample processing

The grown samples were processed to create electrical and optical devices. This requires the use of lithographic processes, etching, metal deposition and insulator deposition. Full details of processes used in this thesis are supplied in the relevant chapters.

2.2.1 Cleaning

Wafers were cleaned before processing by ultrasonicating in acetone to remove particulates and soluble organics, rinsing in isopropyl alcohol (IPA) to remove acetone residues, and drying with a flow of nitrogen gas. Bare GaN wafers were then subjected to a final clean in Piranha solution (a mixture of 3:1 H_2SO_4:H_2O_2) to remove any remaining organic contamination and promote resist adhesion, prior to drying and a dehydration bake on a hotplate.

2.2.2 Lithography

The lithography techniques used in this project transfer a designed geometry into a polymer film, which is then further processed to transfer the pattern into the final material (e.g. metal, insulator or semiconductor). Lower-resolution patterns, with a practical minimum feature size of about 2 μm, can be patterned using ultraviolet (UV) lithography while smaller feature sizes require electron-beam lithography.

2.2.2.1 UV contact lithography

In this project, UV contact lithography was used for patterning larger features. In this process, a quartz mask is produced with the required pattern in a chrome layer on the surface. The masks were designed using CAD software (LayoutEditor) and produced commercially by Compugraphics Ltd.

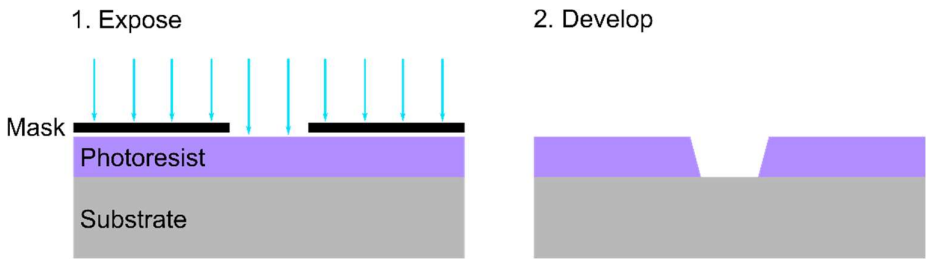

Figure 19: UV contact photolithography process.

The mask is brought into contact with a sample coated with UV-sensitive optical resist and exposed to UV light. The mask is then removed and the resist is immersed in development solution, which removes the exposed areas if the resist is 'positive tone' or the unexposed areas if the resist is 'negative tone'. The process is shown schematically in Figure 19 for positive tone resist. To obtain sufficient contrast between exposed and unexposed regions, i.e. ensuring that the exposed areas can be developed through their entire thickness without eroding the unexposed areas too much, the fluence of UV light used in the exposure must be high enough. However, higher exposures also lead to lower resolution, as areas unintentionally exposed by diffraction from the mask edges or scattering in the resist receive a higher dose and may be eroded more quickly by the developer. There is therefore an optimum dose that can be found for a particular development time that maximises resolution while still providing sufficient contrast.

2.2.2.2 Electron beam lithography

Electron-beam lithography uses a polymer resist that is sensitive to electron irradiation. The sample, coated with a layer of this resist, is placed into a tool which can selectively scan an electron beam across the sample using deflection coils, similarly to a scanning electron microscope (SEM). The resulting regions of exposed resist may then be developed, forming the required pattern.

The effect of dose in e-beam lithography is similar to UV lithography; a threshold dose needs to be reached to ensure proper development of exposed features. The electron beam also travels through the resist and scatters extensively in the substrate, with backscattered and secondary electrons returning and generating a background dose that varies with distance from an exposed area. This means that closely spaced features may require a lower dose from the primary beam than more widely spaced features, and regions near the centre of

large exposures will require a lower dose than regions near edges or corners. Such effects can be compensated manually in the pattern design or calculated with Monte Carlo scattering simulations and compensated automatically.

E-beam lithography in this project was carried out using a Crestec CABL e-beam lithography tool, and patterns were made by hand in LayoutEditor.

2.2.3 Plasma processes

Several devices produced in this project require dry etching of either dielectrics (silicon nitride or silicon dioxide), or semiconductor (GaN). For this purpose, reactive-ion etching (RIE) and inductively-coupled plasma reactive-ion etching (ICP-RIE) are used.

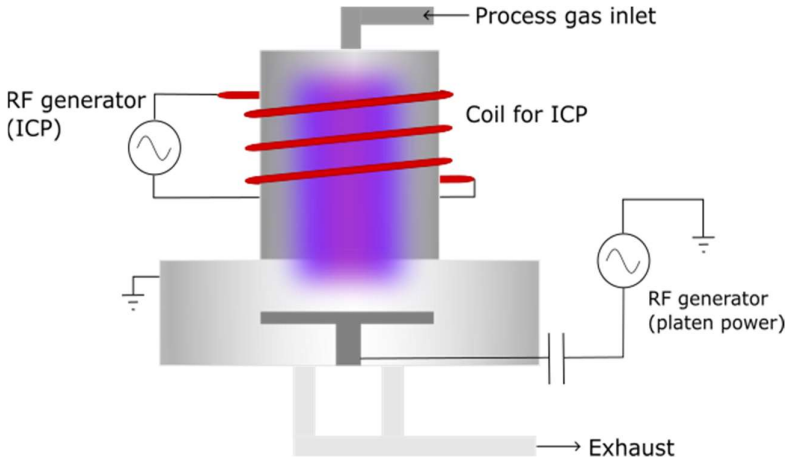

Figure 20: Schematic of an ICP-RIE system

The ICP-RIE (Figure 20) consists of two main parts: a RF coil wrapped around a chamber, and a sample chuck. Gases can flow into the chamber from the top and are pumped out of the bottom at a rate that maintains a certain overall chamber pressure. The gas inlet is connected to several mass-flow controllers (MFCs) which control the rate at which different process gases flow into the chamber, while the exhaust is usually connected to a high vacuum pump via an adjustable valve. The coil around the upper half of the chamber creates an inductively-coupled plasma, and the RF generator connected to the chuck can be used for two purposes: it can strike a capacitively coupled plasma alone (for etching without the ICP), and it can also be used to create a D.C. bias between the plasma and the wafer being etched.

This D.C. bias arises because electrons have a significantly higher mobility than the reactive ions in the plasma. This means that, on each cycle of the RF generator, electrons can move from the plasma to the chuck while the heavier, positively-charged plasma ions remain approximately stationary. Because the chuck is capacitively coupled to the RF source, electrons which arrive there are trapped, and the average number of electrons on the chuck increases. This then leads to a negative D.C. bias with respect to the surrounding grounded chamber and the plasma [110].

The bias attracts ions from the plasma to the sample, increasing the kinetic energy of the reactive species normal to the sample surface. Increased bias thus causes more physical bombardment of the sample, generally making the etch more anisotropic, at the cost of increased surface damage. Lower chamber pressure can also increase bombardment by increasing the mean free path.

Adjustment of the bias is achieved by changing the RF power supplied to the chuck. If the etcher were not equipped with an ICP coil, this would also reduce the density of the plasma. However, the ICP coil allows the plasma density to be controlled more-or-less independently of the D.C. bias. This has the principal advantage of keeping the plasma density high while the D.C. bias is reduced or permitting a higher plasma density (and a faster etch) for a fixed bias.

Plasma-enhanced chemical vapor deposition (PECVD) processes run in a similar process chamber to that used for RIE, although the capacitive isolation from the RF source is removed, removing the D.C. bias, reducing bombardment of the substrate, and encouraging deposition rather than etching. This process is used in this project for depositing dielectrics (silicon dioxide and silicon nitride).

2.2.4 Metal deposition

Metals, used for electrical contacts and hard-masks for dry etching, are deposited by physical vapour deposition (PVD). In this class of processes, a flux of neutral metal atoms is created in a vacuum chamber, which deposit on the sample without any surface reaction. Thermal evaporation is a PVD process that uses resistive heating of a tungsten boat to evaporate the metal, and was used for most metals (Au, Ti, Al, and Ni). Electron-beam evaporation instead

uses a defocused beam of electrons to directly heat a region of material contained in a crucible, allowing for higher temperatures and faster evaporation rates, and was used for Cr depositions.

2.2.5 Metal patterning

Metal patterning is achieved either by lift-off or etching.

Lift-off involves evaporating the metal on to a resist pattern, then removing the resist, leaving behind metal that was evaporated on to the sample surface. In this case, the standard photoresist process is modified to ensure an overhang is created at the edges of the resist pattern, allowing for a clean edge to the lifted-off metal. This is achieved using a pre-development soak in chlorobenzene, to reduce the solubility of a thin layer at the top of the resist film so that the required profile is produced after development as shown in Figure 21. The e-beam process is modified to use a bilayer, with a thin layer of lower-sensitivity resist spun on top of a higher-sensitivity resist. This also provides the required undercut profile.

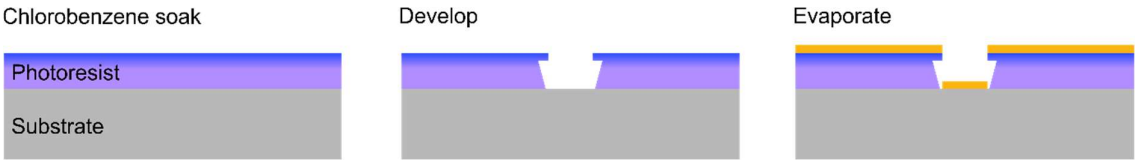

Figure 21: Resist profile created by chlorobenzene soak, suitable for lift-off processes.

Etching requires the use of a wet-chemical or dry etch process to remove metal after it has been deposited on the sample surface, with lithography carried out after metallisation. Ceric ammonium nitrate was used for wet etching of chrome in this project.

2.2.6 Contact annealing

Ohmic contacts to devices often require a post-deposition anneal, to allow diffusion and mixing between different metallic components, reactions at the metal-semiconductor interface, or to ensure intimate contact of the semiconductor surface and the metal layer. Anneals are typically carried out by rapid thermal annealing, where the wafer is heated by radiant heat from halogen lamps, allowing for very fast ramp times and short annealing times on the order of a few minutes.

2.2.7 Bonding

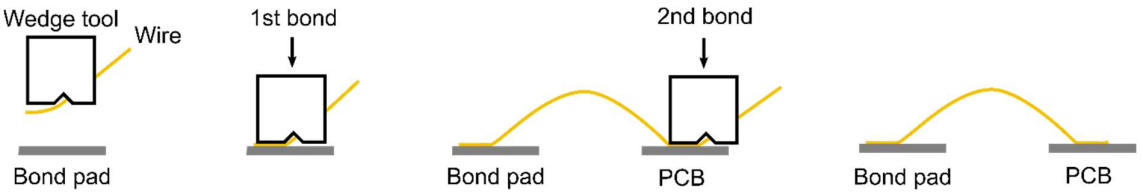

Figure 22: Illustration of the wedge bonding process between a metal bond pad on the sample and a pad on a printed circuit board (PCB).

Electrical contact was made to the devices by wedge bonding, which attaches a wire to the metal pads on the sample using a burst of ultrasonic energy as shown in Figure 22. The force applied to the pad, and the duration and power of the ultrasonic pulse are tuned to obtain a reliable bond without damaging the underlying pad.

2.3 Scanning electron microscopy

A scanning electron microscope (SEM) probes a sample with a beam of electrons, generated by a thermionic or field emitter, and focused to a small spot using electromagnetic lenses. The sample emits various forms of energy while it is being irradiated with the electron beam, and this can be sensed with a variety of detectors.

A diagram of the interaction of the beam with the sample is shown in Figure 23. The electrons scatter in the material, interacting with a teardrop-shaped volume of the sample, and the different signals that can be detected are generated at various depths. Topographical contrast is generated from varying efficiency of emission depending on how close the interaction volume is to the surface.

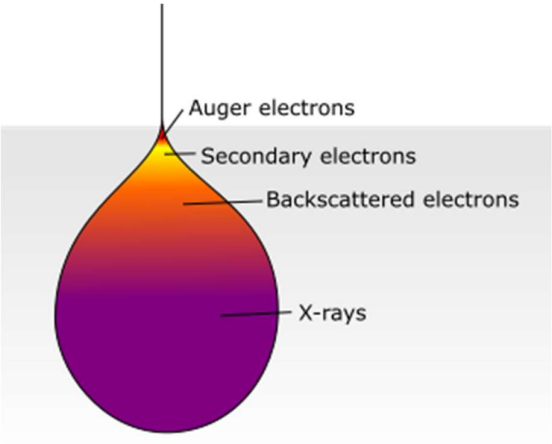

Figure 23: The different signals generated by interaction of electrons with the sample in SEM.

Secondary electrons (SEs) are electrons that are released from the material due to bombardment from the higher-energy electrons from the beam. They are emitted from the sample with relatively low kinetic energy (typically less than 50 eV), and can therefore be sucked into a detector located in the chamber with a modest positive bias of around 300 V applied to a grid covering the detector opening. Due to the suction effect of these detectors, they collect electrons emitted at a variety of angles from a sample. In practice, this means that secondary electron images appear as if illuminated by a diffuse light coming from the position of the detector.

Backscattered electrons (BSEs) are electrons from the incident beam which are scattered directly from atoms in the sample. This means that the yield of BSEs strongly depends on the composition of the sample, and they can therefore be useful for generating compositional contrast. BSEs generally have much higher energies than SEs (up to the beam energy), and therefore travel undeflected from the sample to the detector. The straight paths of electrons mean that BSE images appear as if illuminated by a point source of light coming from the detector. The increased energy also means that BSEs can escape from deeper beneath the surface of the sample compared to SEs.

X-rays emitted via the ionisation and subsequent de-excitation of atoms can also be used to obtain information about the atomic composition of a sample. A silicon drift detector is used to measure the energy spectrum of the x-rays emitted in the SEM as a function of position. This detector is made of silicon, and the degree of ionisation produced by each photon arriving in the silicon is related to the x-ray energy, allowing a spectrum of X-ray energies to be measured. Comparing the collected spectra with known X-ray transitions in pure elements allows the composition of the sample to be estimated. This technique is called energy-dispersive X-ray spectroscopy (EDS).

2.3.1 Focused ion beam

A focused ion beam (FIB) source can also be added to a SEM column. This is a source of heavy ions (frequently gallium), accelerated to several tens of keV, which is used to selectively mill away regions of material. This technique can be used to prepare samples for transmission electron microscopy (TEM, discussed in section 2.4), or to image cross-sections

at precise positions in the sample. It may also be used to fabricate micro- and nanoscale objects such as micropillars, and can be used in conjunction with a gas-injection system to deposit various conducting and dielectric materials.

2.4 Transmission electron microscopy

Transmission electron microscopy passes a high-energy beam of electrons through a very thin sample, and detectors (the simplest of which is a phosphorescent screen) located underneath the sample allow the beam-sample interaction to be investigated. Generally, TEM has the capability to produce much higher resolution images than SEM, due to the reduced interaction volume that can be achieved using a very thin sample. The achievable resolution is usually limited by the aberrations introduced by the lens system.

Many electrons in TEM interact with the sample by purely elastic scattering, and this allows Bragg diffraction to be used to generate several different types of contrast. Diffraction contrast is generated by inserting apertures in the back-focal plane (these apertures are termed 'objective apertures'), either blocking diffracted beams to form a bright-field image, or selecting a particular diffracted beam to form a dark-field image. The geometric optics of this are shown in Figure 24.

Frequently, to maximise intensity in a dark-field image, the sample is tilted so that only one diffraction condition is met. This is called a 'two-beam' condition (the other beam is the direct, undiffracted beam), and the objective aperture is placed around the strongly excited diffraction spot to form the dark-field image.

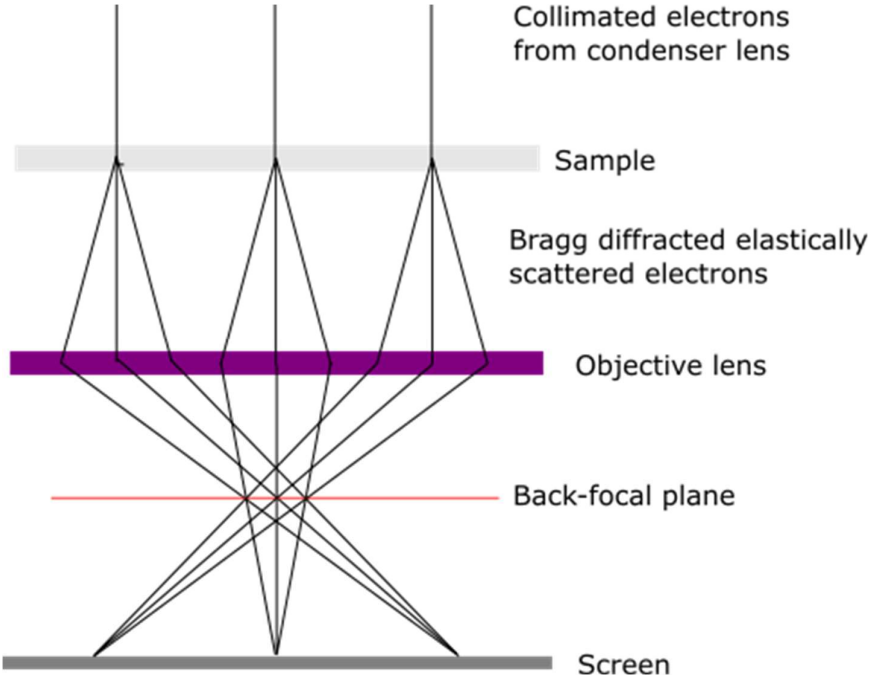

Figure 24: Geometric optics associated with forming a TEM image. Apertures are inserted in the back-focal plane to form a bright-field or dark-field image.

2.4.1 Scanning TEM

The TEM may also be operated in scanning mode (STEM). In this mode, a focused probe is scanned across the sample, and the intensity of electrons transmitted at each beam position is detected and used to construct an image in a similar way to SEM. The detectors used are a high-angle annular dark-field (HAADF) detector, and a bright-field detector. The HAADF detector is a donut-shaped detector that surrounds the optic axis of the microscope, and it collects electrons scattered to high angles (the range of angles is adjustable by changing the camera length). Such high-angle scattering is typically due to Rutherford scattering from nuclei, and is therefore highly sensitive to atomic number. This makes this technique particularly useful for generating compositional contrast.

2.4.1.1 Other signals in the STEM

Signals from other detectors can also be used to obtain position-resolved information while a sample is being imaged in the STEM. For example, EDS can be used (as in SEM) to determine the atomic composition of a sample. Cathodoluminescence may also be collected from the sample while it is being imaged in the STEM, and correlated to beam position. This is discussed in more detail in Chapter 3.

2.4.2 Sample preparation

TEM requires preparation of a sample which is electron-transparent. This may be achieved using conventional sample preparation, where the sample is cross-sectioned using a diamond saw, polished manually to a thickness of several microns using diamond lapping films and a dimple grinder, and mounted to a TEM grid made of either copper (for the techniques outlined above) or beryllium (if x-ray microanalysis is required). Alternatively, the focused ion beam system may be used to cut a thin lamella and attach it to a grid. This requires platinum deposition to protect the top surface of the lamella during milling, and for attachment to the TEM grid. Usually, this is achieved using injection of an organometallic precursor that degrades under the influence of the ion beam to deposit metallic platinum.

Milling using a relatively high-energy (5 keV), but low intensity, beam of argon ions is then performed to slowly thin the sample to electron transparency.

2.5 Atomic force microscopy (AFM)

Atomic force microscopy (AFM) is a technique that uses a sharp tip to probe surface height variations on a sample. A piezoelectric positioner scans the tip across the surface, and the deflection of a cantilever supporting the tip is measured using a laser reflected from the top surface of the cantilever.

Characterisation of samples in this report was done in tapping mode, where the tip is vibrated above the sample surface. The amplitude of vibration decreases as the tip approaches the surface, due to increased tip-sample interaction, and this is corrected by adjustment (by a feedback circuit) of the average height of the tip to maintain a constant vibration amplitude. Several other modes of operation are possible, depending on the application.

An AFM image can then be constructed from the resulting map of average tip height plotted against position in the x-y plane. Resolution is limited to several nanometres in x and y by the physical size of the tip, while the z-direction resolution is often high enough to resolve atomic steps, provided that the active feedback provided to the z-positioner is tuned adequately.

2.6 Photoluminescence

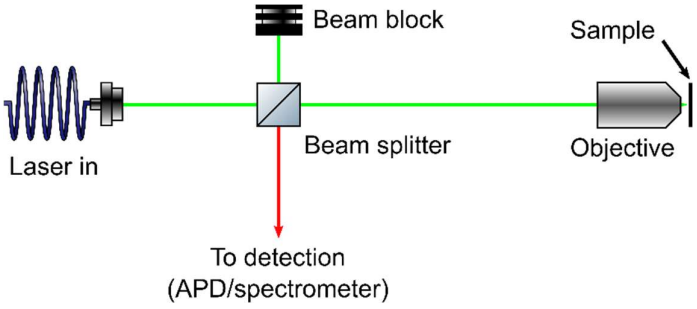

Figure 25: Simplified schematic of confocal photoluminescence setup. Spatial filtering (either using a pinhole or coupling into an optical fibre) is employed on the detection side to remove out-of-focus light.

Samples were also characterised by using a laser to excite electronic transitions and using the resulting luminescence to investigate various aspects of the electronic structure of GaN nanostructures. InGaN nanostructures can be effectively pumped with blue light at around 400 nm, and QDs can be pumped using two-photon excitation at around 800 nm [40].

In both cases, in the confocal geometry, laser is coupled into an objective lens, and the photoluminescence is collected through the same lens. A dichroic beam-splitter is used to direct the photoluminescence into the detection apparatus (avalanche photodiodes and an optical spectrometer) while filtering out the laser light, as shown in Figure 25. The confocal setup ensures that a small spatial volume is illuminated and light is collected from the same region, rejecting light from out-of-focus areas and reducing background [111].

Electronic transitions can be excited with continuous-wave (CW) or pulsed excitation. CW excitation uses continuous illumination to constantly excite these transitions. Pulsed excitation uses ultrashort pulses with a higher peak power, so that each pulse has a high probability of exciting an emitter. The time between the pulses is generally much longer than the radiative lifetime of the transition being probed, while the duration of the pulse is much shorter, allowing for characterisation of the radiative lifetime by recording the intensity of emitted light for the time immediately after each pulse. The decay of the PL intensity can then be built up over many such pulses. This experiment requires a fast avalanche photodiode (APD) and time-correlated single photon counting (TCSPC) unit, as shown in Figure 26(a).

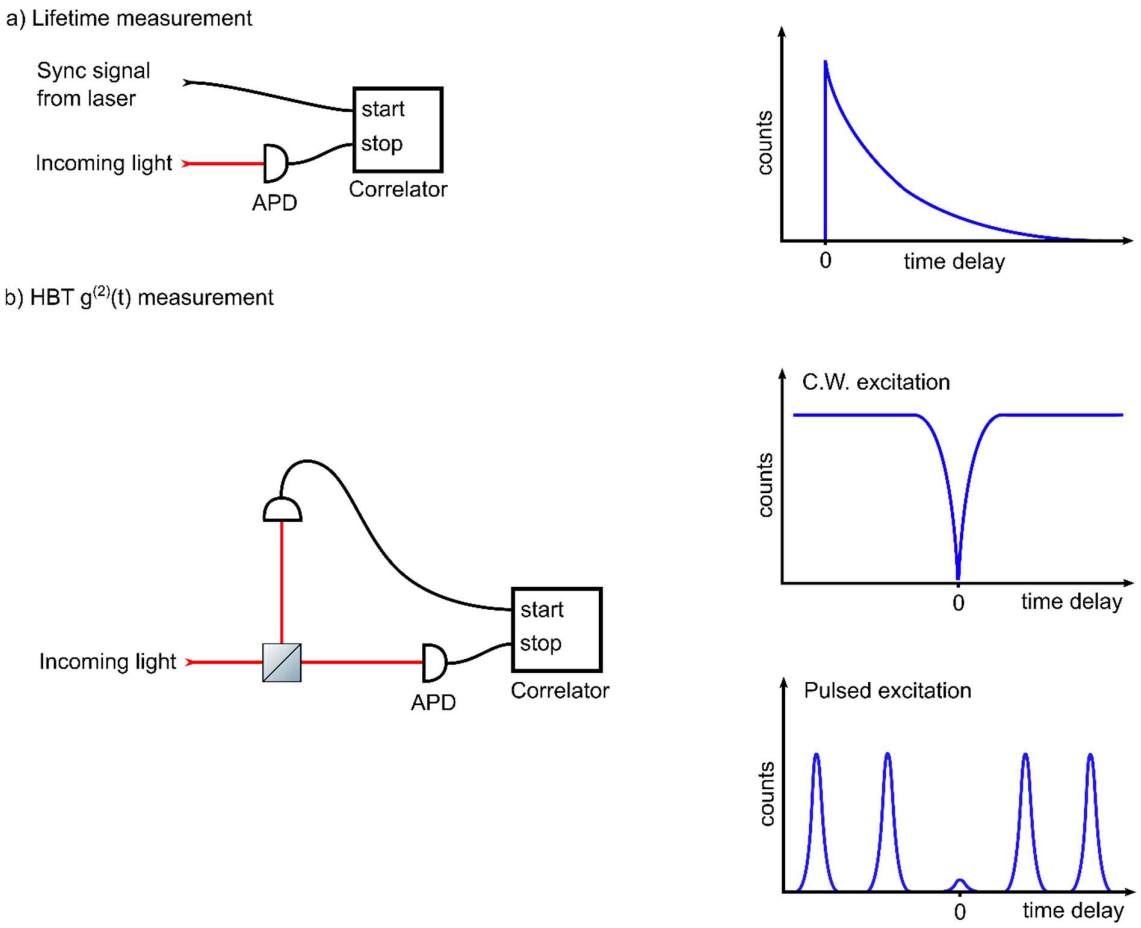

Figure 26: Configurations of fast avalanche photodiodes (APDs) and time correlator for measuring a) radiative lifetime and b) second-order photon correlation function $g^{(2)}(t)$ with the Hanbury Brown Twiss (HBT) interferometer. Schematic start-stop histograms are shown for each measurement, assuming a single-photon emitter is producing the incoming light.

Figure 9(b) shows the Hanbury Brown Twiss interferometer, which is of particular relevance to single-photon sources because of its ability to measure the second-order photon intensity correlation function $g^{(2)}(\tau)$, discussed in the Introduction. It consists of two single-photon sensitive detectors pointed at the two outputs of a beam-splitter, and a TCSPC to correlate the clicks from the detectors and produce a histogram of the time differences between events at each detector.

The single-photon detectors are usually avalanche photodiodes or photomultiplier tubes with response times ranging from a few hundred picoseconds to a few nanoseconds, and they are usually connected to a time-tagging unit which records the timestamp of a detection event with an accuracy of a few picoseconds. Correlating the timestamps of detection events

at the first detector with the timestamps of events at the second detector allows a histogram of time delay between detection events to be built up, which, if the delays between all collected timestamps are used, gives the $g^{(2)}(\tau)$ function.

The HBT interferometer is used because it removes the effect of the detector dead-times (the time where a detector is 'recharging' and unable to detect further photons after a detection event, which would otherwise prevent measurement of $g^{(2)}(\tau)$ at small values of τ if just one detector were used. The use of two detectors also removes the influence of noise originating in the detector itself, since any such noise will be uncorrelated. Only time-correlated photon counts contribute to the $g^{(2)}(\tau)$ as measured by the HBT interferometer [50]. The exact position of the detectors does not need to be controlled accurately; provided the photon correlator records long enough time differences, any additional optical path in one arm of the interferometer can be compensated for when analysing the observed photon arrival times.

Low-temperature measurements are useful for removing thermal (homogeneous) broadening, and for suppressing noise due to charges moving in the material. These experiments were carried out in a helium flow cryostat or an Attocube AttoDRY closed-cycle cryostat. All photoluminescence measurements were carried out at the University of Oxford.

2.6.1 Micro-reflectivity mapping

A setup similar to the confocal microscope shown in Figure 25 can also be used to map the reflectivity of a sample. In this case, a broadband white-light source is employed instead of a laser, and the output is routed to a spectrometer to produce a reflectance spectrum. To correct for a white-light source that does not have a completely flat spectrum, a pre-calibrated aluminium reflectance standard is used to acquire a reference spectrum that can then be used to correct the raw spectrum acquired from a real sample.

2.7 Electrical characterisation

Electrical devices were characterised using a probe station at room temperature. Two titanium probes, connected to a source-measure unit (SMU, Keithley 2400), are placed in contact with the metal pads on the device under test. A voltage ramp can then be performed

while the current is measured, and the resulting plot gives the I-V characteristic of the device.

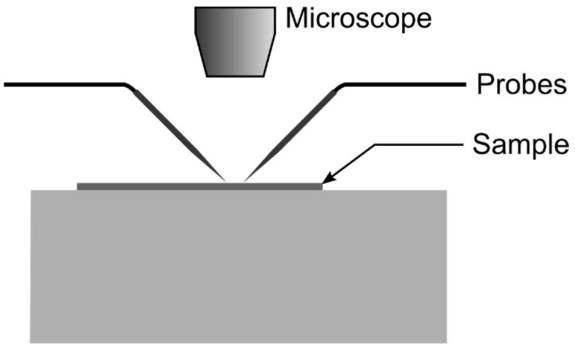

Figure 27: Schematic of electrical characterisation setup

2.7.1 Electroluminescence spectroscopy

Light-emitting devices can also be characterised on the probe station using a microscope mounted above the sample. A large working-distance objective is used to allow access to the sample while the probes are in place, and the microscope can be connected to a Si photodiode or spectrometer (Ocean Optics USB2000+). These are used for measuring overall light output or the emission spectrum produced by the device, respectively.

Varying the input current and measuring the light output (the L-I characteristic) allows for a measurement of the efficiency at different drive currents, by dividing the input current by the output light intensity. Measurements of absolute quantum efficiency needs a well-calibrated collection and detection system, but relative efficiency is still useful for determining the onset of efficiency droop, which will be discussed further in Chapter 4.

To avoid thermal effects, the injection current can also be pulsed, with a spectrum capture triggered at the start of the pulse. For this purpose, a hardware trigger line is connected between the SMU and the spectrometer. The acquisition of a L-I curve can also be done in a similar way, by pulsing the excitation current and synchronising the read-out of the photodiode voltage.

2.7.1.1 Micro-EL

Some electroluminescence measurements were carried out in the PL system described in section 2.6, using the detection arm of the confocal system to limit light collection to a small region of the sample. This is useful for collecting EL from quantum dots, since the electrical

devices used in this project are large and contain many such QDs; the microscope can isolate the emission from a single QD. Contact was made to the sample via wire-bonding to a PCB in the cryostat.

2.7.2 Transfer length method (TLM)

The transfer length method (TLM) can be used to characterise metal contacts to thin films. It is used to determine the contact resistance (Rc), the sheet resistance of the film (Rs) and the transfer length (Lt). The method requires several metal contacts, designed so they are separated by increasingly large gaps. An example of a TLM pattern, with contacts arranged in a line, is shown in Figure 28(a), below.

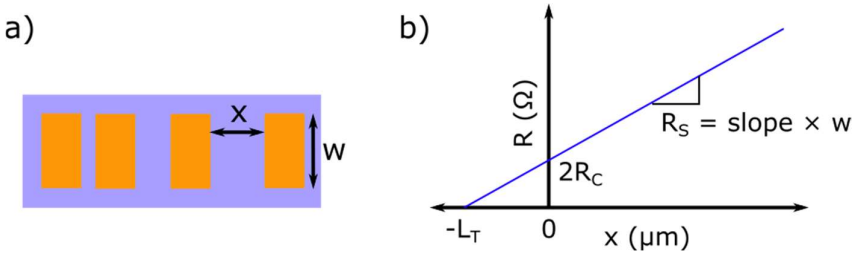

Figure 28: Transfer-length method measurement (TLM). (a) The arrangement of contacts (orange squares) on an isolation mesa (blue). (b) The variation of measured resistance (R) with contact separation (x). The transfer length L_T, the contact resistance R_C and the sheet resistance R_S can all be determined with a TLM measurement.

A TLM pattern allows a graph of resistance (R) against contact separation (x) to be plotted, as shown in Figure 28(b). This can be used to determine the contact resistance R_C from the y-intercept, the sheet resistance of the film (R_S) from the slope, and the transfer length (the effective width of contact area over which current is transferred into the semiconductor), L_T.

Chapter 3

3Nano-cathodoluminescence of non-polar InGaN QDs

Self-assembled InGaN QDs have shown promise as high-temperature single-photon emitters. This chapter investigates the cathodoluminescence produced by QD-containing samples in the scanning transmission electron microscope (STEM), and attempts to correlate this with structural features observed in the electron and X-ray signals.

3.1 Introduction

STEM-CL can be used to investigate electronic processes that lead to light emission in nanoscale objects. It has some potential advantages over photoluminescence measurements, since it can excite a very small (nm-scale) volume of material, revealing details of the spatial distribution of the emission that would otherwise be lost when exciting with a much larger laser spot. It also potentially allows for in-situ correlation of optical and structural features by comparing the CL signal and electron detector signals. However, the large amount of excess energy injected into the material can complicate the interpretation of results, and beam damage is a potential concern.

STEM-CL has been applied to a variety of nanoscale light emitters across several materials systems. A recent review by Kociak *et al.* [112] outlines some of these applications, for example surface plasmon resonances in silver nanoparticles [113], and light emission from GaN quantum discs embedded in AlN nanowires [114].

For most semiconducting structures, the electron beam excites a bulk plasmon, which then decays into many excitons that can diffuse and recombine within the material [112]. The resulting CL emission spectrum is therefore sensitive to local variations in band structure in the material, as well as any point or line defects present in the material that act as recombination sites. The following section reviews some STEM-CL studies relevant to the work in this chapter, highlighting the strengths and drawbacks of the technique.

3.1.1 STEM-CL of single-photon-emitting nanostructures

Several reports of STEM-CL measurements on single-photon emission from point defects and QDs exist in the literature. It is possible to attach a Hanbury-Brown Twiss interferometer (see Chapter 2) to the STEM-CL [115], providing information about the second-order photon intensity correlation function $g^{(2)}(t)$, which should drop to zero at $t = 0$ (i.e., at zero time delay) if photons enter the interferometer one at a time - a useful signature of a single-photon source.

STEM-CL tends to produce tends to produce strong bunching (i.e. a large value of $g^{(2)}(t)$ when $t = 0$), at least for small probe currents below about 100 pA, when ensembles of emitters are excited. This effect was explored by Meuret *et al.* [116], in the context of

nitrogen-vacancy centres in diamond. In the case where multiple NV centres are excited at once, photon bunching is observed that increases as the beam current is decreased. This is suggested to be due to the excitation mechanism; incident electrons create bulk plasmons, which then decay, producing many excitons simultaneously. These excitons will then diffuse to multiple nearby recombination centres, causing time-correlated light emission from the sample, and producing the observed photon bunching.

For isolated single defects, STEM-CL excitation produces anti-bunching in the same way as other excitation mechanisms. Emission from GaN QDs embedded in AlN, that form at threading dislocation sites, has been observed by Schmidt *et al.* [117]. In addition to observing narrow linewidths of around 440 μeV (0.025 nm) at a temperature of 5K, they also demonstrated single-photon emission with a second-order autocorrelation function $g^{(2)}(t)$ that dropped to a raw value of 0.42 at zero time delay.

The GaN islands that exhibited this behaviour were also easily observed in the STEM image, and were shown to form at threading dislocations. This demonstrates one of the principal advantages of STEM-CL, i.e. the potential to correlate structural information with the CL emission.

Photon antibunching has also been observed at bright features in hexagonal [118] and cubic [119] boron nitride by STEM-CL, as well as nano-diamond [120].

3.1.1.1 InGaN nanostructures in STEM-CL

STEM-CL has also been applied to InGaN nanostructures. Zhou *et al.* [121] and Griffiths *et al.* [122] have examined quantum discs (QDiscs) in nanowires and QWs in planar structures respectively, while Gačević *et al.* [123] studied InGaN QDs contained in pencil-like nanowires.

Zhou *et al.* [121] examined the CL emitted from InGaN QDiscs embedded in GaN nanowires. The simultaneous collection of a STEM image then allowed for the defect structure to be correlated with the CL emission from individual nanodisks, allowing the authors to show that the emission was quenched by the presence of stacking faults in the nanowire; making use of the structure to emission correlations possible in STEM-CL.

Griffiths *et al.* [122] use the increased spatial resolution of the optical signal to demonstrate that CL emission can be clearly distinguished from different planar QWs spaced approximately 20 nm apart, when viewed in the cross-section geometry. This allows the effect of different doping levels in the barriers to be distinguished between each QW, something that would not be possible with micro-photoluminescence measurements.

Gačević *et al.* [123] studied InGaN QDs contained in GaN nanowires. While much of the characterisation was carried out using micro-PL and SEM-CL to investigate the emission from quantum structures on the polar, semi-polar and non-polar planes of the nanowire, STEM-CL was applied to provide precise localisation of each of the emission bands observed using the other techniques. A Tecnai F20 STEM was used with a parabolic collection mirror and Gatan MonoCL4 system to collect the CL signal, with the microscope operating at 80 keV to minimise sample damage. Simultaneous collection of the STEM-HAADF signal allowed for the correlation of the CL emission to the structure of the nanowire. This allowed different emission wavelengths to be assigned to the different parts of the nanowire tip, with a spatial resolution of a few tens of nanometres, and therefore allowed each emission band to be assigned to each of the polar, non-polar and semi-polar facets.

3.1.1.2 Beam damage in InGaN structures in STEM-CL

Griffiths *et al.* [124] have also investigated the effect of beam damage on InGaN nanostructures examined using STEM-CL. An exponential reduction in the cathodoluminescence signal with irradiation time was observed for a range of beam energies between 80 and 200 keV. Higher beam energies showed a faster rate of CL signal reduction, suggesting that it is due to varying degrees of knock-on damage, which also scales with beam energy. Extrapolation allows the authors to suggest a damage threshold of around 70 keV.

A beam energy of 80 keV (the lowest available) was used for the measurements reported in this thesis, to minimise the damage rate.

3.1.1.3 GaN/AlGaN nanostructures

Several reports of observations of GaN inclusions in AlGaN nanowires exist in the literature, demonstrating the ability of STEM-CL to investigate nanometre-scale variations in the

cathodoluminescence of compound semiconductors. Some examples are published from the group of Dr. Kociak at the Université Paris-Sud [114, 125-129].

One such example (Zagonel *et al*., 2012 [125]) demonstrates that CL emission can be distinguished from individual GaN QDiscs separated by 4 nm AlGaN barriers. This shows that the localisation of the carriers in the QDisc can cause a substantial intensity enhancement when the probe is positioned over a confinement centre. They also show that the structure of the nanowires can be simultaneously resolved by conventional STEM imaging, achieving atomic resolution and correlating this with the STEM-CL spectra [114].

Overall, the literature shows that STEM-CL can resolve emission from nanostructures spaced as close as a few nanometres. It is also able to locate quantum dots in planar samples and has also been shown to be suitable for examining planar InGaN heterostructures. This indicates that the technique may be suitable for imaging a-plane InGaN quantum dots, and for correlating their CL emission to the structure of the sample as observed by conventional STEM.

3.1.2 Structural observations of InGaN quantum dots

InGaN nanostructures acting as QDs have been imaged using a variety of techniques. As most growth methods involve QD formation as a separate step prior to growth of a capping layer, AFM can be used to investigate uncapped samples and gain an insight into the appearance of QD structures. However, as growth of the cap layer typically occurs at a temperature above that of the QD formation process, there is scope for the capping process to modify the morphology of the QDs. In some processes, such as MDE, the cap growth is also essential to the formation of the QDs themselves. Therefore, methods that can investigate the structure of QDs after capping, such as STEM, are also of interest.

3.1.2.1 AFM observations

Samples grown in the same reactor using the quasi-two-temperature (Q2T) and modified droplet epitaxy (MDE) routes, which are very similar analogues of the two samples examined in this study, were imaged using AFM (published data in Wang *et al.* [62]), and the images are shown in Figure 29.

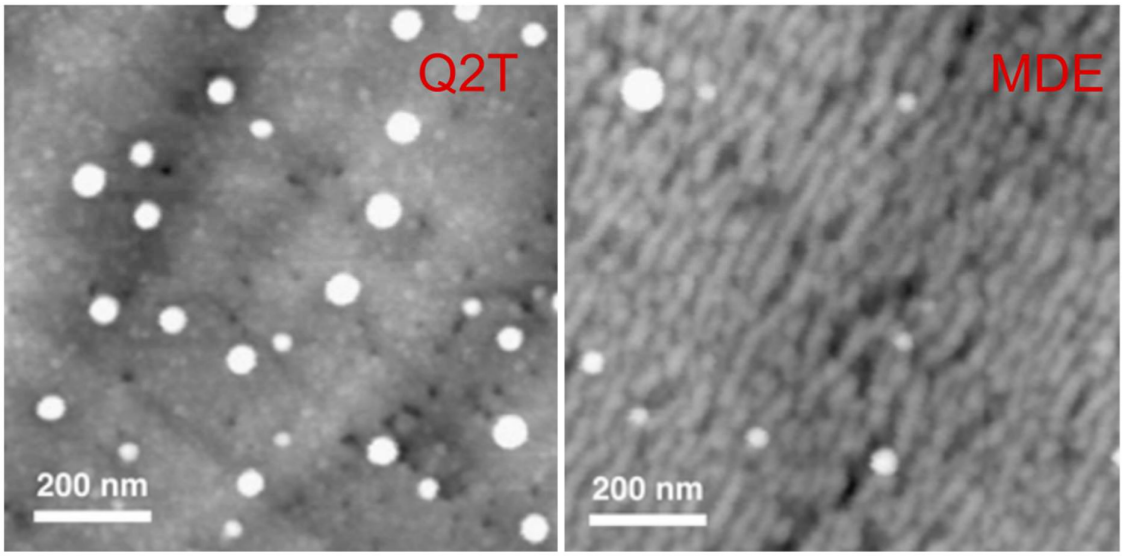

Figure 29: AFM images of samples grown by the Q2T method (left) and the MDE method (right). From Wang *et al.*, reproduced with permission [62].

The bright dots in both images are precursors to QDs. In the MDE case, these are metallic InGa droplets that are etched by a solution of HCl [56], while in the Q2T case they are non-metallic, and are believed to be InGaN islands, but they may be modified during capping. The MDE dots are sitting on a much more disrupted quantum well than in the Q2T case; the remnants of the QW are visible as a series of interconnected fingers in the MDE image, whereas there is a flatter, only somewhat pitted QW layer in the Q2T image.

3.1.2.2 STEM observations

InGaN heterostructures have been studied extensively by transmission electron microscopy, particularly InGaN quantum wells with GaN barriers grown on polar c-plane templates. However, InGaN is susceptible to electron-beam-induced damage. In classic TEM, where a broad area of the sample is illuminated with a collimated beam of electrons, the electron dose is high enough to cause indium segregation within a few minutes of irradiation [130], complicating any TEM observations of InGaN nanostructures.

Scanning transmission electron microscopy (STEM), particularly using aberration-corrected optics, can image the spatially-resolved strain state, indium composition and defect structure in such InGaN heterostructures. The total electron dose is also, in general, much lower than in TEM, which greatly reduces beam damage and makes it suitable for detailed examination of InGaN nanostructures, as demonstrated in [131]. The applicability of STEM to

investigation of InGaN heterostructures has led to several reports of the structure of InGaN QDs.

Koukoula *et al.* [132] investigated self-assembled QDs grown by plasma-assisted MBE on polar c-plane and semi-polar m-plane substrates. QDs were not always clearly resolved in the cross-sectional images, due to overlapping of projected QDs with each other. However, a few examples of well-resolved QDs were found that were suggested to possess a truncated-pyramid morphology on the polar template, while a lenticular morphology was suggested for QDs grown on the semi-polar templates. A wetting layer with a sharply-defined lower interface and more diffuse upper interface was observed underneath the QDs, suggested to be due to the indium surfactant effect in MBE [133] affecting the lower interface (which was grown with indium flux) but not the top one (which was not).

As aberration-corrected STEM was used for this study, the detail of the interface between the QD and the substrate could also be determined. This was performed on an uncapped sample, and revealed an absence of misfit dislocations between the substrate and the QD, supporting the idea of Stranski-Krastanov growth being responsible for QD formation in this case.

Tessarek *et al.* [134] have also used HR-STEM for imaging InGaN QDs, in this case attributing QD formation to spinodal decomposition and subsequent desorption of the resulting In-rich portions of InGaN layers grown by MOVPE. Clear indium-rich regions, approximately 5 nm thick and 10 nm wide, are observed in the QD-containing sample. As projection effects will act to lower the observed indium concentration, they place a lower bound of 20 at% on the indium composition of these QDs.

These HR-STEM results were obtained using a method expanded upon by Rosenauer *et al.* [131]. The images are analysed to obtain In composition from the HAADF signal alone. The analysis involves the use of frozen-lattice simulations to generate a conversion function between HAADF signal and indium composition. The HAADF signal also depends on the specimen thickness, so the pure GaN regions on either side of the InGaN layer are used to extract the variation in the sample thickness which can then be interpolated across the

InGaN for quantitative analysis. FIB-prepared samples are also used, because these tend to have a more uniform thickness than manually-prepared samples.

3.1.3 SEM-CL observations of non-polar InGaN QDs

SEM-CL has been used for examining the emission from MDE [57] and Q2T [59] non-polar QD samples, which are grown using the same techniques and on the same equipment as the samples I am investigating in this chapter.

Zhu *et al.* [57] observe bright spots with dim tails in panchromatic SEM-CL images, such as that shown in Figure 30. Spectra extracted from the bright spots on these images show a broad QW-like background, with superimposed sharp (resolution-limited) peaks that likely arise from QD-like exciton confinement centres. The sharp peaks generally appear on the blue side of the QW background.

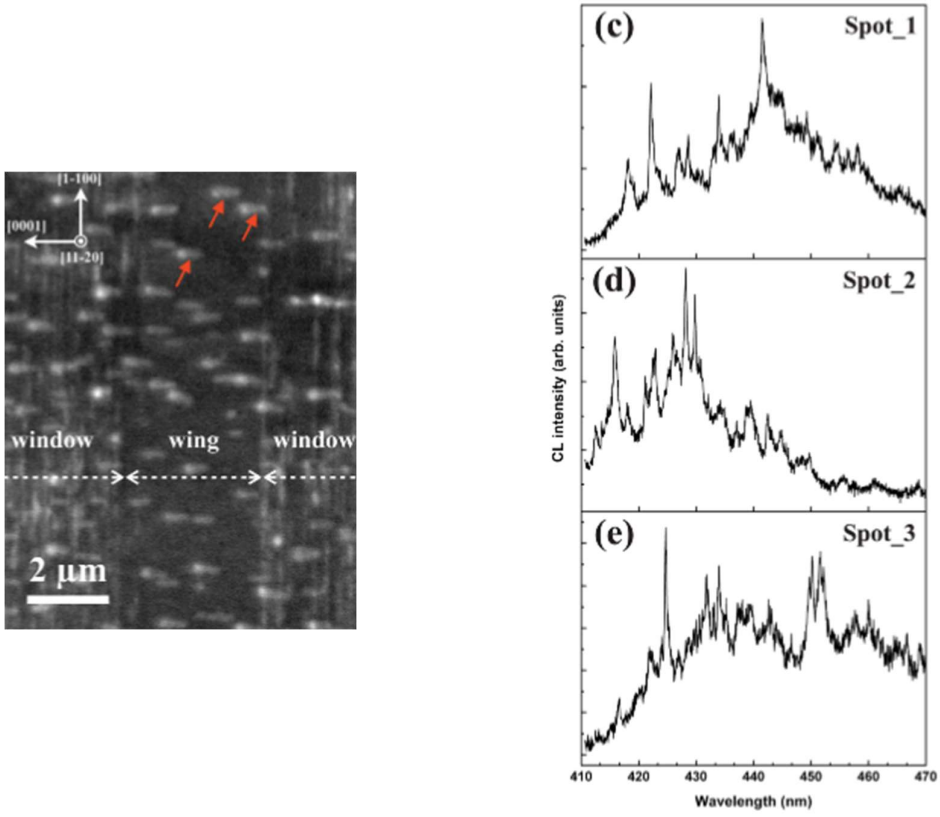

Figure 30: Left: panchromatic SEM-CL image of MDE quantum dots. The 'wing' and 'window' regions refer to low and high defect density regions on a sample grown using the epitaxial lateral overgrowth (ELOG) method. Right: Spectra extracted from three bright spots highlighted by the red arrows. Reproduced with permission from [57].

Griffiths *et al.* [59] report CL observations of Q2T quantum dots, which are reproduced below, in Figure 31.

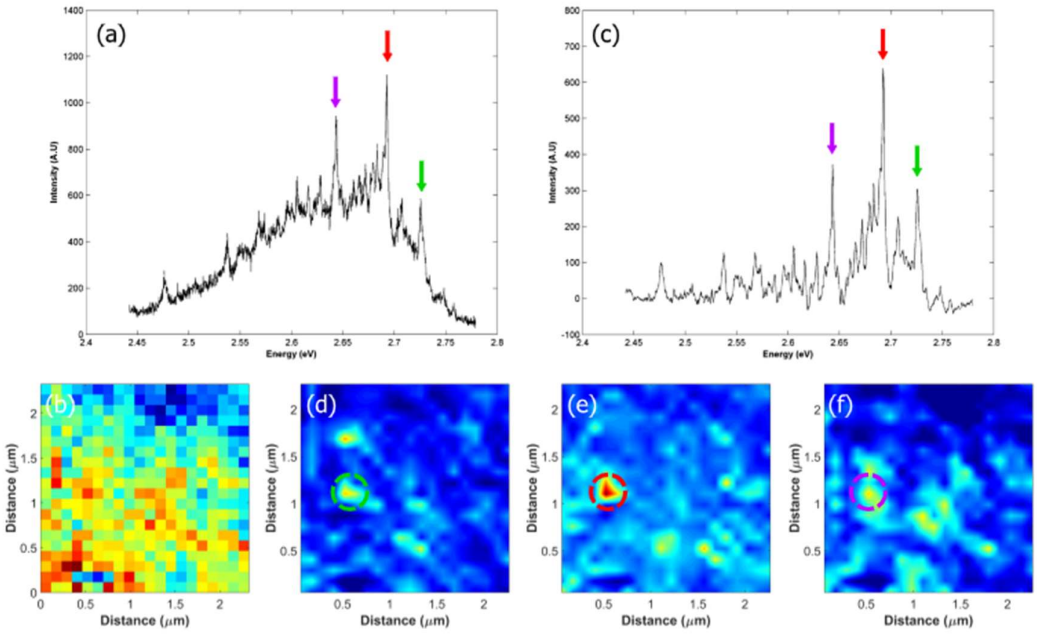

Figure 31: SEM-CL observations of QDs grown by the Q2T method. a) Spectrum extracted from region enclosed with the dotted circle. b) (bottom left) Panchromatic CL image. c) Background subtracted spectrum, clearly showing QD-like sharp peaks. d-f) Monochromatic CL images created by band-pass filtering at the wavelengths indicated by the coloured arrows.

Once again, the QD-like peaks tend to occur on the blue side of the QW background, at least for this example. The panchromatic cathodoluminescence does not show the same bright spots with tails appearance as in the MDE case, but has a more uniform appearance due to the stronger QW background signal. The stronger background is due to the lack of disruption to the QW during the QD growth process, when compared to MDE.

μ-PL measurements on similar samples also show qualitatively similar sharp peaks on a broad QW background, as shown in Figure 5.

3.2 Aims

The published work reviewed above concerning cathodoluminescence from quantum structures in both InGaN and AlGaN, and the structural measurements of InGaN QDs by

STEM, indicate that these are complementary techniques that have potential to provide insights into the structure and emission properties of non-polar InGaN QDs.

The aim of the work in this chapter is to examine the cathodoluminescence emitted from non-polar QDs in the STEM, to investigate whether the technique can resolve luminescence from individual QDs, and whether it is possible to correlate features observed in the CL with structural data obtained from the electron images.

3.3 Methods

3.3.1 Gatan Vulcan STEM-CL system

The nano-CL system used for the experiments in this chapter (a Gatan Vulcan) consists of a modified TEM sample holder containing parabolic mirrors above and below the sample plane. Holes are drilled in the mirrors to allow the incident beam to interact with the sample, and for electrons to continue down the column to reach detectors underneath the sample. Due to the size of the mirror and collection apparatus, the sample cannot be tilted in any direction.

For maximum intensity, the collection mirrors should have a high numerical aperture (N.A.). However, for maximum spectral resolution, light rays entering the spectrometer should be constrained to a small range of angles corresponding to a low N.A. The optical system therefore needs a high magnification of the sample at the entrance slit for maximum light transfer into the spectrometer, which requires precise alignment of the irradiated area of the sample with the rest of the optical system (typically to better than 5 μm [112]) The Vulcan system uses a bundle of optical fibres for coupling the collection optics to the spectrometer, which lessens the need for precise alignment of the sample.

The microscope used is a JEOL JEM-2000EX (S)TEM, fitted with bright-field and high angle annular dark-field detectors. The overall system is shown schematically in Figure 32.

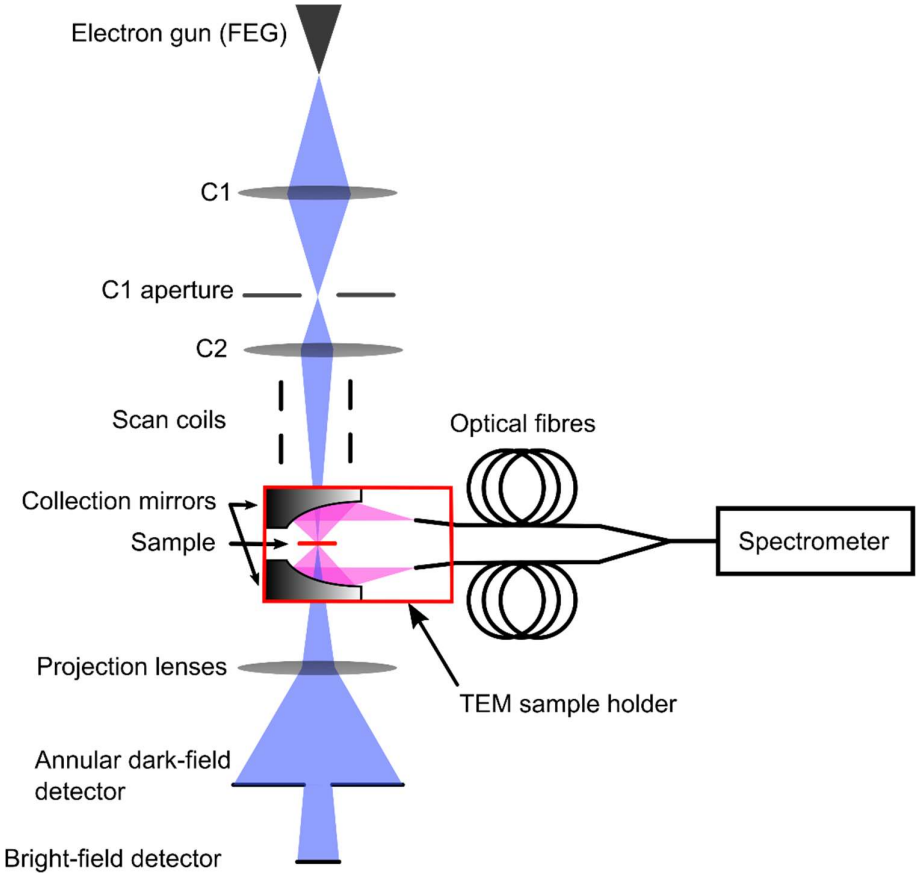

Figure 32: Schematic of the nano-CL setup, showing the electron column, the Vulcan sample holder, and the optical fibres coupling to the spectrometer.

All of the measurements taken in this chapter are spectrum images, where a full spectrum is recorded at every pixel in the image. The system can scan within each spectrum image pixel while the spectrum is being acquired, allowing a higher resolution conventional STEM image to be captured simultaneously.

3.3.2 STEM conditions

All samples were examined at a beam energy of 80 keV to minimise the potential for knock-on damage and increase the intensity of the CL signal. The damage time constant should be around 100 seconds at this voltage, according to measurements in [124].

3.3.3 Analysis methodology

There are several methods that are used to process spectrum images into meaningful 2D images for display. Each of these approaches is described in more detail below.

Monochromatic images can be created using the integrated intensity between two

wavelengths, and several of these images can be assigned colours and summed together to give a qualitative impression of the wavelength ranges emitting at each point on the sample. If a feature is associated with a clear peak in the spectrum, this can be fitted, and the fitted peak's position, intensity and width can be used to generate images. Finally, blind source separation can be used to split out the contributions from different emitting species in the sample.

3.3.3.1 Band-pass filtering

The simplest analysis method integrates each CL spectrum between two wavelengths, generating a scalar value from each spectrum, and then uses this scalar as the pixel intensity at each spatial location. The end effect is the same as a traditional monochromatic CL image.

3.3.3.2 RGB colour mapping

A colour mapping function (CMF) can be used to convert a CL spectrum (with a total of 1,024 spectrum bins) to 3 scalars representing R, G and B channels. The CMF consists of a set of (R,G,B) values at each wavelength (so maps $\lambda \rightarrow (R, G, B)$), and each value is multiplied by the intensity of its corresponding bin. An image can then be drawn with the resulting RGB value obtained for each pixel, with the whole image appropriately normalised to fit within the displayable range of values. This technique works well for the qualitative interpretation of images where some spectral features have very high intensity over the background, but images quickly become muddy and unclear when the peaks are not far above the noise floor.

3.3.3.3 Peak fitting

The CL spectra can also be converted to an array of scalars by fitting a model function to the data. For example, a QW's CL emission spectrum could be fitted by a Gaussian function, allowing the scalars of intensity, standard deviation and mean wavelength to be extracted at each pixel. The method used in this project is to use the `scipy.optimize curve_fit` function [135] (which implements the Levenberg-Marquardt algorithm) to perform the fit of a single Gaussian to each CL spectrum. This is very effective if a certain peak is present in every spectrum on the sample, but starts to introduce artefacts if peaks drop below the noise floor (such that the fit does not converge) or if a variable number of peaks are present at different locations, as is often the case in QD samples. It is also sensitive to the starting point of the optimisation algorithm.

3.3.3.4 Blind source separation

Samples that contain several light-emitting species (QDs, for example) that each have a characteristic spectrum should be amenable to analysis by a machine-learning technique called blind source separation. This technique aims to separate out the components that contribute to a mixed signal (in this case, the components would be various physical objects that contribute to overall mixed signal of the CL spectrum), without any prior knowledge of the components or the proportions in which they are mixed together. In matrix form, this process can be written as:

$$\mathbf{A} = \mathbf{WH}$$

Equation 9

where **A** is the mixed signal, **W** is a matrix whose columns represent the source signals, and **H** is the mixing matrix. Applied to CL spectrum images, **A** will contain n columns, each containing a single CL spectrum, where n is the number of pixels in the SI; while **H** will contain m rows of length n, each containing values that correspond to the 'weighting' of each separated source signal at each spatial position, where m is the number of source signals contained in **W**.

Equation 9 represents a reasonable model for the physical processes that are occurring in the formation of a CL image, as there will be several sources present (each with their own CL spectrum) that combine with various weights at different spatial positions on the sample to form the overall CL SI. The primary assumption made in Equation 9 is that the sources combine linearly; this seems reasonable, since signals emitted in the CL of semiconductor structures are usually incoherent and the spectrometer is also linear if operating inside an appropriate range of intensities.

There are two main methods used for this type of analysis: non-negative matrix factorisation (NMF) and independent component analysis (ICA) [136]. NMF is used in this work.

Non-negative matrix factorisation

This technique uses a linear optimisation algorithm to find non-negative approximations to **H** and **W** in Equation 9. The non-negativity constraint imposed on these matrices helps to ensure that this analysis results in a physically interpretable result, since incoherent light

emitted from any sources in the sample will always increase the intensity in the mixed CL spectrum. It does not make any assumptions about the independence of the components, meaning that further analysis of the relationship between the source components, and how they combine in the sample, is possible.

This optimisation is performed using the `sklearn` Python package [137], which provides the `NMF` object for this purpose. This object uses an objective function after Févotte *et al.* [138] for the linear optimisation, using a coordinate-descent solver. Since the source matrix should be valid for any mixed signal that arises from the same sources, the fitting step can be performed just once – using 'training' data to perform the fit and obtain the source matrix, and then using simple matrix algebra to compute the mixing matrix for another set of data.

Using training data to assist with later source separation could be useful in the case where there are known to be several discrete species in the data; for example, X-ray emission spectra from atoms in the sample. However, in my case, the sources are probably different between different CL spectrum images, since they correspond to unique QDs. Hence, the optimisation algorithm is run separately on each SI.

3.4 Samples

Two a-plane QD samples were used in this study: one grown using the MDE method and one using the Q2T method. TEM specimens were prepared in both plan-view and cross-section by manual polishing (as described in section 2.4.2), followed by Ar ion-beam milling at 5 kV to thin to electron transparency before cleaning at 1 kV and 0.5 kV for 10 minutes each. Another sample, consisting of a single QW grown on a c-plane template, was also prepared by the same method as a reference.

The plan-view MDE sample showed strong emission in the STEM-CL, but the cross-section sample did not. Both cross-section and plan-view specimens taken from the Q2T sample showed strong emission.

3.5 MDE QDs: plan-view

3.5.1 Larger features

Several bright, sharp peaks were observed in the STEM-CL, localised to regions several hundred nanometres in diameter. Spectrum images were acquired from these regions, and a feature with a systematic shift in the emission wavelength with position was observed. Panchromatic CL and qualitative RGB images are shown in Figure 33, together with the peak wavelength and intensity of a series of Gaussian fits to the spectra. A 300 lpmm grating was used, and the sample was held at a temperature of 100 K throughout the measurements.

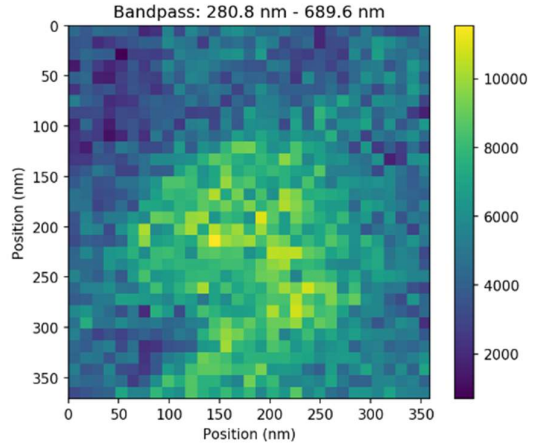

Panchromatic image

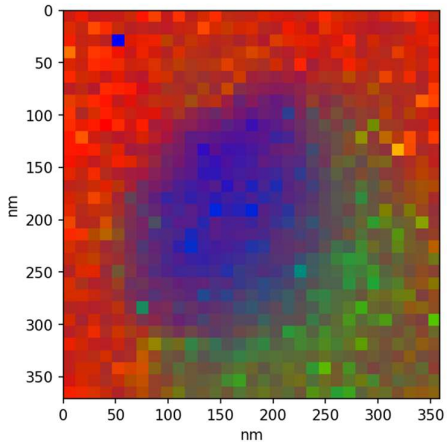

RGB-mapped image (blue: <400 nm, green: 400-500 nm, red: >500 nm)

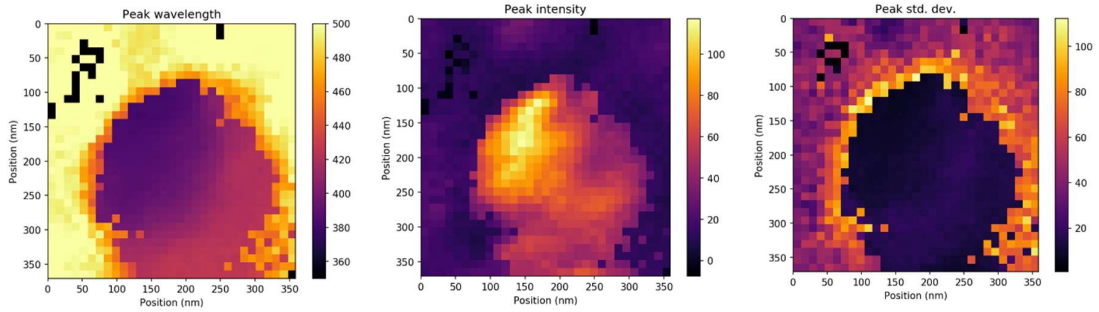

Figure 33: Top left: Panchromatic CL (obtained by integrating spectra in SI) of a feature observed in the MDE plan-view sample. Top right: RGB colour-mapped CL spectrum image. Blue is mapped to shorter wavelengths while red is mapped to longer wavelengths. Bottom: position, intensity and standard deviation of fitted Gaussian peak.

In order to ensure that the direction of the wavelength shift is indeed sample-related, the scan direction was inverted for a second pass. The feature is inverted but otherwise identical in the resulting spectrum image, confirming that the observed wavelength shift is a function of the sample, and not related to beam damage or other imaging-related artefacts.

Blind source separation was carried out using NMF, after the data were pre-processed with a low-pass filter followed by a hard clip at 0, to remove any negative values. Plots of the first three components in the mixing matrix are shown in Figure 34, and the first three components in the source matrix are shown in Figure 35. Images generated with the band-pass filter placed at several wavelength ranges are also shown.

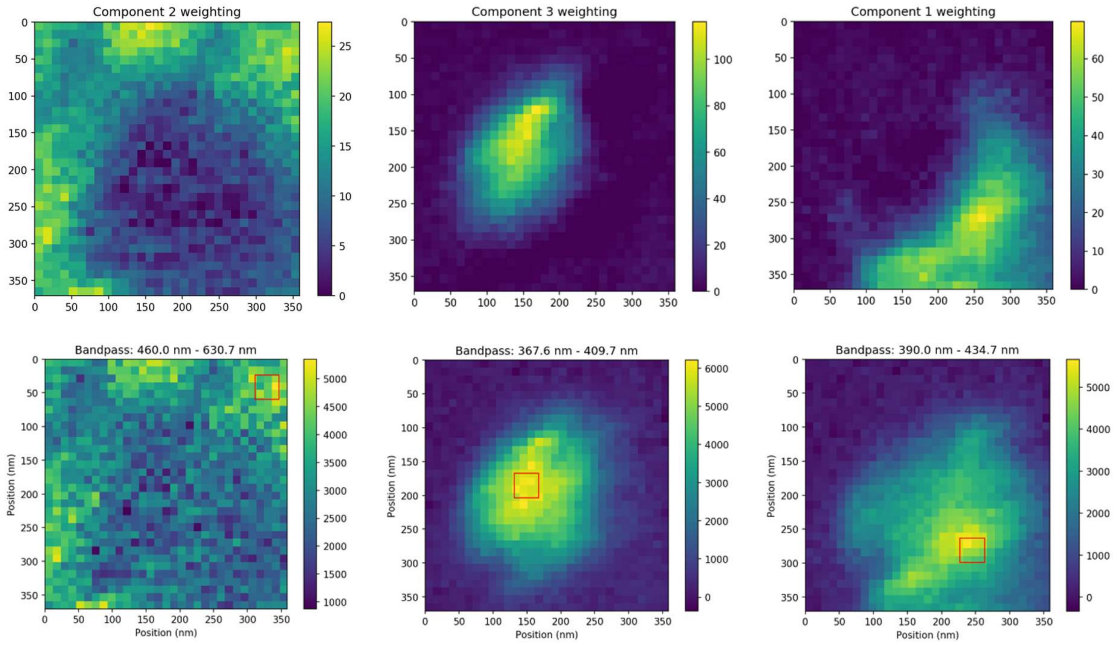

Figure 34: Plots of three components in the mixing matrix (top) compared with band-pass filtered images (bottom)

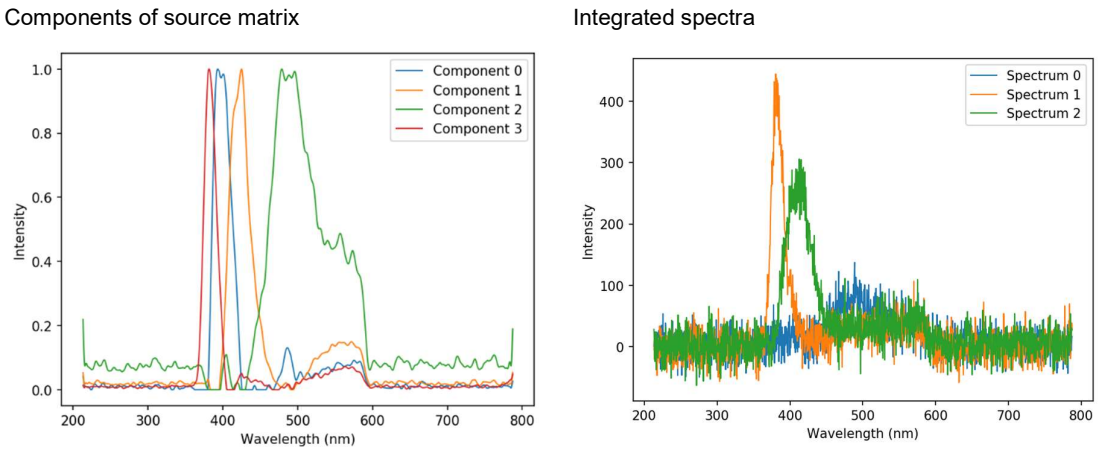

Figure 35: Left: Plots of the first four components in the (normalised) source matrix. Right: Spectra extracted from different positions on the sample (corresponding to the red squares on the band-passed images)

It appears that Component 2 is correlated with background QW emission, with a broad peak centred at ~500 nm. Components 0, 1 and 3 then have clear peaks between 390 and 450 nm, and the plots of the mixing matrix show that the shortest wavelength component is roughly elliptical in shape, whereas the other two components have crescent shapes. Similar results are obtained when the image is band-passed at wavelengths corresponding to these peaks. The main difference is that NMF can assign weight to components which have some intensity at the same wavelength – in this case, the left-hand tail of the crescent feature's spectrum overlaps with the right-hand tail of the elliptical feature. Hence, in the band-passed images, some intensity from the elliptical feature is still present when the band-pass filter is set to mostly enclose the crescent, while NMF allows for separation of spatially overlapping components. Noise is also eliminated very effectively, and, provided that the fit converges well, the sum of all components weighted by the mixing matrix will reproduce the original spectrum image.

However, as this method does not make any physical assumptions about the sample, it is hard to interpret the spectra in the source matrix. In this case, there seems to be a continuous shift in the peak position across the feature (from the Gaussian peak-fit data), and the algorithm has fitted 3 source components to this with short, intermediate and long wavelength. It is hard to be certain whether there is, in fact, a smooth variation in peak position or several discrete peaks that have not been resolved properly by the spectrometer, and this complicates the direct interpretation of the source components. However, the NMF

still provides clear indications of the shape of the regions emitting at different wavelengths, and is more effective at removing background than the simple band-passing technique.

3.5.2 Comparison with structural data

Data from the STEM detectors was collected at the same time as the CL spectra, using sub-pixel scanning to build an image with a greater number of pixels. The HAADF detector signal is shown in Figure 36, below, together with the overlaid NMF components for comparison.

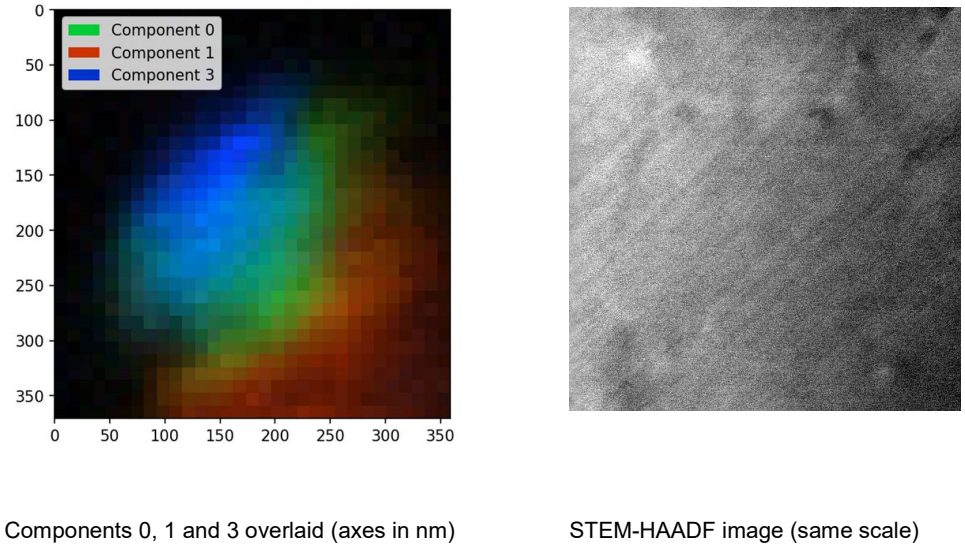

Components 0, 1 and 3 overlaid (axes in nm) STEM-HAADF image (same scale)

Figure 36: Left: Three components from the NMF source matrix, overlaid using different colours. Right: STEM-HAADF image acquired simultaneously.

There is not much contrast visible in the STEM-HAADF image. The sample was also examined in a high-resolution STEM at 300 keV (FEI Titan) with aberration correction to try and identify any structural details, and an image taken from the same sample is shown in Figure 37. Some weak contrast is visible in this image; there appears to be a brighter crescent-shaped region which may correlate with a higher indium content crescent. However, the length scale is quite different from the features observed in STEM-CL, which are around 10× larger.

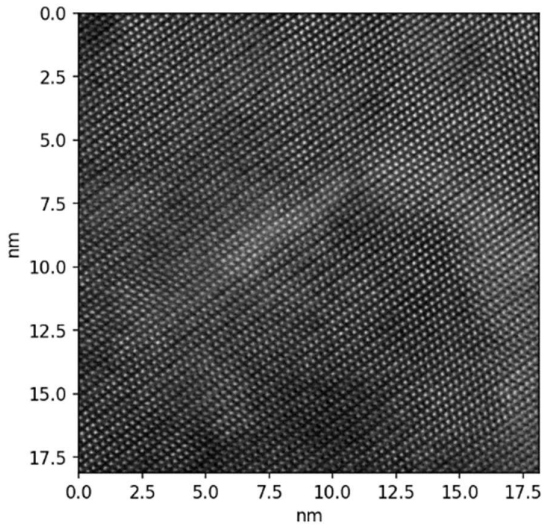

Figure 37: HR-STEM HAADF image of a plan-view MDE sample, showing some bright contrast (increased indium content) that is consistent with a nano-ring structure.

Springbett *et al.* [139] contains structural data obtained using AFM and STEM on uncapped MDE samples. The AFM data shows very clear 'nano-ring' structures that form underneath large metallic droplets on the surface of the sample by a droplet etching mechanism, and extend downwards through the InGaN epilayer.

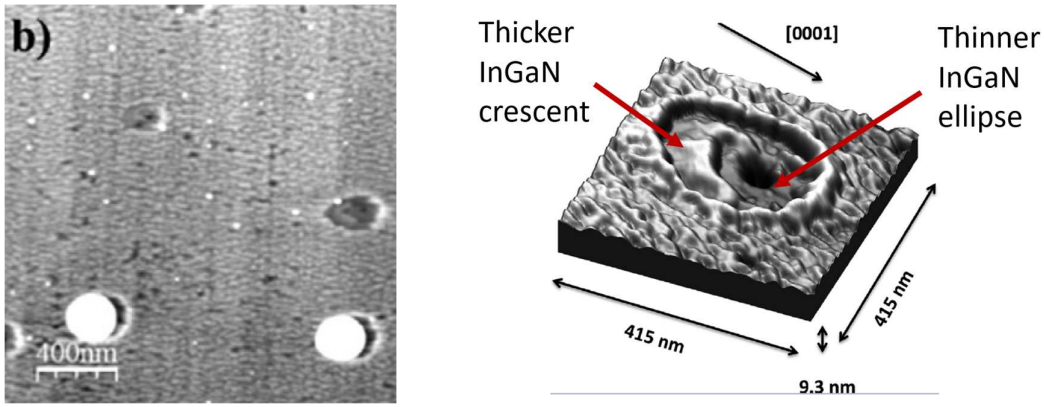

Figure 38: Left: AFM image of an uncapped MDE sample with metallic droplets (white) sitting in nano-ring structures. Right: rendering of a single nano-ring structure, with the metallic droplet removed by etching in hydrochloric acid. Images reproduced with permission from [139].

There is a good correspondence between these structures and the structures observed in the STEM-CL spectrum images. The outer crescent-shaped region would be expected to emit at a longer wavelength, as it corresponds to a thicker region of InGaN, while the adjacent pit will emit at a shorter wavelength; this is exactly as observed in STEM-CL. A total of 9 such

features were observed, and all of them followed the same pattern, with the ellipse and crescent structure emitting on the blue side of the surrounding QW, consistent with the droplet etching mechanism. Additionally, the orientation of the features is always the same, which is consistent with the hypothesis in Ref. [139] that the droplets always migrate along the negative c-direction, $[000\bar{1}]$.

The AFM data also shows a raised ring surrounding the structure, which may also act as a confinement centre (or set of confinement centres). However, there is no obvious spectral feature corresponding to this ring observed in my data.

3.5.3 STEM-CL of surrounding regions

One STEM-CL spectrum image showed strong emission, but did not contain evidence of a nano-ring structure. Instead, 'trail' of material was observed, emitting at a shorter wavelength than its surroundings, as shown in Figure 39. This could be due to a metal droplet travelling a longer distance along the sample, leaving a trail of etched material, and similar features have been observed in previous work ([140], fig. 3.34).

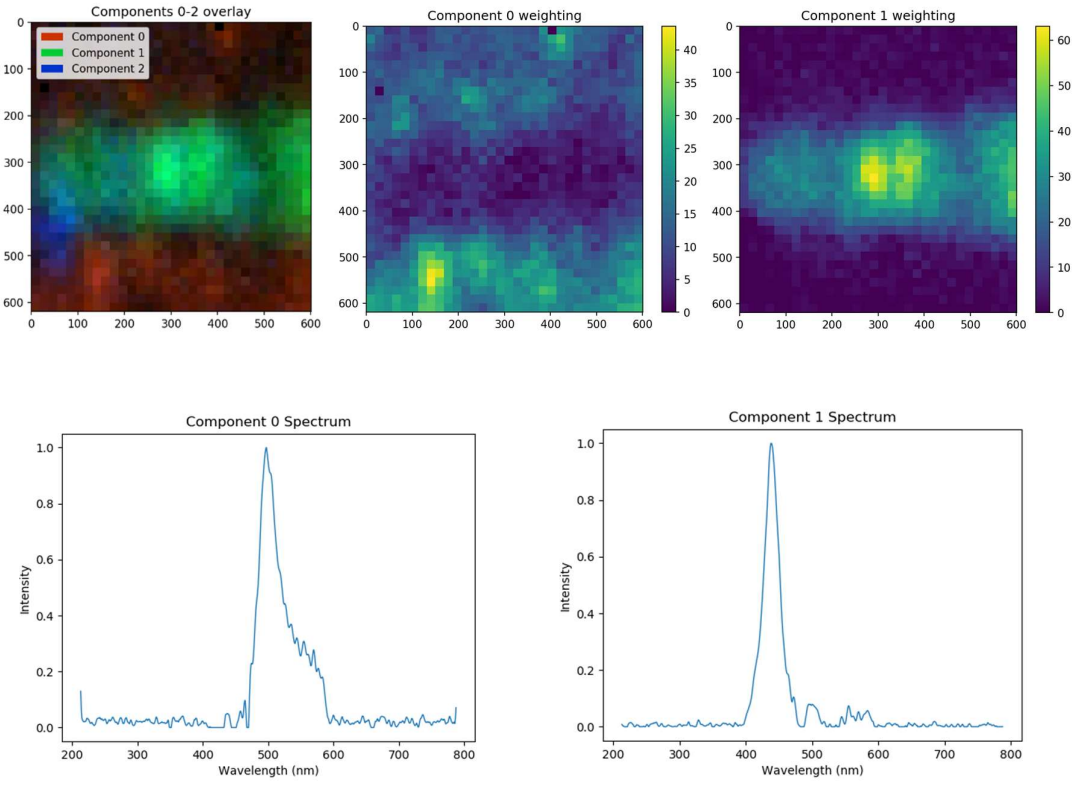

Figure 39: A 'trail'-like structure, possibly the result of a metal droplet travelling a longer distance along the surface.

3.5.4 Comparison with PL

A representative spectrum of a QD in an MDE sample, observed using micro-photoluminescence (μ-PL) is shown in Figure 40. This was acquired using two-photon excitation using a pulsed Ti:sapphire laser operating at 810 nm, with a 76 MHz repetition rate and pulse length of approximately 1 ps. The laser is focused to a spot size of approximately 1 μm through a 100x objective, and the sample is held at a temperature of ~ 12 K in an AttoDRY cryostat. An extremely sharp peak is observed on a broad background. Another example, acquired by collaborators at the University of Oxford under similar conditions and published in [62], is also shown. This specific QD was confirmed to be associated with single-photon emission in [62], using a HBT experiment.

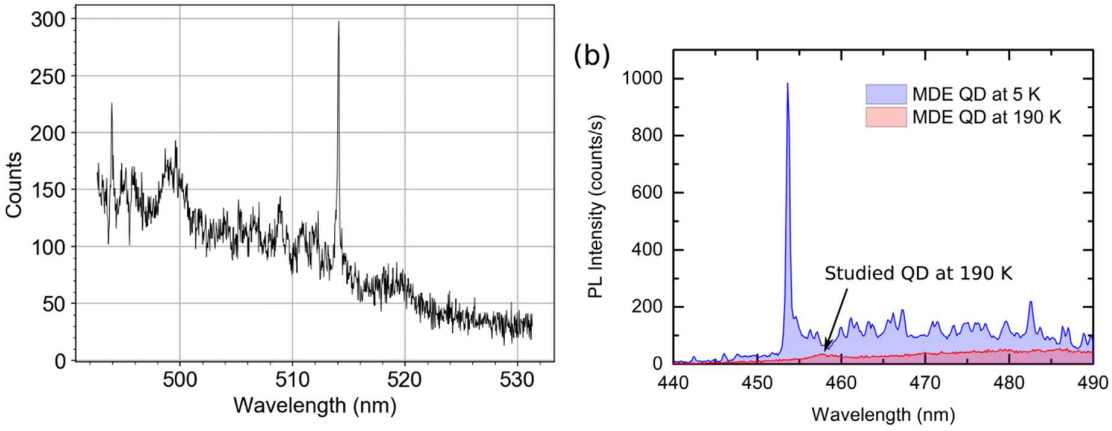

Figure 40: μ-PL spectra of MDE quantum dots. Right-hand spectrum reproduced from [62], with permission.

Since the 1 μm spot size used in PL is substantially larger than the nano-ring features, the observed spectrum from these features in PL should look like a broad peak (including emission from all parts of the nano-ring) on the blue side of the QW background. However, sharp QD peaks are observed at several different locations in the PL spectra, on both the blue and red ends of the QW background. This suggests that some observed QDs could be related to the droplet-etched regions of the sample, while others are more likely to be associated with reductions in the band-gap energy, for example at thickness increases or indium-rich regions.

3.6 Q2T QDs: plan-view

Q2T QD samples also showed sharp peaks in their CL spectra. Some selected regions, band-pass filtered images and closely-matching NMF components are tabulated in Figure 41.

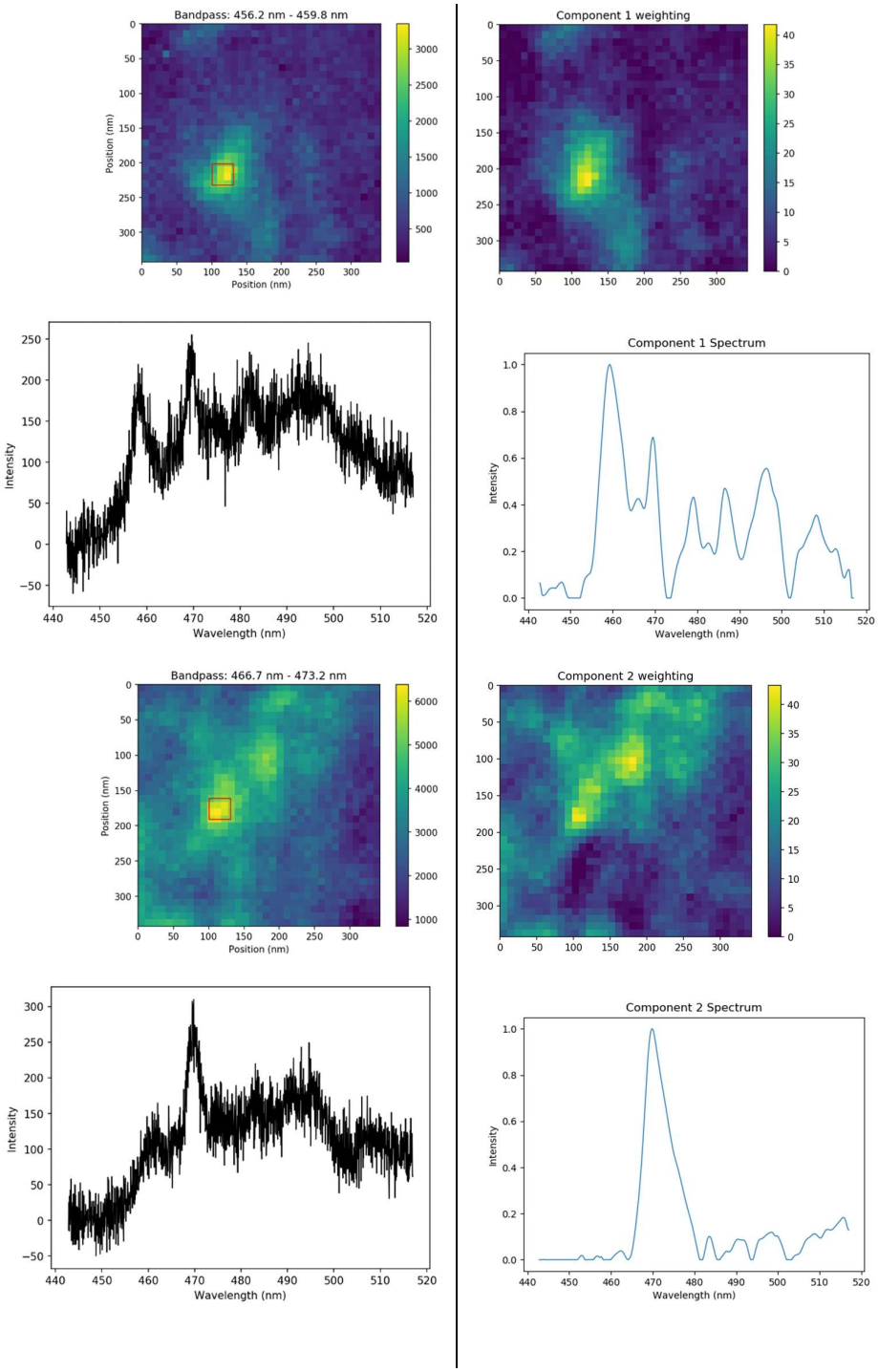

Figure 41: Some sharp peaks observed in a Q2T sample in plan-view, with band-pass filtered images and integrated spectra next to their corresponding NMF components.

The concentration of regions emitting light that shows sharp peaks in the Q2T sample was much higher than in the MDE sample, and the emissive regions are also smaller. For example, Component 1 is a bright region that falls off within around 50 nm of a central point, approximately the limit of the spatial resolution of the CL signal. It also contains a sharp peak at around 459 nm.

3.6.1 HR-STEM

As with the MDE plan-view case, there is not much contrast observed in the plan view STEM images obtained in the STEM-CL, so the sample was also observed using HR-STEM in an FEI Titan at 300 kV. Correlation of the exact region examined in STEM-CL is difficult due to the lack of obvious features on the sample surface, and so regions were selected at random. Some variation in contrast is observed, but it is difficult to conclusively attribute this to variations in indium content (and not, for example, to sample thickness variations arising from the preparation process). This problem is less significant in the case of cross-sectioned samples (described in the next section), as there is a region of pure GaN on either side of the InGaN layer.

However, the variation in indium composition is on about the correct length scale when compared to the STEM-CL emission pattern, i.e. light regions around 10 nm in diameter.

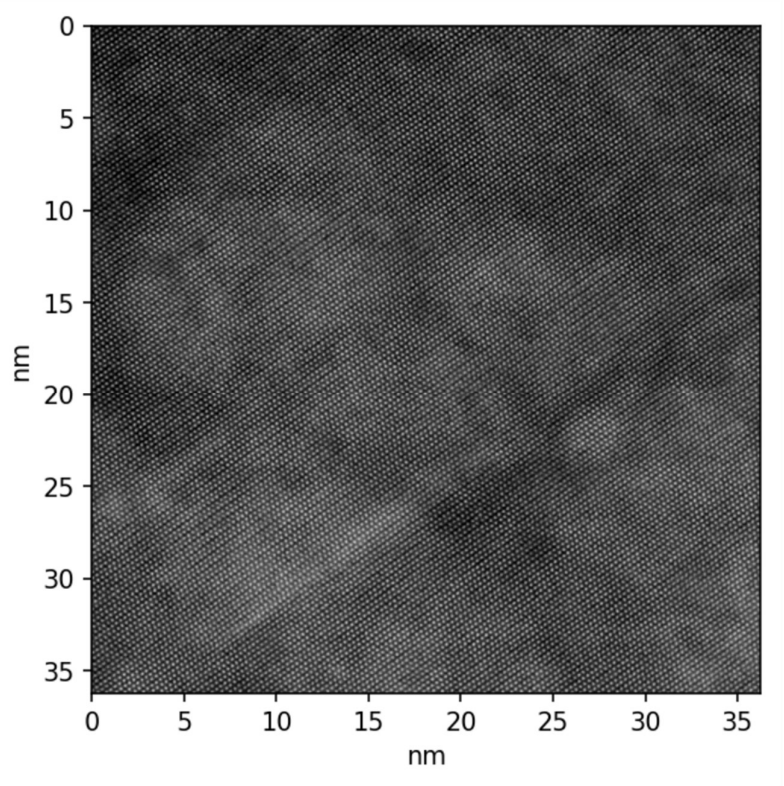

Figure 42: Plan view HR-STEM HAADF image of a Q2T quantum-dot sample, showing some variation in contrast. This could be due to a real variation in indium content, or due to damage incurred during the preparation process. Higher indium content gives brighter contrast.

3.7 Q2T QDs: cross-section

The Q2T sample was also prepared as a cross-section as described in section 2.4.2. Similar spectral features (sharp peaks on a broad background) were observed in this case, although the CL intensity was generally lower. The orientation of the sample relative to the acquired spectrum images is shown schematically in the top left of Figure 43, i.e. with the original surface of the wafer on the left of each image, and with the electron beam aligned along the plane of the InGaN QD layer.

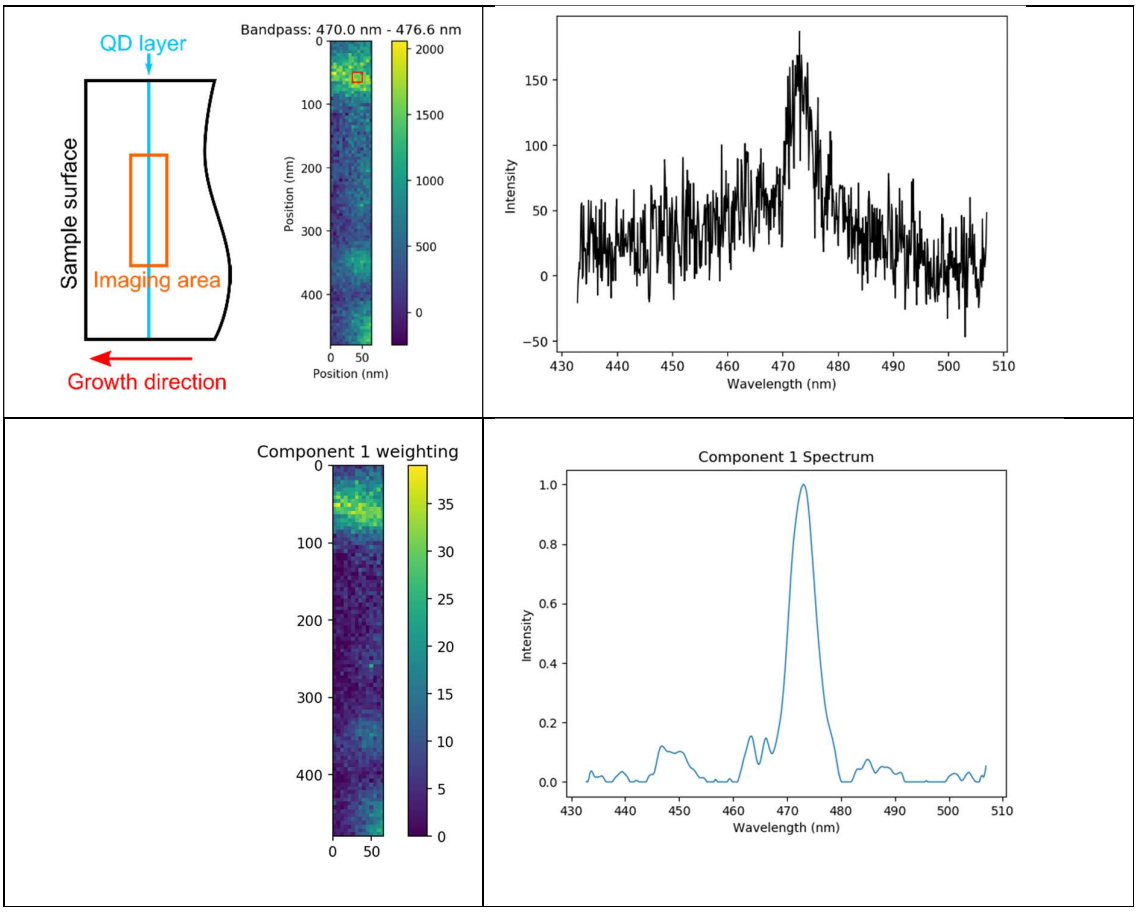

Figure 43: Cross-sectional STEM-CL images of the Q2T sample, showing an example of a region that exhibits a sharp peak in its emission spectrum. Band-passed image (top) is compared to the NMF-extracted component (bottom).

Some sharp spectral peaks localised to small regions of material were observed, with one example shown in Figure 43. Some emitting regions also appear to be larger in the growth direction of the sample compared to the in-plane directions; this could be due to the lateral confinement of carriers in the InGaN layer, meaning that the diffusion distance along the InGaN layer is shorter than the diffusion distance in the surrounding GaN. There is also a general reduction in intensity on the side of the InGaN layer closest to the surface (on the left-hand side of the spectrum images). This suggests that carriers injected on the surface side of the QD layer may diffuse to the surface where they recombine non-radiatively.

3.7.1 Correlation with STEM and EDX

The cross-sectional sample geometry allows threading dislocations to be imaged and correlated to the CL emission. Dislocations appear as lines running perpendicular to the InGaN QD layer, with bright contrast in the HAADF image owing to greater electron

scattering in the vicinity of a dislocation. A comparison between a panchromatic image and its associated HAADF signal is shown in Figure 44, below, showing that the dislocations also show up in the panchromatic CL signal with dark contrast. The contrast in the CL arises due to dislocations acting as non-radiative recombination centres for electrons injected into the material. There is some oscillatory sample drift occurring in these measurements, which causes the InGaN QD layer to appear wavy. STEM images taken with a much faster acquisition time than is required for a CL spectrum image do not show this artefact.

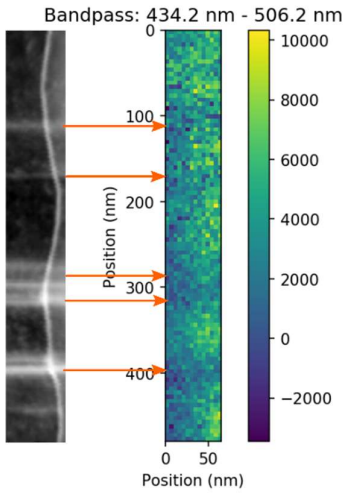

Figure 44: Comparison of HAADF image with STEM-CL intensity summed over the full range of collected wavelengths, showing clear reductions in overall CL intensity around bright dislocation contrast. Note that the wavy appearance of the InGaN line is due to spatial drift in the microscope.

The ease of resolving dislocation structures also allows for imaging the same region in multiple microscopes, since the appearance of unique clusters of dislocations can be used to locate the same submicron region of InGaN QD layer. In this case, HR-STEM was performed on an FEI Titan on the same region associated with the strongest peak in the STEM-CL data, and the resulting dark-field image is shown in Figure 45. The estimated position of the HR-STEM image is shown as a red square on the CL spectrum image. The process of correlating the position of various dislocations introduces some uncertainty in the exact position of the HR-STEM image relative to the CL spectrum image, estimated at ± 50 nm, as indicated by the red error bar. This largely originates from unknown amounts of sample drift in the y-direction along the InGaN layer during CL acquisition.

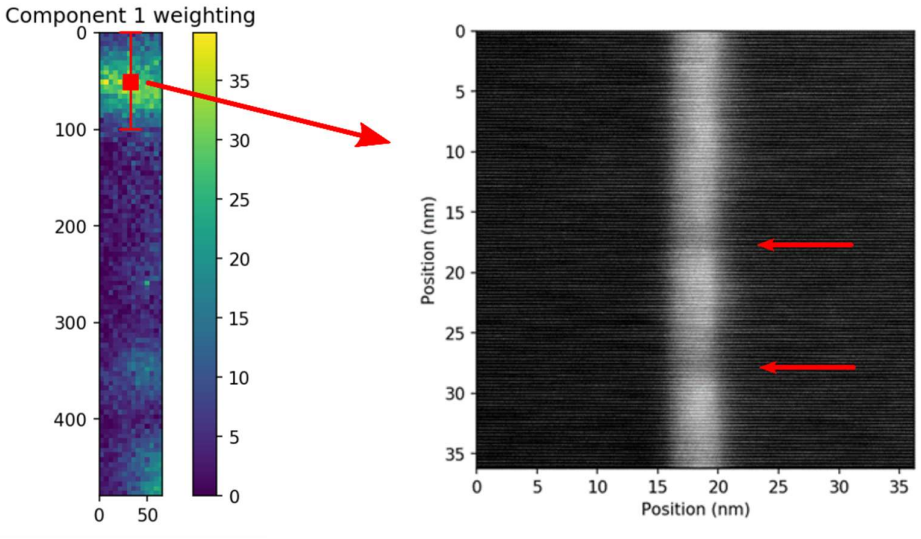

Figure 45: HR-STEM data collected from the same region as a sharp, intense peak in the STEM-CL data. As dislocations were used to find the region in question, some error is possible – an estimate of the positioning error is indicated on the weighting plot. Some inhomogeneity in the HAADF signal is observed along the length of the quantum well, as indicated by the red arrows.

Some non-uniformity in the HAADF signal is observed along the length of the QW, suggesting a variation in indium composition. This was also investigated using energy-dispersive X-ray spectroscopy (EDX), which had to be conducted in a third microscope (an FEI Osiris) due to an issue with the detectors in the Titan. The EDX map was analysed using a script by Siyuan Zhang, which uses NMF to separate signal components from noise before summing the signals back together and performing element quantification using the Cliff-Lorimer method. The indium composition map and a line profile along the QW are shown in Figure 46.

The EDX data were not accompanied by calibration data, so the absolute composition values recorded in the spatial maps are subject to systematic error. To account for this, the extracted line profile in Figure 46 has been normalised to the known average indium composition of the sample used for TEM, as estimated by the average PL emission wavelength of the sample in the vicinity of the TEM lamella. This was measured to be 464 nm, giving an average In composition of 19.5 %at.

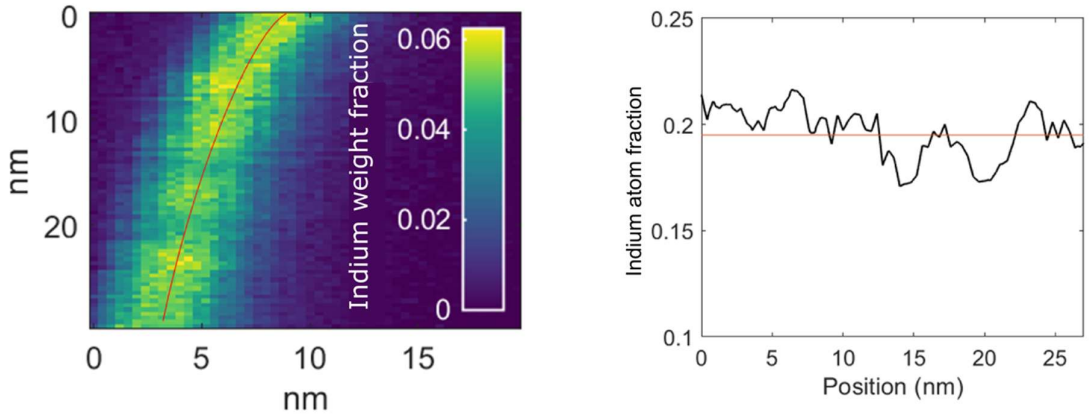

Figure 46: EDS map (left) and extracted line profile along the spline shown in red (right). The line profile is averaged over the 5 pixels on either side of the spline at each point. The indium trace (right) is normalised to the known average indium composition, determined from the average emission wavelength of the sample.

The same variation in indium composition as seen in the HR-STEM HAADF signal is reproduced in the EDX analysis, which shows a region approximately 5 nm wide bordered by 1-2 nm strips with ~15% lower indium. This quantitative analysis of the composition allows a simple model of the dot-in-well structure to be built, based on the estimated thickness of the sample (100 nm). Due to spatial drift in the STEM-EDX map, dimensions of the feature were extracted from the HR-STEM image, while indium compositions were taken from the EDX profile.

A simple model of this dot-in-well structure is a pair of concentric cylinders of differing indium composition, as shown in Figure 47.

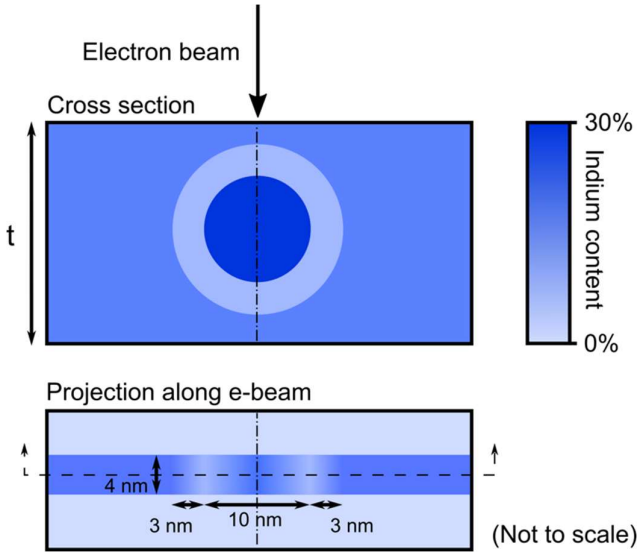

Figure 47: One model of a dot-in-well structure that could produce the observed variation in indium content.

The observed indium content will be approximately the average along the electron-beam direction. For example, along the chain line on Figure 47, which passes through the centre of the dot, a moderate indium composition will be observed that is the average of the QW, the ring, and the dot compositions weighted by their thicknesses.

As the thickness (t) of the sample is not known accurately, some simple calculations can be performed to calculate the observed average indium content along the centre-line:

$$X_{centre} = \frac{6X_{ring} + 10X_{dot} + (t-16)X_{well}}{t} = 20\%$$

The minimum composition will occur just adjacent to the dot, where the beam passes through the largest amount of 'ring' – this has a thickness of 12.5 nm, and so:

$$X_{min} = \frac{12.5X_{ring} + (t-12.5)X_{well}}{t} = 17\%$$

A plot of the dot and ring compositions predicted by these equations for different sample thicknesses is shown in Figure 48; this puts an upper bound on the sample thickness of about 80 nm, at which point the ring would need to have zero indium. The expected sample thickness is typically around 50-100 nm for manually prepared electron-transparent samples.

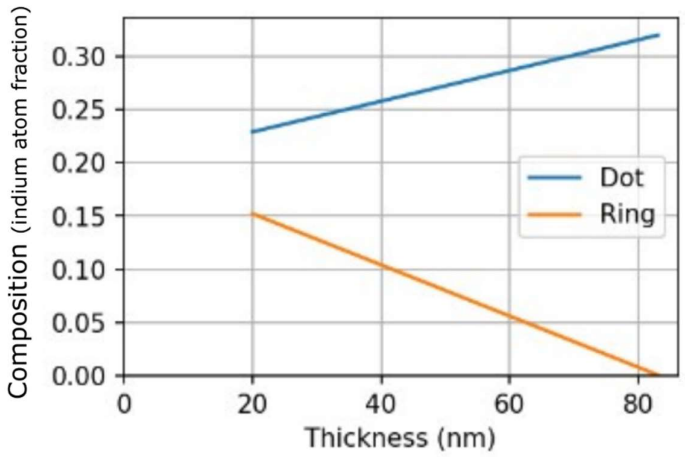

Figure 48: Plausible range of compositions for the dot and ring for different sample thicknesses.

3.8 Single quantum well cross-section

A single c-plane quantum well, not expected to contain single photon emitters, was also examined by STEM-CL, STEM and EDX as a comparison. A broad emission was observed that reduced in intensity as the beam was scanned along the QW, as shown in Figure 49.

Non-negative matrix factorisation

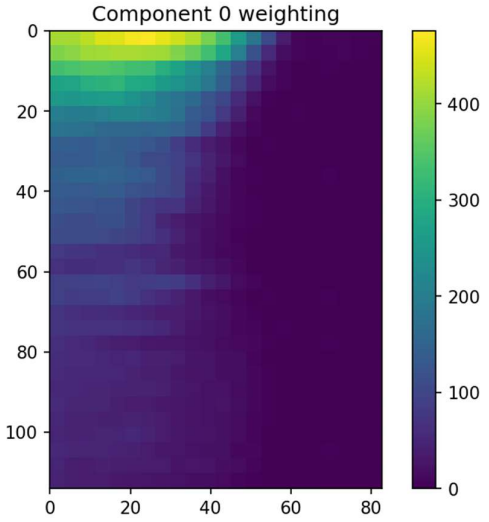

Band-pass filtered

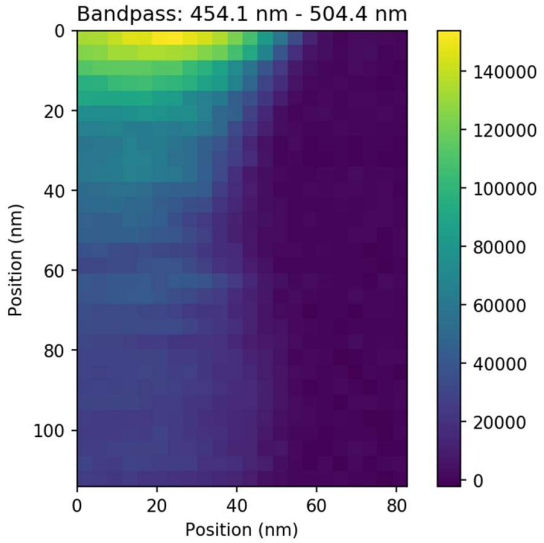

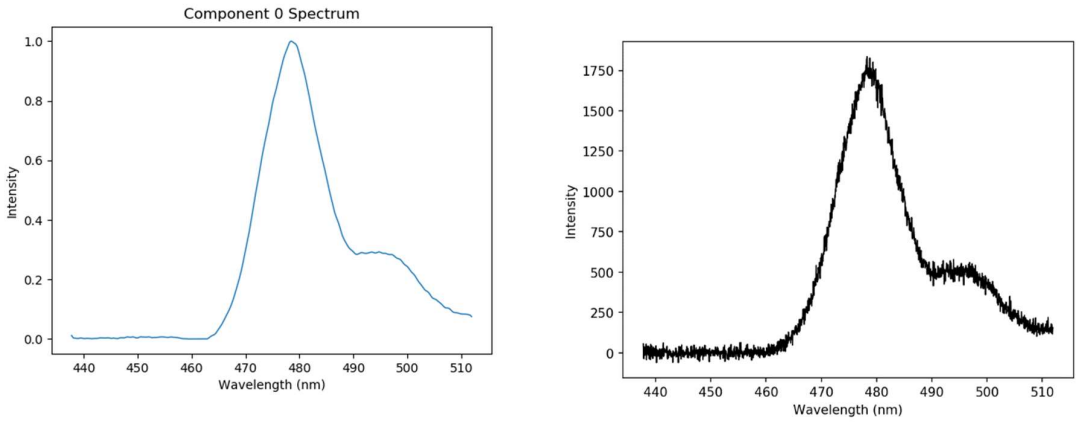

Figure 49: NMF component accounting for most of the variance, compared to band-pass filtered version of SQW sample, showing a broad emission that is quenched during acquisition of the spectrum image.

The data shows no evidence of the sharp peak features seen in the QD samples, and the intensity of the peak is also about an order of magnitude higher. However, there is obvious damage-induced reduction in intensity as the beam is scanned along the QW.

The SQW sample was also subjected to the same sequence of structural characterisation methods as the QD samples. A HR-STEM image of a representative region of SQW is shown in Figure 50. This reveals a reasonably uniform well, both in terms of thickness and HAADF

intensity (which correlates with the indium composition). There is no sign of the type of variation seen in the QD-containing samples.

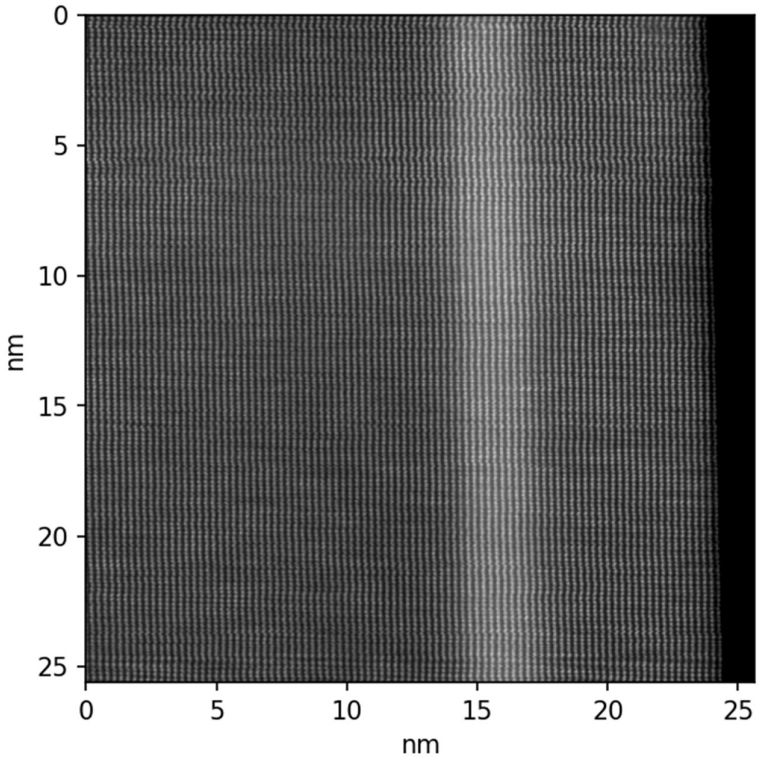

Figure 50: Dark-field HR-STEM image of a single QW sample, showing a reasonably uniform indium-rich layer about 2 nm thick.

The indium content and uniformity in the SQW was also investigated using STEM-EDX, as shown in Figure 51. A line profile was also taken along the SQW, and this shows much less variation than the equivalent profile taken from the QD sample.

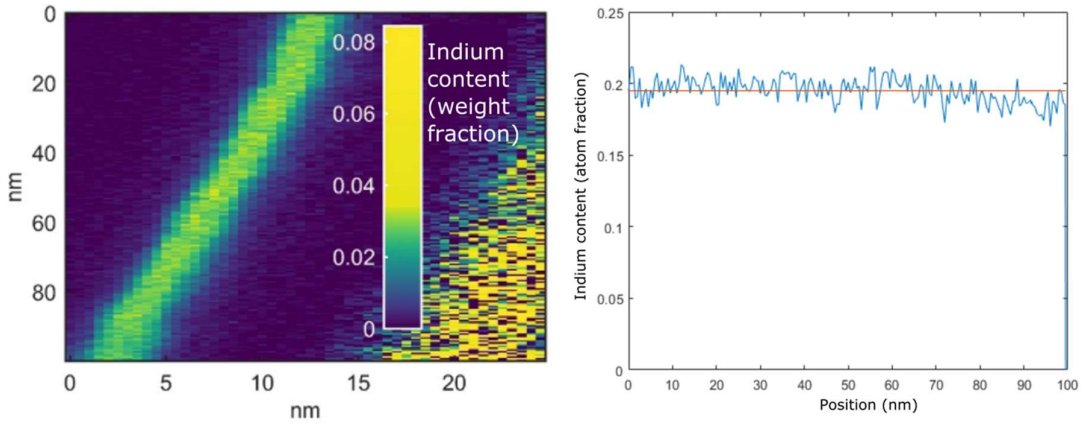

Figure 51: STEM-EDX map of SQW indium content (left), and an extracted line profile (right). The tilted appearance of the InGaN line is due to specimen drift. The extracted line profile has been normalised to the average indium composition of the sample to account for systematic error in the raw data shown in the composition map.

3.9 Discussion

We observed sharp peaks in the nano-cathodoluminescence spectra of QD-containing samples, that were localised to an area approximately consistent with estimates of the minority carrier diffusion length in GaN. Such peaks were not observed in the control single QW sample, indicating that they may be related to the samples' QD-like behaviour. In general, the intensity of QD-like features was relatively low, and this meant that a wide entrance slit had to be used to obtain sufficient intensity. This means that the resolution of the spectrometer was only around 4 nm, which is not narrow enough to suggest whether or not quantum confinement is actually present in the observed features.

Structural features also proved difficult to correlate with the spectra. While the emission-quenching effect of threading dislocations could be seen clearly on the STEM-HAADF signal collected at the same time as the CL spectrum image (in cross-section), the resolution at 80 keV proved to be insufficient to investigate the fine structure of the InGaN layer. Acquiring sufficient resolution to distinguish structural features required moving to an aberration-corrected instrument operating at 300 keV. While the easily visible dislocations allowed the same region (to within a few tens of nanometres) to be located in cross-section samples, plan-view samples were not able to be correlated in this way.

Even when carrying out STEM in a high-resolution instrument at a relatively high accelerating voltage, the resulting image is still a projection of the sample. This is a particular problem for 3D nanostructures (e.g. QDs) embedded in planar slabs of material, and is worsened when using thicker samples. At the same time, thicker samples give a stronger signal in cathodoluminescence. This means that there is a trade-off between STEM image contrast and CL signal intensity. Indeed, most of the literature performs STEM-CL with samples in the nanorod geometry, where light extraction will be more efficient and this trade-off is therefore less important.

AFM data on InGaN quantum dots in uncapped non-polar samples indicates that the metallic droplets (in MDE samples) or InGaN-containing dots (in Q2T samples) are sitting on a fragmented quantum well. This will worsen the projection effects, since there may not be a very large difference in indium content between the quantum dots and the coplanar quantum well.

These complications reduce the likelihood of observing a QD with enough contrast to distinguish it from the background STEM signal. However, some evidence of the nano-ring structure was observed in plan-view STEM, as well as an indium content variation consistent with a dot-in-well structure in cross-section.

The nano-ring structure observed by AFM [139] correlates closely with the feature observed in STEM-CL. However, as these structures sit exclusively on the blue side of the background quantum well, they can only explain some of the QD-like emission observed by micro-photoluminescence.

In the Q2T sample, the dot-in-well structure correlated closely with a peak in the STEM-CL spectrum, suggesting that it may be a source of QD-like emission in the Q2T samples. However, only one such structure was observed by STEM, while many more regions showing similar STEM-CL spectra were examined in the HR-STEM. The structure was found in one of the thinner regions of the sample (nearer the hole created by the argon ion milling process), suggesting that the contrast may be better in this region than others. It is also likely that other types of structures are responsible for the observed emission, that were less well resolved by the HR-STEM technique.

The effect of beam damage on these samples has also not been fully controlled for. While the STEM-CL experiments were carried out at a lowered beam energy of 80 keV, this is still above the damage threshold in GaN [124], and electron damage induced quenching of the emission is therefore possible on the timescales taken to acquire the STEM-CL spectrum images. The observed pattern of emission could conceivably be due to certain regions of the sample being more susceptible to this kind of quenching. A c-plane single QW sample was used as a control, and did show some quenching of the QW emission signal. However, when exposed to the HR-STEM and EDX procedure at higher voltage, it did not show any evidence of indium segregation, suggesting that the structures observed by these techniques in the a-plane QD wafers are not artefacts of electron damage.

There is a question as to why damage-induced quenching is observed in the SQW sample but not in either QD sample. One possibility is that the susceptibility of the c-plane SQW structure to beam damage is higher, possibly due to increased mobility of the generated carriers through the uninterrupted InGaN layer. Another possibility is that the damage rate is much higher in the a-plane QD structures, so that the increased intensity is never observed, and only lower-intensity features with greater stability are seen.

3.10 Conclusions

We have shown that STEM-CL can image nano-ring structures in planar InGaN samples, and can resolve emission localised to small, sub-100 nm sized regions. We have also demonstrated that the same region in a cross-sectional sample can be examined in other STEM instruments to gain further insight into the structure of the emitting regions. However, the technique is limited by the trade-off between CL signal and imaging resolution when choosing a sample thickness. The effect of beam damage on the CL signal from QD-containing samples also remains unclear, and a lack of spectral resolution means that it is hard to confidently assign the observed peaks to structures exhibiting 3D confinement. Future work could combine the spectroscopy with a Hanbury-Brown and Twiss interferometry experiment to confirm if the observed emitters are acting as single-photon sources.

When used to compare MDE and Q2T QD samples, clear differences were observed that support the different postulated QD growth mechanisms. While only evidence of larger

droplets was seen on the MDE sample, this limited set of data may be missing smaller droplets that are otherwise similar in form (as previously observed by AFM). In the Q2T sample, the STEM-CL evidence is consistent with a highly fragmented QW acting to form 3D confinement centres.

Chapter 4

4Regrown LEDs and porous distributed Bragg reflectors

Highly reflective mirrors are essential to the construction of several kinds of optical microcavity, as discussed in section 1.6, and are also useful for increasing the light extraction efficiency from light-emitting structures by redirecting light that would otherwise be lost into the substrate. This chapter will consider one method of fabricating distributed Bragg reflectors (DBRs) containing porous GaN and discuss how it can be integrated into a full light-emitting diode (LED) device structure. The details of the fabrication and optimisation of a porous-DBR LED are presented, and the resulting devices are characterised electrically and optically. Although the specific device fabricated here has a QW emitting region, this may be considered a step towards a potential QD device along the same lines.

4.1 Introduction

4.1.1 Distributed Bragg reflectors

Distributed Bragg reflectors (DBRs) are structures that consist of alternating layers of high and low refractive-index material. A light ray propagating in the DBR therefore encounters regular, sharp changes in the refractive index (n), and this causes the wave to undergo reflection at each interface. The Fresnel amplitude reflection coefficients have opposite sign for each successive interface, as the wave will encounter alternating positive and negative refractive index steps. Constructive interference between the reflected waves of a particular wavelength λ (and strong overall reflection) is seen, therefore, when each layer has an optical path length equal to $\frac{\lambda}{4}$ for waves arriving normal to the DBR layers [141].

The peak reflectance R and stopband width $\frac{\Delta f}{f_0}$ are important figures of merit for a DBR and are both determined by the refractive index contrast between the layers, with a greater difference in refractive index leading to a higher peak reflectance (for the same number of repeats) and a wider bandwidth, which are both desirable when the DBR is used to construct an optical cavity.

DBRs may be constructed using any technique that allows for the creation of regular steps in the refractive index of a thin film. Some common techniques are the use of dielectrics such as SiO_2 and TiO_2 deposited by physical vapour deposition (e.g. e-beam evaporation [142]), chemical vapour deposition (e.g. SiO_2/Si_3N_4 DBRs grown by plasma-enhanced CVD [143]), epitaxial growth of different alloys of AlGaN [144] or AlInN [145], or selectively removing material to create an air gap [92] or layers of porous GaN [84], as discussed in Chapter 1.

4.1.1.1 Simulating DBR structures

The optical characteristics of multilayered thin-films can be simulated using the transfer-matrix method (TMM), which was carried out for this project using the Python `tmm` package [146].

4.1.2 Quantum-well LEDs

High-efficiency blue LEDs are essential to modern solid-state lighting, as blue light can be partially down-converted by a phosphor to generate the broad spectrum required for white

light. Commercial high-efficiency LEDs currently use multiple $In_xGa_{(1-x)}N$ quantum wells (QWs) with the indium composition tuned to give blue emission [147].

The QWs are layers of InGaN typically a few nanometres thick and separated by GaN barriers. The QWs are sandwiched between an n-doped and a p-doped layer, which facilitate electron and hole injection into the active region. Radiative recombination can then occur in the QWs, resulting in light emission when a current flows through the device.

As mentioned previously, the defect density (particularly of threading dislocations) is very high in GaN compared to other semiconductor systems. As dislocations act as non-radiative recombination centres, this could be expected to quench the emission from the QWs. However, in practice, carriers are confined at fluctuations in the QW potential, which prevents them from diffusing along the QWs and arriving at the defects in great numbers [148]. These potential fluctuations could arise from In inhomogeneity (both due to random alloy fluctuations and indium clusters) and well-width variations observed in InGaN QWs.

4.1.2.1 Epitaxial growth of LEDs

The growth of LEDs by MOCVD has a few complications that influence the device design. Firstly, the optimal growth temperature for InGaN is lower than that for GaN. There are therefore a few schemes for growing the QWs, depending on how the temperature is varied during growth. In the single-temperature (1T) method, the temperature is ramped down, and then all of the InGaN QWs and GaN barriers are grown at the same (low) temperature. The 2T method introduces temperature ramps after each InGaN layer is grown, increasing the temperature before GaN barrier growth and then decreasing again prior to the next InGaN QW; this increases the crystal quality of the GaN barriers. The Q2T method is a refinement of this, where a very thin GaN cap is grown on top of each QW at the InGaN growth temperature, before ramping up to a higher temperature for the remainder of the barrier growth. This prevents indium desorption during the temperature ramp, and there is a trade-off between defect density and indium loss depending on the thickness of the low-temperature cap [149].

Secondly, a p-doped layer is required for hole injection. Mg doping is generally used for p-type doping in GaN, as discussed in section 1.3.3. This causes problems for LED structures grown with the layer sequence of p-GaN, QWs, n-GaN, as the Mg doping will tend to diffuse

through the active layers, and the crystalline quality is also affected by growing on p-type GaN. Hence, most practical LED epitaxy schemes grow the p-GaN layer last, on the top surface [150].

GaN is also typically grown on highly resistive sapphire substrates, which also influences the LED design by requiring processing to provide access to the buried n-GaN layers.

4.1.2.2 LED device design

The design objectives of an LED structure are to:

- provide access to buried n-GaN layers;
- form contacts to n- and p-GaN;
- facilitate uniform current injection into the QWs; and
- efficiently extract light from the QWs.

There are two main strategies for accessing the buried n-GaN layer. The first is to remove the sapphire substrate and form contacts directly to the n-GaN; however, this requires several time-consuming steps to bond the wafer to a carrier substrate and remove the sapphire (creating a 'flip-chip' or vertical device). The second is to etch from the top, forming isolated mesas containing the p-i-n structure, and then deposit n-contacts directly adjacent to these mesas. The high conductivity of n-GaN then allows for lateral current spreading into the device layers – this is therefore referred to as a lateral device.

For uniform current injection, the total resistance of any pathway between the positive contact and negative contact should be equal. A solution that uses the geometry of the contacts to uniformly inject current would therefore require the resistivity of the p- and n-GaN layers to be the same [151, 152]. However, the doping concentration and therefore conductivity achievable in p-GaN is much lower than in n-GaN [152]. Trying to equalise the resistivity by adjusting doping levels would, therefore, require increasing the resistance of the n-GaN (and therefore compromising on the overall series resistance of the device).

To overcome this problem in lateral devices, and achieve more uniform current injection, a transparent conducting layer (TCL) is deposited on top of the p-GaN. Several options exist for this: thin metal films (typically Ni/Au) [153], transparent conducting oxides [154], and

graphene [155] have all been explored in the literature. The transparent layer must also form a reasonably low-resistance, preferably ohmic, contact to p-GaN.

Using the flip-chip approach, light can extracted through the n-GaN, and so an opaque metal layer can be used as the p-contact. N-GaN is also conductive enough that a TCL is not required. Contacts can be formed in a wider range of geometries, which can help to alleviate current crowding. For example, interdigitated stripes of n- and p-metal can be used for optimal spreading (as suggested by modelling [156]), or through-wafer vias can be used to minimise the area of contact metal on the top n-GaN surface (used in state-of-the-art high power LEDs [157]).

4.1.2.3 Ohmic contacts to GaN

LED structures require low-resistance contacts to both n- and p-GaN, and contacting schemes have been extensively investigated in the literature. Generally, there are two main mechanisms for creating ohmic contacts. One is to create a metal-semiconductor junction with a low Schottky barrier height (by selecting a metal with a work function closely matched to the electron affinity of the semiconductor, for example), such that a large proportion of carriers have a thermal energy exceeding this barrier at room temperature and can therefore travel into the semiconductor. This mechanism is called thermionic emission. The other mechanism is to generate a narrow enough Schottky barrier that charge carriers can tunnel through the barrier (field emission). This can be achieved by very heavy doping of the semiconductor near the metal interface, causing significant band bending and a very narrow barrier width [158].

Contacts to n-GaN

Ohmic contacts to n-GaN typically consist of multilayer stacks of metal, usually including layers of Ti and Al near the n-GaN surface, and are generally annealed at 700 - 900°C in an inert atmosphere [158]. During annealing, there are reactions between the Ti and the GaN surface, and between the Ti and Al metals [159].

Due to these reactions, and the possibility of forming highly resistive Al_2O_3 and titanium oxides, a metallisation stack of Ti/Al/Ti/Au is often used for forming ohmic contacts to n-GaN. Using this contact scheme, Ti can react with the GaN surface, initially reducing any

residual Ga_2O_3 present and thereby ensuring that the contact is made to a pristine surface. The Ti then reacts with the GaN surface, and high-resolution TEM and X-ray photoelectron spectroscopy studies reveal that a few monolayers of TiN form [160], generating N vacancies in the GaN film that act as donors [161]. In this way, an extremely highly doped ($>10^{20}$ cm^{-2}) layer of n-GaN is generated directly next to the contact metal. The significant band-bending effect of this layer will then facilitate ohmic behaviour by electron tunnelling through the barrier.

The Al layer is used in this contact scheme is suggested to perform two functions. It forms a variety of intermetallic compounds with the Ti during annealing that can be resolved by X-ray diffraction [159]. These compounds form ohmic contacts to the TiN layer, and the Al content of the TiAl layer is suggested to prevent out-diffusion of Ga [162]. Use of e.g. Au in place of Al as an overlayer also results in ohmic contacts, but the thickness of the resulting TiN layer is observed to be smaller.

A second Ti layer is included above this layer to consume any remaining pure Al, preventing the balling-up of the Al layer. A diffusion barrier consisting of Pd, or a layer of Ni, are sometimes used in place of the second Ti layer. Finally, an Au cap provides a surface that is inert to oxygen, to prevent subsequent oxidation when the samples are exposed to air. Such contacts can attain resistivities lower than 8.9×10^{-8} Ωcm^2 [163].

These processes mean that enough annealing time and temperature is required for diffusion processes to complete and form the necessary compounds for low-resistance contact formation. The n-contacts are also typically made to surfaces that have been exposed by dry etching, and this has also been reported to lower the contact resistance. This could be due to roughening, oxide removal and surface damage induced by the RIE process [162].

Contacts to p-GaN

p-GaN contacts tend to be higher resistance than n-GaN contacts, due to the lower achievable dopant concentration [152] that can be lowered further by sensitivity to oxygen contamination during Mg activation [164], resulting in a low free carrier concentration. The high electron affinity (6.5 eV) of p-GaN also makes it hard to form ohmic contacts of any type, as this value exceeds the work function of any appropriate metals [165]. As previously

mentioned, the p-GaN contact in a lateral LED device is also frequently required to be transparent.

A common scheme used for contacts to p-GaN exploits thin layers of Ni and Au, typically just a few nanometres thick to preserve transparency, that are annealed in an oxygen-containing environment [166]. During annealing, the Ni diffuses to the contact surface, forming NiO. Au-rich islands are also observed to form on the GaN surface; the consumption of Ni in the oxidising environment of the annealer reduces the Ni content of these islands to nearly zero [167]. Hence, there is a reversal of the as-deposited layers, and NiO ends up on the top surface while Au tends to migrate towards the GaN interface. The ohmic contact is thought to be related to the Au islands, rather than the NiO layer, and AFM and XPS studies indicate that these islands are in fact Au:Ga phases that form at the surface of the p-GaN [166]. Indeed, SIMS and synchrotron radiation photoelectron spectroscopy also indicate outdiffusion of Ga from the p-GaN structure, providing a mechanism for this Au:Ga phase formation [168]. Ga vacancies also act as acceptors, increasing the local p-doping level in an analogous way to N vacancies in n-GaN.

This mechanism places some restrictions on the contact annealing process: it must allow for sufficient diffusion to reverse the metals, form the transparent NiO layer on the top surface and form Au:Ga islands, but not so long as to start oxidising the GaN itself.

4.1.2.4 Internal and external quantum efficiency

Light-emitting diode efficiency is characterised in terms of two efficiencies: the internal quantum efficiency (IQE), which is the efficiency with which carriers recombine radiatively once they have arrived in the quantum wells; and the external quantum efficiency (EQE) that also includes losses incurred by the contact resistances, current injection into the quantum wells, and the efficiency with which light can be extracted from the QWs. Wall-plug efficiency is also sometimes referenced, and this also includes the efficiency of any power converters or LED driver circuitry.

4.1.2.5 Efficiency droop in InGaN LEDs

InGaN-based LEDs exhibit a reduction in their IQE at high current densities, which is a phenomenon that is called efficiency droop. Initially, the IQE increases with current, before reaching a peak at a few A cm^{-2} and subsequently decreasing by as much as half its peak

value at current densities of a few 10^2 A cm^{-2} [150]. Such reduction in efficiency at high current can be due to heating, but droop also occurs in the absence of thermal effects [169]. It is also an effect unique to InGaN LEDs, and is not observed in similar devices in other material systems, such as GaAs [170].

IQE depends on the rate of radiative recombination compared to the rate of non-radiative processes, and the general form of the droop behaviour is often interpreted using the 'ABC' model [150]:

$$\text{IQE} = \frac{\text{Radiative recombination}}{\text{Total recombination}} = \frac{Bn^2}{An + Bn^2 + Cn^3 + k(n - n_0)^m + \frac{I_{leak}}{qV_{QW}}}$$

There are several terms with different dependencies on n, the carrier density in the active region. The A, B and C coefficients model Shockley-Read-Hall (SRH), radiative, and Auger recombination (with linear, square and cubic dependence on n respectively), and form the basis of the simple 'ABC' model. The remaining two terms compensate for deviations from the simple model at very high current densities. The n^m term relates to carriers escaping from confined states in the QW, and subsequently contributing to nonradiative recombination, while the final term accounts for carriers that can avoid recombination within the QW and leak to the surrounding n- or p-doped material, where they also undergo non-radiative recombination. Overall, this can be used to fit a typical IQE vs injection current characteristic, such as that shown in Figure 52. An IQE vs current curve for a GaAs-based QW LED (with AlGaAs barriers) emitting in the IR region is also shown, to show the difference in behaviour between a droop-affected device and a semiconductor system that is not affected by this problem at practical current densities.

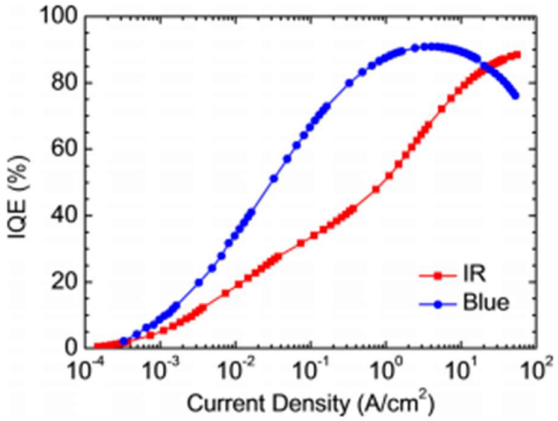

Figure 52: Sample IQE vs current characteristics for blue (InGaN) and red (GaAs) LEDs. Reproduced from Lee et al. [170], under a Creative Commons CC-BY licence.

IQE may be measured directly using resonant excitation in photoluminescence experiments, where carriers are excited directly in the QWs. In practical devices, however, carriers must be injected into the active region and light needs to be extracted from the QWs, and so EQE becomes the relevant measure. Several additional factors then become important, particularly under electrical injection, such as the uniformity of current injection into the active region (which will locally modify the value of n), resistance of the metal contacts, and how the overall device design facilitates light extraction. Light extraction efficiency can also vary with current in real devices, since practical metallisation schemes tend to distribute current unevenly, and the regions of highest injection can also correlate to the thickest metal layers (which have the lowest transparency) [156, 157].

As my work on NP-DBR LEDs involves a measurement of device efficiency with current, a short summary of the mechanisms thought to be involved in efficiency droop follows.

Low-current regime

SRH recombination is a process where carriers recombine via defect-related deep levels that lie in the band-gap of the bulk semiconductor. Its rate is expected to increase linearly with current density, since it is a monomolecular process that depends on the electron density only. The rate of radiative recombination, by contrast, increases with current density squared, since it is a bimolecular process that depends on both electron and hole density, which can also be assumed to be equal at non-negligible current injection [169], with some

deviation from the ideal behaviour due to carrier localisation in the InGaN QW. Observations of carrier lifetimes in InGaN carried out using observations of electroluminescence under high-frequency drive provide evidence that the rates of radiative and non-radiative processes follow these dynamics in the low-current regime [171].

High-current regime

The origin of droop in the high-current regime is a relatively controversial topic. This section will summarise some of the theories on this subject, drawing mainly on a review by Verzellesi *et al.* [150].

Increased temperatures, expected to arise during high-current operation, reduces the EQE of LEDs. However, efficiency droop is still observed when measures are taken to eliminate heating effects (e.g. by using pulsed excitation) [172]. This suggests that there are other processes that lead to efficiency droop in the high-current regime.

Auger recombination is another possible contributing mechanism. In this process, an electron and hole recombine across the bandgap with excess energy transmitted to a third electron or hole, making it a three-particle process with a consequent dependence on n^3. However, determining the value of the Auger coefficient C (within the ABC model in Equation 10) is difficult, as it relies on assumed or measured values of the A and B coefficients, and on assumed current density, as well as the inherent difficulty in decoupling Auger contributions from other possible high-current-density nonradiative processes [150].

Ab-initio calculations indicate that the Auger coefficient is lower than 10^{-32} $\mathrm{cm^6 s^{-1}}$ for direct Auger processes [173], and somewhere between 10^{-32} - 10^{-31} $\mathrm{cm^6 s^{-1}}$ for indirect (i.e. phonon or alloy-fluctuation assisted) Auger recombination [174]. However, Verzellesi *et al.* contend that C should be larger, on the order of 10^{-30} $\mathrm{cm^6 s^{-1}}$, to completely explain the droop effects commonly observed in InGaN QW LEDs. As may be expected, given the difficulty in measuring C directly, some literature contradicts this point. For example, Laubsch *et al.* [175] can model their devices with a simple ABC rate equation and $C = 3.5 \times 10^{-31}$ $\mathrm{cm^6 s^{-1}}$, which is in the range of indirect Auger processes.

In case the C coefficient is, in fact, insufficient to fully explain the observed droop, there are several theories that try and address the discrepancy. They fit into two classes; some theories

seek to explain why n (the carrier density) might be higher than expected, causing droop to occur at a lower average current density than the droop equation predicts. Other theories suggest a different mechanism altogether as a possible contributory factor.

A locally increased carrier density may occur due to carrier confinement by alloy or well-width fluctuations in InGaN QWs, effectively reducing the volume of QW that is participating in radiative recombination. Polarisation fields can also reduce the effective width of the QW by separating electrons and holes into smaller regions on opposite sides of the QW [176], also reducing the effective volume. However, radiative recombination would need to be restricted to about 3% of the total well volume for this to fully explain the droop behaviour, which is an implausibly large degree of confinement. Additionally, nanostructured LEDs, such as QD LEDs, tend to show reduced droop, suggesting that increased confinement tends to have a beneficial effect [177].

The polarisation fields present across c-plane QWs may also increase the value of n by another mechanism. These fields, arising from both piezoelectric and spontaneous polarisation, can affect the rates of both radiative and SRH recombination by reducing the spatial overlap of the electron and hole wavefunctions in the QWs. This causes the carrier density in the QWs to increase as the rate of recombination slows down, shifting the efficiency peak towards lower currents for greater polarisation fields [178, 179]. The droop difference between c- and m-plane samples (with larger and smaller polarisation fields, respectively) demonstrates this well, with m-plane samples proving to be less susceptible to droop at the same overall current density. However, the difference in droop behaviour between c- and m-plane samples is greatly reduced when the samples are excited by a pulsed laser with the spacing between the pulses much longer than the recombination time [180], meaning that the carrier density in the QWs only depends on pulse energy and not on the kinetics of the recombination processes. This supports the idea that polarisation fields increase the overall carrier density under continuous excitation by slowing down both radiative and non-radiative recombination, thereby worsening droop.

It is also suggested that carriers are, in fact, only confined at QW potential fluctuations at low current density. As the average current density is increased, some of the carriers in the QW are no longer confined the local variations in the QW potential, and diffuse to defects where

they recombine non-radiatively [181]. PL studies indicate that this could occur due to saturation of the localised states at high carrier concentrations [148], which then means that extra carriers injected into the wells are free to diffuse to non-radiative recombination centres. This mechanism is referred to as density-activated defect recombination (DADR).

In addition to the mechanisms observed in PL, outlined above, there can be additional mechanisms contributing to efficiency droop in electrically pumped devices. Some high-current mechanisms are related to electron leakage through the active region; electrons are particularly important in the leakage processes because the hole concentration in p-GaN is always much lower than the electron concentration in n-GaN. There are several ways for electrons to survive recombination and leak through the QWs into the p-GaN: electron overfly, where electrons are not captured into QWs [182]; defect-assisted tunnelling [183]; poor hole injection into the QWs [184]; a strong asymmetry in the electron and hole concentrations [185]; and current crowding [156].

High-performance devices often include an electron-blocking layer (EBL) close to the QWs on the p-GaN side, which is a thin AlGaN layer designed to present a barrier to electrons that overflow the active layers. This increases EQE in both c- and m-plane devices, indicating that the EBL is indeed primarily affecting electron leakage rather than any polarisation fields across the QWs [186]. The overall effectiveness of the layer depends on the band engineering, as the EBL can also impede hole injection if the valence band is misaligned [187]. This has the effect of increasing EQE at low currents but worsening efficiency droop. However, refined designs such as graded composition EBLs increase EQE at all currents and indeed act to mitigate efficiency droop [188].

Finally, the effect of current crowding can be important in practical devices. Simulations conducted by Li *et al.* [156] show that this is the case for both flip-chip and lateral devices. Lateral devices experience current crowding either under the opaque p-metal on the top of the mesa, or if the transparent conducting layer is conductive enough, current can instead crowd towards the edges of the mesa due to insufficient current spreading in the n-GaN. Vertical devices also show current concentration underneath the opaque metallisation on the n-GaN top surface. Inhomogeneous lateral current spreading in either n or p-GaN also modifies the local value of n, and this means that simply changing the design of the

metallisation has a significant effect on the observed droop [189], even for quite subtle design differences [151]. The current crowding effect is also shown to have an impact on the light extraction efficiency [190], as the current tends to crowd under opaque regions of metal, reducing the LEE as injection current increases. This effect both a droop mechanism in itself, and can also increase the impact of other droop mechanisms by increasing the local current density.

Overall, high-current efficiency droop appears to be a combination of effects, with the epitaxy, device design and operating conditions able to alter the balance between the different contributory factors. While some degree of droop may be inherent to InGaN devices (via DADR and/or Auger), droop can also be strongly influenced by other factors in practical devices.

4.1.3 Strategies for improving light extraction

In many practical applications, the light emitted from the QWs needs to be redirected forwards, away from the substrate that holds the device. A reflector is therefore required underneath the QWs, ideally positioned as near as possible to them to avoid absorption in any intervening layers. Total internal reflection from the flat surface of the as-grown GaN wafer is another obstacle to light extraction, with any rays striking the surface above the critical angle of about 25° possibly becoming confined to laterally propagating modes in the LED die.

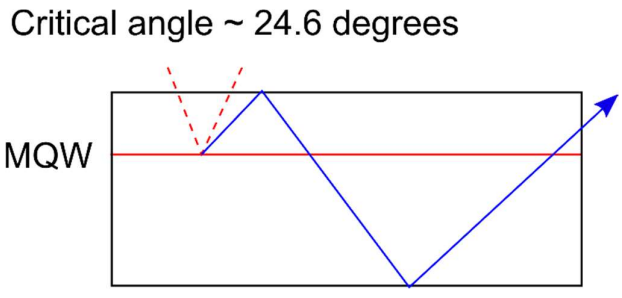

Figure 53: Schematic indicating the critical angle confining light to a GaN wafer, indicated by the red dashed lines. Any rays striking the surface above this angle may laterally propagate inside the wafer, as shown by the blue arrow. In air, the critical angle is ~24.6°.

The top surface can be textured to help scatter incident light, preventing lateral confinement. This texturing can be achieved by a variety of methods, generally involving dry [191] or wet etching [192]. Patterned sapphire substrates can also be used for the growth of the GaN layer,

scattering light at the GaN/sapphire interface, as well as acting to increase the quality of the overgrown GaN film [193-195]. A metallic bottom reflector can then be used to direct light away from the substrate.

DBRs, previously discussed in section 1.6.1, provide a way of creating a very highly-reflective mirror that can be positioned close to the QWs, with the consequent advantage of removing any absorption that would otherwise happen on the round-trip through the sapphire. The difficulties in fabricating these structures, outlined in the previous discussion, means that they are not typically included in practical, commercial devices at present. However, many reports exist of experimental LED structures containing DBRs to improve light extraction, or to create resonant-cavity structures that enhance the spontaneous emission rate. AlGaN/GaN reflectors [196], dielectric DBRs [197] and nanoporous GaN [198] have all been used in this way. Nanoporous GaN, in particular, stands out as having the potential to fabricate low-cost DBRs without the kinds of growth or processing problems associated with other kinds of DBRs.

Another technique, that involves more complex processing steps, is to remove the sapphire substrate altogether. This approach is applied in the highest-brightness vertical devices, since substrate removal is one of the necessary steps for fabricating a vertical device. Texturing of the top n-GaN surface and application of a highly-reflective metal reflector to the p-GaN then greatly increase the extraction efficiency from the thin GaN lamella. This approach is used in, for example, Osram ThinGaN devices [157, 190].

4.1.4 LED structures incorporating NP-GaN

Several reports of LED devices that incorporate NP-GaN layers exist in the literature, either as a template for growth [199, 200], or to form DBRs in InGaN [198, 201] or AlGaN [202, 203] LEDs.

4.1.4.1 NP-GaN templates

Templates consisting of thick layers of NP-GaN have been used to overgrow GaN layers and LED devices. In many reports, e.g. works by Soh *et al.* [200, 204, 205] the NP-GaN extends to the surface of the template, so that regrowth occurs on a porous surface (i.e. a surface that contains penetrating holes). 3D growth of islands which coalesce and form flat layers is observed, and a reduction in the strain present in the overgrown layers is observed by micro-

Raman measurements. XRD asymmetric ω-scans also show a reduction in FWHM, which indicates a reduction in dislocation density [200]. Reduced strain also increases indium incorporation, and so a red-shifted emission is also observed in several reports [200, 206].

The use of NP-GaN templates improves the emission intensity in PL [200] as well as CL and EL [199] with the enhancement attributed to the reduced strain, reduced defect density and enhanced carrier localisation at indium inhomogeneities. There is also enhanced light extraction due to scattering from the porous layer.

The regrowth process has also been observed to cause some changes in the NP-GaN itself, in the form of pore size and shape changes [207] [206]. In the literature reports, columnar or branching pore structures in thick NP-GaN layers were observed to change into ellipsoidal or facetted voids upon regrowth, and it is suggested that this is due to etching, dissociation and joining together of smaller pores. The morphology of the pores before and after regrowth are shown in Figure 54, showing the shape changes. The reconstruction of the porous layers during regrowth is also suggested to contribute to strain relief in the overgrown layers [206].

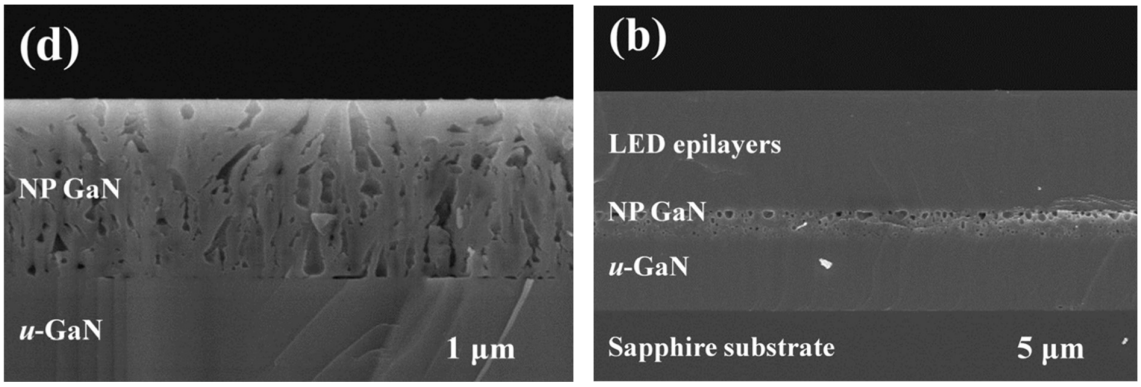

Figure 54: Columnar pore morphology before regrowth (left) observed to change to enlarged, ellipsoidal pores after regrowth (right). Reproduced from [206], with permission.

4.1.4.2 NP-GaN DBRs

There are some reports of InGaN LEDs incorporating NP-GaN DBRs in the literature; for example, Shiu *et al.* [198], Shieh *et al.* [201] and Zhang *et al.* [208]. In these works, the latent DBR and LED device layers were all grown in the same run, followed by EC etching to porosify the DBR. Trenches or mesas were patterned into the wafers prior to EC etching, so that the porosification proceeded via a lateral etching mechanism.

Enhanced emission power normal to the wafer surface was observed in both PL and EL due to the presence of the reflective DBR, and an increase in the directionality of emission was also reported (the emission angle decreased from 120° to 80° in Shieh, and from 98° to 52° in Shiu).

Both reports indicate some electrical changes to the resulting devices. Shieh *et al.* report increased on-resistance in their NP-DBR device, but see a reduced forward voltage (V_f). They attribute the increased resistance to the presence of the DBR in the n-GaN layer. Shiu *et al.* found a similarly increased resistance, but no change in the forward voltage. This may be principally due to differences in device design. While both reports use laser scribing to create isolation mesas, Shieh *et al.* allow the light emitting area to extend all the way to the edge of the mesa, while Shiu *et al.* define the active region using smaller squares of transparent indium tin oxide (ITO), keeping the laser scribing lines away from the active area. The surface damage induced by the laser scribing could then provide a lower-barrier pathway for carriers to leak across the device without emitting light in the QWs, possibly explaining the lower apparent V_f in the devices reported in Shieh *et al.*

Shiu *et al.* suggest that there are some changes to the strain state of the LED device stack after the NP-DBR has been porosified. They observe a blue-shift in the emission wavelength for the porous device, which is assigned to strain relaxation causing a reduction in the quantum-confined Stark effect (QCSE). Reported data on the wavelength dependence with EL excitation current does not follow the same behaviour, though; a blue-shift is observed with increasing injection current in both cases, but the shift is larger for the porous LED than the non-porous one. As the wavelength shift with increasing injection current is linked to the magnitude of the QCSE, since increased injection causes screening of internal fields across the QWs, this data does not support the presence of reduced piezoelectric fields. Indeed, Shieh *et al.* actually observe a red-shift in the emission wavelength of their porous devices compared to the non-porous ones; as these devices are not regrown, but are grown in one run, strain relief contributing to increased In incorporation is not a plausible explanation in this case.

The effect of the NP-DBR on the emission spectrum is also reported, with cavity effects observed in both papers. Shiu *et al.* observe linewidth narrowing with increased EL power

density, indicating cavity effects. They also observe lasing behaviour at high excitation powers in PL, with a threshold at 33.1 μW (although no estimate of power density is provided). A resonant-cavity effect was also reported in Zhang *et al.*, using an extra dielectric DBR on top of the LED device structure to intentionally engineer an optical cavity. They observed a reduction in the linewidth of the emission spectrum from 19.4 nm (no cavity) to 2.5 nm (with the NP-GaN and dielectric DBRs forming a resonant cavity).

There are also reports of AlGaN LEDs incorporating porous AlGaN DBRs that show broadly similar results. Device results in Fan *et al.* also show the increased light output and increased series resistance [202], together with red-shifted emission in porous devices when compared to non-porous ones [203].

4.2 Aims

This chapter reports on a comparison between LED heterostructures that have been re-grown on a template containing a NP-DBR and a non-porous GaN template. Regrowth of the LED structures on a template containing NP-DBRs is a useful refinement compared to etching the NP-DBR with the device layers in place; it allows for the NP-DBR and LED structure to be optimised separately, without constraints on (for example) the doping levels present in the LED heterostructure, and it removes the possibility of causing damage to the InGaN active layers and n-doped device layers during the electrochemical etching process. Structural, electrical and optical characterisation of the resulting wafers and devices is investigated, to assess whether the NP-DBR and regrowth process enhance the performance of the resulting devices.

4.3 Samples

Two sets of samples were grown for this study; one set of LED heterostructures regrown on non-porous n-GaN templates, and one set regrown on templates containing NP-DBRs.

4.3.1 Growth

The samples were grown by MOVPE. Initially, low dislocation-density template wafers were grown using the high-resistivity SiN interlayer method described earlier (section 1.3.2), with 2 μm undoped GaN grown before 2 μm n-doped GaN. One of these LDD templates was then

used for the growth of 10 pairs of highly-doped n-GaN alternating with undoped GaN, forming a latent DBR structure.

The template containing the latent DBR was etched using the process outlined in section 1.6.4, with a bias of 6.0 V in 0.1 M oxalic acid, by Peter Griffin. After etching, the template was examined using AFM by Dr Tongtong Zhu. The AFM images in Figure 55 show that the electrochemical etching process leaves the surface of wafer locally flat, with atomic terraces visible, ready for regrowth. The r.m.s. roughness of the template before etching is 0.38 nm in a 5 x 5 µm region and remains almost unchanged at 0.40 nm after the EC etch.

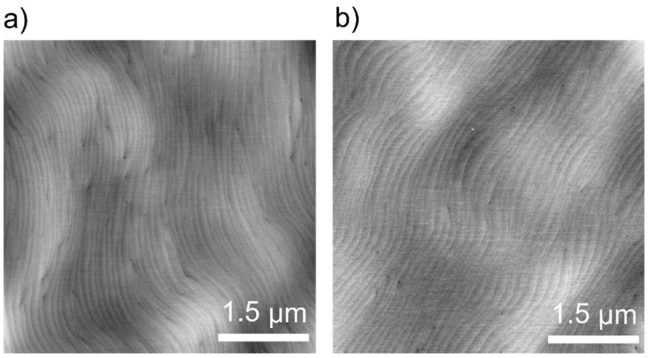

Figure 55: AFM images of the surface of a porous DBR template a) before and b) after EC etching, showing a smooth surface that is undamaged by the etching process and has epi-ready atomic terraces. Z-scale (black to white): 4 nm. Images acquired by Dr Tongtong Zhu.

After electrochemical porosification was carried out on the DBR sample, regrowth of LED layers was carried out simultaneously on the porous and non-porous templates. A 500 nm layer of n-GaN was grown at a temperature of 1050°C in H_2 ambient, before 5 InGaN QWs and undoped GaN barriers grown using the Q2T method and with an indium composition of around 18 at%. A 3-period p-doped AlGaN/GaN superlattice was then grown on top of the QWs with layer thicknesses of AlGaN 76nm / GaN 57nm and an aluminium content of ~10 at%; this superlattice was included to improve the conductivity of the p-type layer by increasing the ionisation of Mg acceptors. A final 10 nm p-GaN layer with higher doping concentration finishes the structure, to improve the properties of the p-contact.

4.4 Characterisation of regrown wafers

Three sets of samples were characterised after the growth runs were completed:

1. Porous DBR template

2. LED regrown on a non-porous template
3. LED regrown on a porous template

4.4.1 Microscopy

The structure of the as-grown wafers was investigated using SEM and STEM. Cross-sectional SEM samples were prepared by cleaving the wafer in a region well away from the edges that were exposed during regrowth. SEM images were then acquired using the circular backscatter detector in an FEI Nova, to reduce the contrast coming from the surface of the sample and emphasise the porosity in each layer. The images of the porous template before regrowth, and the final LED structure after regrowth, are shown in Figure 56.

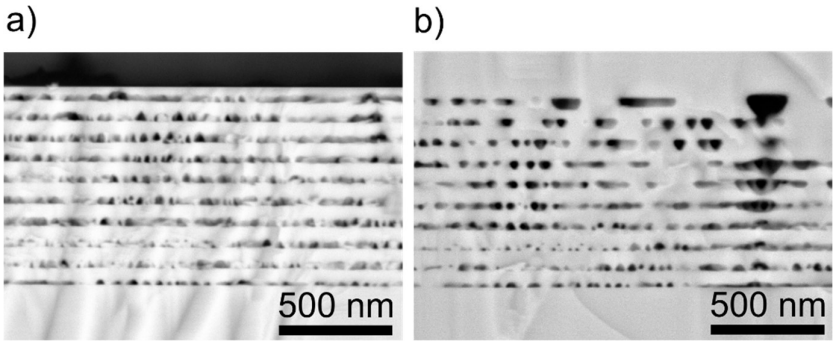

Figure 56: SEM images of the NP-DBR template a) before and b) after regrowth of the LED device layers. Enlarged holes are observed in the NP-DBR after the regrowth process.

The SEM image shows that pores have been enlarged in some areas after regrowth, and now impinge on the previously non-porous layers.

To assess whether the pore morphology is changing due to loss of material or redistribution within the DBR stack, the overall fraction of dark contrast present in each SEM image was quantified. Any region of the image with a lightness below a certain threshold was counted as a region of air, and this threshold was set at an appropriate value visually. Two analysed images are shown in Figure 57, with the below-threshold regions coloured red.

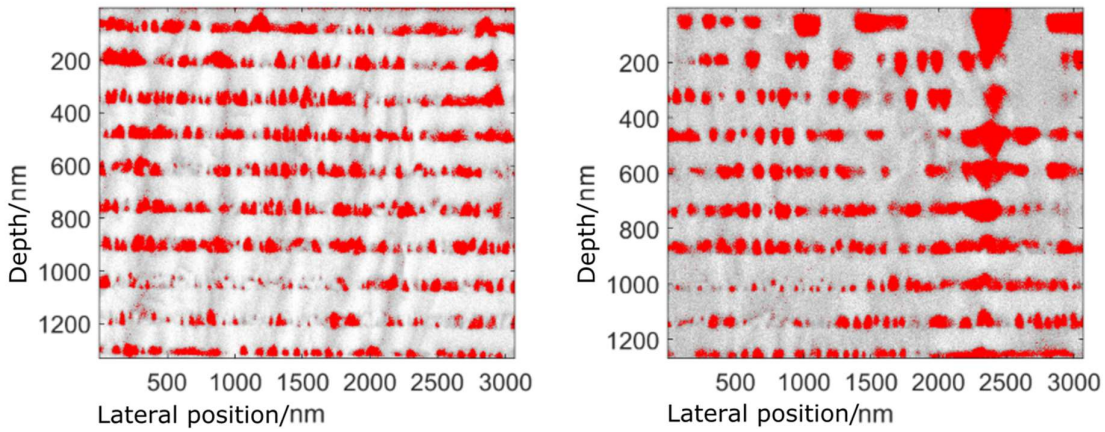

Figure 57: SEM images of NP-DBR templates before regrowth (left) and after regrowth (right) analysed to determine overall fraction of air, and therefore estimate porosity. Red regions are below the lightness threshold and are counted as air.

The result of this simple analysis shows that the pore fraction does in fact increase after regrowth, from 17% to 19%. This indicates that material is being lost from the DBR during the regrowth process, although the measurement is limited in accuracy due to the small sampled area and errors in discriminating porous/non-porous regions.

To further study the cause of this loss of material, cross-sectional TEM samples were prepared by the conventional method (as described in section 2.4.2) and examined in a FEI Osiris STEM. Dark-field STEM images were obtained using the high-angle annular dark-field detector (HAADF), which is mainly used to provide compositional (Z) contrast, but can produce contrast from dislocations as well [209]. A STEM image of an LED layer overgrown on a non-porous template was also obtained for comparison and is presented in Figure 58. The regrowth interface is not visible, and there does not appear to be defect generation

arising from the regrowth process. The 5 quantum wells and p-AlGaN/GaN superlattice are clearly visible, as labelled in Figure 58.

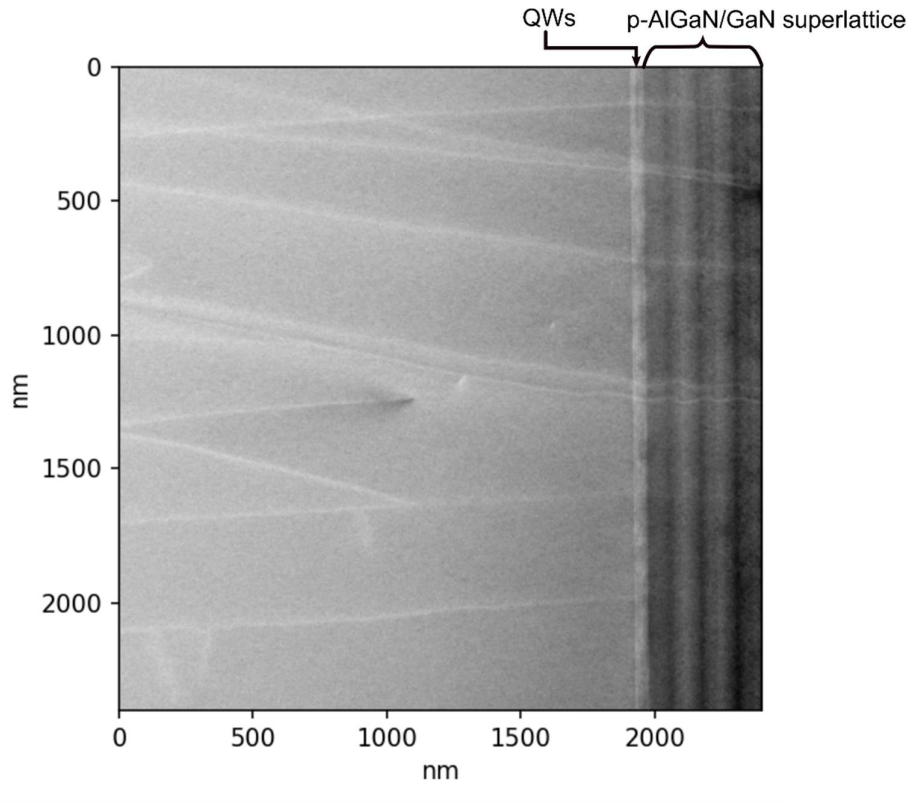

Figure 58: STEM image of a LED heterostructure regrown on a non-porous template. The quantum wells and p-AlGaN/GaN superlattice are visible, as are dislocations (bright lines).

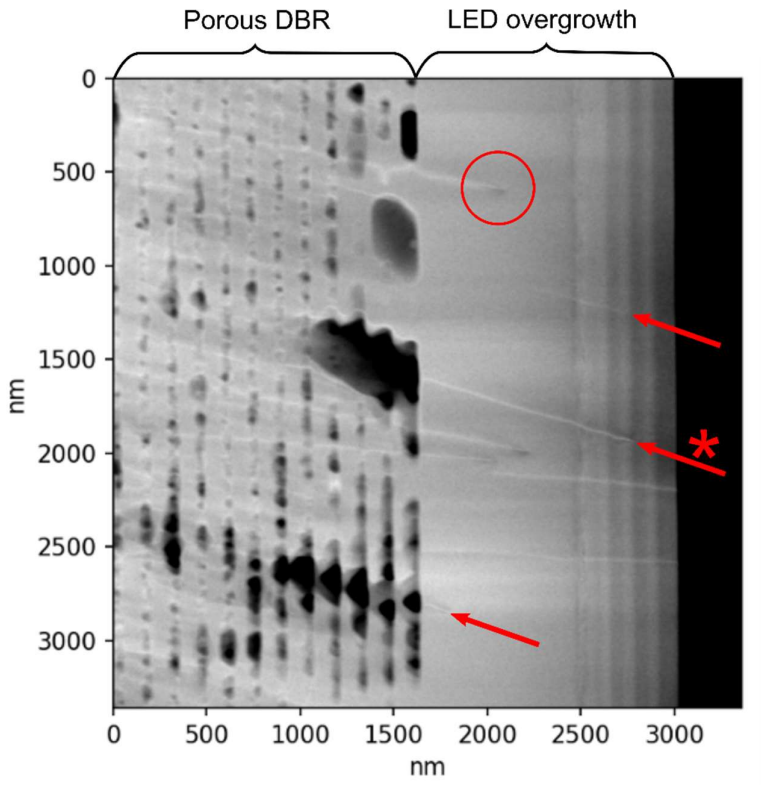

Figure 59: HAADF STEM image of LED layers overgrown on a porous DBR. Dislocations are indicated by red arrows, and can be seen to connect to regions that exhibit a large loss of material (one particularly clear example is labelled with an asterisk). Dislocations thread through the thickness of the film, so may not be continuously evident. One dislocation exiting the film is highlighted with a red circle.

A STEM image of the regrown LED on a porous template is shown in Figure 59, with threading dislocations visible as bright contrast and highlighted with red arrows. Regions with locally enlarged pores are often found to be associated with a dislocation, suggesting that these defects play some role in their formation. Additionally, the presence of a line defect that allows material to evaporate would explain the tendency for enlarged pores to align with each other, along one of these defects.

Enlarged pores are sometimes seen without an associated dislocation immediately attached to the region; this may be due to their associated defect originally existing in a region outside the TEM foil (as the holes are ~100-400 nm in size, and the TEM foil is likely to be around 100 nm thick). Indeed, dislocations can be seen to enter and exit the thickness of the film in several places, evidenced by the dark contrast seen where they apparently terminate (e.g. at the circled point) [209].

The diffusion of material along dislocation-related channels is also suggested to occur during the porosification process, where these channels are seen to permit sub-surface etching [89]. This leads to a radiating pore structure as shown in Figure 60. The nano-pipe structures left behind after etching could then permit the evaporation of material, leading to the observed pore enlargement. This is also supported by the appearance of larger pores nearer the surface, where diffusion to the reactor chamber will occur more quickly than for pores buried further in the sample.

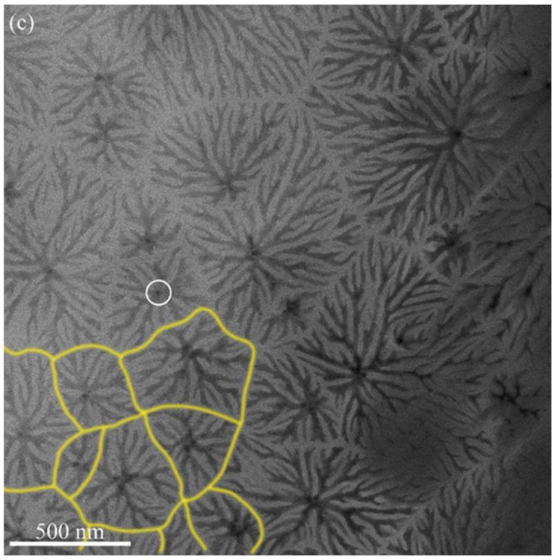

Figure 60: Radiating pore structures around dislocation-related nanopipes that permit sub-surface etching. Plan-view STEM acquired by Fabien Massabuau [89].

4.4.2 Micro-reflectivity

Micro-reflectivity spectra of all three samples were obtained using an Olympus BX51 microscope with a 100x N.A. 0.8 objective, tungsten white-light source and Ocean Optics QE Pro spectrometer. The spectra were collected from the top surface of the wafer, and the relatively high N.A. of the objective lens means that the reflectivity spectra are effectively averaged over a semi-angle of 53°. A specular aluminium reflectance standard and corresponding reflectance spectrum was used to calibrate the system.

The reflectance spectra for all three samples are presented in Figure 61. The NP-DBR template shows a peak reflectivity of 95%, which reduces to 80% when the LED layers are regrown on top of the sample. A non-porous LED structure shows low reflectance of ~20%, due to weak reflection from the GaN-air and GaN-sapphire refractive index steps.

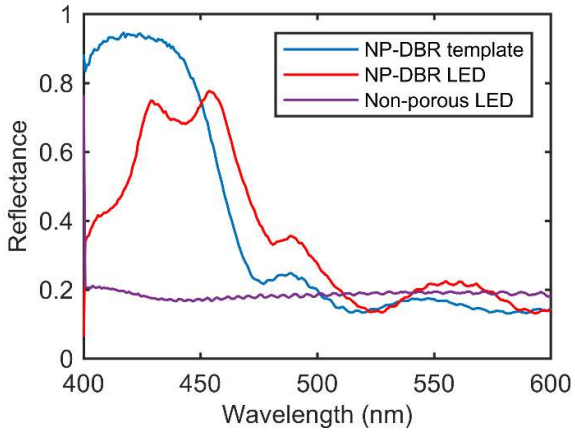

Figure 61: Reflectance spectra from the regrown NP-DBR LED, the NP-DBR template, and a non-porous LED. Measured through the top surface of the wafer with a 100x (N.A. 0.8) objective lens.

The reduction in peak reflectance on regrowth is partly due to degradation of the NP-DBR during the regrowth process, as discussed in section 4.4.1. There could also be some contribution from absorption in the LED device layers; to investigate this, measurements were also taken through the back surface of the double-polished NP-DBR wafers. The thickness of the sample meant that the 10x, N.A. 0.3 objective had to be used to ensure the DBR was correctly brought into focus. All calibrations were repeated after changing the optical system.

The reflectance plots taken from the back side are shown in Figure 62, where a reflectivity drop from 75% - 63% is observed. This is a similar reduction in reflectivity to that observed through the top surface of the wafer, suggesting that degradation of the DBR itself is the major factor.

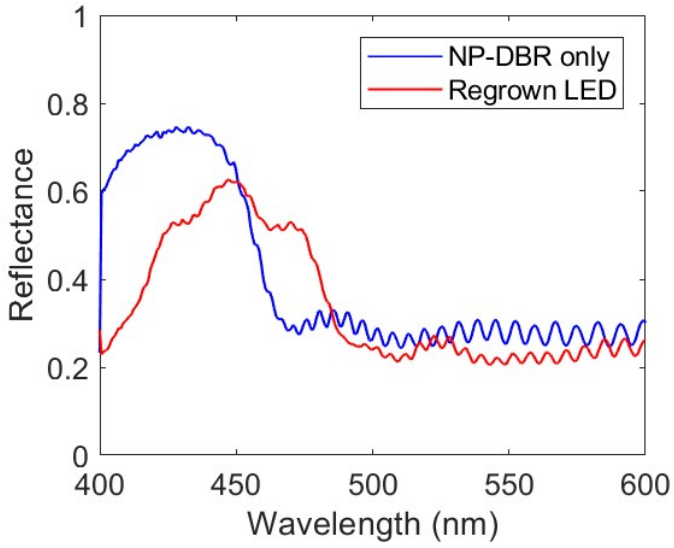

Figure 62: Reflectance measurements taken through the back surface of a NP-DBR wafer before and after regrowth of an LED structure. A 10x objective was used for this measurement, with a N.A. of 0.3 (collection semi-angle of 18°).

The DBR structures were also modelled using the Python `tmm` package [210], including graded interfaces simulated as a stack of 2 nm layers with progressively varying composition. Two structures were simulated: firstly, a porous DBR alone, and then a porous DBR with a 1200 nm GaN slab on top to represent the LED regrowth.

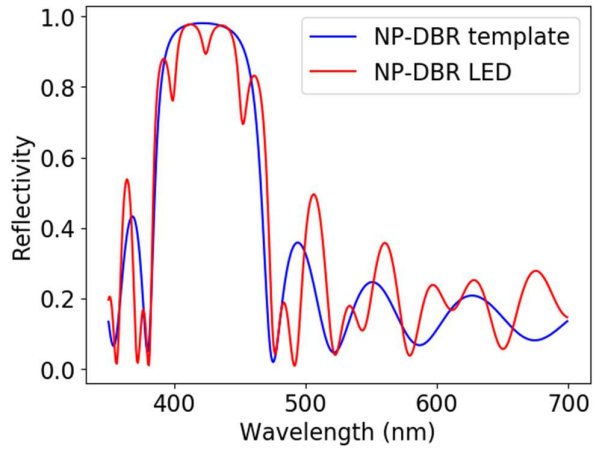

Figure 63: Transfer-matrix method simulation of DBR structure with and without a 1200 nm GaN slab on the top surface.

The additional thick layer on top introduces extra peaks and troughs into the reflectivity spectrum due to interference from the additional wave reflected from the top GaN surface.

However, the simple model does not explain the wavelength shift or drop in peak reflectance observed in the regrown LED sample.

To fully understand the effect of the changes observed during regrowth, a more advanced modelling method may need to be adopted (for example, finite-difference time-domain simulations) to investigate the relative importance of the porosification of the GaN layers, change in shape of the pores, differences in the layers near the surface of the GaN film, etc. This could inform future experimental work related to optimisation of the regrowth process to maximise the reflectivity after growth of the device layers.

4.5 Device processing

4.5.1 Device design

A lateral design was chosen for these devices for ease of fabrication. A transparent conducting layer (TCL) was used as the p-GaN contact, with annealed Ti/Al/Ti/Au contacts used for the n-GaN and opaque Ti/Au pads used on top of the TCL to allow for electrical injection and current spreading across the TCL. A schematic of the design, which incorporates an isolation mesa to separate the devices and provide access to the n-GaN, is shown in Figure 64.

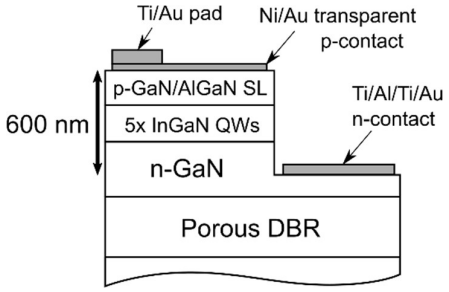

Figure 64: Schematic cross-section of LED design.

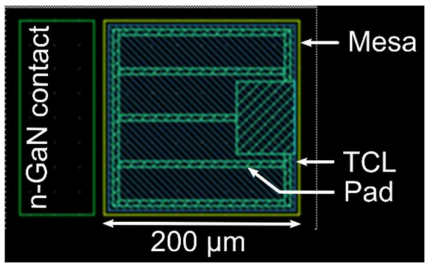

Figure 65: Plan-view of the LED mesa mask design

The opaque p-GaN pads are designed to spread current across the top surface of the mesa, under the assumption that the n-GaN is substantially more conductive than the TCL. Hence, stripes of pad metal are patterned across the entire top surface of the mesa as shown in the plan-view image of the mask design, shown in Figure 65.

4.5.2 Cleanroom processing

The regrown wafers were etched using ICP-RIE to form the isolation mesa, followed by contact deposition using thermal evaporation and subsequent rapid thermal annealing (RTA). All patterning was done using photolithography, as described in section 2.2.2.1, with the chlorobenzene lift-off process used for the metal patterning steps. The important aspects of the process are outlined below.

The ICP-RIE step used hard-baked Shipley s1828 resist as the masking material. Dry-etch parameters were already optimised by Dr Muhammad Ali (Toshiba), and are listed in **Table 2**, below.

Parameter	Pressure	Platen temp	ICP power	RF power	Cl_2 flow	Ar flow
Value	3	10	450	125	30	3
Units	mtorr	°C	W	W	sccm	sccm

Table 2: ICP-RIE parameters for LED isolation mesa etch.

These result in a reasonably fast etch of about 480 nm/min, and sidewall angles of around 45°, as shown in Figure 66. Smooth etched surfaces are also obtained.

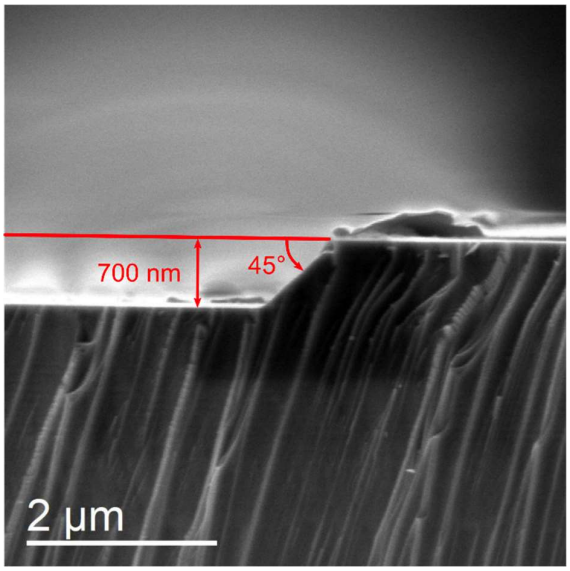

Figure 66: Profile of ICP-RIE mesa etch.

N-contacts were comprised of a Ti/Al/Ti/Au multilayer stack, with respective layer thicknesses of 15, 50, 30 and 80 nm as estimated by a quartz crystal thickness monitor in the

deposition chamber. After deposition, these contacts were annealed at 710°C for 2 minutes under 6 slpm N_2 flow.

The transparent p-GaN contacts were deposited as a Ni/Au stack, with a layer thickness of 4.5 nm for each metal. This contact was annealed at 470°C for 5 minutes under a mixture of O_2 and N_2, with flows of 2 and 5 slpm respectively to form a transparent conducting layer.

To ensure compatibility of the chips with each annealing and dry-etching step, the dry etch was carried out first, followed by the higher-temperature n-contact anneal, then the lower-temperature p-contact anneal. Finally, Ti/Au pads were deposited with layer thicknesses of 20 and 100 nm respectively.

4.6 Device characterisation

4.6.1 Contact performance

The deposited and annealed contacts were characterised using the transfer-length method (TLM), described in section 2.6.1.

4.6.1.1 p-GaN contacts

The p-GaN contacts were characterised using a mesa-isolated linear TLM structure, as shown in Figure 67.

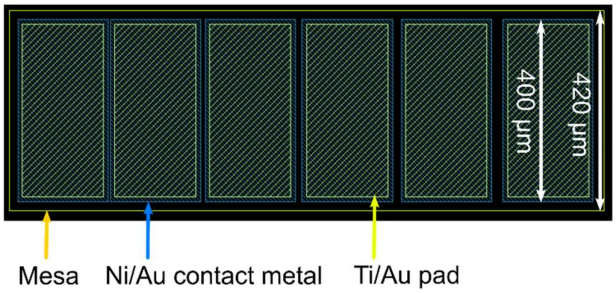

Figure 67: p-GaN linear TLM mask layout, consisting of 3 layers as labelled. The gap between metallised areas increases from 5 to 25 µm in steps of 5 µm.

The sheet resistance and contact resistance were calculated using measurements taken on four TLM patterns located at different positions on the mask, using a voltage sweep of +/- 0.1 V to determine resistance between each pair of contacts. The porous sample showed a higher average contact resistance of 1.89×10^{-2} Ωcm^2, compared to 4.15×10^{-3} Ωcm^2 for the non-porous sample. However, there is a large variation in the values measured at different

locations on the sample, with values ranging from 1.99×10^{-3} Ωcm^2 - 5.04×10^{-2} Ωcm^2 for the porous wafer and 8.23×10^{-4} Ωcm^2 - 9.75×10^{-3} Ωcm^2 on the non-porous wafer.

The measured sheet resistance was also somewhat higher for the porous wafer, with a value of $3.3 \pm 0.6 \times 10^5$ $\Omega/\blacksquare$ for the porous wafer and $2.0 \pm 0.2 \times 10^5$ $\Omega/\blacksquare$ for the non-porous wafer.

4.6.1.2 p-GaN contact annealing

The contacts were annealed using rapid thermal annealing, which is a method that uses an array of tungsten/halogen lamps to directly heat a Si carrier wafer. The temperature is controlled in a closed loop using feedback from a thermocouple attached to the bottom surface of the Si wafer. As the chips are placed on top of the carrier wafer, this means that the actual temperature at the chip surface is not being measured directly. This introduces the possibility that the porous DBR may affect the actual annealing temperature by two mechanisms: reflection of light by the DBR, and increased thermal resistance from the porous layers. This could provide an explanation for the differences in p-contact performance observed between wafers.

To investigate the effect of annealing temperature, circular TLM (cTLM) structures were defined on a total of 10 chips, 5 of which were taken from unused portions of the non-porous sample and 5 from the porous sample. cTLMs were used to eliminate the need for an ICP mesa etch. Identical Ni/Au layers were evaporated and annealed under the same conditions as before, but at a range of temperature setpoints between 430°C and 510°C. Ti/Au pads were then defined after annealing, giving the cTLM structure shown in Figure 68.

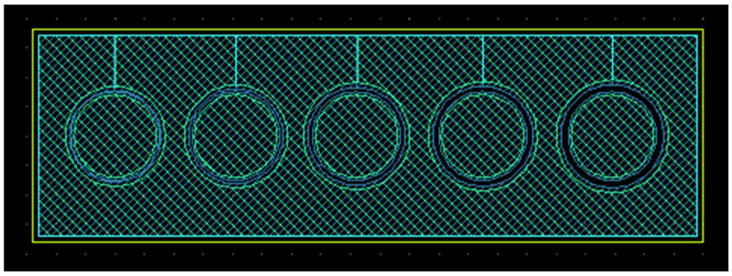

Figure 68: cTLM mask layout used for the p-GaN contact annealing series. Gap widths vary from 5 to 25 μm in steps of 5 μm.

The variation in I-V characteristics with temperature for both the porous and non-porous chips is plotted in Figure 69. The local slope of the I-V curve, computed using the NumPy `gradient` function [211], more clearly shows the effect of annealing. An ideally Ohmic contact would show a constant gradient, and the increased resistance (on both samples, and at all temperatures) around 0 V indicates the presence of a Schottky barrier, which, as discussed in section 4.1.2.3, is not unusual for p-GaN contacts.

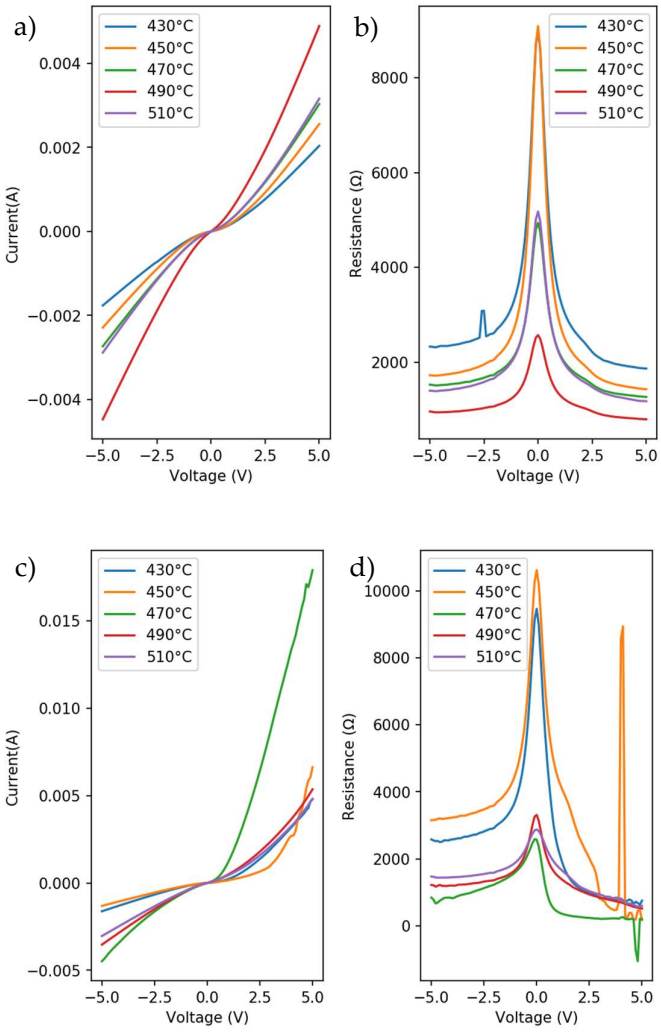

Figure 69: I-V characteristics for a 5 µm gap on non-porous (top) and porous (bottom) wafers at a range of annealing temperatures. (a): Non-porous I-V characteristic. (b) Non-porous differential resistance. (c) Porous I-V characteristic. (d) Porous differential resistance. Resistance plots obtained by numerical differentiation of the respective I-V plot.

For the non-porous wafer, a clear optimum is observed at 490°C, which is the lowest resistance point and the closest to an ideally ohmic I-V. The porous wafer shows less clear

results. Three of the wafers (430, 450 and 470°C) show highly asymmetric I-Vs, which are likely to be related to the asymmetry in the TLM mask design, as one contact covers a much larger area than the other. Optical microscope examination confirms that the metal structures are correctly reproduced on all the samples, with no flakes of metal, breaks in the pattern or other lithography-related defects.

TLM measurements (Figure 70) yielded sensible results for the non-porous wafer, with a similar trend in contact resistance to that seen from the raw I-Vs, and an approximately constant value of sheet resistance measured. The compromised TLM structures on the porous wafer meant that the results for the porous device were less reliable; this is also indicated by the variability in the measured sheet resistance, which should be approximately constant with annealing temperature.

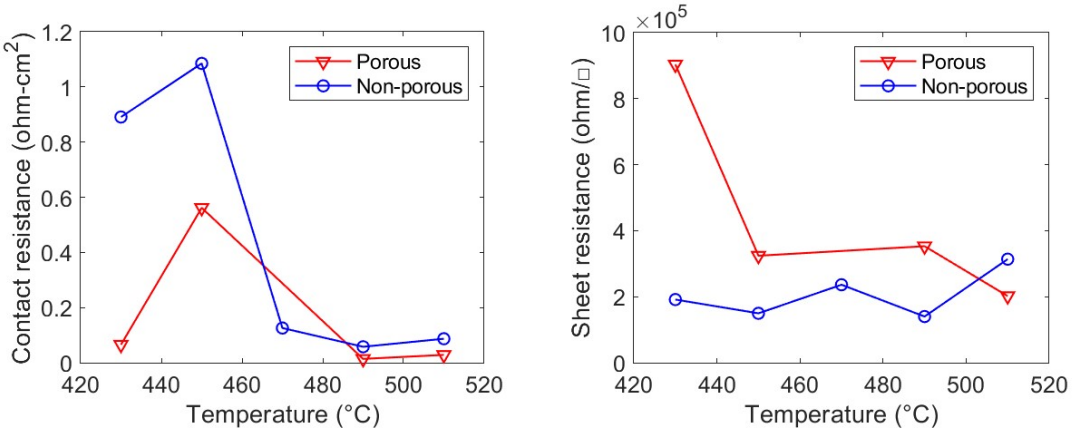

Figure 70: TLM measurements of contact and sheet resistance for various annealing temperatures.

The variation in contact and sheet resistance observed across the samples (section 4.6.1.1), especially the porous samples, indicate that some differences may be due to variance within a particular sample. The evidence that some of the TLM structures may be compromised on the porous wafer also reduces the reliability of these measurements (indeed it was not possible to conduct a TLM measurement at all on the wafer annealed at 470°C).

Unfortunately, this problem makes it difficult to draw any definite conclusions from these data. There is a drop in resistance at around 470°C for both samples, although there is also some indication that the optimum point might exist at around 490°C for the non-porous

wafer and at a slightly lower temperature of 470°C for the porous wafer. Further work to improve the reliability of the TLM structures on the porous wafer could help to draw better conclusions about the impact of the porous layers on the contact annealing behaviour.

4.6.2 NP-DBR conductivity

The NP-DBR present in the n-type layer underneath the devices could influence their performance. Two experiments were therefore carried out to assess the impact of the NP-DBR on the electrical conductivity of the n-GaN layer.

4.6.2.1 Vertical conductivity

The vertical conductivity was investigated by patterning 1.8 μm deep mesas into two samples by ICP-RIE, followed by the deposition of n-GaN contacts covering the top surface of the mesa using the same metal and annealing scheme as the LED devices. One sample contained a 20-pair NP-DBR, while the other contained the unetched latent DBR structure.

An I-V characteristic was then measured between adjacent mesas, and is shown in Figure 71 together with a schematic of the measurement geometry. A total of 6 pairs of mesas were measured, and the average resistance was $(7.16 \pm 1) \times 10^{-4}$ Ω for the NP-DBR and $(3.14 \pm 0.5) \times 10^{-4}$ Ω for the non-porous sample.

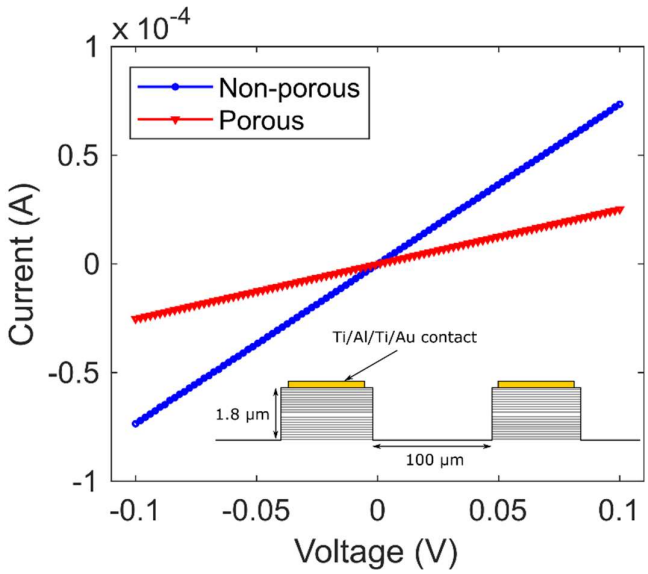

Figure 71: I-V characteristics measured between adjacent mesas containing porous DBRs or un-etched (non-porous) n-GaN layers.

4.6.2.2 Lateral conductivity

There is also a possibility that the presence of the NP-DBR underneath the solid n-GaN layer could reduce the lateral conductivity, as it is only located around 600 nm below the bottom of the device mesa. To investigate this, circular TLM structures with gaps ranging between 20 and 100 μm were fabricated on pieces of the porous and non-porous LED wafers. These wafers were then etched by ICP-RIE to a depth of 600 nm, in the same way as the studied LED devices. N-GaN contacts were then evaporated with the same layer thicknesses and were annealed under the same conditions as the NP-GaN LEDs.

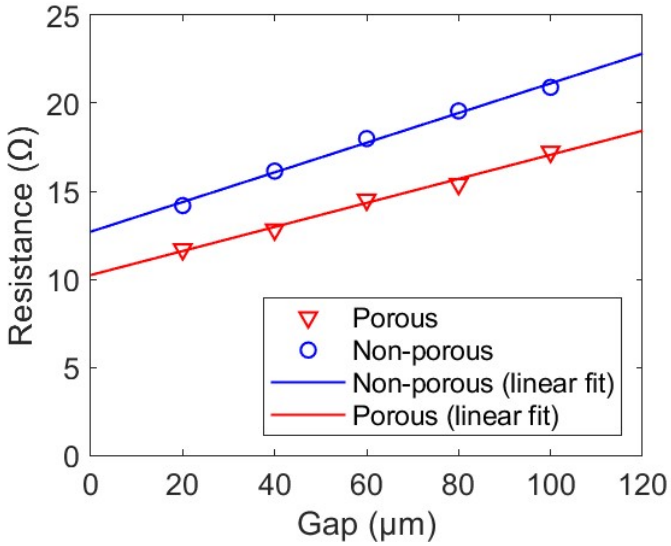

Figure 72: TLM results for n-GaN layer on porous and non-porous LED wafers.

The TLM was acquired using +/- 0.1 V sweeps, and is shown in Figure 72. The measurements indicate a sheet resistance of 79 Ω/■ in the non-porous wafer and 65 Ω/■ for the porous wafer, and contact resistances of $4.51 \times 10^{-3}\ \Omega \cdot \mathrm{cm}^{-2}$ in the non-porous wafer and $3.62 \times 10^{-3}\ \Omega \cdot \mathrm{cm}^{-2}$ in the porous wafer. These values are reasonably close to each other, and are in fact higher in the case of the non-porous wafer, indicating that the n-GaN DBR is not increasing the resistance by a significant amount (at least over distances of up to 100 μm).

4.6.3 Electroluminescence

The electroluminescence from the processed devices was examined using a 50x optical microscope. Microscope images taken under a forward current of 20 mA are shown in Figure 73; the emission is reasonably uniform across the mesa, although a brighter halo can be seen

around the edges of the device mesa on the porous device, as well as a few dark patches on the top of the mesa.

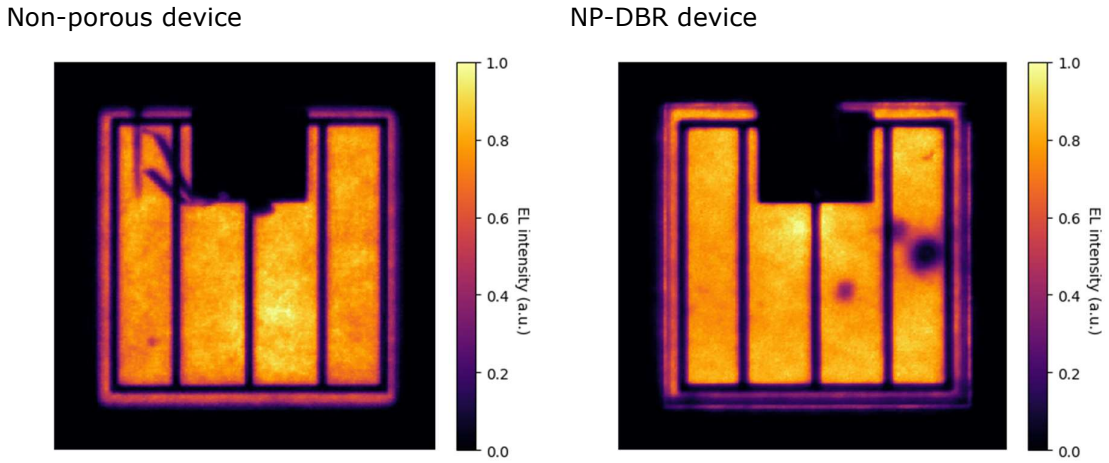

Figure 73: Normalised electroluminescence intensity maps for the studied LED devices grown on non-porous (left) and NP-DBR (right) templates. The mesa is square and measures 200 μm on an edge.

Emission spectra were collected from the devices using a 400 μm optical fibre coupled to the microscope eyepiece. The spectra, also collected at an injection current of 20 mA, are presented in Figure 74.

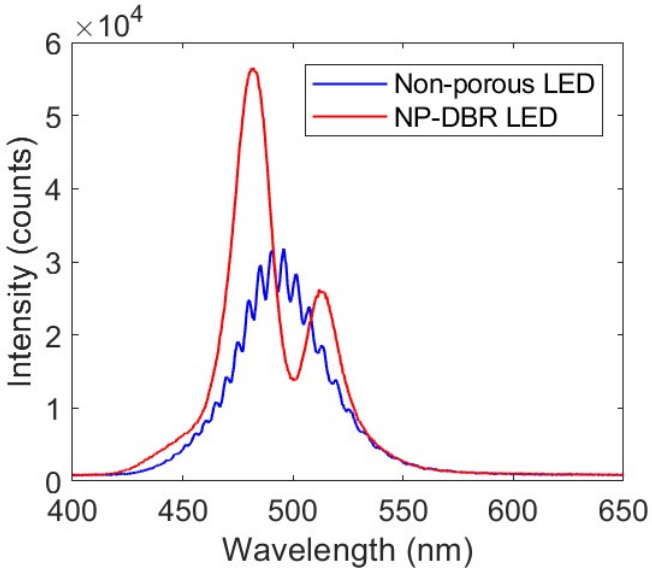

Figure 74: EL emission spectra from the porous and non-porous LEDs. Both spectra were collected with an excitation current of 20 mA.

A Gaussian peak with superposed Fabry-Pérot interference fringes is observed in the spectrum of the non-porous device. The fringes arise from reflections at the refractive index

steps between the GaN/air interface and the GaN/sapphire interfaces, and modulate the Gaussian spectrum of the QW emission. These fringes disappear in the porous device, and are replaced by a large reduction in intensity at around 500 nm. This is likely to be due to interference between waves reflected from the GaN/air interface at the top surface of the wafer and the NP-DBR, related to the peaks seen in the TMM simulations in section 4.4.2, although enhanced in intensity by the semi-transparent Ni/Au layer that is present in the processed device. The peak intensity is also increased in the porous device by a factor of 1.8, and the integrated intensity is increased by a factor of 1.3.

The collection semi-angle is around 18°, estimated by measuring the working distance and diameter of the objective aperture. This means that the results give extra weight to light that is emitted and extracted at angles that are nearly perpendicular to the wafer surface. This will tend to exaggerate any enhancement in light extraction efficiency, as DBRs show the highest reflectivity for light arriving at normal incidence. Light that is emitted from the QWs at different angles may be reflected less efficiently, and light that arrives at the GaN/air interface at angles exceeding the critical angle will be subject to total internal reflection. Further work that examines the far-field emission pattern would be needed to try and quantify the magnitude of these effects, provide useful indications of how much extra light is extracted and how much the directionality of the device is affected. The appearance of a halo around the mesa edge in the EL emission micrograph could be an indication that some light is being trapped in laterally-propagating modes between the DBR and the top surface.

4.6.4 Electrical characterisation

Current-voltage (I-V) characteristics were collected from the studied devices on both porous and non-porous templates. A representative I-V curve from a NP-DBR LED is shown in Figure 75. At low voltages, the current is limited by the p-i-n junction itself (with some excess current due to any shunt resistance), and rises exponentially with voltage. At higher voltages, the curve deviates from an exponential as the effect of the series resistance of the device becomes more significant [212]. Exponential (red) and linear (green) fits to the two parts of the I-V curve are included.

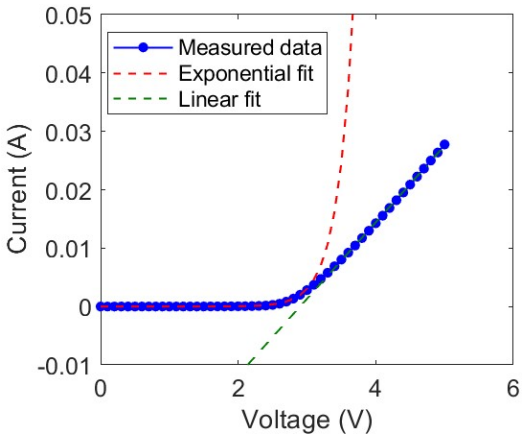

Figure 75: I-V characteristic from a NP-DBR LED, with qualitative fits of exponential and linear functions showing two regimes of behaviour.

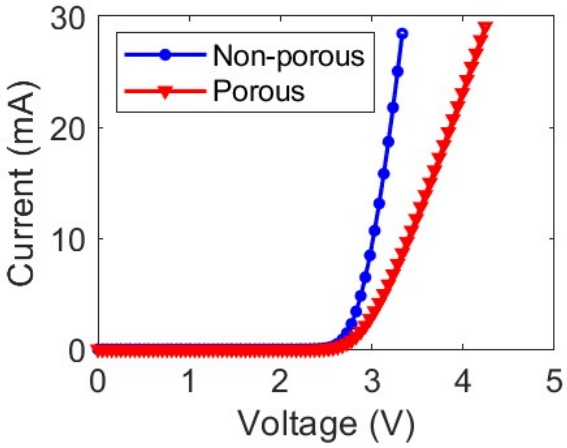

Figure 76: I-V characteristic from LEDs regrown on porous and non-porous templates.

A comparison between the studied NP-DBR and non-porous LEDs is shown in Figure 76. In general, the porous devices show a higher forward voltage (V_f) at 20 mA, due to a greater series resistance. A similar behaviour was found by Shieh *et al.*, who attribute the difference to the presence of the NP-DBR in the n-GaN layers [201]. As the total thickness of the n-GaN and DBR stack is around 4 μm, while the lateral dimensions of the LED mesa are two orders of magnitude higher (200-400 μm), current flow should be approximately uniform through the entire film. The presence of the NP-DBR in this layer could therefore reduce the conductivity by reducing the carrier concentration or possibly from mobility reduction via, for example, electron scattering from the new surfaces in the porous structure. Such a reduction in concentration is observed by Zhang *et al.* in Hall-effect measurements, although they also indicate that the carrier mobility is unaffected [85]. My own measurements of lateral conductivity do not seem to show an increased sheet resistance in the n-GaN, suggesting that another mechanism is responsible for the increased forward resistance.

The p-GaN TLM measurements also indicate a higher contact and sheet resistance in the porous device, which will contribute to the increased forward resistance.

Some other NP-DBR devices also showed increased current before the knee voltage. A very similar modification to I-V characteristic in NP-DBR LEDs is reported in Shieh *et al.* [201], who do not suggest a reason for the difference. Optical microscopy of the EL emission from high-leakage devices shows that dark patches are present in the mesa, while lower-leakage

devices show fewer dark patches. Figure 77 shows two examples, where Device A shows lower current leakage before the onset of conduction at around 2.8 V (and fewer dark patches), while Device B shows substantially greater current flow before the steep increase in current (and correspondingly more dark patches).

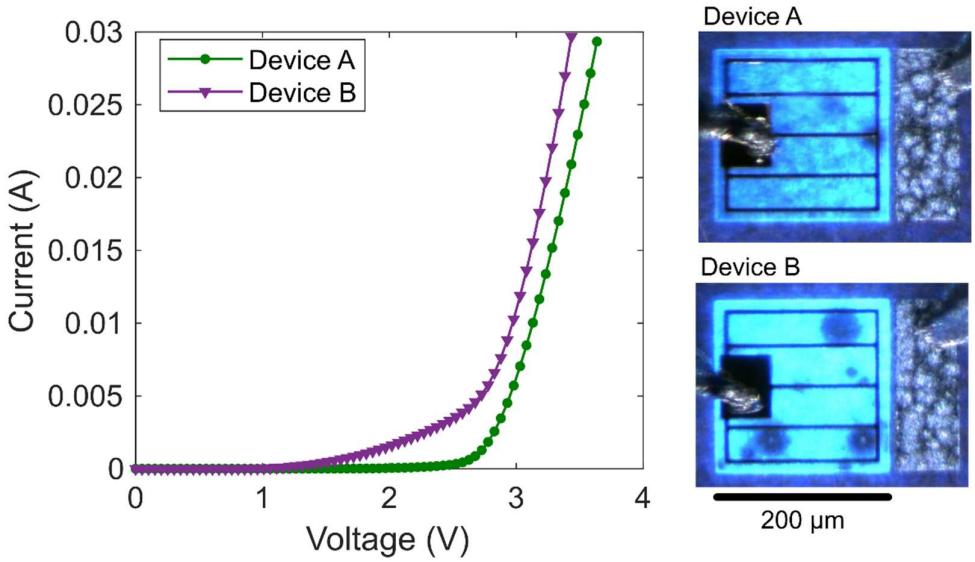

Figure 77: Comparison of devices with lower and higher degrees of leakage. Device A shows lower leakage, and has a correspondingly lower density of dark patches than device B.

The dark patches were also investigated by SEM. The metallisation on top of the mesa allows for easy correlation between optical microscope and SEM images, and a large pit was found in the vicinity of the dark patch as shown in Figure 78.

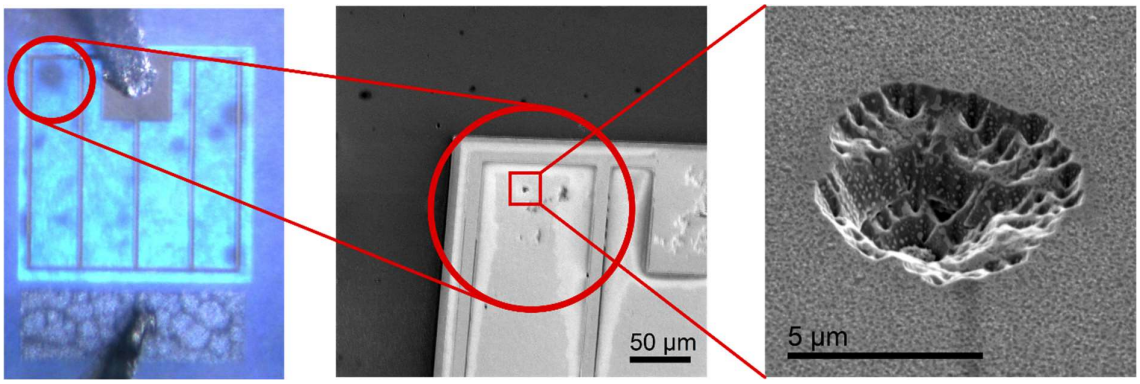

Figure 78: Correlation of a dark patch in the LED mesa with SEM image. A deep pit can be observed in the vicinity of the dark patch.

The pit appears to be several microns deep in the 45° SEM image, and will therefore penetrate through the p-i-n structure. The correlation of the I-Vs and optical microscope images with SEM data could suggest an explanation for the observed change in I-V characteristics; the increased current flow before the normal turn-on voltage of the p-i-n structure could be due to a leakage pathway present in the device, that allows current to bypass the p-i-n structure. The observed deep pits in the mesas could be associated with this leakage pathway.

The ideality factor for the I-V curves of the studied devices was also calculated at various voltages. The I-Vs, replotted on a semi-log scale, together with the calculated ideality factor at each voltage are shown in Figure 79. The factor was calculated by re-arranging the Shockley diode equation (Equation 10), determining the gradient of the V vs $\ln(I)$ plot numerically using the Matlab `gradient` function and assuming a temperature of 300 K.

$$n = \frac{q}{kT}\left(\frac{dV}{d\ln(I)}\right)$$

Equation 10

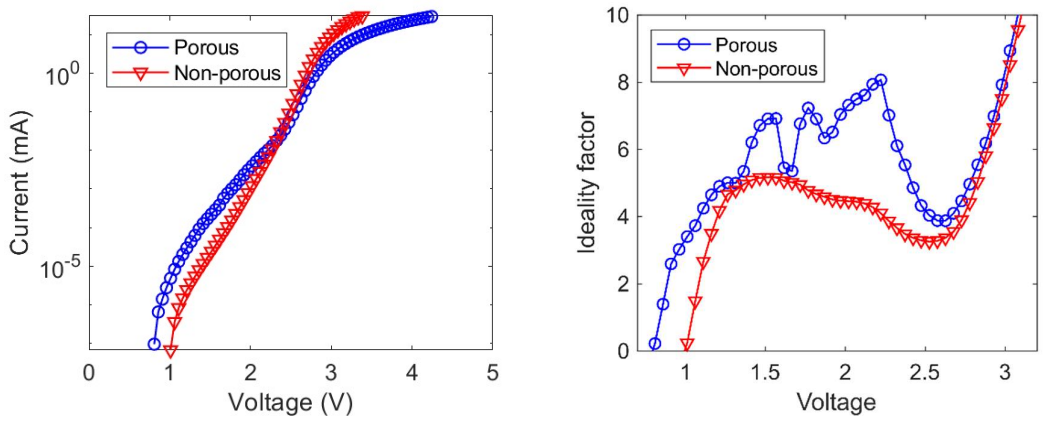

Figure 79: Semilog I-V plots for studied devices (left) and ideality factor (right).

While the absolute values of the ideality factor may not be entirely accurate, the general trends can be interpreted. Between about 1.5 and 2.5 V, the ideality factor decreases, indicating the increasing dominance of radiative recombination (ideality factor of 1) over Shockley-Read-Hall recombination (ideality factor of 2) and defect-assisted processes (ideality factor $\gg$ 2). The rapid rise in the ideality factor after 2.5 V is then due to the series resistance of each device starting to limit the forward voltage applied to the p-i-n junction

itself [170, 213]. The porous device starts with a higher ideality factor, indicating a higher rate of defect-assisted tunnelling when compared to the non-porous device. This suggests that the defects in the porous LED may be more electrically active than the defects in the non-porous device (since TEM data does not indicate generation of dislocations – see section 4.4.1). As dislocations are intimately involved in the electrochemical porosification process [84], it is possible that they are modified in a way that increases their effectiveness in promoting electron leakage and non-radiative recombination. For example, if the dislocation cores facilitate etching and are transformed into larger pipes through the material, they may induce more surface leakage-like transport.

4.6.5 Efficiency measurements

Light output was measured as a function of current, using a Si photodiode coupled to the same optical fibre used to gather the spectra in section 4.6.3. Pulsed injection is used, with a ~1 ms current pulse applied to the device while the signal from the photodiode is recorded using a Keithley 2700 multimeter. The multimeter is triggered using a hardware output from the SMU, which provides a signal once its output has stabilised. The external quantum efficiency (EQE) vs current is plotted in Figure 80. The EQE is estimated by dividing the

detector signal by injection current, under the assumption is that detector signal is linearly related to the number of photons impinging on the Si photodiode.

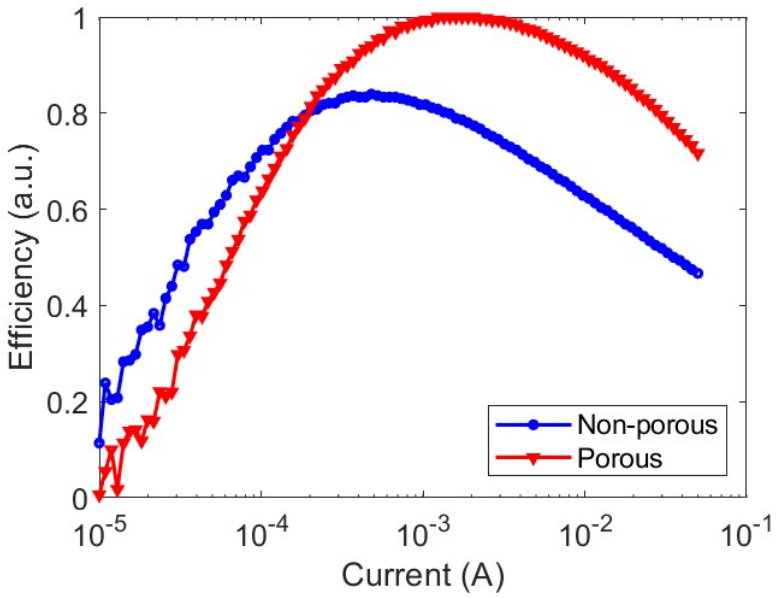

Figure 80: EQE vs current for the studied porous and non-porous regrown LEDs. The efficiency is estimated by dividing the detector signal by the input current, and is on an arbitrary scale between 0 and 1 (where 1 is the highest efficiency shown by the porous device).

In the low-current regime, the non-porous device has a higher efficiency. As previously discussed, this regime is dominated by a competition between radiative recombination and non-radiative recombination via deep traps associated with crystal defects (termed Shockley-Read-Hall (SRH) recombination), where radiative recombination increases with the square of the carrier density while SRH recombination increases linearly [172]. Hence, this could indicate a higher rate of non-radiative recombination and therefore a higher density of deep traps in the porous device. Leakage pathways separate from the p-i-n structure itself might also allow carriers to completely bypass the diode structure, contributing to reduced efficiency in the low-current regime.

The peak efficiency is both higher and at a greater current for the porous LED compared to the non-porous LED. The efficiency at 50 mA (current density of 125 $A{\cdot}cm^{-2}$) is 72% of its peak value for the porous wafer, and 56% for the non-porous wafer.

The presence of the porous layers could affect the internal electric fields across the quantum wells by permitting strain relaxation. Higher internal electric fields present across the quantum wells can decrease the radiative and non-radiative recombination rate by reducing wavefunction overlap, which affects droop behaviour by increasing the carrier density for a particular injection current density [178]. This has been suggested to be the case for structures overgrown on thick layers of porous GaN [199], and lowered fields have also been suggested as the cause of blue-shifted emission in the LED structures on NP-GaN DBRs reported by Shiu *et al*. [198] – although no such blue-shift is observed by Shieh *et al.* in similar structures [201], and our LED measurements also do not indicate a systematic blue shift after EC etching. Nonetheless, I carried out an investigation into the internal fields that might be present in our structures, as a possible explanation for the observed efficiency droop.

4.6.6 Current-dependent spectroscopy

One way to investigate the internal fields across the QWs is by examining the wavelength of the emission peak as a function of injection current. As the flow of carriers into the QW increases, the charges present in the well begin to screen the electric fields, causing a blue-shift in the emission peak that depends on the magnitude of the field that originally existed across the QW [214, 215].

Initial experiments were done by applying a constant current and then taking a spectrum manually. These spectra showed a red-shift with increasing current, due to the increased temperature of the LED die at high currents and corresponding change in the band-gap [216]. To counteract this, and examine the screening effect, the setup was modified to allow the spectrometer to be triggered directly from the SMU so that a spectrum can be acquired before heating becomes a significant factor. Figure 81 shows that this approach produces a measurable reduction in the red-shift as the time delay between current on and spectrometer trigger is reduced. While this does not prove that the heating has been mitigated completely, it does show that the method reduces its effect by a significant amount. There is also a reduction in the intensity as the delay is increased, which is consistent with the theory that EQE is reduced at higher temperatures.

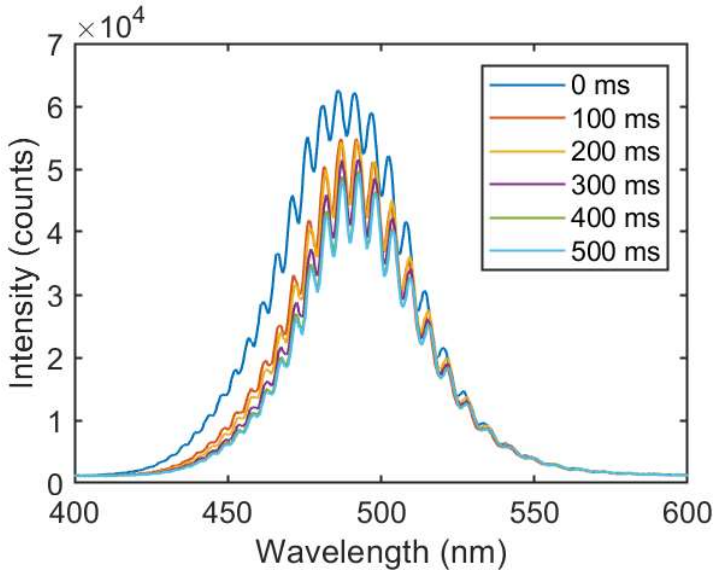

Figure 81: Spectra acquired at different time delays after turning on the current source. A red-shift is observed as the time is increased, showing increased heating from the sample. All spectra acquired at 500 mA forward current (5 kA/cm^2), with 1 ms integration time.

The measurement setup was also modified to collect light that was emitted from the side of the chip, rather than the top surface. This aimed to remove the effect of the cavity from the measurement, as the superposed cavity-related peaks will not move even if the underlying QW's emission peak does, obscuring the effect of interest. A second microscope was added for this purpose, focused on the edge of the chip.

The resulting spectra are plotted in Figure 82, showing porous and non-porous devices.

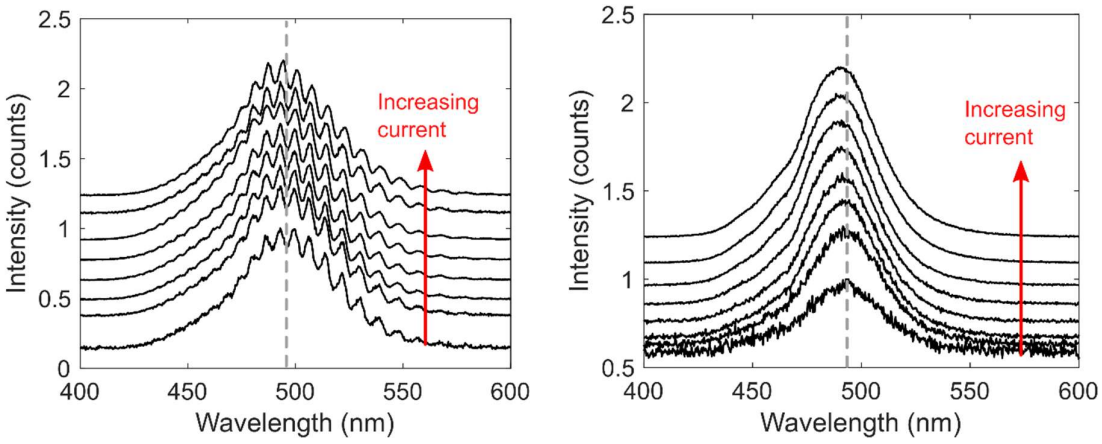

Figure 82: Spectra taken at a range of currents (10 - 600 mA, 0.1-6 kA/cm^2) for porous (left) and non-porous (right) devices. Light extracted through the side of the wafers.

The curves were fitted with Gaussian functions using the Levenberg-Marquardt algorithm, and the peak position of the fitted curve is shown in Figure 83. A similar degree of blue-shift is observed in both cases, with a slightly faster shift observed in the porous device.

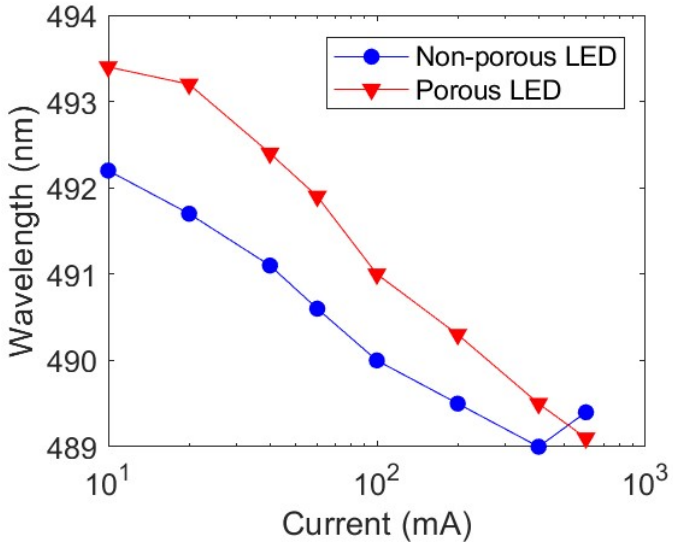

Figure 83: Peak wavelength variation with injection current, for LEDs regrown on porous and nonporous templates. Mesa size 0.01 mm^2.

These results indicate that the internal fields are not substantially modified by the presence of the NP-DBR, or are possibly slightly increased in the porous device. This suggests that the radiative recombination rate is unlikely to be higher in the porous device, and weighs against this as an explanation for the delayed droop observed in the porous devices. They are also reasonably consistent with the observations in the literature on other LED structures with buried porous DBRs [198].

X-ray diffraction measurements carried out by Peter Griffin also indicate that the QWs are fully strained to the underlying GaN in both the porous and non-porous devices, suggesting that there is no change in the strain state when QWs are grown on porous DBRs. The measurements, in the form of reciprocal-space maps taken around the $(20\bar{2}4)$ asymmetric reflection, are shown in Figure 84. The GaN peak occurs at the same 2-theta value as the InGaN satellite peaks, showing that the layers have the same lattice parameter. The lack of a difference in strain state between the porous and non-porous wafers is consistent with the current-dependent measurements.

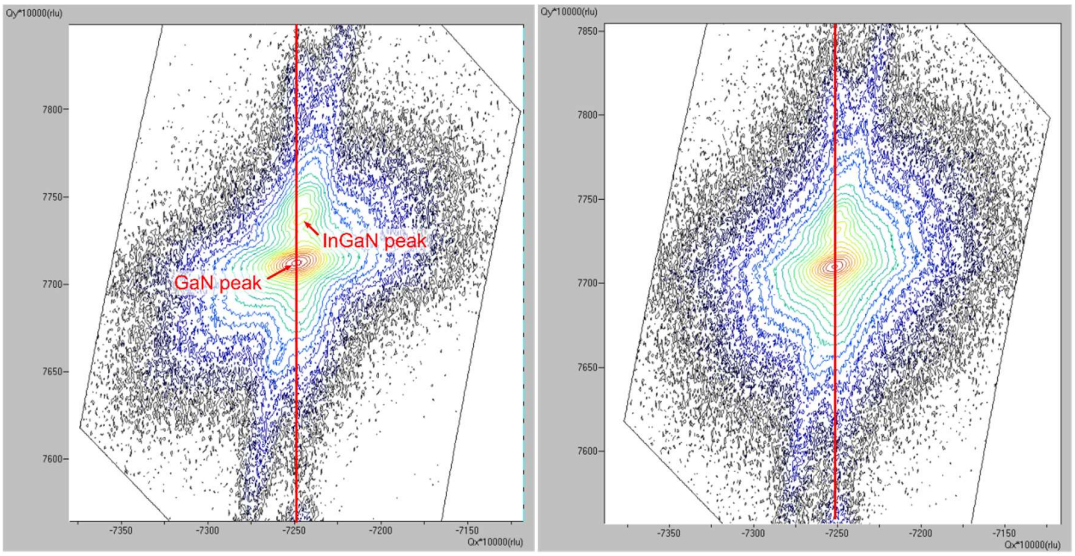

Figure 84: Reciprocal-space maps, taken around the $(20\bar{2}4)$ reflection, showing that the InGaN layers are fully strained in both the non-porous (left) and porous (right) cases. Data collected and analysed by Peter Griffin.

4.6.7 Possible droop mechanisms

As previously discussed, another factor that can affect the droop behaviour of LEDs is related more directly to the light extraction efficiency by current crowding effects. Circular TLM structures patterned on the transparent conducting layer (TCL) indicate a sheet resistance of 300 Ω/■, while n-GaN TLMs indicate a sheet resistance around 65 Ω/■ as reported in section 4.6.2.2. This indicates that there is room for greater optimisation of the TCL, but also suggests that as the current injected into the LED mesa increases, the lateral current spreading across the device will not remain uniform; the current may crowd underneath low-resistance metallisation on the TCL instead [152, 190] (see section 4.1.2.5). Since the metallisation is opaque, light emitted in these regions will tend to be reflected down into the substrate, thereby decreasing the light extraction efficiency as the current increases. The presence of the porous DBR underneath the QWs may then help to mitigate this, by reflecting some light that would otherwise be lost into the substrate and allowing it to leave the device through a transparent region of the mesa surface instead.

The difference in device geometry between my devices and those presented in e.g. Shiu *et al.* [198] could also explain why delayed droop was not observed in their paper; their devices were constructed using ITO as the top contact, without any opaque metal pads, and so this droop mechanism would not be expected to have a strong effect in their devices.

However, this explanation may not be the only reason for the observed difference. While I have shown that the porous DBR does not seem to be affecting the strain state or polarisation fields experienced by the QWs, it is possible that it may affect the LED heterostructure in other ways, for example by altering the nanostructure of the well itself, the carrier concentration in the n- or p-GaN, or the structure of defects in the device. Assessing the magnitude of the current-crowding effect by, for example, investigating a systematic array of metallisation designs could be an interesting starting point.

Finally, although there is improved droop performance observed in these non-optimised devices, droop is associated with a broad range of mechanisms. If the improvement in droop performance is indeed due to the modified light extraction, further optimisation of the metallisation design may show that the intrinsic droop of the QWs is, in fact, unchanged by the presence of the NP-DBR. Likewise, if the droop in these devices is limited by electron leakage, a more refined epitaxial design (e.g. including electron blocking layers) may also change the observed behaviour.

4.7 Summary

LED devices regrown on non-porous and porous wafers are presented and characterised. Some damage to the DBR is observed as a result of the regrowth process, degrading the reflectivity, but there is otherwise no defect generation observed at the regrowth interface. The devices grown on porous wafers show higher emission intensity and peak EQE at normal incidence, due to the reflectance of the NP-DBR. The efficiency droop of the porous device is reduced, with the peak efficiency occurring at a higher current and remaining at is 72% of its peak value for the porous wafer, compared with 56% for the non-porous wafer. The origin of this change to the droop behaviour is not entirely clear, but current-dependent spectroscopy and XRD indicate that the polarisation fields are unaffected by the presence of the NP-DBR. The modified droop could be related to enhanced light extraction from regions underneath the opaque p-pads. The device design described here could in future be used to enhance extraction efficiency for the light emitted from quantum dots in a single photon LED.

Chapter 5

5Optical microcavities

Optical microcavity structures are an essential part of a bright, efficient and practical single photon source, due to the enhancement of the QD emission rate by the Purcell effect. This chapter considers several ways of fabricating such microcavities, using stochastic silica sphere lithography and deterministic electron-beam lithography.

5.1 Introduction

Optical microcavities can be constructed in a variety of geometries that confine light in 3D around a light-emitting nanostructure. Some common geometries include a micropillar containing distributed Bragg reflectors, a microdisk, a defect in a photonic crystal (embedded in a suspended beam or lamella), a microsphere or microtoroid [66], as discussed in the introduction (section 1.6.6). This chapter will present work towards the fabrication of micropillar cavities incorporating DBRs based on porous GaN.

5.2 Aims

The work in this chapter aims to investigate the two components of a micropillar cavity, beginning with a high-reflectivity DBR. While established techniques exist for forming DBRs using dielectric layers, this chapter will aim to investigate DBRs constructed using porous GaN, allowing them to be easily integrated into GaN wafers without introducing excess strain. Then, the dry-etching process necessary to produce micropillars will be investigated, including its interaction with the porous layers. Two processing routes, one relying on stochastic placement of silica spheres and the other on deterministic electron-beam lithography, will be investigated for the etching step. The resulting structures will be examined using photoluminescence measurements, initially to look for cavity modes and lasing on c-plane quantum well samples, in a step towards developing a process to produce high-Q microcavities for single-photon source applications.

5.3 Porous distributed Bragg reflectors

Porous DBRs were fabricated by Dr Tongtong Zhu and Dr Peter Griffin on the non-polar a-plane following the electrochemical etching technique outlined in section 1.6.4. The performance of these DBRs was measured using micro-reflectivity, and FIB-SEM was subsequently used to correlate the reflectivity map with the structure of the porous DBR.

5.3.1 Micro-reflectivity mapping

The reflectivity of a 10-pair a-plane nanoporous DBR was mapped using the apparatus outlined in section 2.6.1. A peak reflectivity of 98% was observed, although there were variations in both the magnitude of the peak and its wavelength. An optical micrograph of

the DBR surface is shown in Figure 85, showing the variation in colour over a length scale of a few tens of μm. Such a variation is not observed in c-plane reflectors.

To relate the variation in observed reflection colour to the underlying structure of the porous DBR, metal markers were patterned on to the surface of the wafer using UV lithography and thermal evaporation. 10 nm Ti was used as an adhesion layer, followed by 50 nm Au to ensure that a clearly visible metal pattern was formed on the wafer.

A series of micro-reflectivity spectra were then acquired along a line, and the resulting spectra are also plotted in Figure 85. The colour observed in the optical micrograph is clearly related to the shift in a prominent peak in the reflectance spectrum, with red regions showing a broader peak shifted to longer wavelength. There is also a general reduction in reflectance at longer wavelengths.

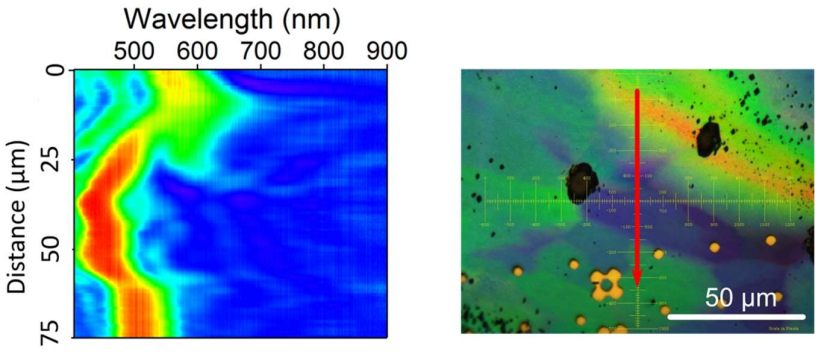

Figure 85: Line profile (left) shown together with an optical micrograph (right), showing the approximate location of the line-scan using the red arrow. The variation in apparent colour is clearly visible across the OM image, and correlates with the shift of the main peak in the line-scan towards shorter wavelengths in the blue region and longer wavelengths in the green and red regions. Some pits (black) can also be seen clearly in the surface of the wafer. The gold dots are lithographically-patterned markers used later to locate the same regions in the FIB-SEM.

Three individual micro-reflectivity spectra from a red, green and blue region were then selected, and are plotted in Figure 86. An optical micrograph overlaid with red crosses indicating the acquisition location of each reflectance spectrum is also shown.

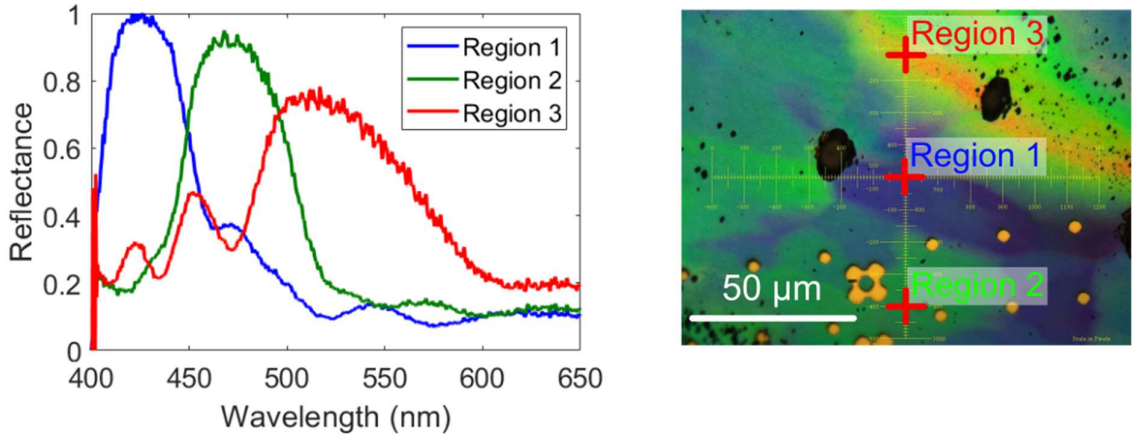

Figure 86: Left: Micro-reflectivity plots taken from three regions of the porous DBR sample. Right: optical micrograph overlaid with red crosses showing the acquisition location for each extracted spectrum. Regions numbered according to peak emission wavelength.

The markers allowed these three regions to be located in the FIB-SEM, and cross-sections were milled and imaged to investigate the relationship between the structure of the DBR and the spectra observed at each position by micro-reflectivity. Three cross-sections corresponding to the three extracted micro-reflectivity spectra were taken, as shown in overview in Figure 87.

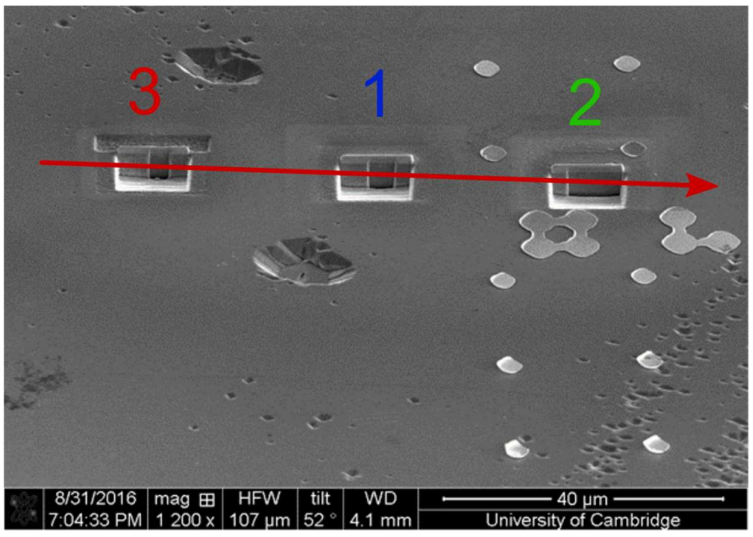

Figure 87: Overview of FIB-milled cross-sections taken at the same places as the micro-reflectivity spectra in Figure 86. Regions 1-3 labelled (ordered based on emission wavelength). The approximate location of the micro-reflectivity line-scan is indicated with a red arrow.

A three-step procedure was used for milling the cross-sections, using a beam current of 0.28 nA and an acceleration voltage of 30 kV. First, a strip of platinum was deposited using the

ion beam with injection of a gaseous metalorganic platinum precursor to protect the surface of the wafer from unintended milling during subsequent ion-beam alignments. Then, a large box was milled to provide access to the vertical surface, and to remove enough material to allow it to be viewed with the electron beam (which is angled at 52 degrees to the ion beam column). A smaller section was then milled for a shorter amount of time to remove redeposited material and produce a clean surface for imaging.

During milling, the FIB scans continuously inside a software-defined box. The edge of the milled region recedes away from the scanned box as the milling time increases, since the milled sidewalls are not perfectly vertical, and redeposition of material removed from the base can then occur on the sides of the box. A clean section therefore requires an appropriate selection of milling time to ensure a clean slice is taken through the region of interest while minimising redeposition.

The resulting SEM images are shown in Figure 88. Region 1 shows a more complete etch than Region 2, which also shows a higher degree of porosity than Region 3. In Region 3, the level of porosity in each layer is lower and some layers have not been etched at all.

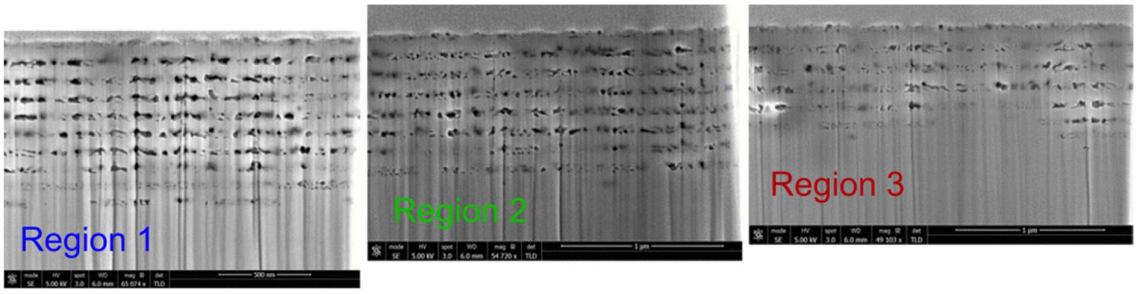

Figure 88: FIB cross-sections taken from each region, showing a reduction in the number of layers etched as well as the degree of porosity. Note that the first layer has been etched somewhat by the Pt deposition process. The wafer contained a 10-pair latent DBR prior to etching.

Some artefacts of the FIB-milling process are also visible. Vertical stripes can be seen in the etched sections, which is a phenomenon called 'curtaining' and arises when an inhomogeneous sample deflects the ion beam differently in different places, causing inhomogeneous milling further down the specimen. This is an artefact introduced by porous

materials in general, and can be mitigated by rocking the stage during milling (although this is not straightforward in our instrument and was not attempted).

5.3.1.1 Transfer-matrix modelling

A simple transfer-matrix model of the porous DBRs was constructed. A repeat unit consisting of 40 nm solid GaN and 60 nm porous GaN was used. The DBR was bounded by semi-infinite layers of air and GaN on each side, with the incoming wave coming from the air side. The porosity of the DBR was then varied, using volume-average theory to convert porosity to refractive index using the following equation [86]:

$$n_{porous} = \sqrt{p{n_{air}}^2 + (1-p){n_{GaN}}^2}$$

where n_{air} and n_{GaN} are the refractive indices of air and solid GaN, respectively, and p is the porosity.

A series of TMM models were run using the same technique as in section 4.1.1.1, varying the porosity over the range of 0 to 100%, and varying the number of repeat layers from 0 to 15. As porosity is increased, the peak reflectance increases and shifts to shorter wavelength. As the number of repeats are increased at constant porosity, the peak reflectance increases while the wavelength stays about the same. The variation in peak reflectance and wavelength of this peak as porosity is varied are shown in Figure 89, together with the variation in peak reflectance with the number of repeats.

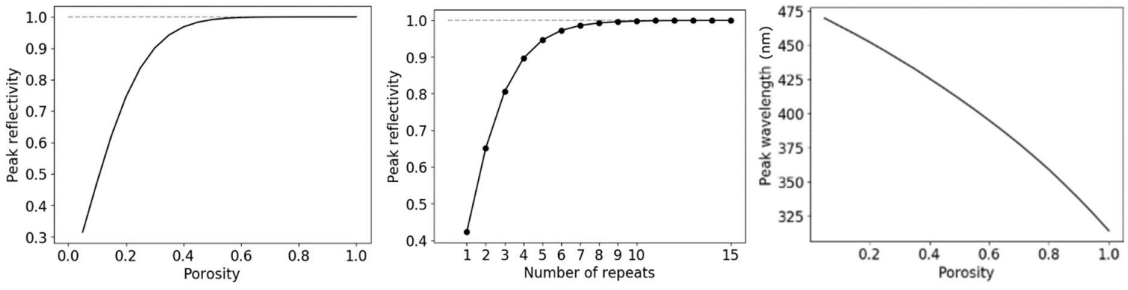

Figure 89: Results of transfer-matrix method modelling of porous DBRs. Left: Variation of peak reflectivity of a 10-pair DBR with porosity. Middle: Variation of peak reflectivity of a 60% porosity DBR with number of repeat units. Right: Variation of the wavelength of peak reflectivity as the porosity is varied in a 10-pair DBR.

The simulated reflectance spectra for three (arbitrarily chosen) values of porosity are shown in Figure 90, together with actual measurements on the porous DBRs.

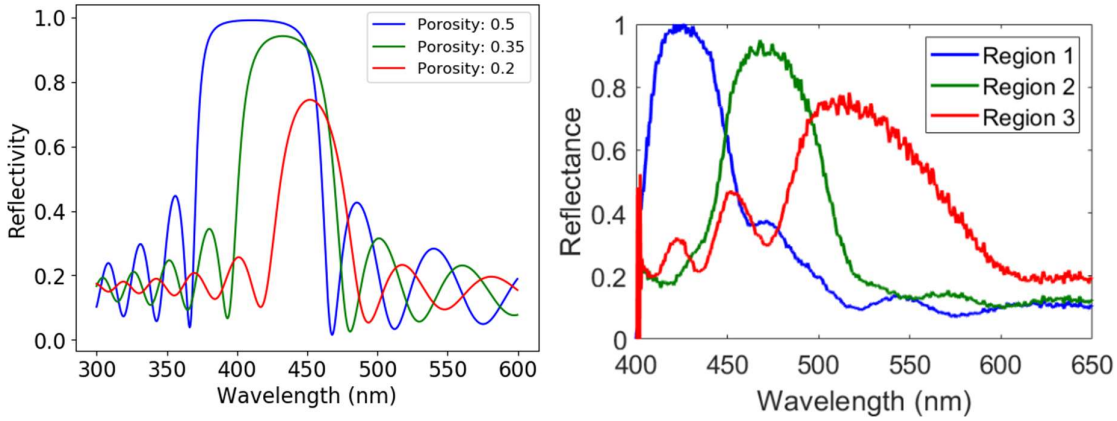

Figure 90: Comparison of transfer-matrix modelling (left) with real data (right). The model shows a similar reduction in peak intensity and red-shift in peak wavelength as the porosity is reduced.

A reduction in the peak reflectance and a red-shift in the peak wavelength is observed as the porosity is reduced. This corresponds with the data obtained in the FIB-SEM experiments; the red-reflecting regions appear to be less completely etched, and have lower porosity as a result. There are also fewer layers etched in the red-reflecting regions, which may act to reduce reflectance further.

This suggests that a solution to this issue may be to increase the voltage bias used for etching, to try and drive the etch closer to completion over the entire wafer. Another possibility may be to pattern the wafer such that the etchant can access the n-doped layers more directly, producing smaller regions of uniformly-etched DBR layers.

The differences between the TMM simulation and the experimental data arise because the SEM images show that other parameters (such as the number of layers etched, and the layer thicknesses) vary as the etch proceeds. Another source of inaccuracy is due to the use of a constant value of refractive index in the simulation, while the refractive index of GaN actually varies quite strongly with wavelength in this range. More quantitative comparisons could be achieved by taking this into account, as well as taking and analysing more SEM images to gain a more accurate idea of the actual porosities and layer thicknesses present in each of the different regions and incorporating these into the model.

5.3.2 Dry etching of porous DBRs

Dry etching through the porous layer is required to construct a micropillar cavity (or some other practical devices) containing porous DBRs. To examine how this process differs from

etching through solid GaN, a wafer containing a 10-pair latent DBR was partly electrochemically etched leaving a region of etched DBR and a region of unetched DBR. UV photolithography was then employed to pattern ~2.8 μm thick hard-baked Shipley s1828 into squares on the wafer surface, which were then etched to a depth of 2 μm using the same procedure as listed in Chapter 4.

A SEM image of a mesa that spans the boundary between porosified and non-porosified regions of the wafer is shown in Figure 91. Surface roughness is clearly visible as a result of etching through the porous DBR, and takes the form of a forest of fine spikes.

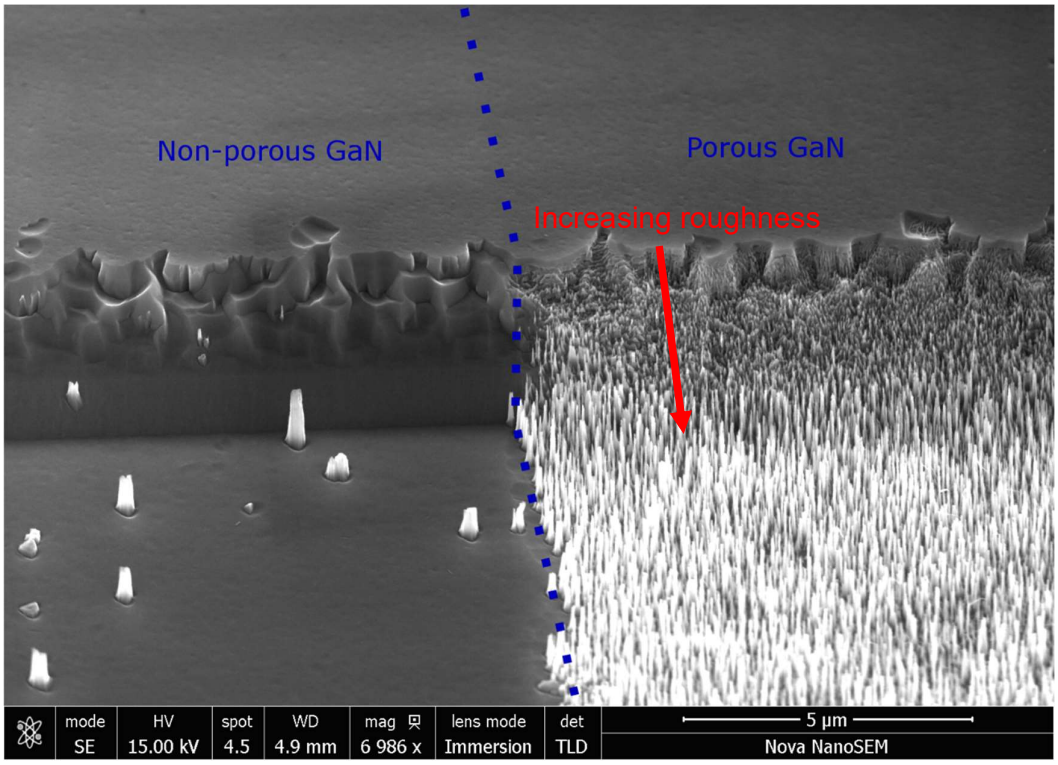

Figure 91: A mesa etched into the boundary between porous and non-porous regions of a 10-pair DBR wafer. Surface roughness induced by etching through the porous region is clearly visible, and has a morphology of fine spikes on the wafer surface.

As the etch depth is quite deep compared to the thickness of photoresist used, mask erosion is also seen in the top portion of the mesa sidewall. This also shows how the roughness develops, starting as a minor roughening in the first layers that is amplified as the etch continues (indicated by the red arrow).

One advantage of GaN over other systems is the relative ease of creating doped structures for electrical injection or gating. Therefore, contact formation to the etched surface was investigated. Ti/Au contacts were deposited onto a roughened sample using thermal evaporation and patterned by lift-off. As shown in Figure 92, the contact metal is prevented from coming into good contact with the etched surface by the spikes. This gives a very high contact resistance, meaning that any surface created by etching through porous DBRs is unsuitable for contact formation without further treatment, such as wet etching to remove the spikes.

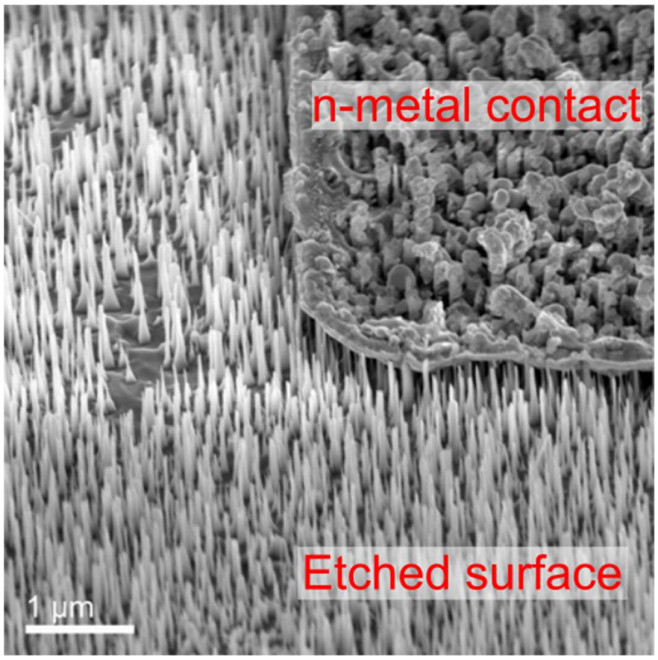

Figure 92: Ti/Al/Ti/Au n-metal contact evaporated on the rough etched surface left after porous etching.

5.4 Processing of optical cavity structures

Fabrication of micropillar and microdisk cavities requires optical isolation normal to the wafer surface, which can be provided by the porous GaN structures already outlined. For full 3D confinement, an etch into the surface of the wafer is required to produce the pillars or disks that complete each type of cavity.

I followed two approaches to fabricate these structures: nanosphere lithography, which uses randomly-placed colloidal silica nanospheres to resist the GaN etch, and electron-beam

lithography, which can create arbitrary and pre-determined patterns using PECVD silicon nitride as a hard-mask. ICP-RIE was then used to define the features.

5.4.1 ICP-RIE for high aspect ratio structures

Irrespective of the masking method used, an ICP-RIE process that can produce vertical sidewalls and high aspect ratio structures is required, particularly when fabricating micropillar cavities. The etch used in this case was a pure RIE process, using 30 sccm Cl, 15 sccm Ar, 175W RF power at the lowest possible chamber pressure of 1-3 mTorr, developing an etch rate of around 50 nm min^{-1}. This process was previously optimised for nanopillars by Muhammad Ali, and was carried out by Tom Mitchell in the Cavendish Semiconductor Physics group.

This process is intended to provide a higher plasma potential, accelerating ions to a higher speed before they strike the sample. This helps to increase the anisotropy of the etch, producing steeper sidewalls, at the expense of selectivity over the mask.

5.4.2 Nanosphere lithography

This technique uses silica micro- or nanospheres as a random mask on the surface of a wafer. The spheres are suspended in a solvent, and the suspension is dropped by disposable pipette on the chip before spinning dry. The chip is then left with some areas of densely-packed multilayers of spheres, some regions with a close-packed monolayer of spheres, and some areas that have small clumps and isolated spheres that are well separated from each other.

As the aim of the process is to fabricate isolated microdisk or micropillar cavities, only regions with widely-spaced spheres are useful, and so care is taken to use a minimum of the sphere suspension prior to spinning dry. Once the spheres have been distributed on the wafer, the solvent is allowed to evaporate completely before ICP etching as described in section 5.4.1. The silica spheres are then removed by a 90 second etch in buffered hydrofluoric acid (BHF) to allow optical characterisation of the resulting structures. The process is outlined in Figure 93.

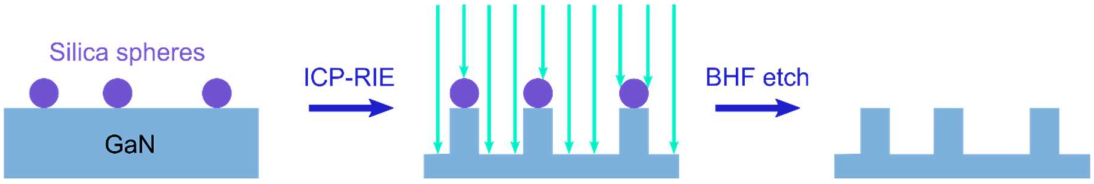

Figure 93: Outline of the micro/nanosphere lithography process flow. Silica spheres are dispersed on the surface of the wafer before ICP-RIE to define pillars. The spheres are then removed with a BHF etch.

Two diameters of spheres are used in this project: one is around 150 nm, for creating arrays of nanopillars designed to separate individual quantum dots from the surrounding QW background (and from other QDs), while increasing the light extraction efficiency; while another one is 1.5 μm in diameter and is used for creating micropillar and microdisk cavities. Some micrographs of each of these types of structure are shown in Figure 94, with the masking spheres still attached to the GaN pillars. The images in Figure 94 are taken on regions without porous layers, so there is no roughening on the etched surfaces. The pillar sidewalls are also smooth and reasonably vertical, indicating that the dry etch parameters are in an acceptable range for pillar formation.

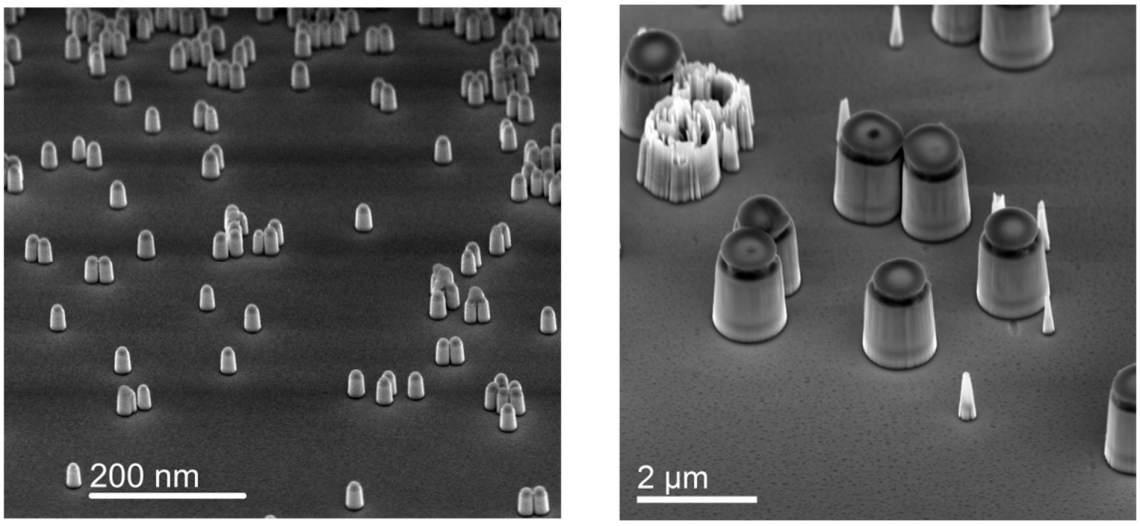

Figure 94: Nanopillars (left) and micropillars (right) patterned by sphere lithography. The spheres are still attached to the top of the etched pillars.

The spheres are eroded by the GaN etching process and can withstand an etch up to approximately their own diameter in depth. The shape of the sphere also changes as the etch proceeds, starting as a perfect sphere and ending up as a cone, as shown in Figure 95.

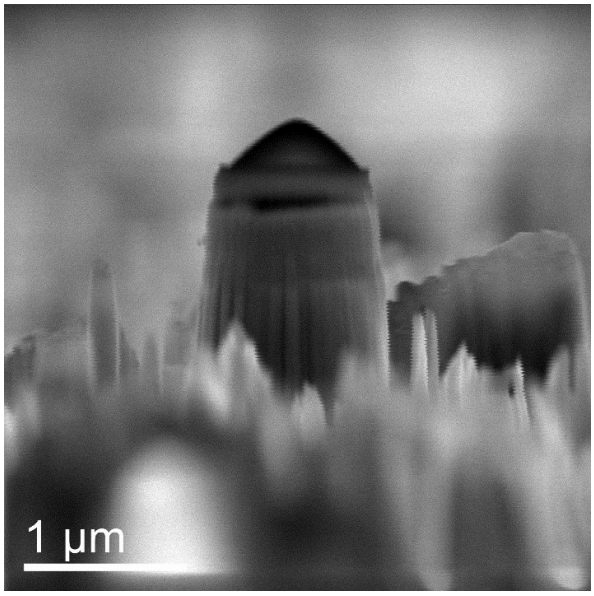

Figure 95: A view of an etched micropillar from the side, showing the shape change of the silica sphere as the etch proceeds.

The process can also be applied to samples containing porous DBRs, which produces the same kind of roughness on the etched surfaces as seen previously in section 5.3.2. An example of some micropillars etched through a stack of two 10-pair porous DBRs separated by a solid GaN cavity is shown in Figure 96.

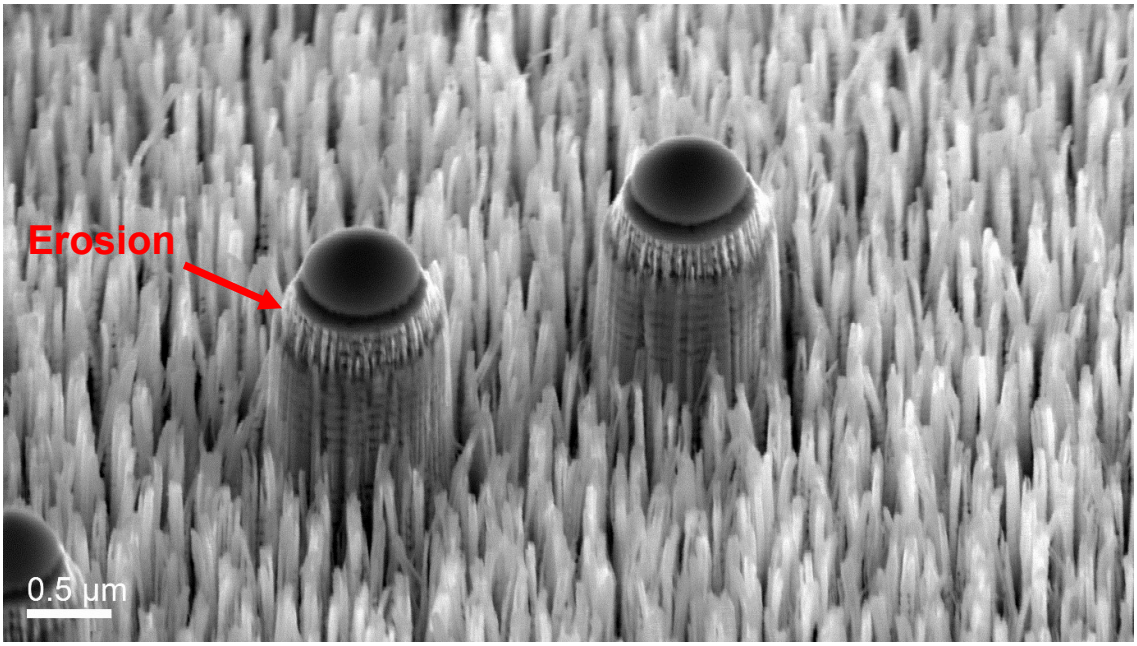

Figure 96: Micropillars defined using sphere lithography and etched to a depth of 2 um. The wafer contains two porosified 10-pair DBRs separated by a thin region of solid GaN. Erosion of the top part of the pillar is visible, along with the appearance of grass on the etched surface.

In this case, some erosion of the top of the micropillar is clearly visible due to the somewhat deeper etch than in the previous case. As this erosion is some distance from the active layers in a full micropillar cavity, it might not significantly affect the cavity Q-factor. However, the erosion also causes increased roughening further down the pillar, which will affect the lateral confinement in the centre of the cavity. This roughening is apparently enhanced by the presence of the pores in the material, by comparison to the non-porous pillars.

5.4.2.1 Cathodoluminescence

To confirm that the samples still showed luminescence after processing, they were investigated using SEM-CL. The room-temperature panchromatic CL image is overlaid in blue on the SEM image in Figure 97. The observed light emission indicates that the InGaN active layers are still able to luminesce after processing.

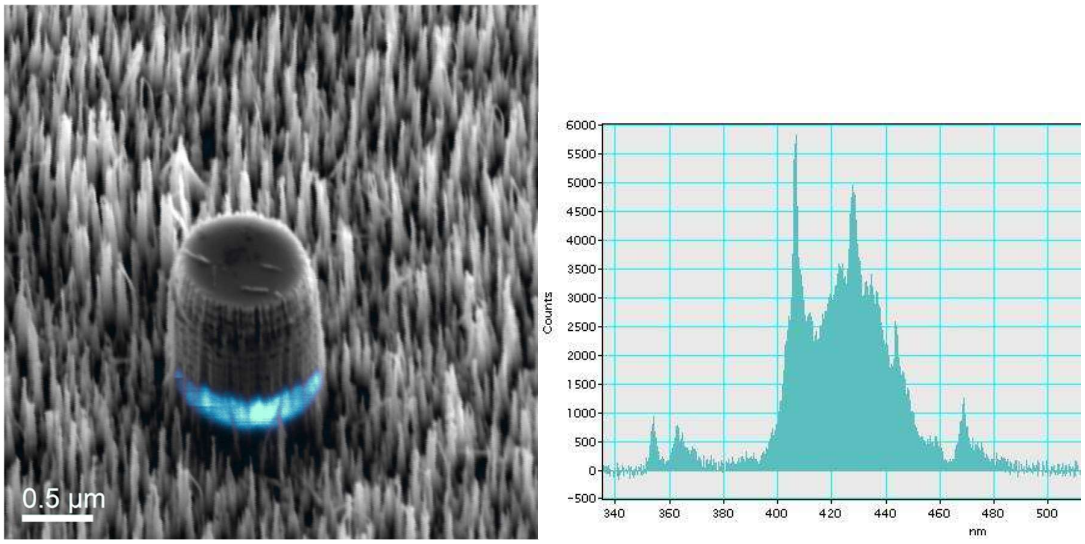

Figure 97: SEM-CL examination of porous micropillars, showing the emission originating from the QD layer in the middle of the pillar. Right: Panchromatic CL image coloured blue and overlaid on the SEM image. Right: spectrum taken from the emitting region, showing sharp peaks on a broad background characteristic of InGaN QDs.

5.4.3 Electron-beam lithography

Electron-beam lithography is a technique for creating sub-micron patterns in an electron-sensitive resist, described in detail in As arbitrary patterns can be written into resist, it is more flexible than the sphere lithography method, and it allows for deterministic placement of cavities with a well-defined spacing. This means that single photon sources could be more easily integrated with other structures such as electrical contacts and optical components.

Typical electron-beam resists are not very resistant to dry etching. The most resilient types are negative resists, where electron-exposed regions remain after development. ZEP and MA-N series resists fit this category, as well as hydrogen silsesquioxane (HSQ). Positive resists, such as poly(methylmethacrylate) (PMMA), tend to be less resistant to dry etch processes [217].

One solution to this problem is to adopt a two-step process, where an e-beam resist is used to pattern an intermediate hard-mask, which is then used to resist the main dry etching step into the GaN. My process will use a silicon nitride layer as the hardmask, in a similar approach to that used by Lu *et al.* (for 400 nm holes in photonic crystal defect cavities) [107], Tao *et al.* [92] for their air-gap cavities (where SiO_2 was used as the mask), or Tamboli *et al.* [105] (again using SiO_2).

SiN_x was selected because it has previously been used as a masking material on the GaN ICP-RIE system, developing a selectivity of about 2:1. Due to the relatively deep GaN etches envisaged, running to depths of 1 – 2 μm, around 0.5 – 1 μm of SiNx will be required. This will need a hard-mask of its own to achieve the required selectivity, and I used Cr for this purpose. The overall flow of the process is shown in Figure 98, and is very similar to that used by (for example) Reddy *et al.* [218].

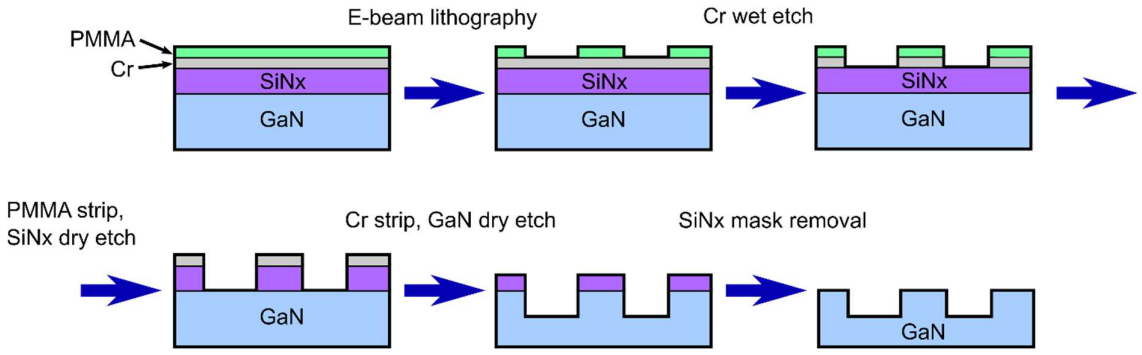

Figure 98: Overview of process flow envisaged for creating deep etched structures in GaN wafers using electron-beam lithography. Silicon nitride, chrome and electron-beam resist are deposited on the sample, and sequentially etched by wet and dry etches to achieve pattern transfer into GaN.

The process will permit the creation of cavities connected to a surrounding mesa, opening up the possibility of using these structures in electrically-injected devices in a way similar to Nowak *et al.* [100].

5.4.3.1 Silicon nitride hardmask fabrication

Silicon nitride was deposited on GaN samples using plasma-enhanced chemical vapour deposition (PECVD) by Melanie Tribble and Philip Cameron in the Cavendish Semiconductor Physics group. An Oxford Instruments parallel-plate reactor was used for the deposition, with a low-stress nitride deposition sequence that alternates between a high-frequency (13.56 MHz) RF power supply and a lower frequency supply (300 kHz) during deposition. The gases used during deposition are silane and ammonia as silicon and nitrogen sources, diluted in argon.

The high frequency RF supply generates a plasma which has a very high electron temperature, but low ion temperature (as the ions are heavy and unable to accelerate very far before the field reverses). This leads to a high density of ions that are accelerated only by the d.c. bias that develops across the plasma sheath around the sample platter, generating a film

which has a built-in tensile stress due to hydrogen incorporation in the film. The lower frequency RF excitation accelerates the heavy ions as well as the electrons, increasing the amount of ion bombardment of the surface. This creates a compressively-stressed layer [219, 220] that compensates for the tensile stress in the high-frequency layer. Overall, this procedure lowers the residual stress in the film and increases the refractive index [221].

A silicon nitride thickness of 800 nm was selected initially, as this should be suitable for a GaN etch to a depth of up to 1.6 μm.

After SiN_x deposition, a 50 nm chrome layer was deposited using electron-beam evaporation. A rate of 1 Å/s was used in a vacuum of 2×10^{-6} Torr or better. This chrome layer is easily patterned using a wet etch, and due to its relatively low thickness, it should be suitable for creating e-beam defined features down to about 100 nm across. Subsequent cleaning in acetone in an ultrasonic bath followed by IPA and nitrogen drying was used to remove particle contamination.

5.4.3.2 Dry etching of silicon nitride films

Silicon nitride may be etched in fluorine-containing plasmas, such as gas mixtures containing CHF_3, SiF_4, SF_6 or others [222]. In gas mixtures containing fluorocarbons such as CHF_3, a layer of a teflon-like polymer forms on the surface as the etch proceeds [223]. This polymer is simultaneously deposited and etched, and this gives a steady-state thickness of the film above a threshold value of the self-bias (where the etch rate begins to match the deposition rate) [224, 225]. The etch rate of the silicon nitride also shows a sharp increase when the thickness of the steady-state film is reduced (by altering the etch conditions) to around 1 nm; this marks the transition between a regime where the etching is limited by fluorine diffusion through the fluorocarbon film, to one where silicon nitride is removed by direct contact of incident ions with the material, as shown in Figure 99. It is worth noting that the fluorocarbon film is not just an etch-inhibiting layer; ions impacting the film defluorinate it, meaning that it also acts as a source of fluorine for the etch [223].

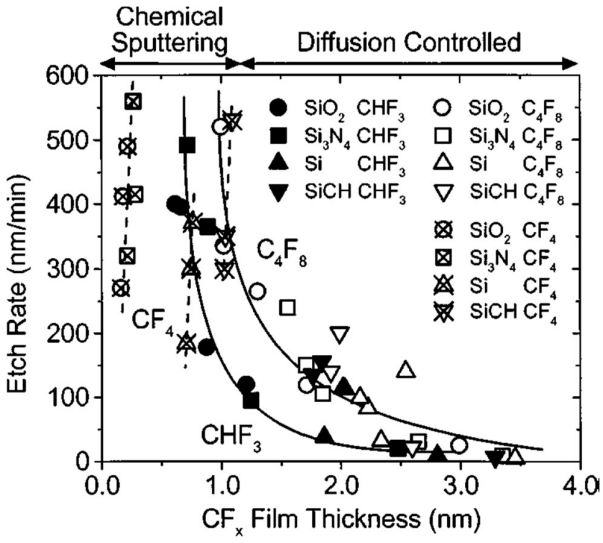

Figure 99: Relationship between steady-state fluorocarbon film thickness and etch rate for various films in various etch chemistries. Reproduced from Standaert et al., with permission [223]

Oxygen may also be added to the gas mixture to influence the etch; adding 10 vol% O_2 approximately halves the steady-state thickness of the fluorocarbon polymer [225]. This is due to the reaction between O_2 and carbon to form products such as CO, which then increases the concentration of F compared to carbon-containing compounds in the plasma. Addition of nitrogen has a similar, but less pronounced, effect. This is also an explanation for the relative etch rates of Si, SiN_x and SiO_2; the nitrogen and oxygen produced when the latter two materials are etched tends to attack the fluorocarbon film and reduces its thickness. This gives a general trend of SiO_2 etching fastest, and Si slowest [225].

Kaspar et al. investigated a cyclic SiN_x etching and O_2 cleaning process for forming highly vertical sidewalls for nanoscale silicon nitride hardmasks. They observed that the etch rate is initially high, and then reduces to a steady-state value as the fluorocarbon layer increases in thickness during CHF_3 etching [226]. Selection of the amount of time between O_2 cleaning steps (which remove the polymer layer) then permits adjustment of both the etch rate and sidewall profile.

Design of experiments optimising ICP-RIE of SiNx

Initial etching experiments on silicon nitride layers masked using chrome were performed using a recipe on an Oxford PlasmaLab 100 ICP180 that had previously been used for etching thin (<50 nm) layers of the same material. This recipe is a pure RIE process (i.e., there

is no power applied to the ICP tube) using CHF_3-based plasma, with a small addition of O_2, at a chamber pressure of 55 mTorr.

Test samples were coated with chrome using e-beam evaporation, which was patterned by a photolithographic lift-off process, and then etched with this recipe.

SEM images taken at 45° to the sample surface and looking at the edge of a hole in samples etched for 5, 10, 15 and 20 minutes are presented in Figure 100. The etch parameters used were: 150 W RF power, 0 W ICP power, 50 sccm CHF_3, 5 sccm O_2 and 55 mTorr chamber pressure, developing a D.C. bias of ~315 V. A cross-section of the sample etched for 20 minutes is included in Figure 101, where the columnar morphology of the RIE grass can be clearly seen.

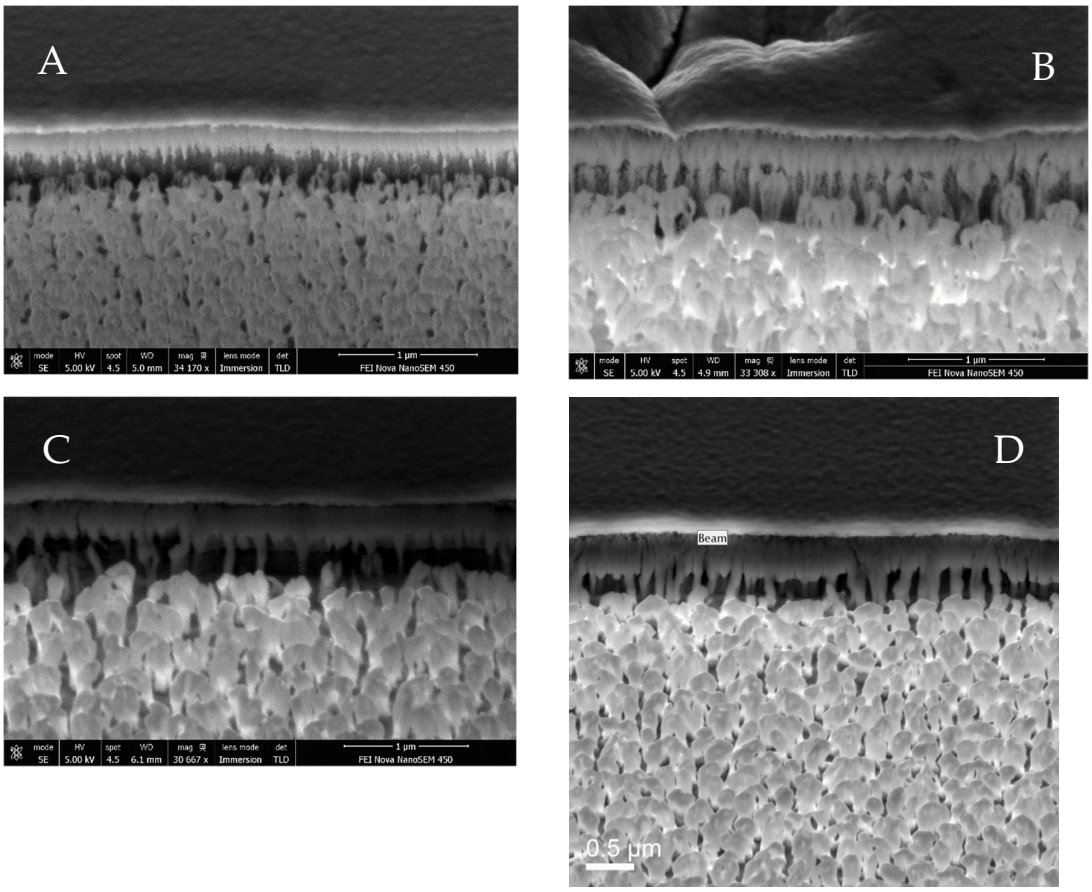

Figure 100: Samples etched for 5 min (A), 10 min (B), 15 min (C) and 20 min (D) using 50 sccm CHF_3, 5 sccm O_2 and 150 W RF power at a chamber pressure of 55 mTorr.

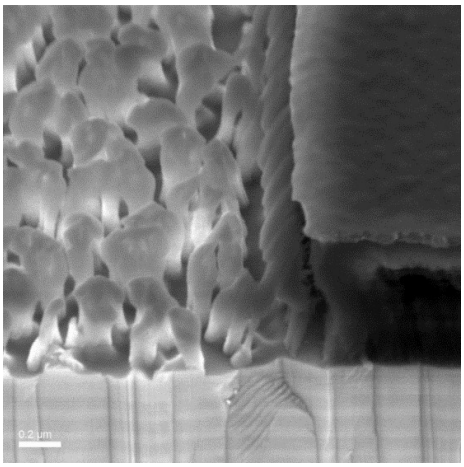

Figure 101: Cross-sectional SEM image of the Cr mask, etched SiNx and GaN layers on sample D, etched on the Oxford system.

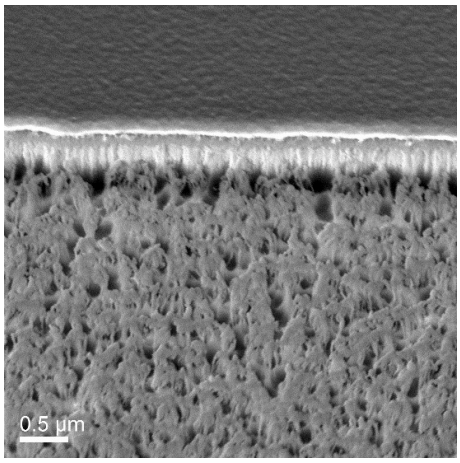

Figure 102: Etched silicon nitride surface for a sample processed with a PlasmaPod RIE system.

Significant roughening of the etched surfaces was observed. The columnar structures formed, sometimes referred to as 'RIE grass', can be due to uneven fluorocarbon polymer deposition on the surface, which then acts as a micromask to further etching and leads to the observed roughening. Another possibility is that Cr is sputtered from the mask and re-deposited, also leading to micromasking.

Similar results were obtained for an etch performed on a different RIE etcher (a JLS Designs PlasmaPod), showing that the grass is a function of etch conditions rather than a specific problem with the etching system used. The etched surface produced by this system is shown in Figure 102. This etch was carried out by Tom Mitchell in the Cavendish Semiconductor Physics group.

To investigate how to suppress this RIE grass, a series of experiments were performed, as outlined in Table 3.

Experiment	**O_2/CHF_3 ratio**	**RF power**
E	Low (5/50 sccm)	Low (75 W)
F	High (10/45 sccm)	Low (75 W)
G	Low (5/50 sccm)	High (150 W)
H	High (10/45 sccm)	High (150 W)

Table 3: Randomised-block design of experiments to investigate RIE grass formation.

The results of these experiments showed that neither O_2/CHF_3 ratio nor RF power had any noticeable effect on the severity of grass formation, at the levels tested and for the process conditions, and in spite of significant changes in D.C. bias and etch rate.

Further experiments were then performed at a lower chamber pressure (10 mTorr). To keep the plasma density high at lower pressure, ICP power was also increased. An immediate improvement was found for samples etched with 400W ICP power, 50 sccm CHF_3 and 5 sccm O_2, although surface features were still present as can be seen in Figure 103. Features line up along the etched edge for 150W RF power (d.c. bias = 295 V), possibly due to local electric field modification by the metal mask. For 75 W RF power, the d.c. bias dropped to 140 V, which is still well in excess of the threshold bias for etching, and the density of features along the edge of the chrome was lowered.

The fact that increasing physical bombardment by lowering the pressure was observed to reduce the formation of grass suggests that its origin is indeed in uneven fluorocarbon deposition, and not Cr sputtering.

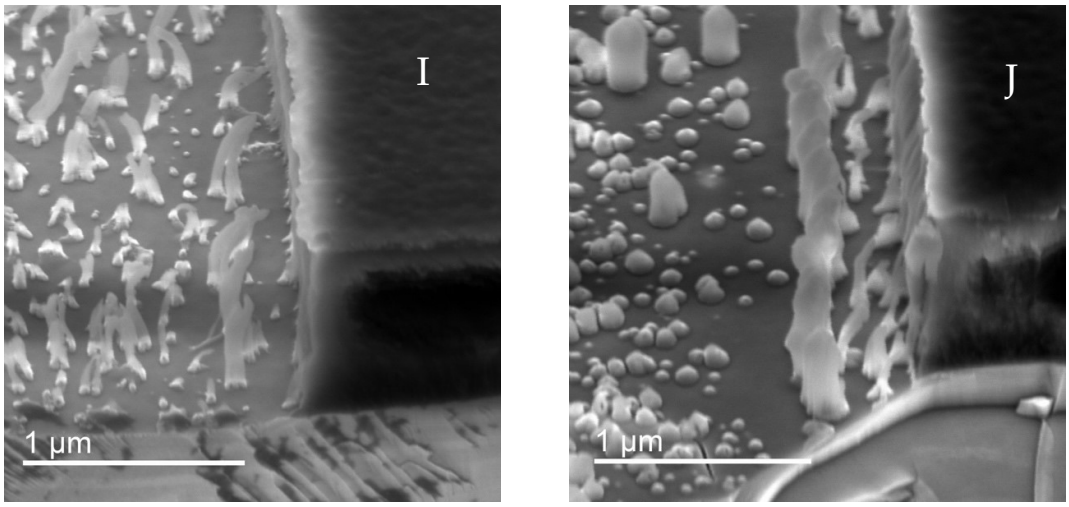

Figure 103: ICP-RIE etched samples at 10 mTorr, 50 sccm CHF_3, 5 sccm O_2, 400W ICP power. RF power: 75W (I), 150W (J). Both samples etched for 5 min.

Lowering chamber pressure further to 8 mTorr while adding a small amount of argon to the gas mixture was then tried, to increase the sputtering yield and hopefully reduce polymer formation rate. The flow rate of oxygen was reduced to maintain a constant overall gas flow. An etch carried out for 3m 30 s showed a reasonably clean etched surface, but a sample etched for 5m 20s (clearing the nitride) showed a recurrence of the polymer grass, albeit reduced in density (Figure 104). This observation indicates that formation of a micromask happens at some point in the middle of the etch.

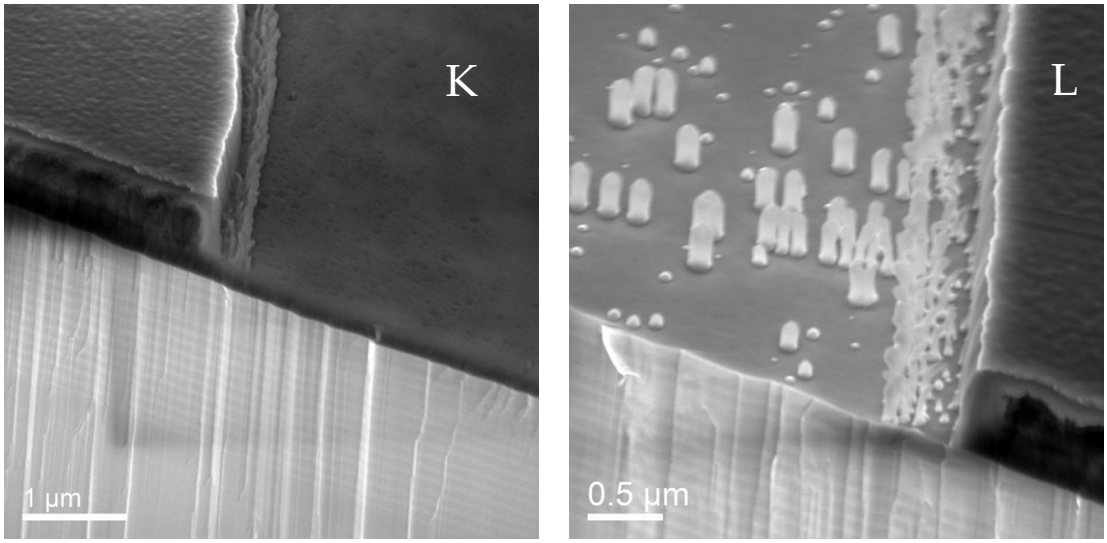

Figure 104: ICP-RIE etched samples at 100 W RF, 400 W ICP, 8 mTorr, 50 sccm CHF_3, 3 sccm O_2 and 2 sccm Ar. Etched for 3 min 30 s (K) and 5 min 20 s (L).

Restoring the oxygen flow rate to 5 sccm caused a further reduction in the micromasking, leaving a clean etched surface with some damage remaining to the silicon nitride sidewalls, as shown in Figure 105.

There also seems to be a layer of material that forms near the mask edge, though the source of this layer is not clear. It appears to have peeled off from the sidewall in Figure 105, though this may have happened while the sample was being transferred between the etcher and the SEM rather than during the etch itself.

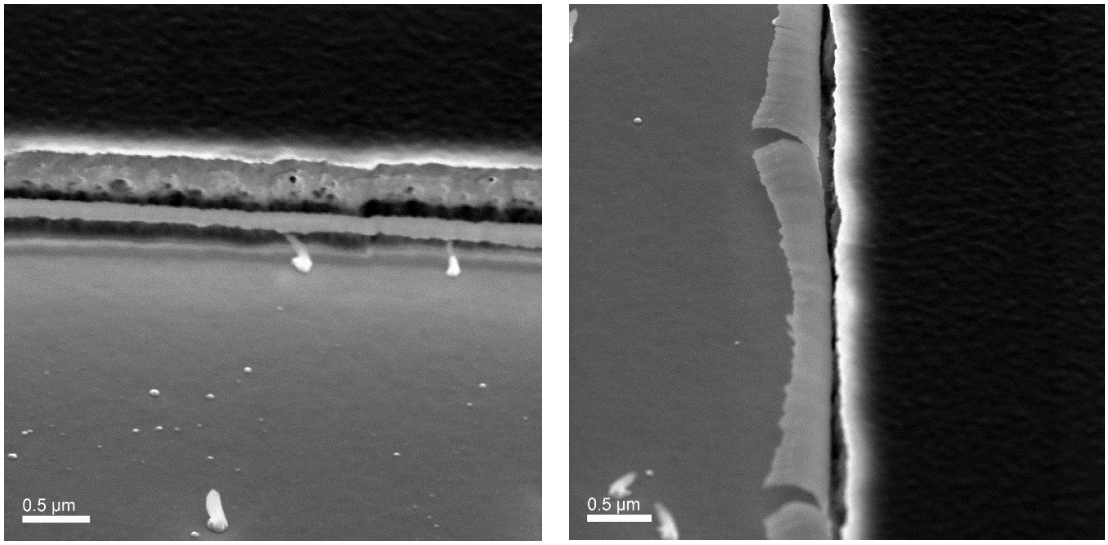

Figure 105: Two perspectives on ICP-RIE etched samples at 100 W RF, 400 W ICP, 8 mTorr, 50 sccm CHF3, 5 sccm O2 and 2 sccm Ar. Etched for 5 min 20 s.

Silicon nitride masked etching of GaN

Once an acceptable quality of silicon nitride mask had been attained, the chrome was stripped using a 2-minute etch in chrome etchant, followed by cleaning in acetone and IPA. The samples were then etched using the same recipe as that used in the nanosphere lithography process, to a depth of approximately 500 nm. Due to charging issues in the SEM, the sample was coated with a thin layer (1-2 nm) of gold, deposited by d.c. argon sputtering in a desktop sputtering system (Emitech). The resulting image is shown in Figure 106. A very steep sidewall is observed, and the retained thickness of silicon nitride is around 700 nm, consistent with the 2:1 selectivity expected from the process.

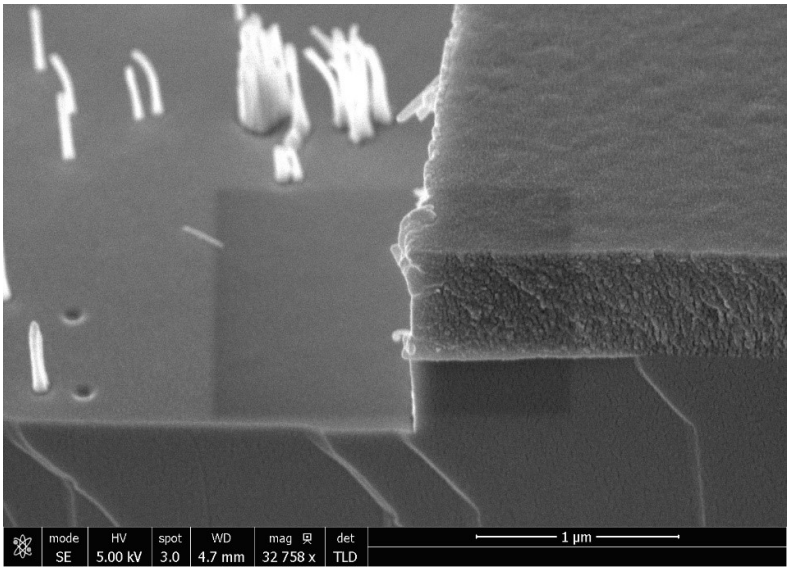

Figure 106: Silicon nitride masked GaN etch, using the GaN etching recipe previously developed for use with the sphere lithography method. A reasonably clean etched surface and vertical sidewall is obtained.

Unfortunately, shortly after an optimised process was obtained, the decision was made by the Nanoscience Centre, who own the instruments, to remove the ICP-RIE tool I had been using from service due to ongoing maintenance issues and a lack of funding. The PlasmaPod tool was therefore the only remaining possibility for etching these films. The pressure in this tool cannot be reduced much below 40 mTorr, and although some trials with increased RF power and increased oxygen flow were done, there did not seem to be a way of eliminating the grass in this system by adjusting etch parameters. An etch on an array of chrome discs is shown in Figure 107.

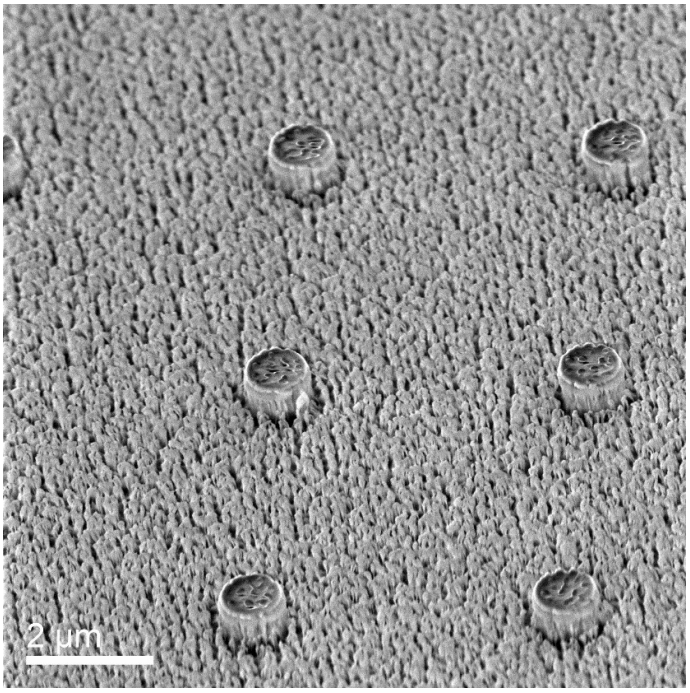

Figure 107: RIE etch using a JLS Designs PlasmaPod parallel-plate RIE, showing the RIE grass from etching through silicon nitride.

To overcome the issue, the process needed to be modified to remove the SiN_x grass using a wet-chemical etch. For this purpose, a 60 second dip in buffered hydrofluoric acid (BHF) was used. The acid uniformly erodes the SiN_x features and leaves small tips where the larger-scale grass previously existed, as shown in Figure 108.

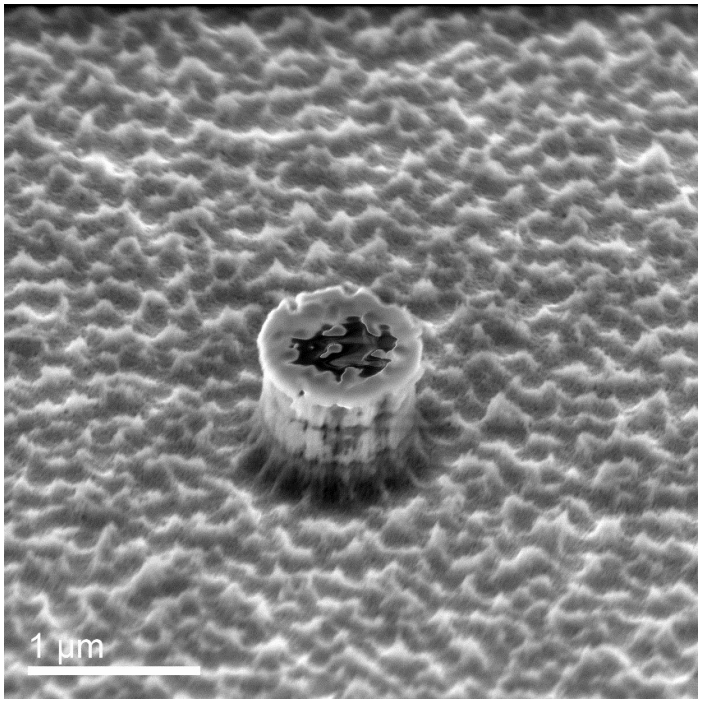

Figure 108: PlasmaPod etched sample after 60 second etch in buffered hydrofluoric acid.

The sample was then returned to the RIE for another short etch to remove the remainder of the film. The resulting sample is shown in Figure 109.

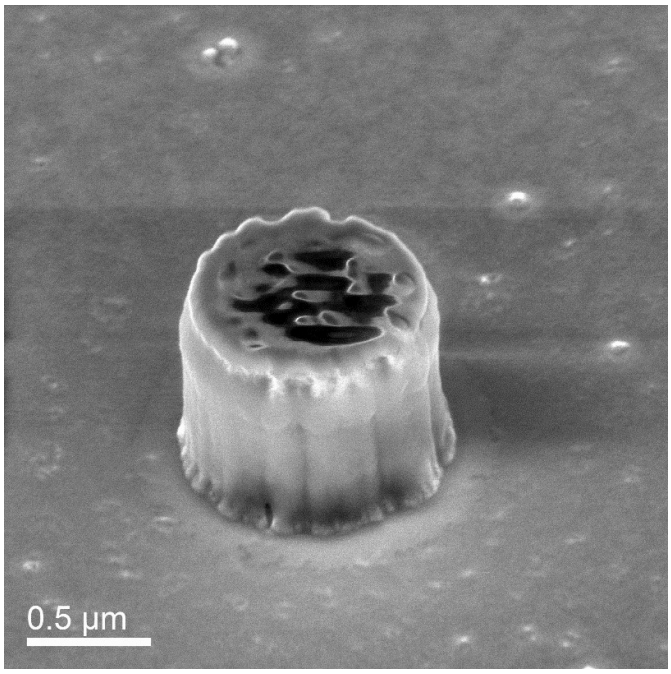

Figure 109: Micropillar after RIE, BHF etching and second RIE run, revealing reasonably clear etched surfaces.

A GaN etch to a depth of 2 μm was then carried out. The mask erosion rate is higher in the case of smaller structures, and so the 800 nm thick layer of silicon nitride was completely eroded. However, reasonably smooth and well-defined pillars were obtained as shown in Figure 110, except for the regions near the very top of the pillar which were damaged by the mask failure. Selection of a thicker SiN masking layer or a shallower pillar etch depth would resolve this issue.

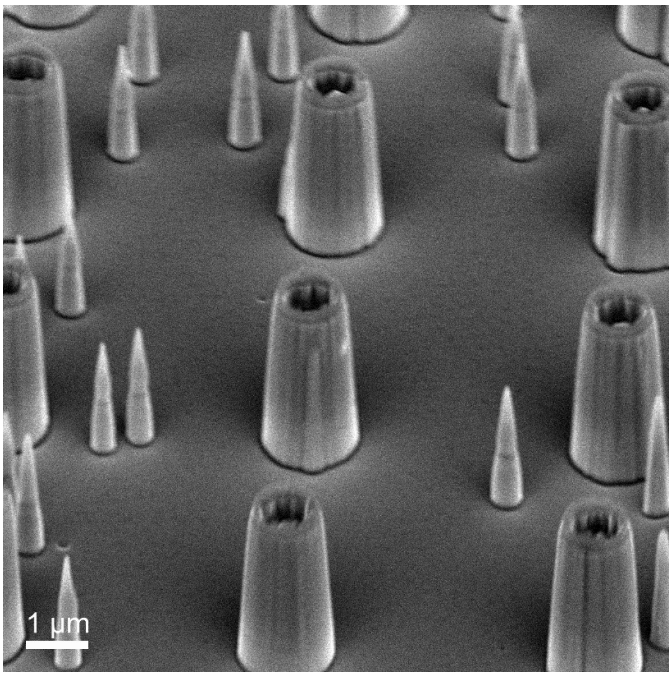

Figure 110: Micropillars etched into GaN, using a silicon nitride mask.

5.4.3.3 Electron-beam lithography

To carry out e-beam lithography, PMMA with an average molecular weight of 9.5×10^5 monomer units dissolved in anisole to a concentration of 4% (referred to as PMMA 950k A4) was spin-coated at a speed of 4000 rpm on the SiN_x and Cr-coated chips, leaving a nominal resist thickness of 200 nm.

Electron exposure was carried out in a Crestec CABL 9000 system, using a beam energy of 50 keV and a beam current of 1 nA. Patterns were generated manually using the CAD software LayoutEditor (Justpertor) and converted to the native Crestec format. The exposure mode was set to raster the beam over a grid of 6×10^5 dots arranged in a field 600 μm across.

To determine the optimal exposure time, several fields of features were patterned with a dose varied in increments of 50 μC cm^{-2} between 300 μC cm^{-2} to 800 μC cm^{-2}, with the dose variation achieved by adjusting the dwell time of the beam on each point in the field at fixed beam current. The best pattern definition was seen for a dose of 550 μC cm^{-2}, with the finest features clear of resist without losing resolution due to overexposure.

Development was carried out using methyl isobutyl ketone (MIBK) mixed with isopropyl alcohol (IPA) in a ratio of 1:3. Chips were immersed for 30 seconds in the developing mixture, followed by 30 seconds in fresh IPA before blow-drying with nitrogen.

The resulting chips were then used as the starting point for the rest of the process as outlined in Figure 98.

5.4.4 Fin-connected pillar structures

Fin-connected pillars, intended for electrical injection and to allow for the etching of porous DBRs after the ICP etching steps, were patterned using the electron-beam lithography procedure described above. The patterning was carried out on samples containing a latent porous DBR (i.e. alternating layers of n-doped and undoped material).

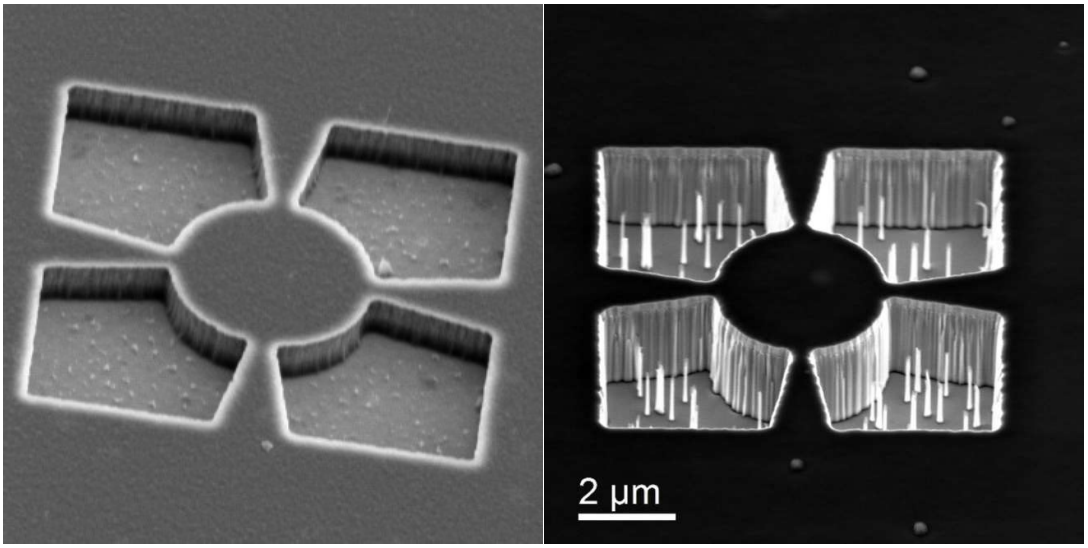

Figure 111: Left: fin pillar mask, with chrome layer still in place on top of SiN. Right: the same structure etched to a depth of 1.8 μm into GaN. The central disk has a diameter of 4μm.

These structures were patterned with a variety of diameters, with and without fins connecting them to the surrounding material. Examples with the Cr mask still present on top of the SiN, and following the etch into the underlying GaN, are shown in Figure 111.

5.4.4.1 Electrochemical etching trials

The wafers were electrochemically etched after patterning, but before removing the silicon nitride hardmask. This was intended to protect the top surface from damage during etching, and ensure a controlled lateral etching process. It will also constrain the porous etching process to the pillars themselves, leaving the rest of the wafer untouched and suitable for conventional device processing (e.g. to integrate the pillars into electrical devices).

Patterned wafers containing a double latent DBR (10 pairs above and below a half-wave cavity layer containing Q2T QDs) were etched in a 1 M aqueous solution of oxalic acid, with the wafer as the anode and a platinum foil counter-electrode as the cathode. Contact was made to the wafer by scratching the surface with a diamond scribe and attaching a copper wire using indium solder. The first test was carried out at 6 V, which is the bias used for previous full-wafer and chip-scale electrochemical etches. This resulted in destruction of the sample, with some surviving pillars showing layers of material completely removed instead of porosified. A thin layer, corresponding to the central layer in this double-DBR structure, is left suspended after the etch. These effects can be seen in Figure 112.

The destructive effect of this bias voltage is likely due to the different etching mechanism; the chip-scale etching uses dislocation channels to etch vertically through the wafer, while these fin-pillar samples use lateral etching through the sidewalls.

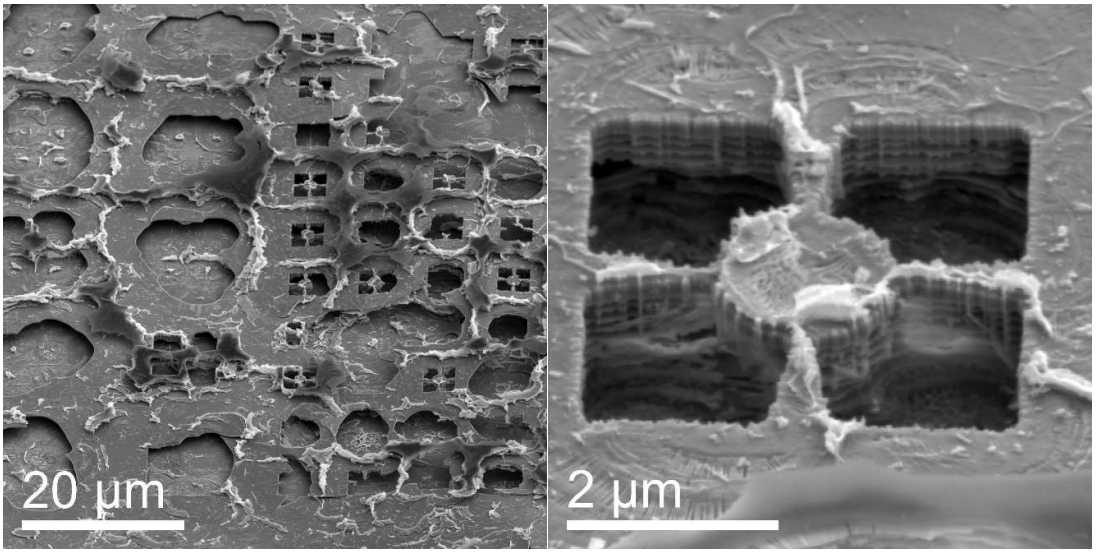

Figure 112: Fin-connected pillar sample etched at a bias of 6 V in 1 M aqueous solution of oxalic acid. Left: overview of destroyed sample, with suspended membrane visible. Right: Partially intact micropillar, showing completely etched layers (rather than porosified layers).

New wafers were patterned, and etching experiments were carried out at a lower voltage of 1.5 V, increasing in increments of 0.5 V up to 6 V to determine the onset of etching without damage to the sample. The sample showed a visible colour at 4 V and above, indicating that the etch was producing significant porosity in the n-GaN layers at this point. An optical and electron micrograph of the sample etched at 4.5 V is shown in Figure 113. The samples were etched for a period of around 30 minutes each, although the etch appears to be self-limiting

and so the etching time is not critical, with the extent of the etched region not appearing to increase further after a few minutes of etching.

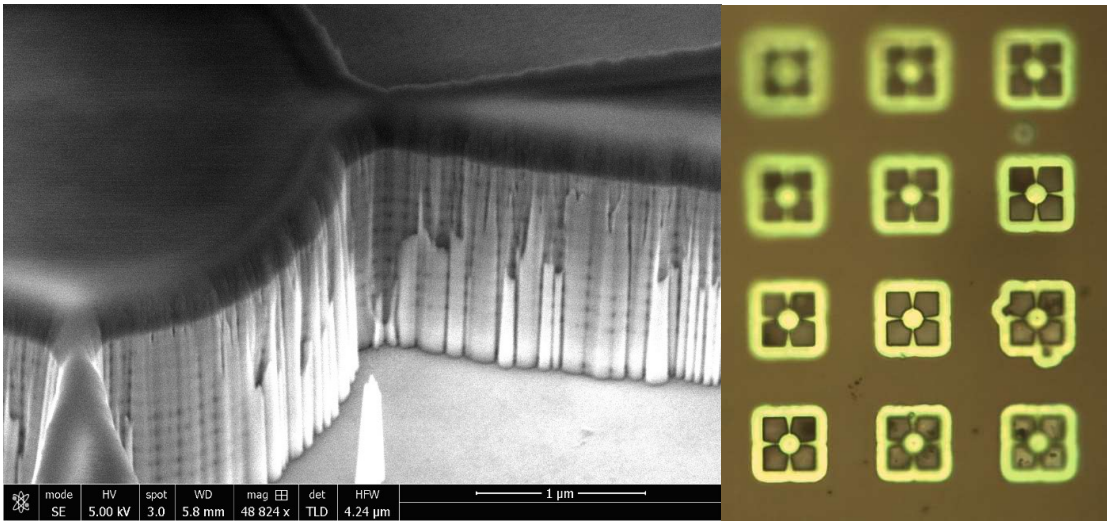

Figure 113: SEM (left) and optical micrograph (right) showing the porosity and reflective appearance of fin-connected pillar structures subjected to an electrochemical etch with a bias of 4.5 V. The bright regions on the optical micrograph correspond to porosified parts of the DBR, and are confined to the pillar and the region surrounding it due to the protective silicon nitride layer.

After the silicon nitride masking layer was stripped off by a further RIE etch and BHF residue removal, micro-reflectivity measurements were carried out on the samples etched at 4.5, 5, and 5.5 V, as shown in Figure 114. Samples etched at increasing etching voltage showed increases in both peak reflectivity and stopband width, together with a small shift in peak wavelength, occurred as the etching voltage was increased, which is consistent with increasing porosity.

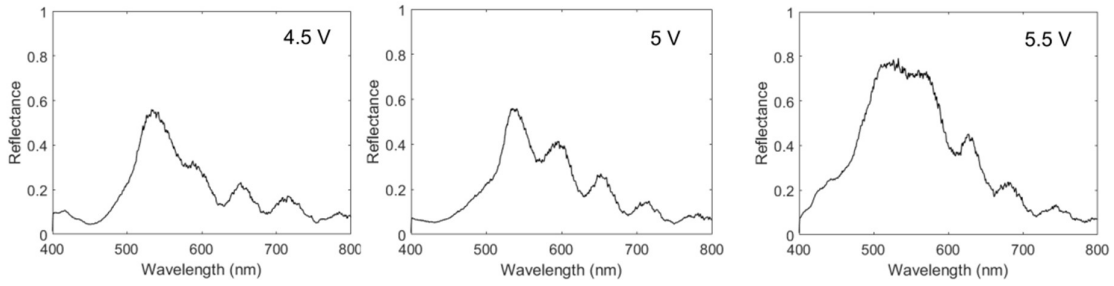

Figure 114: Micro-reflectivity plots acquired from the central region of a 4 um fin-pillar.

The peak reflectance remains relatively low at only around 80%. This could indicate a less complete EC etch than in the planar case (which showed reflectance exceeding 95%). There is

also no clear cavity-related dip in the reflectance spectrum. However, the reflected wavelength is more consistent between cavities, suggesting that the inhomogeneities in the etched DBR observed in section 5.3.1 can be solved by etching laterally into the cavity structures after processing.

Focused ion beam cross-sections were also taken of the processed and EC-etched structure, using the same procedure as in section 5.3.1. The resulting SEM image is shown in Figure 115.

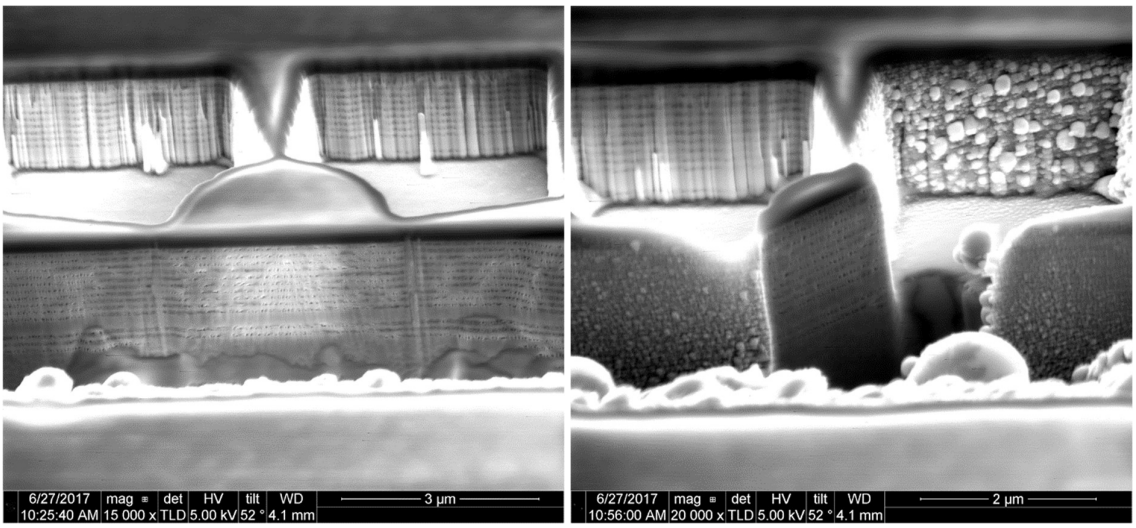

Figure 115: Focused ion beam (FIB) cross section of a fin-pillar optical device, showing the etched porous layers. Two slices are shown, with similar DBR appearance, indicating that the etch is uniform in both the radial and azimuthal directions of the pillar.

The top 10-pair DBR has been porosified completely, while only the top two layers of the bottom DBR etched. These layers are the ones that are exposed at the sidewall of the pillar, and this indicates that the etch does not propagate effectively in the vertical direction when constrained to a small region of material in this way (unlike in the chip-scale case, where the etch proceeds through all layers of the DBR even though the etchant only has access to the top surface).

5.4.4.2 SiN deposition issues

The first sample, etched at 6 V, was later discovered to be part of a run that was deposited while the PECVD system had a problem with the low-frequency power supply. This meant that the entire film thickness was deposited using high-frequency RF energy only, and there

may be a tensile stress in the deposited film as a result (as discussed in section 5.4.3.2). The presence of a SiN layer under tensile stress on the surface of the wafer could explain why that particular sample set failed upon etching, and in fact samples with correctly deposited SiN may be rather more robust to electrochemical etching than suggested by that experiment.

Further work could therefore increase the EC etching bias beyond 5.5 V, to see if the resulting reflectivity can be increased further.

1.1.1 Porous GaN ICP-RIE grass removal by wet etching

The GaN grass generated by etching through porous DBRs is very fine compared to the size of the micropillars patterned by the techniques presented here, and therefore an isotropic wet etch was investigated as a possible method for removing the grass.

1.1.1.1 Wet chemical etches in GaN

Wet chemical etches (i.e. etches not requiring photo- or electrochemical enhancement) reported in the literature mainly use potassium hydroxide (KOH) to etch GaN, in solutions made up with water [227] or ethylene glycol [228]. The latter allows temperatures exceeding the boiling point of water to be used, and shows higher etch rates than molten KOH due to solubility of the etch products in the solvent [228]. The etching mechanism relies on the initial attack of dangling bonds exposed by nitrogen-polar c-plane surfaces and other crystal planes that expose nitrogen [229]. Hence, +c (Ga-polar) planes are inert while -c (N-polar) planes are readily etched.

Of particular relevance to my experiment is the results reported by Debnath *et al.*, who showed that dry-etched c-plane micropillars with diameters of 500 and 250 nm could be etched in 10 wt% KOH in ethylene glycol at 80°C [95]. The pillars showed a reduction in tapering, and the c-plane surfaces remained unaffected by the etch both at the top surface of the pillar and on the etched surface surrounding the pillars.

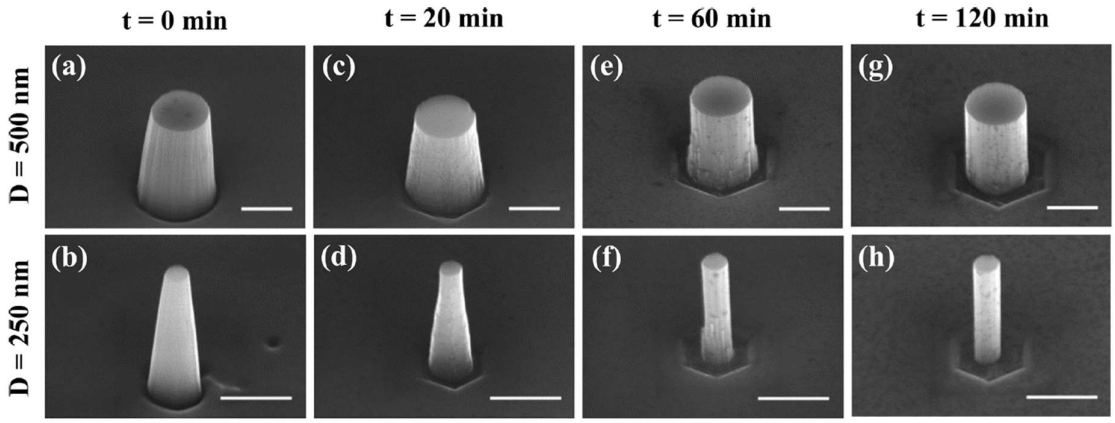

Figure 116: Dry-etched micropillars exposed to 10 wt% KOH in ethylene glycol solution at 80°C, showing the evolution of the morphology as the etch proceeds. Reproduced with permission from [95].

1.1.1.2 KOH etching experiments

Wet etches were performed using conditions similar to those reported by Debnath *et al*. [95], using a solution of 10% KOH in ethylene glycol at a temperature of 70°C stabilised in a water bath (this was the highest temperature the bath could sustain reliably). Pure KOH pellets were dissolved in ethylene glycol, taking around 45 minutes with stirring at 70°C, prior to the introduction of 1.5 μm diameter micropillar etched a-plane and c-plane chips. These micropillars were formed by etching through porous DBR layers, and so they showed the ICP-RIE grass that appeared on other etched porous GaN wafers (see images in section 5.3.2). After etching, the chips were rinsed in de-ionised water before drying with nitrogen.

Initially, the etch was run for 30 minutes, as this was expected to give noticeable but subtle results, based on the experience of Debnath *et al*. Instead, extensive damage was observed in both the a- and c-plane samples as shown in the scanning electron micrographs in Figure 116. The selectivity of the etch for particular crystallographic orientations is clearly visible, with c and m-plane facets (which have the slowest etch rate) exposed.

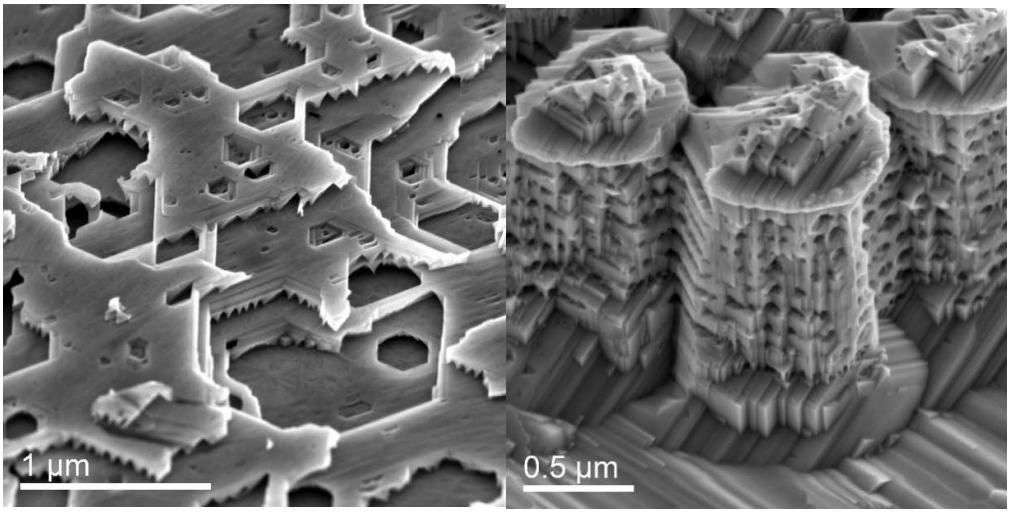

Figure 117: C-plane (left) and a-plane (right) 10-pair porous DBR structures ICP etched into pillars using microsphere lithography followed by an etch in 10% KOH solution for 30 min at 70°C.

The results of etching for different lengths of time under these conditions are shown in the micrographs in Figure 118. The pillars and wafer surface are clearly attacked by the etchant, and so a compromise between grass reduction and damage to the pillar cavities is necessary. A-plane wafers require around 5 minutes whereas c-plane wafers need around 10 minutes to produce a significant reduction in grass without extensive damage to the pillars. However, in either case, the etched surface is not completely smooth and is still, therefore, unsuitable for making contacts.

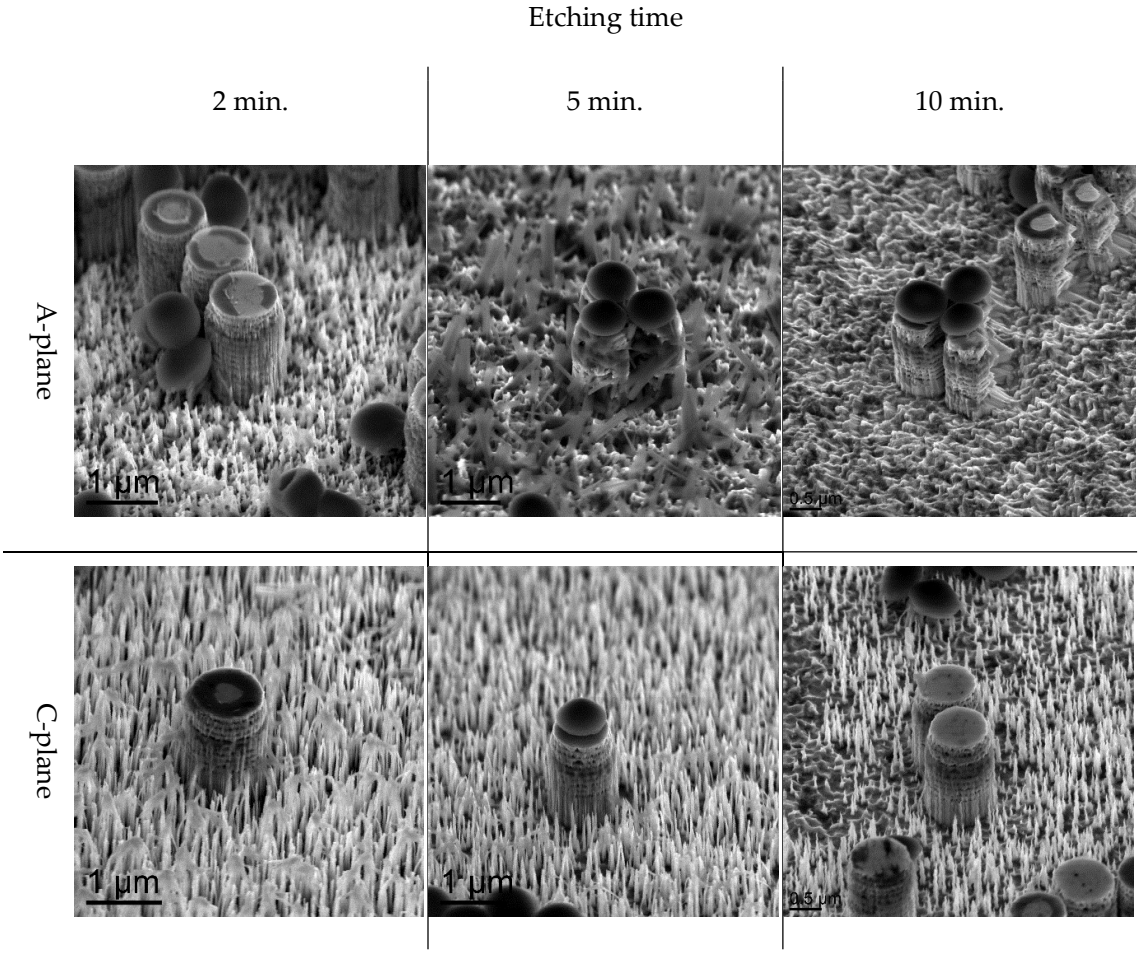

Figure 118: Results of wet-etching a-plane and c-plane porous micropillars in a solution of 10% KOH in ethylene glycol at 70°C.

The pillars and surface are etched much more quickly and aggressively than reported in Debnath *et al.* [95], even for the same concentration and similar temperature. The etch is sensitive to the polarity and orientation of the exposed crystal surface; exposure of different facets of the crystal in surface pores may therefore allow the etch to proceed more quickly and with lower uniformity across the height of the pillar.

5.5 Photoluminescence

Several processed samples were examined by micro-photoluminescence at the University of Oxford. A simplified schematic of the set-up is given in Figure 119.

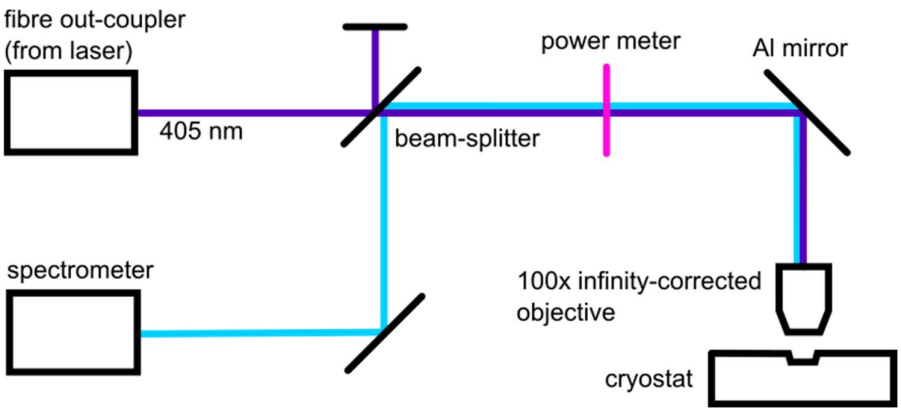

Figure 119: Schematic of photoluminescence set-up used for measurements on optical devices.

A Nd:YVO_4 diode-pumped CW laser (Verdi V8) was used to pump a Ti:Sapphire oscillator (Spectra-Physics Tsunami), generating femtosecond pulses with a repetition rate of around 82 MHz at 810 nm. This was then frequency doubled using a barium borate crystal (Inrad Optics) to generate the blue PL excitation signal at 405 nm, which was fibre coupled to the measurement system. A red excitation signal at 810 nm can also be generated by omitting the frequency doubling step, and is used for two-photon excitation. Picosecond pulses can also be used, and are generated by a different Ti:sapphire laser (Coherent Mira 900).

The excitation signal is then transmitted through a beam splitter, aluminium mirror and 100x infinity-corrected objective to the sample surface. The photoluminescence signal is collected by the same objective, before being transmitted to a spectrometer. 300 and 1200 lines per millimetre (lpmm) diffraction gratings are available, with the latter giving approximately 0.04 nm resolution in the particular configuration used. Light is focused from the diffraction grating on to a cooled CCD using a lens with a focal length of 300 mm.

5.5.1 C-plane lasers

5.5.1.1 Sample design

Two wafers were grown with a 10-pair bottom DBR, a half-wavelength cavity containing quantum wells, and a 3-pair top DBR. One wafer contained 3 QWs (sample number: C6729A), while the other contained 10 QWs (C6831A). C6729A was patterned with sphere lithography only, while C6831A was patterned with electron-beam lithography.

5.5.1.2 Sphere lithography

C-plane wafers containing 10 QWs embedded in a cavity formed between a 10-pair bottom NP-DBR and a 3-pair top NP-DBR were porosified by electrochemical etching, followed by patterning using the sphere lithography method. A SEM image of one of these pillars (prior to sphere removal), together with a STEM image of the porous layers before processing, is shown in Figure 126.

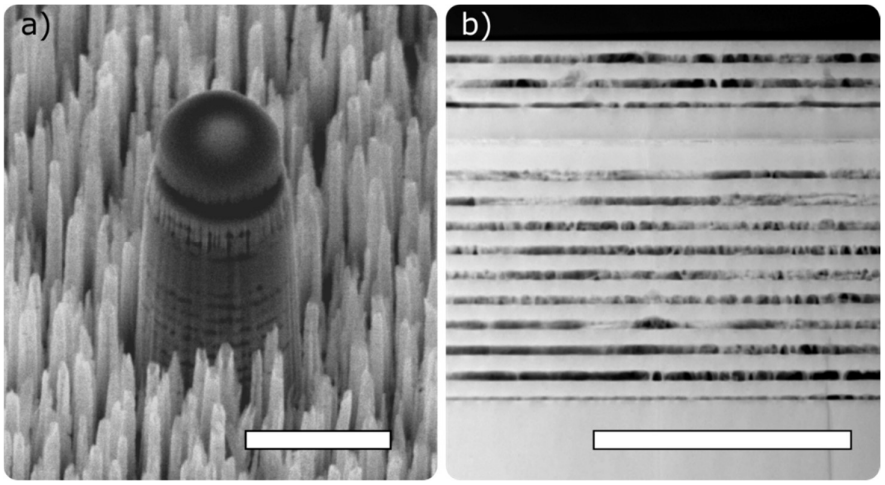

Figure 120: Left: SEM image of an etched porous pillar. Right: STEM image of the porous layers before processing. Bar: 1 μ m in both panels.

These samples were then examined by Dr Tim Puchtler (University of Oxford) using the photoluminescence system with 410 nm excitation. A pulse picker was used to absorb 9 out of 10 pulses, reducing the thermal load on the sample.

Spectra acquired from a micropillar at three excitation powers are shown in Figure 121, with clear peaks superimposed on the broad QW spectrum.

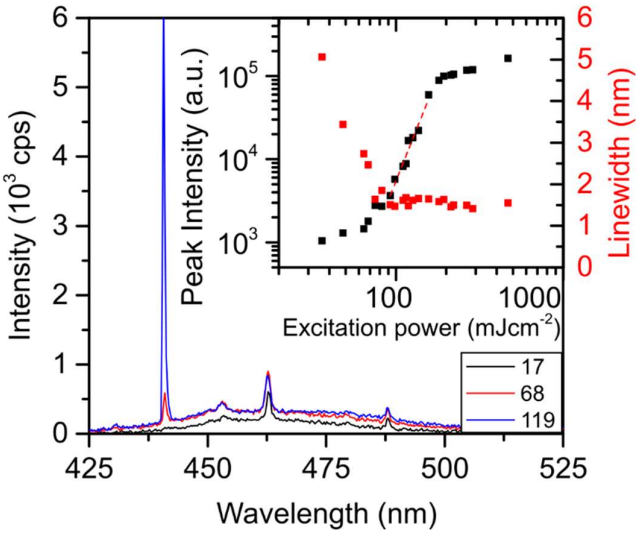

Figure 121: Power-dependent photoluminescence spectra obtained from a c-plane porous DBR micropillar containing 3 InGaN quantum wells. The linewidth narrowing and rapid increase in intensity show that one whispering-gallery mode supports lasing in the device. The powers indicated in the legend are in kW/cm^2. Data recorded and graph produced by Tim Puchtler.

These peaks are assigned to whispering gallery modes (WGMs, as discussed in section 1.6.6.2), owing to their close and equidistant spacing, with a free spectral range (FSR) of 22 nm; the Fabry-Perot modes would be expected to have a much larger FSR. One peak undergoes a strong reduction in linewidth and increase in intensity as the power is increased, indicating lasing, with a threshold of 207 ± 1 kWcm^{-2} and gain saturation occurring at 368 ± 1 kWcm^{-2}. This is about three orders of magnitude higher than literature values for GaN microdisk lasers with a central supporting post [105].

Active layer modification

Examination of the sample by STEM and EDX revealed that the active layers were also modified by the electrochemical etching process. The STEM image shows the etching of active layers, with the indium distribution (determined by EDX) also showing fragmentation.

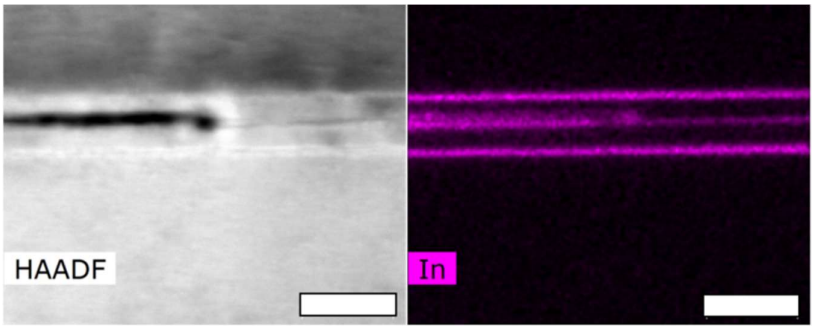

Figure 122: HAADF (left) and EDX indium signal (right) showing etching of the active layers. Data acquired and figure produced by Hiuxin Xiu. Bar: 30 nm.

Further evidence for the modification of the active layers by the electrochemical etch was found in low-temperature photoluminescence measurements, carried out under two-photon excitation at 800 nm and shown in Figure 123. This excitation method has been found to suppress the QW background, allowing for clearer spectroscopy of 3D confinement centres [40].

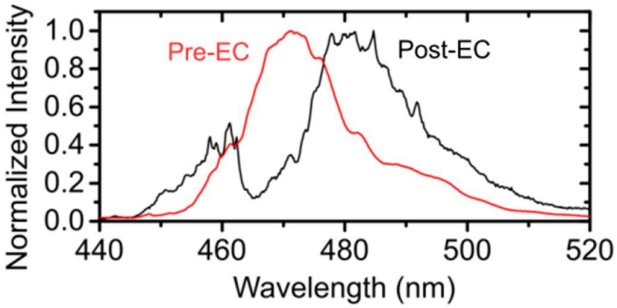

Figure 123: Photoluminescence spectra of planar 3QW samples under two-photon excitation at 800 nm. The spectrum before electrochemical (EC) etching (red) and after (black) are compared; the spectrum is less smooth after EC etching, showing peaks that are potentially consistent with the creation of 3D confinement centres. Spectra acquired by Dr Tim Puchtler.

The spectrum becomes less smooth after electrochemical etching, with sharp QD-like features present in the post-EC-etch spectrum. This could indicate the creation of 3D confinement centres in the EC-etched active layers, which are pumped particularly efficiently by two-photon PL excitation.

Cavity modelling

The opposing distributed Bragg reflectors incorporated into the pillar design were intended to support Fabry-Perot modes along the length of the pillar. However, the large refractive

index contrast between the porous layers and the central solid GaN cavity is also high enough to support whispering gallery modes. The quality (Q) factor of these modes was found to be up to 860, with most modes around 100.

Finite-difference time-domain modelling of the cavity structure (Lumerical), carried out by Dr Tim Puchtler, shows the effect of porosity of the bounding layers (modelled as refractive index contrast between the cavity disk and the bounding layers) on the leakage and therefore cavity Q-factor. Above a porosity of about 20%, there is a sharp increase in mode confinement, with much smaller gains between about 60% and 100% porosity, with porosity over 50% (which is readily achievable by electrochemical etching) yielding a Q of around 4×10^5. This value is nearly two orders of magnitude larger than the best experimentally-measured result, suggesting that the refractive index contrast is not the limiting factor in this case.

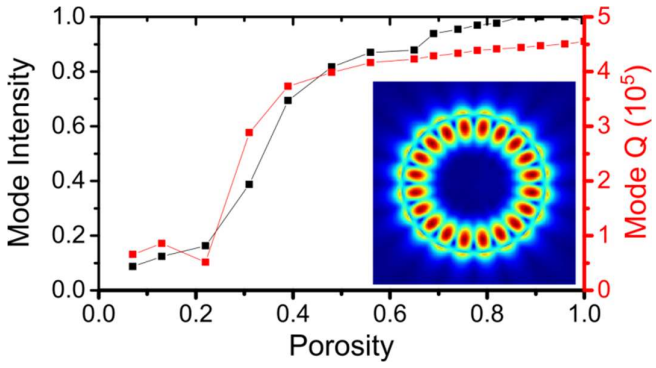

Figure 124: Finite-difference time-domain modelling of a whispering-gallery mode supported by the cavity, showing the effect on the mode's Q factor as the refractive index contrast of the bounding layers is varied (approximating the porosity). Inset: a 2D slice of the electric field distribution for this mode, taken through the middle of the cavity disk. Simulation carried out and figure produced by Dr Tim Puchtler (Oxford).

Instead, scattering at the surfaces bounding the central cavity disk will act to reduce the Q factor below the modelled maximum. This scattering will occur from the sidewalls of the pillar as well as from the imperfectly flat surface between the porous material and the solid GaN. Therefore, the cavity Q could be increased by further optimising the ICP-RIE process to limit the surface roughness on the sidewalls of the pillar, and by optimising the electrochemical etch to give the sharpest possible boundary between solid and porous GaN.

5.5.1.3 Electron-beam lithography

Some devices were constructed from the wafer C6831A, using electron-beam lithography, in both a fin-connected and isolated pillar geometry with pillar diameters of 1, 2 and 4 μm. Two sets of samples were fabricated; one was electrochemically etched before processing, and the other was etched after processing.

The samples were excited with a laser power of 2 mW (measured before the objective lens). No modes were observed in any of the samples with either the fin-connected or isolated pillar geometry, in either the samples etched before or after processing; instead, a broad Gaussian emission from the QWs was observed as shown in the left-hand panel of Figure 125. This can be compared with a spectrum taken from a pillar patterned by sphere lithography in the right-hand panel of Figure 125 (the same sample as examined in section 5.5.1.2, with the spectrum taken here under the same conditions as the e-beam patterned samples).

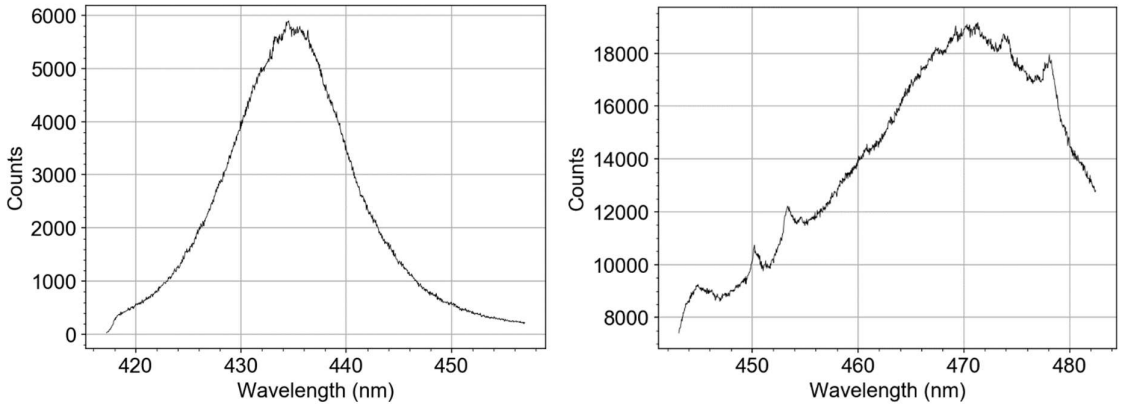

Figure 125: Left: Representative spectrum of a 4 μm diameter e-beam fin-connected pillar on C6831A, etched after processing, showing the broad QW emission. The small peaks that decorate the top of the Gaussian are an artefact of the aluminium mirror used above the objective lens, and identical peaks appear in each spectrum as a result. Right: Spectrum from sphere lithography c-plane laser sample C6729A (examined in section 5.5.1.2). Both samples were examined under the same conditions.

The lack of WGMs on any of the pillars indicates substantially higher scattering losses. This could be due to the rougher sidewall surfaces created by the multiple-step lithography process.

A small shift in emission wavelength was observed with varying pillar diameter. On the sample C6831A, the pillars with a larger diameter showed a longer emission wavelength

than the smaller ones, as shown in Figure 126. This is true for both fin-connected and isolated pillar structures, and for samples that were EC-etched both before and after lithographic processing.

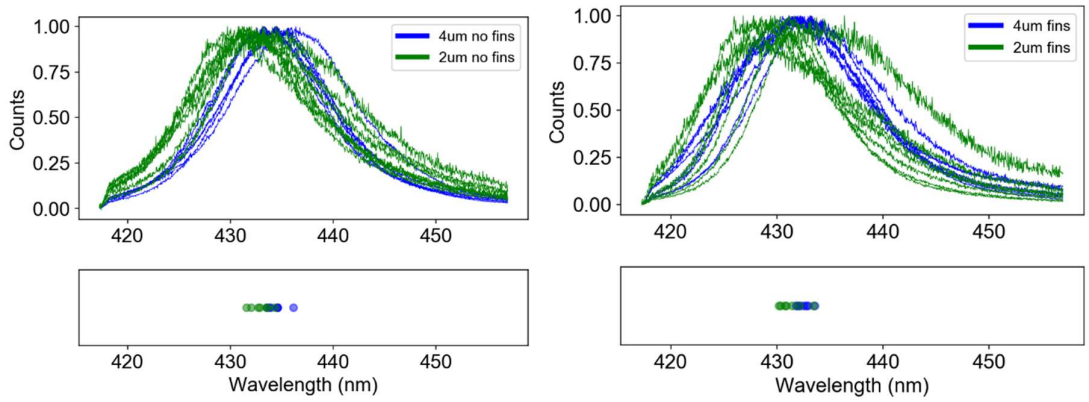

Figure 126: PL spectra from isolated (left) and fin-connected (right) pillars of two diameters (2 and 4 μm), showing a systematic blue-shift of the smaller pillars. The peak position of a Gaussian fit to the spectrum is shown in the lower panel. The intensities of each spectrum are normalised to 1.

A similar effect has been reported in the literature, where dry-etched pillars of varying diameters showed blue-shifted emission at smaller diameters [230]. The variation was assigned to strain relief in the active layers at smaller diameters. While our pillars are at least 10x larger than the ones reported in that study, it is conceivable that the effectively thinned membrane in the centre of the pillar, bounded by porous GaN, is less constrained by the surrounding material and so the strain-relief effect is visible even for larger diameters. Another explanation could be that the heat dissipation is improved in the smaller pillars, due to an increased surface area to volume ratio, leading to a smaller thermally induced red-shift in these devices under laser excitation.

5.5.2 A-plane single photon sources

A-plane samples containing InGaN QD layers were also patterned using sphere lithography.

5.5.2.1 Microsphere patterned samples (containing DBRs)

A-plane samples similar to the c-plane samples outlined above, consisting of two porous DBRs on either side of an active region, were patterned using microsphere lithography. In this case, the active region contained InGaN QDs, with the aim of investigating single photon emission. These samples were investigated in the group of Mark Holmes (Institute of

Industrial Science, The University of Tokyo), and were found to show short lifetimes of 640 ps and high purity of single photon emission ($g^{(2)}(0) < 0.05$) using an excitation wavelength selected to excite carriers in the QD but that sits below the absorption wavelength of the surrounding QW or GaN barrier [231]. The $g^{(2)}(\tau)$ measurement (using pulsed excitation at 80 MHz) is shown in Figure 127. No Purcell-type enhancement or cavity effects were seen with the porous DBR/pillar structure, although it is suggested to have improved the extraction efficiency of photons from the QD.

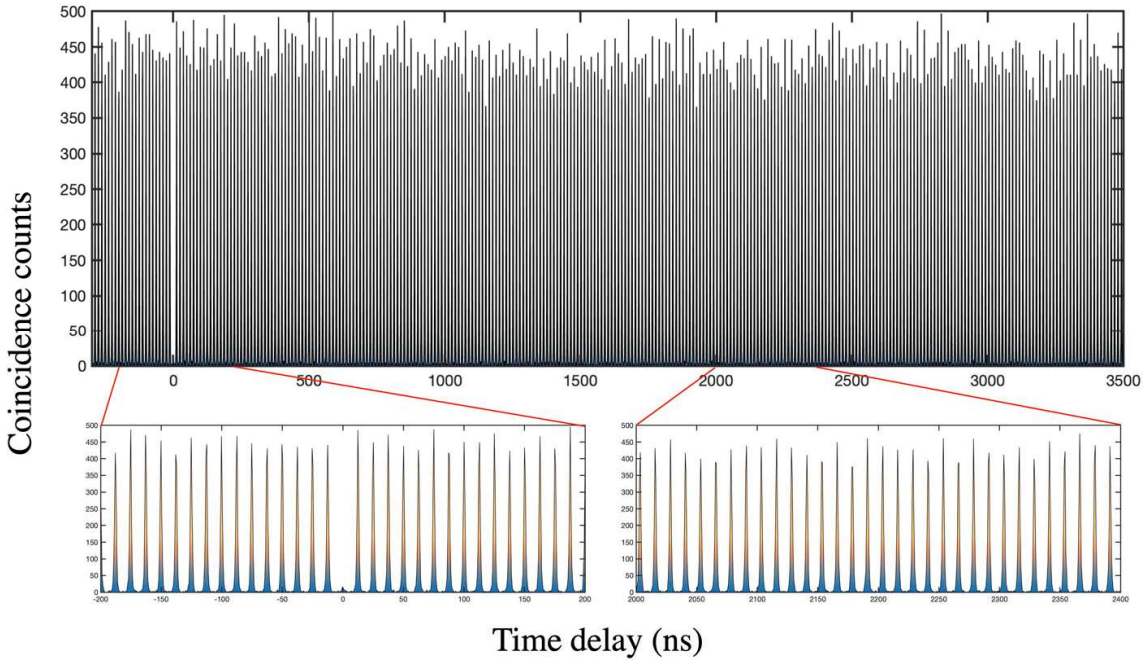

Figure 127: g2(t) measurement of a-plane QDs embedded in micropillars containing two porous DBRs. Reproduced with permission from [231].

5.5.2.2 Nanosphere patterned samples

Samples containing QDs, but not DBRs, were patterned using nanospheres to try and isolate individual QDs with the aim of reducing background QW emission and increasing extraction efficiency. 150 nm diameter silica spheres were used, and the process flow is identical for 150 nm pillars as it is for larger pillars patterned by sphere lithography, as shown in section 5.4.2.

Two-photon photoluminescence measurements were carried out on an MDE sample patterned using this technique by Tong Wang and Tim Puchtler at the University of Oxford, to examine the emission spectrum of the QD-containing samples and to measure

autocorrelation in photon emission times. These measurements were done at liquid helium temperatures (4 K) and at elevated temperatures (up to 220 K), with a reduction in emission intensity due to enhanced carrier escape, and an increase in linewidth, as can be seen in the spectra taken as a function of temperature in Figure 128. The patterned wafers show evidence of single-photon emission at both 4.2 K and 220 K, as can be seen in Figure 129, and the emission also remains highly polarised as the temperature is increased.

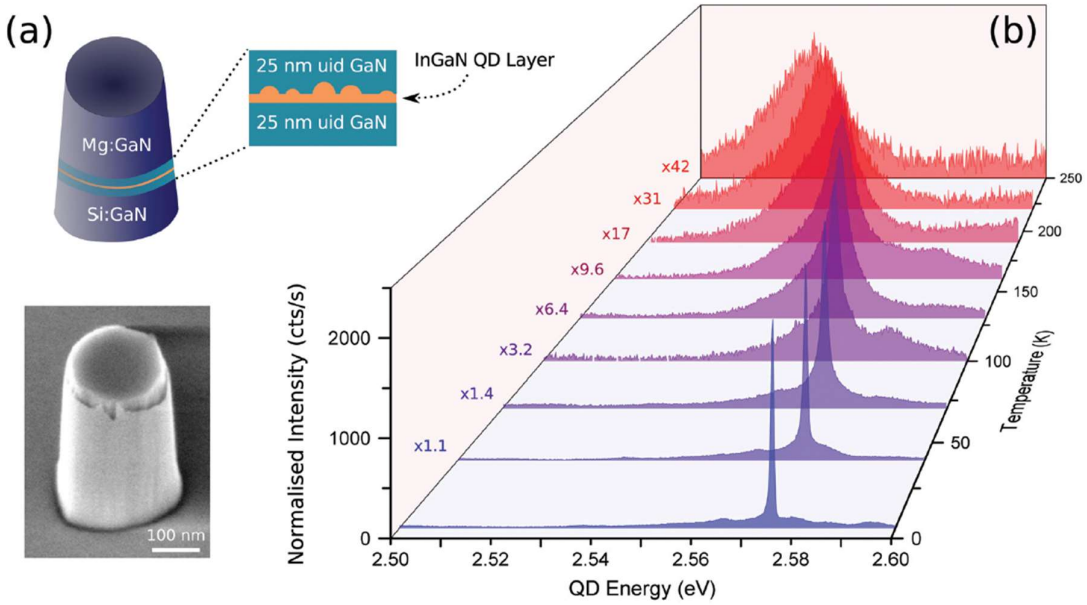

Figure 128: a) schematic and SEM image of nanopillar. b) Two-photon PL spectra taken at a range of temperatures, showing decreased intensity (normalisation factors given by each spectrum) and increased linewidth. Figure reproduced from [232], under a CC-BY licence.

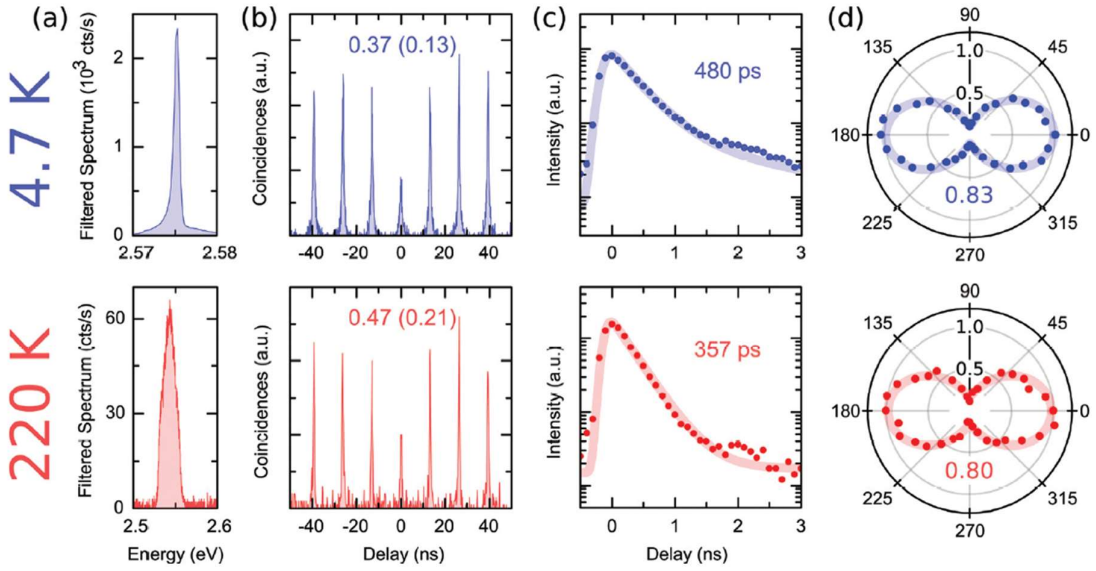

Figure 129: a) Band-pass filtered two-photon PL spectrum; b) raw photon correlation data, showing reduced coincidence counts at zero time delay, indicating single-photon emission; c) lifetime and d) polarisation measurements. Data from the same QD at low temperature (4.7 K) is shown in blue, and high-temperature measurements (220 K) are shown in red. Figure reproduced from [232], under a CC-BY licence.

The high degree of polarisation arises due to the asymmetry of the c- and m-directions that lie in the a-plane surface of the GaN crystal, causing single photon emission that is highly linearly polarised and lies deterministically along the m-direction [232-234].

While the results outlined above were produced using modified droplet epitaxy (MDE) QDs, highly-polarised emission was also observed from quasi-two-temperature (Q2T) QDs at temperatures up to 200 K, which I also patterned using nanosphere lithography [62].

5.6 Summary

An initial investigation into the spatial variation of reflectivity spectra measured on non-polar porous distributed Bragg reflectors was carried out. This revealed a dependence between the porosity developed in the DBR and the observed wavelength of peak reflectivity, with less complete etches tending to give red-shifted peak reflectance when compared to the fully-etched DBRs. The observed dependence was borne out by transfer-matrix modelling of porous DBRs, which reproduce a reduction in the peak reflectance, coupled with a red-shift in the wavelength at which the peak occurs, as the porosity is reduced. Further work on a-plane reflectors may resolve these issues across a full wafer.

Two routes to creating pillars in GaN wafers have been explored, using either silica spheres or electron-beam lithography together with dry etching steps to create micro- and nano-pillars. Some optimisation of the electron-beam process is presented. The electron-beam process is found to give rougher sidewalls than the sphere lithography process, but allows for deterministic placement of pillars, possibly permitting later registration to optical or electrical structures.

Pillars were then fabricated using both techniques. Using sphere lithography, the DBR was porosified before the processing, leading to roughness on the etched surfaces that could be reduced by employing a KOH etch. With e-beam lithography, samples were fabricated with the DBR porosified both before and after processing.

Optical results are presented, using above-bandgap and two-photon photoluminescence to examine the fabricated pillars. Whispering-gallery modes with Q-factors up to around 800 and lasing with a threshold of 207 ± 1 kWcm^{-2} were observed (by Dr Tim Puchtler) on a c-plane sample patterned with microsphere lithography, showing that porous GaN can be used to engineer an optical microcavity. However, electron-beam patterned samples failed to show cavity modes, suggesting that this part of the process requires further development.

Results (collected by Tong Wang) for nanopillars patterned on non-polar quantum-dot samples also show the performance of InGaN QDs, demonstrating high-temperature operation and highly-polarised single photon emission. Recent results collected in the group of Mark Holmes [235] also show that, with appropriate excitation conditions, the QDs can achieve very pure single photon emission. This suggests that the dry-etching processes are compatible with QD emission in this system, and suggesting that further development of optical cavities incorporating self-assembled InGaN QDs could be a good route to achieving higher-performance single photon sources than are currently available.

Chapter 6

6Quantum dots in electrical devices

Semiconductor QDs can be integrated into doped structures such as p-i-n diodes, allowing for electrical injection of charge carriers. This removes the requirement for the lasers and optics associated with optical excitation, which is desirable in a practical on-chip single-photon source. This chapter explores electrical carrier injection into a-plane InGaN QDs, and investigates several contact geometries for applying electric fields to QDs in three dimensions.

6.1 Introduction

In Chapter 4, device processing of light-emitting diodes containing quantum wells (QWs) was discussed, providing a process for efficient electrical pumping into InGaN nanostructures. Replacing the QW with a layer of quantum dots (QDs) embedded in the intrinsic layer of a p-i-n diode, in a similar approach to that followed by Jarjour *et al.* [43] or Deshpande *et al.* [45] (using c-plane InGaN QDs), may allow electrical injection into the a-plane QDs examined in Chapter 3.

Electrical contacts to quantum-dot-containing wafers may also be used to examine the change in the photon emission spectrum as an externally applied field is varied, providing a way to investigate the spontaneous and piezoelectric fields that may exist in the vicinity of a QD. Reverse- and forward-biased LEDs can be used to investigate the fields that exist in the

growth direction , while electrodes deposited on the surface of the crystal can be used to probe the response to lateral fields [236].

6.2 Aims

This chapter reports on work that aims to develop processes for two kinds of devices: p-i-n LEDs containing a-plane QD layers for the study of the electroluminescence (EL) produced by the QDs, and suitable for operation at low temperatures; and lateral contact structures, designed so that electric fields can be applied across the QDs while their photoluminescence (PL) spectrum is studied. The devices were processed and initially tested in Cambridge, and the optical measurements were carried out in Oxford by Claudius Kocher (as attributed, where appropriate, in the rest of the chapter).

The p-i-n LEDs will be reported in section 6.3, and the lateral-contact structures in section 6.4.

6.3 Quantum dot LEDs

In principle, electrical injection into the QD layers can be achieved using the design of LED devices in Chapter 4. In practice, however, the mechanical strength of the contact to the p-type layer is not high enough to reliably withstand the cooling-down process required for low-temperature electroluminescence measurements.

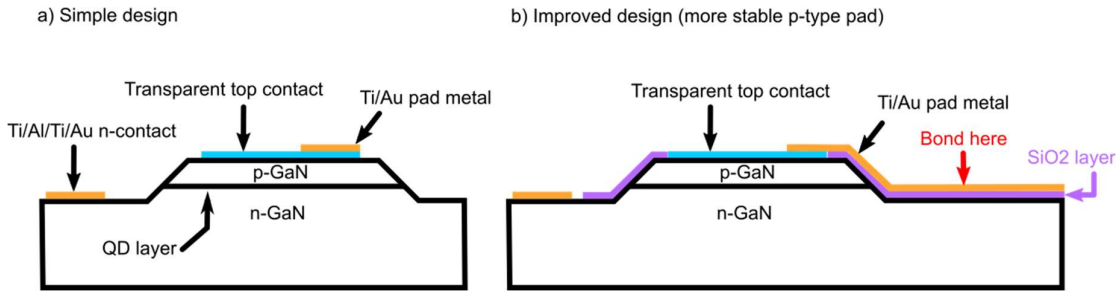

Figure 130: Schematics of QD-containing LEDs. a) Design used in Chapter 4, with low mechanical stability of the p-GaN contact pad. b) Design with improved mechanical strength due to SiO2 layer.

Figure 130 shows a modification of the LED design that improves the mechanical strength of the p-GaN contact pad. A SiO_2 layer is deposited over the etched mesa, and apertures are etched in the oxide film to allow deposition of the transparent conducting p-contact and n-contact. This leaves an oxide coating on the mesa sidewalls and on most of the etched

surface, allowing the Ti/Au contact pad to be extended away from the fragile transparent contact. In this design, the bond to connect the p-type layer is then made on the oxide layer above the etched surface adjacent to the mesa.

This design is similar to that used by Yuan *et al.* [237] in the creation of an electrically-pumped InAs single-photon source. The device reported in [237] additionally includes an opaque metal layer on the top surface of the device mesa, with apertures etched to isolate emission from individual dots. In the Oxford measurement set-up, the collection area is already relatively small, on the order of 1 μm^2, which makes such aperture arrays unnecessary. However, a practical single-photon source could use such apertures to ensure pure emission from a single QD while reducing the complexity of the required optical system.

6.3.1 SiO_2 deposition and etch

After the ICP mesa etch, SiO_2 films of 200 nm thickness were deposited using PECVD by Melanie Tribble in the Cavendish laboratory. SiO_2 was selected because it is more readily wet-etched than silicon nitride, and buffered hydrofluoric acid was used to pattern the oxide layer. To avoid possible damage to the metal contacts on contact with the etching solution, the SiO_2 was deposited and patterned before contacts were defined. Given the relatively high temperature of the n-metal anneal, the potential exists to modify the film properties through hydrogen desorption, Si-N bond formation and Si-O bond rearrangement during the metal anneal [238], potentially inducing tensile stress. However, no obvious damage to the film was seen, indicating that this is not a problem in this case.

Shipley s1813 was used to pattern the oxide layer, using hexamethyldisilazane as a pre-treatment to improve resist adhesion. Buffered hydrofluoric acid was then used to etch the required apertures in the oxide film. An etch rate of approximately 240 nm min^{-1} was observed, and so an etching time of 1 min was used to pattern the 200 nm SiO_2 film. This provides a slight over-etch, ensuring that the oxide is completely cleared, while lateral undercut etching of the oxide under the photoresist is limited to an acceptable amount.

6.3.2 Contact deposition and annealing

The same contact scheme used for the LEDs in Chapter 4 was used to contact the n- and p-GaN, with a Ti/Al/Ti/Au stack with layer thicknesses of 15/50/30/80 nm annealed at 710°C for 2 min in a flow of 6 slpm N_2 as the n-contact. The transparent p-contact was a Ni/Au stack of 4.5/4.5 nm thickness, annealed for 5 min in a mixture of 2 slpm O_2 and 5 slpm N_2 at 470°C. The pad metal was a stack of Ti/Au, with thickness 20/80 nm.

6.3.3 Bonding

First trial devices were bonded to a gold-plated printed circuit board (PCB) using a ball bonder (Kulicke & Soffa) and gold wire. It was initially found that there was poor adhesion between the bond and the annealed n-contact surface for all reasonable bonder settings. To solve this problem, an extra Ti/Au pad was evaporated on top of the n-metal, providing a pristine Au surface that offered more reliable bonding.

Final devices were bonded using a wedge bonder and gold wire at the University of Oxford to avoid damage to the bond wires during transport. A gold-plated PCB of suitable size for the cryostat was used to make the electrical connections to the sample, with the sample itself stuck to a metal plate with silver paint for good thermal contact with the cryo-cooler.

6.3.4 Device characterisation

LEDs were fabricated from a-plane samples containing Q2T QD layers in a p-i-n diode stack. While the devices functioned (an illuminated example of an a-plane, two-temperature QD sample is shown in Figure 131), many of these diodes showed a high leakage current. I-V characteristics from LEDs with high and low leakage are presented in Figure 131, with both measured devices on the same processed wafer.

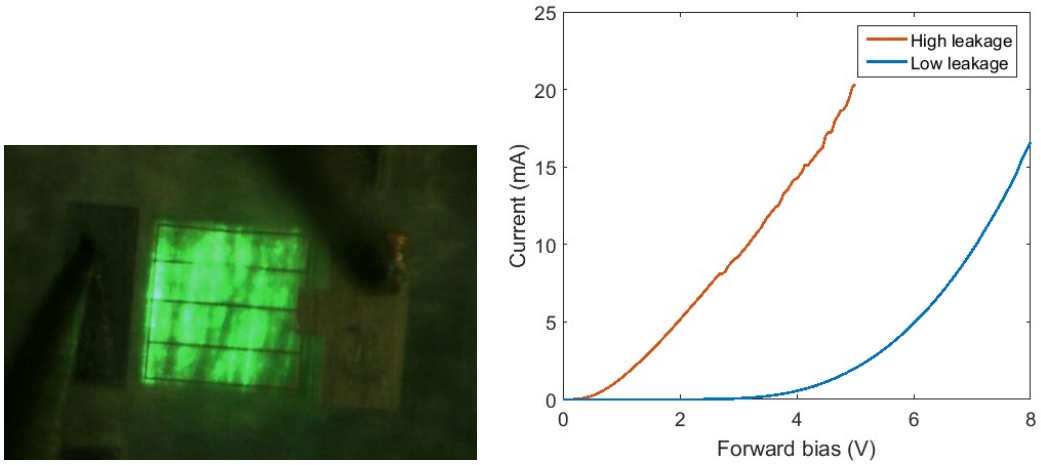

Figure 131: Left: Illuminated a-plane Q2T quantum-dot LED. Mesa size = 400 μm. Right: I-V characteristics for LEDs showing high and low leakage on the same wafer.

The I-V characteristics for all devices on a processed chip were measured, and around 92% of them were found to show highly leaky I-V characteristics, passing more than 1 mA of current at a forward voltage of 2 V.

LEDs were also fabricated from a c-plane 5 quantum well heterostructure embedded in a p-i-n diode. This wafer showed a much lower failure rate of 57%, suggesting that a difference between the epitaxy of the c- and a-plane wafers contributes to the failure of the a-plane devices.

6.3.5 Origin of leakage

Unprocessed a-plane wafers were examined using AFM. A large number of deep pits in the surface were discovered, which could be deep enough to cause shorts through the oxide layer. The pits also appear to be deepened by the ICP etching. AFM images and the extracted line profiles are shown in Figure 132. The facetted morphology of the pit can be seen more clearly in Figure 133.

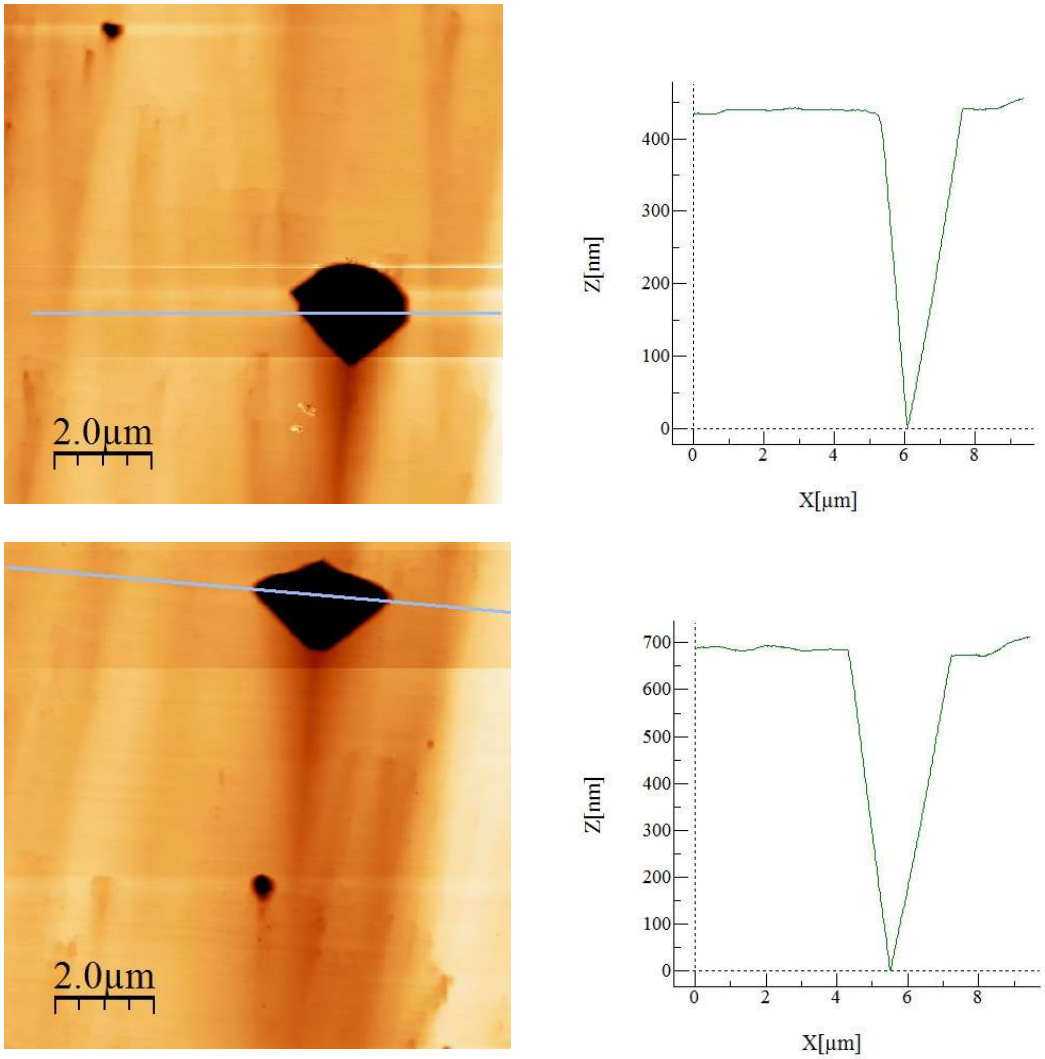

Figure 132: AFM images and line profiles from the unetched (top) and etched (bottom) regions of an LED sample.

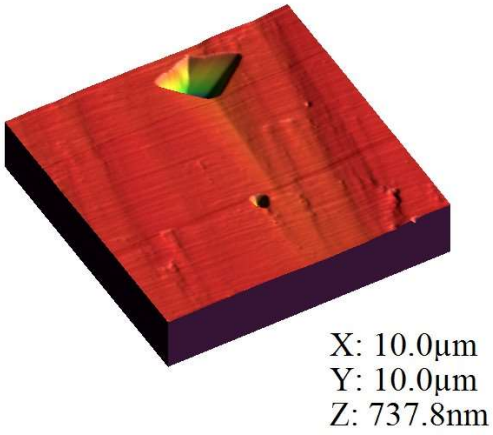

Figure 133: AFM image of a pit in the etched surface, showing the facetted morphology.

Analysis of the line profiles gives sidewall angles of around 30° from the horizontal. As the AFM tip has a front-side angle of 15° from the vertical, and is 15-20 µm long, these features are likely to have been accurately resolved by the AFM.

SEM investigation provided further evidence that the pits might be the root cause of the leakage; the oxide layer could be clearly seen to conformally coat the sidewall of the LED mesa, and a high density of these pits was observed on the etched surface, as can be seen in Figure 134.

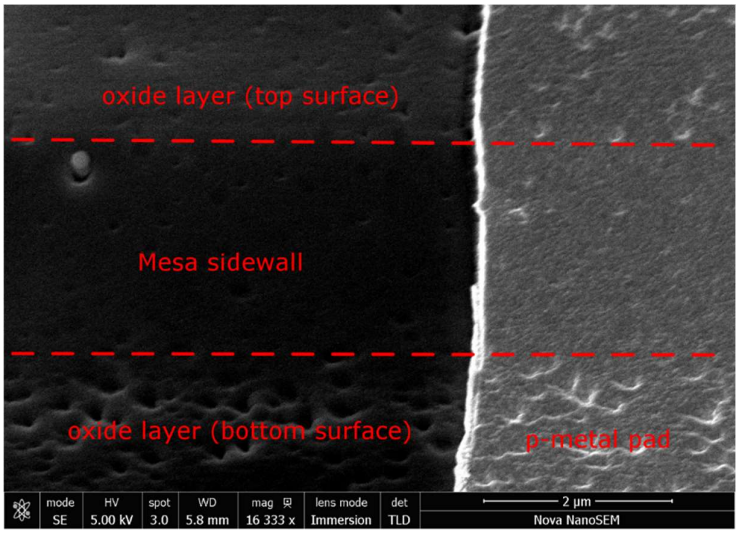

Figure 134: 45° SEM image of the sidewall of an etched mesa, showing the conformal coating of oxide on the mesa sidewall, and a high density of pits on both the etched and unetched surfaces.

Although the failure rate was high, there were enough working devices on a typical wafer to allow for bonding several mesas for further examination.

6.3.6 Low-temperature measurements

Two wafers were processed into arrays of LEDs; one containing Q2T QDs (C6379A) and the other with MDE QDs (C5965A) both embedded in a p-i-n diode.

After assaying each processed wafer to find low-leakage devices that showed some light emission under forward bias, the wafers were diced into 8 mm squares using a diamond wafer saw and sent to Oxford for bonding and low-temperature measurements.

Once the devices were bonded to a suitable PCB, they were loaded into the AttoDRY cryostat for low-temperature spectroscopy of the electroluminescence produced under forward bias. A Keithley 236 source-measure unit was used to provide the DC supply. All measurements and analysis in the following sections (6.3.6.1 and 6.3.6.2) were performed by Claudius Kocher at the University of Oxford.

6.3.6.1 Electrical behaviour

After bonding and testing in the cryostat, one device on the Q2T QD sample (C6379A) showed low leakage. The I-V characteristic of the working LED was measured at room temperature, and again at a temperature of 4.5 K. An increased forward voltage and increased series resistance is observed, which is consistent with reduced dopant ionisation and hole mobility at low temperature [239].

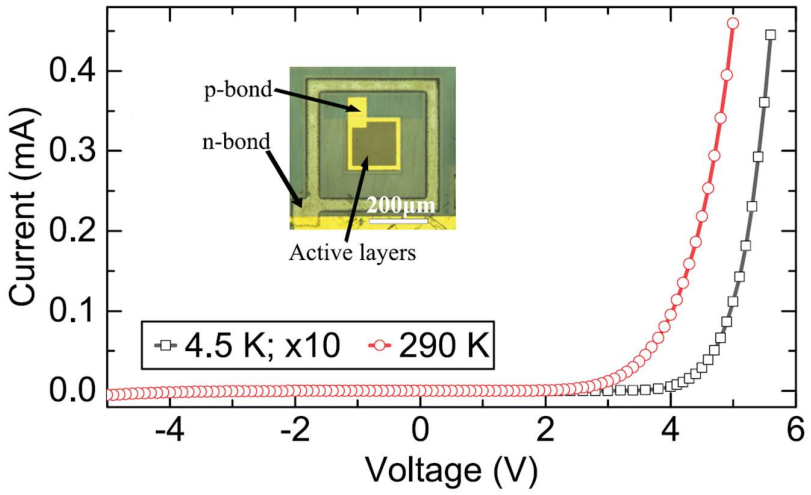

Figure 135: I-V characteristics of a bonded device at room temperature and low temperature. An increased forward voltage and increased series resistance are observed (note 4.5 K current measurements are rescaled by 10 times). Inset: optical micrograph of processed device, before bonding. I-V measured and graph produced by Claudius Kocher, reproduced with permission from [240].

6.3.6.2 Electroluminescence

The Q2T sample showed electroluminescence (EL) at room temperature when a voltage of above about 4 V was applied, as shown in the camera image in Figure 136. There is clear non-uniformity in the emission pattern, with bright spots visible on the emitting area on the device mesa.

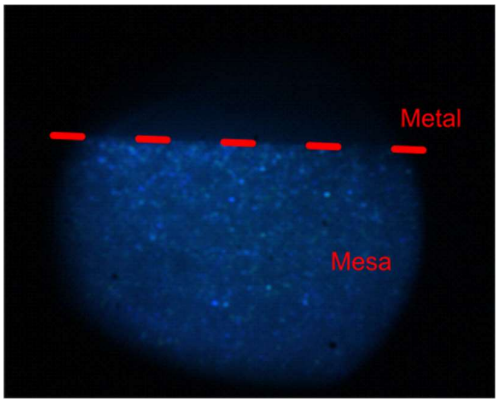

Figure 136: Microscope image showing electroluminescence from the examined device at room temperature. Acquired by Claudius Kocher.

The EL spectrum at a temperature of 4.5 K consists of sharp peaks due to QDs superimposed on a broad QW-related background, as shown in Figure 137. An optical band-pass filter can

be used to isolate a single peak, helping to increase the signal from a single dot compared to the noise from other QDs and the surrounding QW.

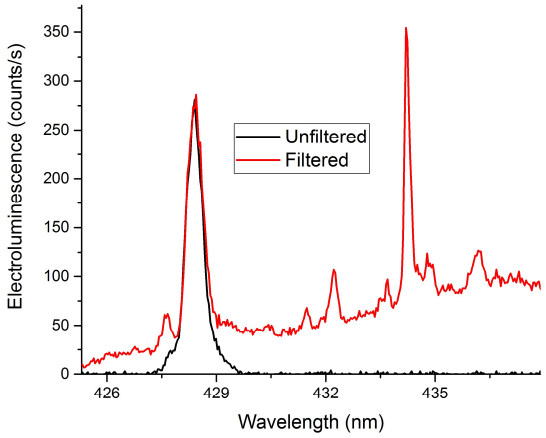

Figure 137: Example of an EL spectrum taken at low temperature (~5 K) from the device, showing sharp peaks superimposed on a broad quantum-well background. Spectral filtering can be used to isolate a single peak for further investigation. Acquired and graph produced by Claudius Kocher.

The monochromated QD emission can be passed to a beam-splitter, that creates two paths of equal length to two photomultiplier tubes (PMTs, Hamamatsu H10720). The signals from these PMTs are then passed to a time-correlated single-photon counting device (Picoquant TimeHarp 260), which can record the time of each detection event with a resolution of 25 ps.

This set-up was used to measure the photon correlation between the two detectors, in a Hanbury Brown and Twiss (HBT) experiment. Coincidence counts, i.e. photon pairs arriving at both detectors at similar times, were recorded together with the time delay between the arrival of the two photons. If the device under test is emitting a stream of single photons, there should be a significant reduction in the number of photon pairs recorded with zero time delay compared to greater delays.

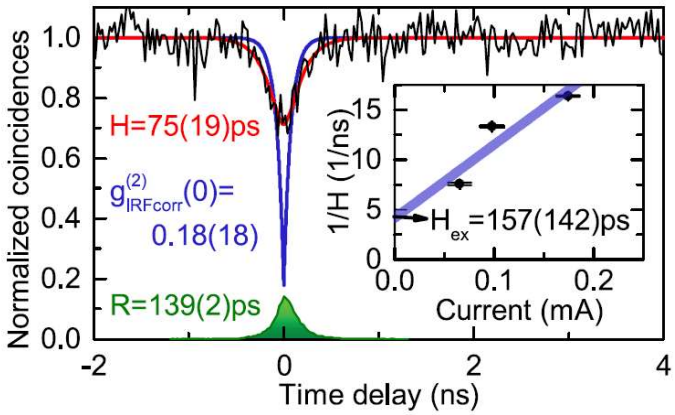

Figure 138: Coincidence counts (black) from the two PMTs, showing a reduction in the number of counts that occur with zero time delay, indicating single photon emission. The blue trace has been corrected for the slow response of the PMTs compared to the rate of photon emission; the instrument response function (IRF) of the PMTs, which was used for the correction, is shown in green. Inset: Radiative lifetime estimation based on parameters extracted from fits to $g^{(2)}(\tau)$ measurements at varying current, with the extrapolation to 0 excitation current approximating the lifetime of the radiative process that emits the detected photons. Measurements, fitting, correction and graph production by Claudius Kocher. Figure reproduced from [240], with permission.

The resulting measurement is shown in Figure 138. The black trace is a histogram showing the number of coincidence counts recorded at each value of time delay, with the time delay divided into bins 25 ps wide. There is a reduction in counts near to zero time delay, as expected for a light source that emits single photons, and this dip in counts can be modelled as a single exponential decay [241]:

$$g^{(2)}(\tau) = 1 - A \exp\left(-\frac{|\tau|}{H}\right)$$

Equation 11

where the second-order photon autocorrelation function $g^{(2)}(\tau)$ is the quantity measured by the HBT experiment, where τ is the time delay and H is a characteristic decay time.

The value of H is related to the lifetime of the process giving rise to spontaneous photon emission, since (if the QD is an ideal two-level system) a photon emitted at $t = 0$ will leave the QD in the ground state at $t = 0$ as well, meaning that a time delay related to the spontaneous emission lifetime will be observed before the next photon is emitted [241].

If it is assumed that the excited state which produces the single photons is filled by means of fast incoherent relaxation from a higher excited state filled by the electrical injection of carriers to the QD, the relationship between H and the actual radiative lifetime is given by [241]:

$$H = \frac{1}{\Gamma + W_p}$$

Equation 12

where Γ is the rate of the radiative recombination and W_p is the pump rate into the higher excited state.

Instrument response correction

The photomultiplier tubes used to measure the $g^{(2)}(\tau)$ function have a finite response time, as shown in green on Figure 138. This is a similar order of magnitude to the radiative lifetime found for a-plane QDs in photoluminescence studies [59], and it will, therefore, significantly affect the HBT measurement by both broadening the $g^{(2)}(0)$ dip and increasing the measured value of $g^{(2)}(0)$. In the absence of faster detectors it becomes necessary to correct for this effect.

The response of the PMTs was measured using a pulsed femtosecond laser and fitted with a mono-exponential decay of the form

$$IRF(\tau) = B\exp\left(\frac{-|\tau|}{R}\right)$$

Equation 13

where R is the decay term that corresponds to the response time of the detector. The measured IRF is shown in green on Figure 138, and can be fitted with Equation 13 to give $R = 139(2)$ ps. The measured $g^{(2)}(\tau)$ is then the convolution of this instrument response function (IRF) and the actual $g^{(2)}(\tau)$. Deconvolution yields a corrected $g^{(2)}(\tau)$, which is shown in blue on Figure 138. The corrected $g^{(2)}(0) = 0.18(0.18)$, which shows a reduction in the likelihood of multi-photon emission of over 5 times compared to a classical coherent and monochromatic light source.

A large proportion of the remaining counts at $g^{(2)}(0)$ are then likely to come from the spectrally overlapping background emission from the QW surrounding the QD.

Lifetime estimation

Equation 12 expresses the relationship between spontaneous emission rate, Γ, and the observed decay time on the $g^{(2)}(\tau)$ plot, allowing for an estimation of the lifetime of the state responsible for the radiative transition in the QD. The decay time also depends on the pump rate W_p. To extract the value of Γ, therefore, a plot of $\frac{1}{H}$ against injection current (which is assumed to be proportional to W_p) is produced, shown inset in Figure 138, and the extrapolation to zero current (zero W_p) gives a radiative lifetime $1/\Gamma$ of 157(142) ps. This is on the same order of magnitude to other values measured with time-resolved photoluminescence on a-plane QDs, which range from 538ps for MDE QDs at 4.2 K [57], 533 ps for Q2T QDs at 4.2 K [59] to 357 ps for MDE dots at 220 K [232]. The large uncertainty is due to finite bin width in the photon-timing module and uncertainties in correcting for the instrument response function [240].

Polarisation

The QD emission was also found to be highly polarised, in common with other measurements on a-plane QDs [232, 233, 242]. The polarisation measurement, acquired by rotating a linear polarising filter and acquiring spectra every 10°, is shown inset in Figure 139 on a polar plot, where the radial coordinate is the measured intensity and the angular coordinate is the position of the polarising filter. This plot shows the highest intensity for polariser angles of 0° and 180°, where the polariser is aligned with the crystallographic m-direction, and intensity minima at 90° and 270°, where the polariser is aligned with the c-direction. A high degree of linear polarisation (DOLP) is found, with a value of $\mathrm{DOLP} = \frac{I_{max}-I_{min}}{I_{max}+I_{min}} = 0.94(1)$, where I_{max} and I_{min} are the maximum and minimum intensities respectively.

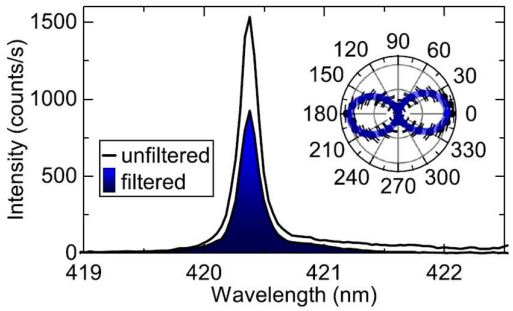

Figure 139: Filtered spectrum of the studied QD, together with a measurement of its polarisation (inset) showing a high degree of linear polarisation perpendicular to the crystallographic c-axis of the sample. Data acquired and figure produced by Claudius Kocher.

6.4 Lateral electric fields

Planar contacts were explored for applying electric fields in the growth plane. On the $(11\bar{2}0)$ growth plane (the a-plane), there are two principal crystallographic directions, which are the [0001] c-direction and the $[1\bar{1}00]$ m-direction. A spontaneous polarisation is expected to exist along the c-direction, as well as a possible piezoelectric polarisation arising from any strain in this direction. From this picture of the internal fields, it could be expected that applying an external field along the non-polar m-direction would cause symmetric red-shifts in the peak emission wavelength for both positive and negative applied field, while applying a field along the polar c-direction would either reinforce or counteract the internal field, leading to red- or blue-shifted emission respectively, depending on the direction of the applied field.

The lateral contacts were therefore designed to facilitate the application of fields along these two directions. Two geometries were used: one design with four separate contacts that come together at a point, designed to allow fields to be applied in an arbitrary direction to an individual QD by varying the voltage on each contact; and another design with a pair of L-shaped contacts separated by a small gap, allowing larger numbers of QDs to be examined per device with the field aligned along either m- or c-axis. The two designs are shown in Figure 140.

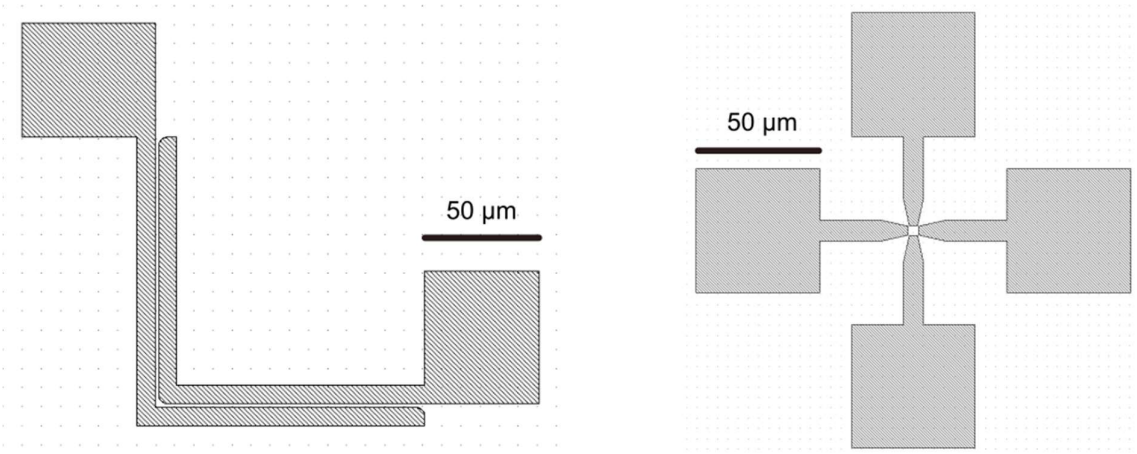

Figure 140: E-beam lithography patterns for L-shaped contacts (left) and cross-type contacts (right).

6.4.1 Samples

Contacts were patterned on three samples, listed below in Table 4. In addition to the epitaxial layers specified in the table, all the samples were grown on a stack consisting of 1.2 µm undoped GaN, 2 µm n-doped GaN and 2 µm of unintentionally doped template layer on sapphire.

Sample number	Description
C5636A	20 nm undoped GaN cap, MDE QD layer, a-plane
C5714F	20 nm undoped GaN cap, Q2T QD layer, a-plane
C5906F	20 nm undoped GaN cap, MDE QD layer, a-plane
C5910F	20 nm undoped GaN cap, Q2T QD layer, a-plane

Table 4: Sample numbers and description of samples used in lateral electric field experiments.

6.4.2 Process development

Previous work on lateral fields applied to InGaN QDs used aluminium contacts patterned using electron-beam lithography and $SiCl_4$ reactive-ion etching [236, 243]. To remove the requirement for reactive ion etching, I developed a lift-off process for patterning contacts.

A lift-off process has some practical advantages for R&D compared to dry etching, as it allows patterning of any combination of metals, unlike etching which generally needs a change in chemistry for different metals. However, its resolution is additionally limited by the grain size of the deposited metal and the thickness of the resist.

As the metal layers were intended for bonding, a top capping layer of Au was desirable, and this layer needed to have sufficient thickness for the bonding process (50 – 100 nm). To achieve clean lift-off with this thickness of metal, I decided to try using a resist bilayer, which uses a low-sensitivity resist on top of a high-sensitivity resist to provide an undercut profile as shown schematically in Figure 141.

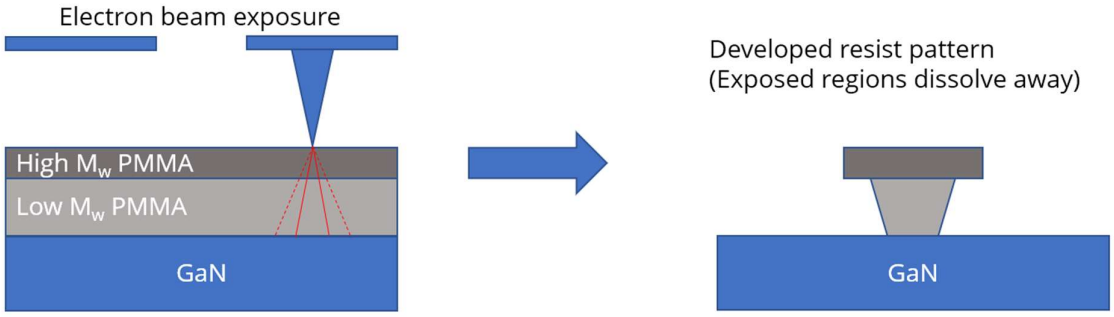

Figure 141: Schematic of intended effect of the PMMA bilayer. The top layer is less sensitive to the electron beam, so the dose contour indicated by the solid red line is required for full removal of this layer. The bottom layer is more sensitive, and so all the resist up to the dose contour indicated by the dotted red line is developed away. This leaves the desired undercut profile.

The two resist layers were both PMMA solutions, with different peak molecular weight. The high-sensitivity layer had a peak molecular weight of 4.5×10^5 g mol^{-1} (referred to in shorthand as '450k') while the low sensitivity layer had a peak molecular weight of 9.5×10^5 g mol^{-1} ('950k'). The shorter chains in the 450k polymer reduce the dose to clear by reducing the number of chain scission events needed to make the polymer soluble in the developer [244]. As shown in Figure 141, this should lead to an undercut profile of the developed resist that is suitable for metal lift-off that leaves well-defined edges and is able to tolerate the relatively large thickness of metal required.

Both resists were dissolved in anisole. The high-sensitivity layer was 4% PMMA (450k A4), while the low-sensitivity layer was 2% PMMA (950K A2). The spin curves provided by the manufacturer were consulted to select spin speeds that give a 200 nm layer of each resist, and the wafer was baked at 200°C for 2 min after each layer was spun on the sample. The thickness of the top layer was deliberately larger than required to try and compensate for the intermixing that will occur when the second layer of resist is spun on top of the first.

The final resist processing flow was as follows:

- Clean samples (ultrasonic clean in acetone, rinse in IPA, dry, 5 min. O_2 ash)
- Spin PMMA 450K A4 at 2000 rpm for 60 seconds
- Bake 200°C 2 min.
- Spin PMMA 950K A2 at 2000 rpm for 60 seconds
- Bake 200°C 2 min.

Once the resist had been processed, the samples were loaded into the e-beam lithography system (Crestec CABL 9000) with a cleaved edge corresponding to either the m- or c-direction tightly aligned with a fixed edge in the sample platen. This allows the structures to be aligned with these principal crystallographic directions.

Electron-beam exposure was then carried out at a beam current of 1 nA and acceleration voltage of 50 kV. A dose matrix with exposures varying between 300 and 600 $\mu C\ cm^{-1}$ in steps of 50 $C\ cm^{-1}$ was used to determine the optimum pattern definition for the resist system and process, as with the e-beam lithography in Chapter 5.

Following lithography, the patterns were developed in a 3:1 mixture of isopropyl alcohol (IPA) and methyl isobutyl ketone (MIBK) for 30 seconds, followed by a 30 second rinse in IPA and blow dry with nitrogen.

At this stage, a test sample was sputtered with ~5 nm Au and examined by SEM (Figure 142). Although the quality of the SEM is not perfect due to stage vibrations and an unevenly cleaved wafer, it appears that there is an undercut on the resist as intended.

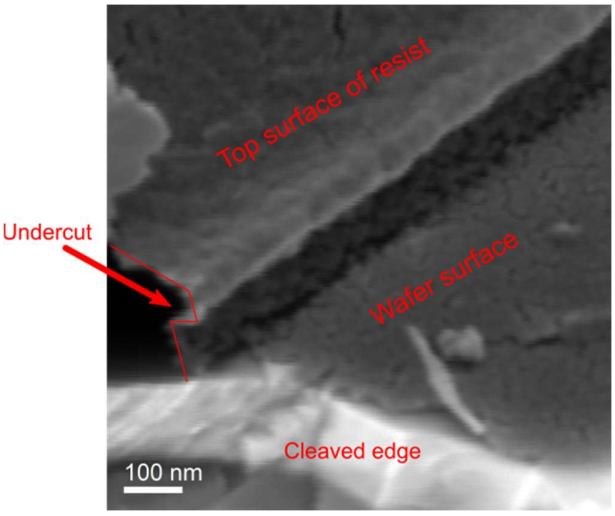

Figure 142: SEM image of e-beam resist after development. Sputtered with approx. 5 nm Au.

The rest of the samples were exposed to oxygen plasma for 10 seconds to help ensure the developed surface is free of resist residues. Thermal evaporation was then used to deposit 10 nm Ti and 50 nm Au, at 1 and 2 $Å s^{-1}$ respectively using an Edwards Auto 306 turbo-pumped bell-jar evaporator. The chips were then immersed in acetone overnight to dissolve the resist, before a short (<1 min) ultrasonic clean in acetone to remove any residual flakes. The resulting pattern was then imaged by SEM, and one feature is shown in Figure 143.

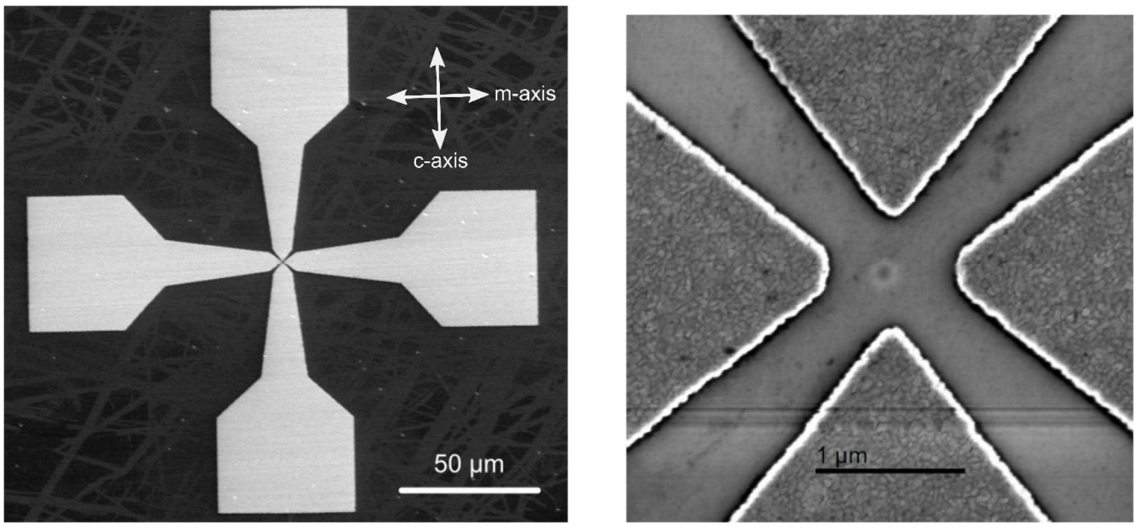

Figure 143: Cross-type lateral contacts, designed to apply lateral fields in both m- and c-direction to a single region of semiconductor. Left: overview; right: detail of the central region of the cross.

L-shaped contacts were also patterned, designed to provide a long strip of material for PL examination (to increase the chances of finding a bright, stable QD) while allowing fields to

be applied in both the m- and c-direction with the same physical contacts. An example of such a device is shown in Figure 144. Devices were constructed with 2 µm, 1 µm and 500 nm gaps between the contacts.

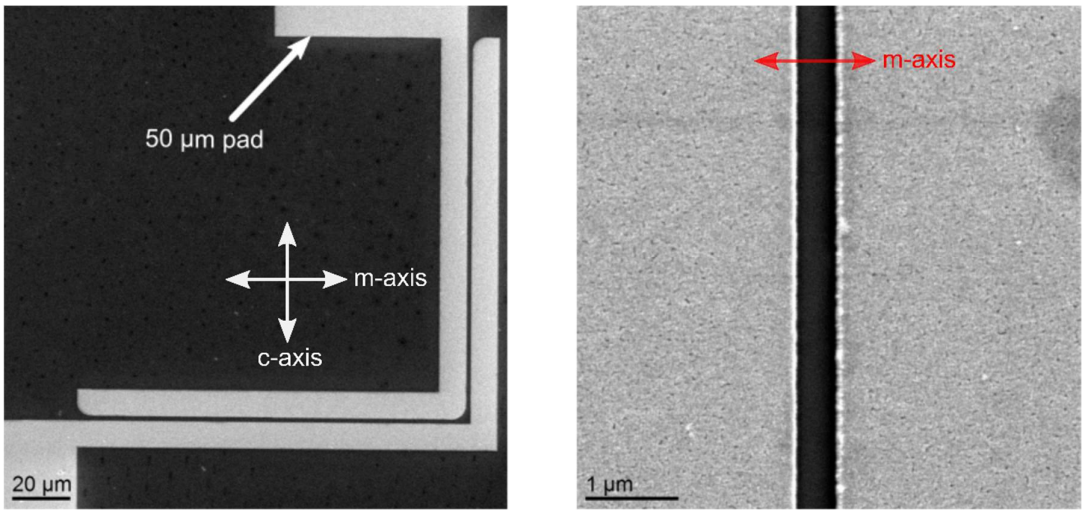

Figure 144: L-shaped contacts for applying fields to long strips of material, increasing the likelihood of finding a suitable QD. Left: Overview of a contact pair with 2 µm gap. Right: Detail of a 500 nm gap.

The close proximity of the large pads to the narrow gap caused problems due to the proximity effect; it was found that the contact metal gap did not open properly in these regions, shorting the device, due to the larger overall e-beam dose in these regions. To avoid this issue, I rounded off the corners and added extra separation between the 50 µm pad and the narrow gap. In addition, this design was more sensitive to the e-beam dose than the cross-type contacts, with only about 50 µC cm^{-1} of latitude between under-exposed (i.e. resist remaining on open regions) and over-exposed (gap between metal regions closed) when exposed with a uniform dose across the whole pattern. A more refined process could compensate for the proximity effect by varying the electron dose used on different regions of the device.

6.4.3 Surface passivation

To try and reduce any surface leakage, SiO_2 passivation was explored. The SiO_2 deposition was carried out after the contact lift-off process, following a 10 minute ash in oxygen plasma to remove any organic contamination. After the blanket deposition of SiO_2 over the entire structure, photolithography and buffered hydrofluoric acid (BHF) were used to expose the

contact pads. The resulting device is shown in a microscope image in Figure 145, taken by Claudius Kocher. This also shows the final design for the cross-type contacts, with flat ends to the contacts in order to apply a more uniform field (compared to the test structure shown in Figure 143, with pointed ends). The room-temperature I-V was also measured using the probe station, and showed linear behaviour as can be seen in Figure 145.

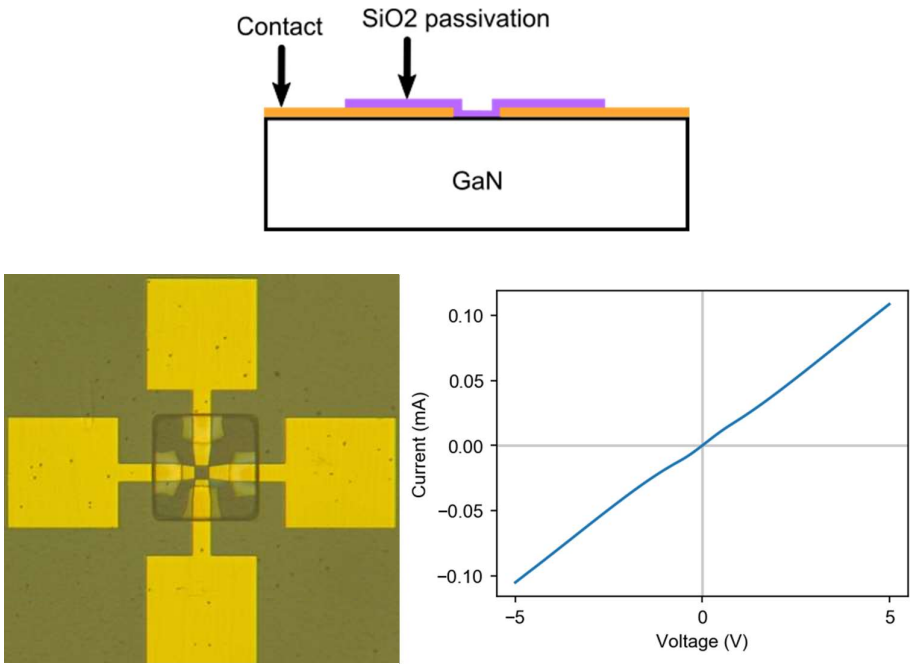

Figure 145: Top: schematic of passivation scheme. Bottom left: Microscope image of Ti/Au contacts arranged in a cross shape, with SiO2 surface passivation (central transparent square). Etching of the SiO2 is visible along the metal lines, probably due to BHF finding an easy pathway under the film at this location. Image acquired by Claudius Kocher. Bottom right: I-V characteristic of one pair of contacts, measured on the probe station at room temperature.

6.4.4 Schottky contacts

Different contact metals were explored as a means of reducing the current flow between the contacts, and therefore any heating effect that might mask the shift of the QDs due to the electric field. Nickel is a high-work-function metal (Φ = 5.04 - 5.35 eV [245]) that forms Schottky contacts to n-GaN with a barrier height of around 0.56 - 0.66 eV [246]. Platinum, palladium, gold and unannealed titanium all also form Schottky barriers when deposited on GaN, producing barrier heights of 1.04, 0.94, 0.94 and 0.58 eV respectively [246], although I found that unannealed Ti seemed to form reasonable ohmic contacts to our GaN layers as outlined in the previous section.

Ni/Au contacts were deposited by thermal evaporation, with a layer thickness of 20 nm (Ni) and 80 nm (Au). An I-V measurement (Figure 146) showed a highly non-ohmic behaviour, and current values about two orders of magnitude lower than the Ti/Au contacts at 1 V.

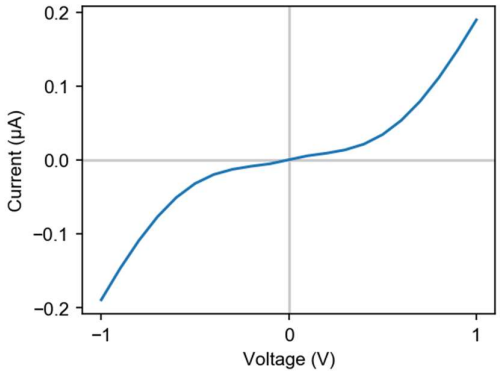

Figure 146: I-V for a Ni/Au contact pair, in the cross geometry with a 5 μm gap.

6.4.5 Room-temperature electrical measurements

Ni/Au contacts were fabricated on C5910F (Q2T dots) and on C5906F (MDE dots), and were tested at room temperature prior to bonding using the probe station to determine the max current observed during a ±1 V sweep. The devices tended to form two groups: one that showed high current and ohmic behaviour (shorted), and one group that showed the back-to-back diode characteristic, with both wafers showing similar I-V characteristics within each group. This allowed a 'pass' or 'fail' to be assigned to each device, depending on the current flow, narrowing down the selection of devices available for further examination in Oxford. One example from each group is given in Figure 147.

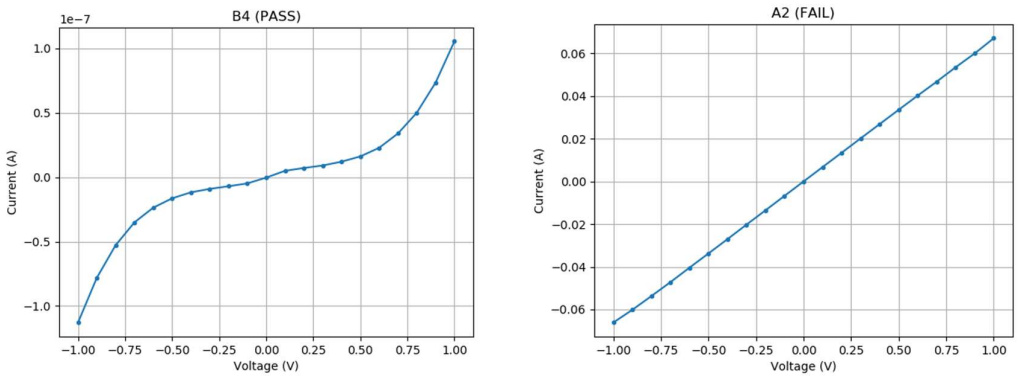

Figure 147: Room temperature I-V characteristics for a normal device (left), showing an I-V curve characteristic of two back-to-back diodes, and a failed device (right), showing high current and ohmic behaviour. Note the graph on the left has its current axis scaled by a factor of 10^7 A.

Only two devices out of 100 had failed in this way, due to contact metal bridging the gap. After this assessment, the devices were sent to Oxford for bonding and further examination; all measurements reported in the following sections (6.4.6 and 6.4.7) were carried out by Claudius Kocher.

6.4.6 Low-temperature electrical measurements

The samples were wedge bonded with Au wire and low-temperature I-V measurements were carried out by Claudius Kocher at the University of Oxford. These were found to be broadly similar to the I-Vs at room temperature, but with higher resistance and a wider central low current region. A representative I-V plot is shown in Figure 148.

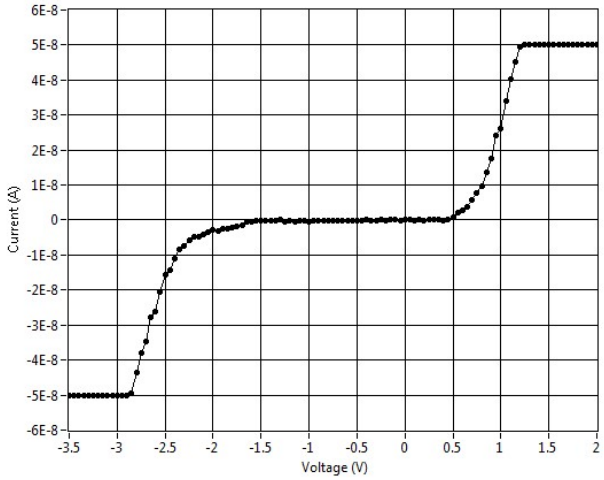

Figure 148: I-V plot, taken at 4.2 K after bonding. Similar in form to the characteristic measured at room temperature, but with a more extended central flat region and lower current. Data acquired and graph produced by Claudius Kocher.

6.4.7 Photoluminescence measurements (early results)

Photoluminescence measurements of the bonded devices with L-shaped contacts on C5910F (Q2T dots) were carried out using two-photon excitation, in the same way as the QD measurements described in Chapter 5. QD peaks were found in both gaps between the electrodes, allowing electric fields to be applied parallel to either the m or c-direction for different QDs. Spectra were then recorded at each applied voltage setting, with an integration time of 10 s at each voltage step.

Several types of behaviour were observed in both orientations of the applied field; some QDs showed the symmetric parabolic shift that would be expected from nearly field-free QDs, while others showed a monotonic shift in peak position, and some showed a shift only for one polarity of applied voltage. Plots of peak position against applied voltage, showing each of these effects, are given in Figure 149 for a field applied parallel to the c-axis.

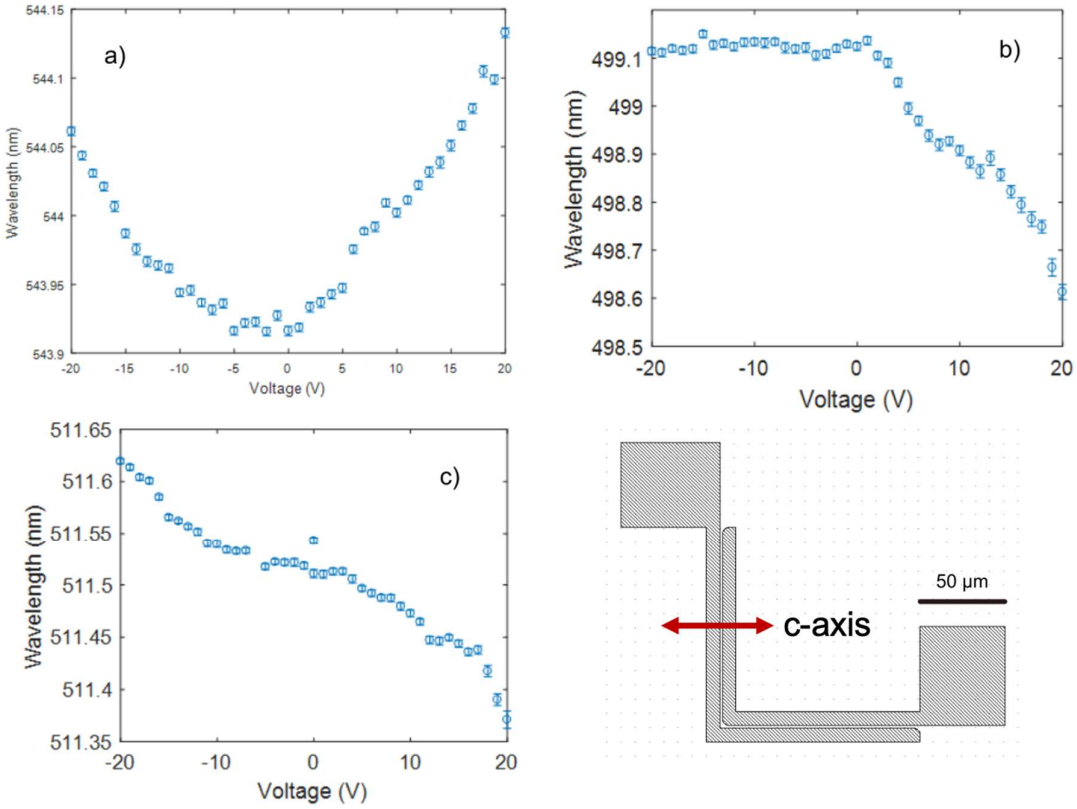

Figure 149: Three types of QD peak shift behaviour observed as the applied voltage is varied on a L-shaped lateral contact on a Q2T QD wafer, with the electric field applied parallel to the crystallographic c-axis. a) parabolic behaviour not quite centred on 0 V, b) peak shift observed for one direction of applied voltage only, and c) monotonic shift in peak position as voltage is changed from -20 V to +20 V. Data recorded, analysed and graphs produced by Claudius Kocher.

The quantum-confined Stark effect (QCSE) is expected to produce an increasing red-shift with increasing field, as described in section 1.4.2.1. Therefore, the parabolic shift shown in Figure 149(a), where the dot's emission wavelength is red-shifted for both positive and negative applied voltages, could be a signature of a dot with low built-in field. The parabola is not perfectly centred on 0 V, which could indicate that there is a small field in the +V direction.

Some dots show the behaviour shown in Figure 149(c), where there is a monotonic shift in emission wavelength with applied voltage. This could indicate a larger field in the -V direction, compensated by applying a voltage in the +V direction, giving the observed blue-shift.

Finally, some dots show a shift for one direction of applied field only, as shown in Figure 149(b). This behaviour is not easily explained by the simple model of the red-shift due to the QCSE.

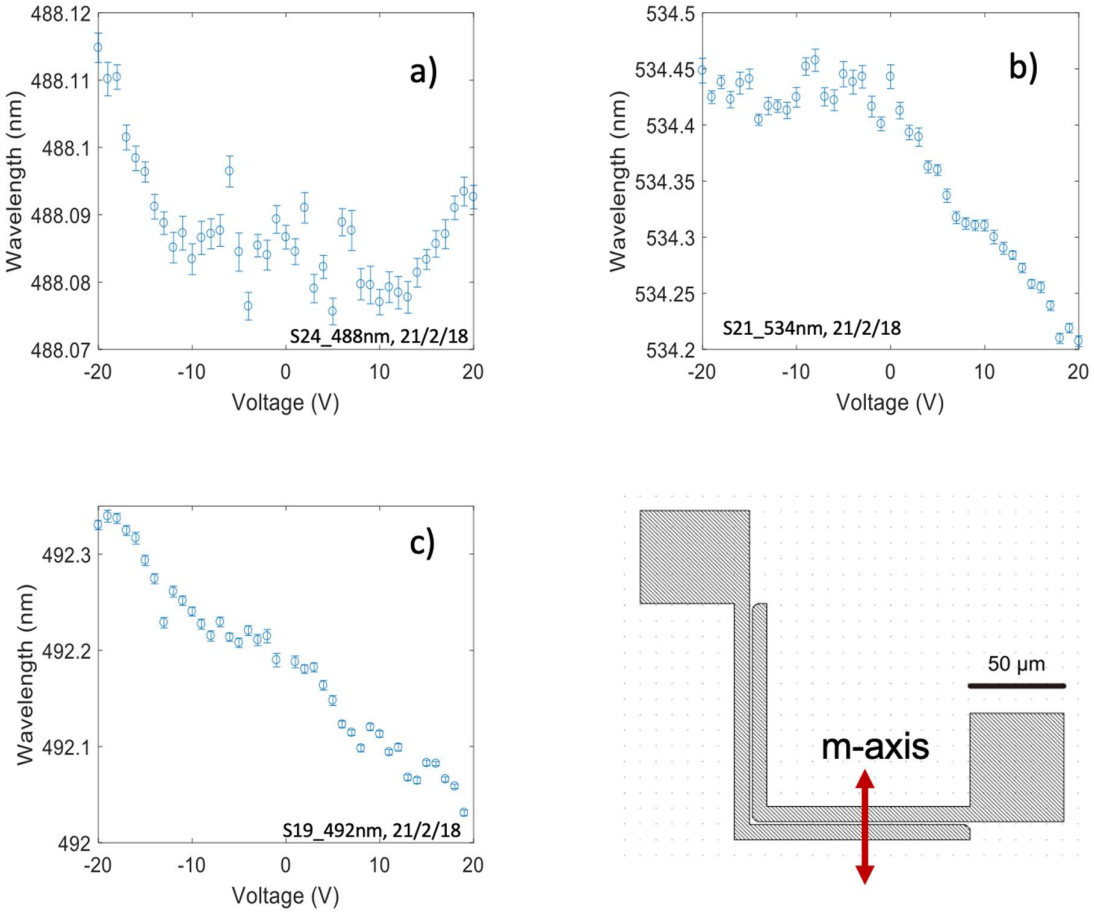

Figure 150: When applying an electric field along the crystallographic m-direction, QDs can be found that show the same classes of behaviour as for fields applied along the c-direction, with the peak wavelength of emission shifting a) parabolically (with increased spectral diffusion observed around 0 V), b) linearly for one applied polarity only, and c) linearly for all applied voltages.

There was no systematic difference between dots in each arm of the L-contact pattern (i.e. for fields applied along the m- and c-directions), as would have been expected in a simple model of the polarisation fields likely to be present across individual homogeneous QDs. The same classes of behaviour can be seen in the shifts of peak wavelength with voltage for each direction, with different QDs showing parabolic shifts, linear shifts for one polarity or linear shifts for all voltages.

These results suggest that the differences between individual dots are larger than the perturbations that can be introduced by applying fields. This may be either due to large variations in dot geometry and the local charge environment or may indicate that the QDs do not have a significant built-in field or significantly anisotropic polarisability. Modelling using a symmetry adapted k · p model by Patra *et al.* [247] indicates that, once second-order piezoelectric effects are accounted for, lens-shaped non-polar InGaN QDs should be almost field-free in all directions. This may explain the lack of an observed difference between fields applied along the in-plane m- and c-axes for these QDs.

The calculated electron and hole charge density is shown in Figure 151 for both polar and non-polar QDs. A substantial overlap of the electron and hole density is seen for non-polar QDs when both excitonic and second-order piezoelectric effects are considered.

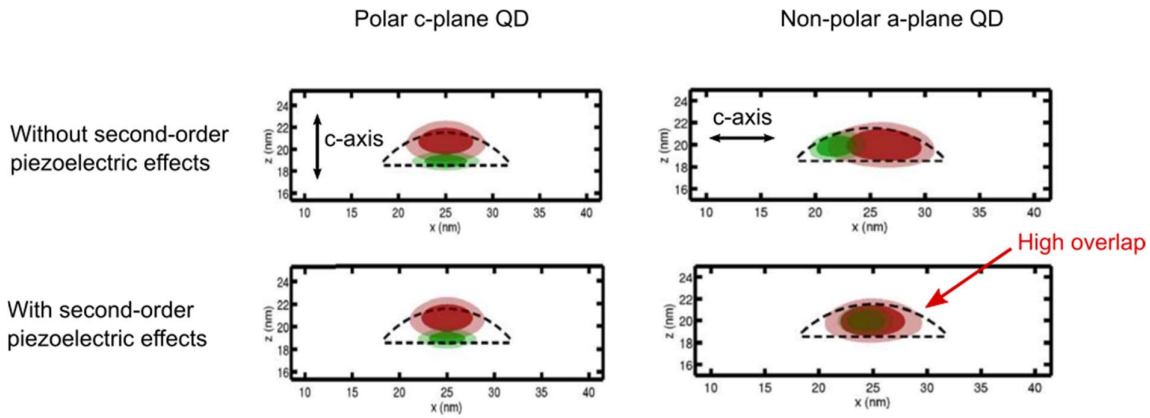

Figure 151: Ground-state charge density of electrons (red) and holes (green) of a lens-shaped InGaN QD grown on the polar c-plane (left) or non-polar a-plane (right). Once second-order piezoelectricity is included, the a-plane QD shows a high degree of overlap in the electron and hole charge density indicating low field across the dot. The c-plane QD shows a substantial separation of electron and hole density along the polar c-axis. Reproduced with permission from [247].

Real QDs may not be lens-shaped and will be in complex environments, possibly influenced by other nearby InGaN nanostructures as well as line and point defects. The different types of QD behaviour observed under applied fields may be a manifestation of this heterogeneity in the quantum emitters present in InGaN QD samples, and future work could investigate this further.

6.5 Summary

Electrical devices were designed and fabricated on a-plane QD-containing wafers, and examined at cryogenic temperatures using a micro-photoluminescence apparatus. Quantum-dot LEDs were designed and produced, and found to show highly polarised single-photon emission under electrical excitation. Lateral contact structures were also designed and fabricated, and a shift in the wavelength of QD-related peaks in the photoluminescence spectrum was observed as voltage was applied to the contacts. This could be useful for tuning of the QD emission wavelength to match a fabricated optical cavity resonance.

In initial experiments the peak shifts varied more between individual QDs than between the (non-polar) m- and (polar) c-directions in the growth plane, indicating that local variations in dot geometry and electric field may dominate over any effects introduced by the crystal structure of the sample. Numerical modelling indicates that it is plausible for ideal lens-shaped InGaN QDs grown on the non-polar a-plane to be field-free in all directions, possibly explaining this result.

Chapter 7

7Conclusions

7.1 Conclusions and suggestions for future work

The aim of this thesis was to explore methods and materials for creating a practical electrically injected single photon source based on InGaN nanostructures. These nanostructures were investigated in Chapter 3 using STEM-CL, and were incorporated into various electrical devices in Chapter 6, allowing electrically pumped single photon emission to be demonstrated with a $g^{(2)}(\tau) = 0.18$, when spectrally filtered and corrected for the instrument response function. Electrical tuning of the emission wavelength was also demonstrated, providing a possible route to matching of the QD emission to a cavity resonance.

The STEM-CL technique explored in Chapter 3 proved to be useful for exploring detail below the diffraction limited photoluminescence volume, allowing investigation of the detailed structure of the luminescence from nano-ring structures and other parts of QD samples grown by both MDE and Q2T techniques. While there is an inherent trade-off between the quality of the CL data (which was generally better in thicker regions) and the quality of structural information (generally better in thinner regions), the technique was also found to be potentially useful for correlating defects that can be easily resolved in STEM (e.g. dislocations and stacking faults) to the observed CL signal.

Porous GaN DBRs were shown to enhance the emission from QW-based LEDs in Chapter 4. These DBRs could also be used with QD heterostructures in LEDs as a method of increasing the directionality and extraction efficiency of electrically injected single photon sources. The regrowth approach used in Chapter 4 also allows the fabrication of a high-reflectance porous DBR prior to regrowth of the QD layers, removing the possibility of damage to the active layers by the etching process and assisting in the fabrication of the highest possible reflectance of the porous DBR.

A high-Q optical cavity could also be used to enhance the radiative emission rate and indistinguishability of photons emitted by the single-photon source. Some possible fabrication routes were explored in Chapter 5, using porous GaN for refractive index engineering. While whispering-gallery lasing modes were observed in one c-plane QW micropillar sample, other cavity geometries were unsuccessful in producing even low-Q cavity modes. It remains unclear whether this was due to insufficient reflectivity in the DBR stacks or sidewall roughness induced by the processing. Particularly for the structures containing both top and bottom porous GaN DBR, the top DBR is etched more completely than the lower DBR, which also lowers extraction efficiency from the top surface of the wafer in addition to reducing cavity Q. Therefore, a hybrid cavity consisting of a porous GaN lower DBR, with well-optimised and characterised reflectance, and a conventional dielectric DBR or an open cavity structure in place of the top porous structure would be a good starting point for future work on planar and pillar cavities.

The combination of a high-Q cavity with an electrical device would be desirable for a high-performance electrically injected single photon source. Pillar cavity geometries relevant to this aim have been explored in Chapter 5, and the post-processing etching of a porous GaN DBR into this structure was also demonstrated. Evaporation of a dielectric DBR on top of the complete electrical device containing such pillars could provide one route to an integrated cavity-device system, similarly to the porous-GaN VCSELs demonstrated in the literature [248].

The InGaN system generally has several advantages over other technologies for single photon sources operating in the visible wavelength range, such as the potential for room temperature operation and the ability to construct doped layers needed for electrical

injection. They are also capable of fast and highly pure single photon emission under optical excitation conditions designed to selectively pump the QDs [231], showing that these QDs, in isolation, are very promising candidates for room-temperature single photon sources.

However, the performance of this system under electrical injection may be limited by background emission from the fragmented QW. This can be mitigated somewhat by spectral filtering and etching of nanopillars through the active layer, but significant improvements to the $g^{(2)}(0)$ are needed to allow these QDs to become competitive with simpler systems such as attenuated lasers, or more mature single-photon emitters such as GaAs QDs, for quantum key distribution.

This suggests that an interesting focus for future research would be to investigate how to manipulate growth conditions to suppress background emission from the fragmented QW at the QD emission wavelength. In parallel, further improvement of optical excitation conditions could yield brighter and purer single photon emission from these QDs; and this would be the best way to investigate improvements to the cavity structures (such as sidewall roughness and DBR reflectance) that could be achieved with further refinements of the processing techniques. For example, sidewall roughness could be addressed with further refinements to the masking, e.g. by using a Ni mask that is easier to pattern, or by optimising the SiN hardmask etch in an appropriate etch tool, and by further improving the dry-etch process into GaN.

While there are clearly several technical barriers remaining before the realisation of a practical room-temperature single photon source using InGaN QDs, the development of an electrically pumped emitter with sub-Poissonian photon statistics described in this thesis is a useful proof of principle and illustrates how these QDs can be used in practical devices. Further, the demonstration of highly pure single photon emission from these QDs subjected to all the required processing steps, including dry etching and porous GaN DBR formation, suggests that this approach is feasible for the creation of high-performance single photon sources.

References

1. Lounis, B. and M. Orrit, *Single-photon sources.* Reports on Progress in Physics, 2005. **68**(5): p. 1129-1179.
2. Thomas, S. and P. Senellart, *The race for the ideal single-photon source is on.* Nature Nanotechnology, 2021. **16**(4): p. 367-368.
3. Tomm, N., et al., *A bright and fast source of coherent single photons.* Nature Nanotechnology, 2021. **16**(4): p. 399-403.
4. Jarjour, A.F., R.A. Oliver, and R.A. Taylor, *Nitride-based quantum dots for single photon source applications.* physica status solidi (a), 2009. **206**(11): p. 2510-2523.
5. Romanov, A.E., et al., *Strain-induced polarization in wurtzite III-nitride semipolar layers.* Journal of Applied Physics, 2006. **100**(2): p. 10.
6. Takeuchi, T., H. Amano, and I. Akasaki, *Theoretical study of orientation dependence of piezoelectric effects in wurtzite strained GaInN/GaN heterostructures and quantum wells.* Japanese Journal of Applied Physics, 2000. **39**(2R): p. 413.
7. Vennegues, P., et al., *In-plane polarities of nonpolar wurtzite epitaxial films deposited on m-and r-plane sapphire substrates.* Japanese Journal of Applied Physics, 2009. **48**(9R): p. 090211.
8. Gibart, P., *Metal organic vapour phase epitaxy of GaN and lateral overgrowth.* Reports on Progress in Physics, 2004. **67**(5): p. 667-715.
9. Frayssinet, E., et al., *Micro epitaxial lateral overgrowth of GaN/sapphire by metal organic vapour phase epitaxy.* MRS Internet Journal of Nitride Semiconductor Research, 2002. **7**(8): p. 7.
10. Chakraborty, A., et al., *Defect reduction in nonpolar a-plane GaN films using in situ SiNx nanomask.* Applied Physics Letters, 2006. **89**(4): p. 3.
11. Emery, R.M., et al., *Non-polar (11-20) InGaN quantum dots with short exciton lifetimes grown by metal-organic vapour phase epitaxy*, in *Physica Status Solidi C: Current Topics in Solid State Physics, Vol 11, No 3-4*, C.R. Eddy, et al., Editors. 2014. p. 698-701.

12. Götz, W., et al., *Activation energies of Si donors in GaN.* Applied Physics Letters, 1996. **68**(22): p. 3144-3146.
13. Ajay, A., et al., *Ge doping of GaN beyond the Mott transition.* Journal of Physics D: Applied Physics, 2016. **49**(44): p. 445301.
14. Nenstiel, C., et al., *Germanium–the superior dopant in n-type GaN.* physica status solidi (RRL)–Rapid Research Letters, 2015. **9**(12): p. 716-721.
15. Lyons, J.L., et al., *First-principles theory of acceptors in nitride semiconductors.* physica status solidi (b), 2015. **252**(5): p. 900-908.
16. Van de Walle, C.G., C. Stampfl, and J. Neugebauer, *Theory of doping and defects in III–V nitrides.* Journal of crystal growth, 1998. **189**: p. 505-510.
17. Götz, W., et al., *Activation of acceptors in Mg-doped GaN grown by metalorganic chemical vapor deposition.* Applied Physics Letters, 1996. **68**(5): p. 667-669.
18. Lyons, J., A. Janotti, and C. Van de Walle, *Carbon impurities and the yellow luminescence in GaN.* Applied Physics Letters, 2010. **97**(15): p. 152108.
19. Tang, H., et al., *Properties of carbon-doped GaN.* Applied Physics Letters, 2001. **78**(6): p. 757-759.
20. Pelá, R., et al., *Accurate band gaps of AlGaN, InGaN, and AlInN alloys calculations based on LDA-1/2 approach.* Applied Physics Letters, 2011. **98**(15): p. 151907.
21. Vurgaftman, I. and J.n. Meyer, *Band parameters for nitrogen-containing semiconductors.* Journal of Applied Physics, 2003. **94**(6): p. 3675-3696.
22. Ramvall, P., et al., *Observation of confinement-dependent exciton binding energy of GaN quantum dots.* Applied Physics Letters, 1998. **73**(8): p. 1104-1106.
23. Harrison, P. and A. Valavanis, *Quantum wells, wires and dots: theoretical and computational physics of semiconductor nanostructures*. 2016: John Wiley & Sons.
24. Yoshimoto, N., et al., *Photoluminescence of InGaN films grown at high temperature by metalorganic vapor phase epitaxy.* Applied physics letters, 1991. **59**(18): p. 2251-2253.
25. Keller, S., et al., *Growth and characterization of bulk InGaN films and quantum wells.* Applied physics letters, 1996. **68**(22): p. 3147-3149.
26. Pendlebury, S., et al., *InGaN/GaN quantum wells with low growth temperature GaN cap layers.* Journal of crystal growth, 2007. **307**(2): p. 363-366.

27. Winkelnkemper, M., et al., *Polarized emission lines from A-and B-type excitonic complexes in single InGaN/GaN quantum dots.* Journal of applied physics, 2007. **101**(11): p. 113708.

28. Lu, C.-Y. and J.-W. Pan, *Quantum optics: push-button photon entanglement.* Nature Photonics, 2014. **8**(3): p. 174.

29. Rice, J.H., et al., *Biexciton and exciton dynamics in single InGaN quantum dots.* Nanotechnology, 2005. **16**(9): p. 1477.

30. Reid, B., et al., *High temperature stability in non-polar (11$\underline{2}$0) InGaN quantum dots: Exciton and biexciton dynamics.* physica status solidi (c), 2014. **11**(3-4): p. 702-705.

31. Reimer, M., et al. *Biexciton binding energy control in site-selected quantum dots*. in *Journal of Physics: Conference Series*. 2010. IOP Publishing.

32. Reimer, M.E., et al., *Electric field induced removal of the biexciton binding energy in a single quantum dot.* Nano letters, 2011. **11**(2): p. 645-650.

33. Empedocles, S.A. and M.G. Bawendi, *Quantum-confined stark effect in single CdSe nanocrystallite quantum dots.* Science, 1997. **278**(5346): p. 2114-2117.

34. Jarjour, A.F., et al., *Control of the oscillator strength of the exciton in a single InGaN-GaN quantum dot.* Physical review letters, 2007. **99**(19): p. 197403.

35. Reid, B.P.L., et al., *Origins of Spectral Diffusion in the Micro-Photoluminescence of Single InGaN Quantum Dots.* Japanese Journal of Applied Physics, 2013. **52**(8): p. 4.

36. Ostapenko, I.A., et al., *Large internal dipole moment in InGaN/GaN quantum dots.* Applied Physics Letters, 2010. **97**(6).

37. Kanta Patra, S., et al., *Theoretical and experimental analysis of radiative recombination lifetimes in nonpolar InGaN/GaN quantum dots.* physica status solidi (b), 2017. **254**(8): p. 1600675.

38. Rice, J.H., et al., *Temporal variation in photoluminescence from single InGaN quantum dots.* Applied Physics Letters, 2004. **84**(20): p. 4110-4112.

39. Fedorov, A., A. Baranov, and K. Inoue, *Two-photon transitions in systems with semiconductor quantum dots.* Physical Review B, 1996. **54**(12): p. 8627.

40. Jarjour, A.F., et al., *Two-photon absorption from single InGaN/GaN quantum dots.* Physica E: Low-dimensional Systems and Nanostructures, 2006. **32**(1-2): p. 119-122.

41. Tasco, V., et al., *Electrically injected InGaAs/GaAs quantum-dot microcavity light-emitting diode operating at 1.3 μm and grown by metalorganic chemical vapor deposition.* Applied physics letters, 2004. **84**(21): p. 4155-4157.
42. Ellis, D., et al., *Electrically addressing a single self-assembled quantum dot.* Applied physics letters, 2006. **88**(13): p. 133509.
43. Jarjour, A.F., et al., *Electrically driven single InGaN/GaN quantum dot emission.* Applied Physics Letters, 2008. **93**(23).
44. Bhattacharya, P., et al. *III-Nitride High Temperature Single-Photon Sources*. in *Conference on Novel In-Plane Semiconductor Lasers XIV*. 2015. San Francisco, CA: Spie-Int Soc Optical Engineering.
45. Deshpande, S., et al., *Electrically pumped single-photon emission at room temperature from a single InGaN/GaN quantum dot.* Applied Physics Letters, 2014. **105**(14): p. 5.
46. Deshpande, S., et al., *Electrically driven polarized single-photon emission from an InGaN quantum dot in a GaN nanowire.* Nature communications, 2013. **4**: p. 1675.
47. Zubairy, M.O.S.M.S., *Quantum Optics*. 1997: Cambridge University Press.
48. Fox, M., *Quantum optics: an introduction*. Vol. 15. 2006: OUP Oxford.
49. Gao, K., et al., *Spectral diffusion time scales in InGaN/GaN quantum dots.* Applied Physics Letters, 2019. **114**(11): p. 112109.
50. Brown, R.H., R.Q. Twiss, and g. surName, *Interferometry of the intensity fluctuations in light-I. Basic theory: the correlation between photons in coherent beams of radiation.* Proceedings of the Royal Society of London. Series A. Mathematical and Physical Sciences, 1957. **242**(1230): p. 300-324.
51. Aharonovich, I., D. Englund, and M. Toth, *Solid-state single-photon emitters.* Nature Photonics, 2016. **10**(10): p. 631-641.
52. Chunnilall, C.J., et al., *Metrology of single-photon sources and detectors: a review.* Optical Engineering, 2014. **53**(8): p. 081910.
53. Holmes, M.J., M. Arita, and Y. Arakawa, *III-nitride quantum dots as single photon emitters.* Semiconductor Science and Technology, 2019. **34**(3): p. 033001.
54. Tachibana, K., et al., *Selective growth of InGaN quantum dot structures and their microphotoluminescence at room temperature.* Applied Physics Letters, 2000. **76**(22): p. 3212-3214.

55. Holmes, M.J., et al., *Room-temperature triggered single photon emission from a III-nitride site-controlled nanowire quantum dot.* Nano letters, 2014. **14**(2): p. 982-986.

56. Oliver, R.A., et al., *InGaN quantum dots grown by metalorganic vapor phase epitaxy employing a post-growth nitrogen anneal.* Applied Physics Letters, 2003. **83**(4): p. 755-757.

57. Zhu, T., et al., *Non-polar (11-20) InGaN quantum dots with short exciton lifetimes grown by metal-organic vapor phase epitaxy.* Applied Physics Letters, 2013. **102**(25).

58. Mantovani, V., et al., *Low density GaAs/AlGaAs quantum dots grown by modified droplet epitaxy.* Journal of Applied Physics, 2004. **96**(8): p. 4416-4420.

59. Griffiths, J.T., et al., *Growth of non-polar (11-20) InGaN quantum dots by metal organic vapour phase epitaxy using a two temperature method.* APL Materials, 2014. **2**(12).

60. Oliver, R.A., et al., *Morphological changes of InGaN epilayers during annealing assessed by spectral analysis of atomic force microscopy images.* Journal of Applied Physics, 2009. **106**(5): p. 054319.

61. Neugebauer, J., *Surfactants and antisurfactants on group-III-nitride surfaces.* physica status solidi (c), 2003(6): p. 1651-1667.

62. Wang, T., et al., *High-temperature performance of non-polar (11-20) InGaN quantum dots grown by a quasi-two-temperature method.* Physica Status Solidi B-Basic Solid State Physics, 2017. **254**(8).

63. Kremling, S., et al., *Single photon emission from InGaN/GaN quantum dots up to 50 K.* Applied Physics Letters, 2012. **100**(6): p. 061115.

64. Andreev, A.D. and E.P. O'Reilly, *Optical transitions and radiative lifetime in GaN/AlN self-organized quantum dots.* Applied Physics Letters, 2001. **79**(4): p. 521-523.

65. Holmes, M.J., et al., *Single photons from a hot solid-state emitter at 350 K.* ACS photonics, 2016. **3**(4): p. 543-546.

66. Vahala, K.J., *Optical microcavities.* Nature, 2003. **424**(6950): p. 839-846.

67. Kavokin, A., et al., *Microcavities*. 2017: Oxford university press.

68. Lu, T.C., et al., *Development of GaN-Based Vertical-Cavity Surface-Emitting Lasers.* Ieee Journal of Selected Topics in Quantum Electronics, 2009. **15**(3): p. 850-860.

69. Onishi, T., et al., *Continuous Wave Operation of GaN Vertical Cavity Surface Emitting Lasers at Room Temperature.* IEEE Journal of Quantum Electronics, 2012. **48**(9): p. 1107-1112.

70. Zhang, C., R. ElAfandy, and J. Han, *Distributed Bragg Reflectors for GaN-Based Vertical-Cavity Surface-Emitting Lasers.* Applied Sciences, 2019. **9**(8): p. 1593.

71. Bejtka, K., et al., *Strong light-matter coupling in ultrathin double dielectric mirror GaN microcavities.* Applied Physics Letters, 2008. **92**(24): p. 241105.

72. Holder, C., et al., *Demonstration of Nonpolar GaN-Based Vertical-Cavity Surface-Emitting Lasers.* Applied Physics Express, 2012. **5**(9): p. 3.

73. Chu, J.T., et al., *Room-temperature operation of optically pumped blue-violet GaN-based vertical-cavity surface-emitting lasers fabricated by laser lift-off.* Japanese Journal of Applied Physics Part 1-Regular Papers Brief Communications & Review Papers, 2006. **45**(4A): p. 2556-2560.

74. Holder, C.O., et al., *Nonpolar III-nitride vertical-cavity surface emitting lasers with a polarization ratio of 100% fabricated using photoelectrochemical etching.* Applied Physics Letters, 2014. **105**(3): p. 5.

75. Daskalakis, K., et al., *All-dielectric GaN microcavity: Strong coupling and lasing at room temperature.* Applied Physics Letters, 2013. **102**(10): p. 101113.

76. Carlin, J.F. and M. Ilegems, *High-quality AlInN for high index contrast Bragg mirrors lattice matched to GaN.* Applied Physics Letters, 2003. **83**(4): p. 668-670.

77. Brunner, D., et al., *Optical constants of epitaxial AlGaN films and their temperature dependence.* Journal of Applied Physics, 1997. **82**(10): p. 5090-5096.

78. Nakada, N., et al., *Suppression of crack generation in GaN/AlGaN distributed Bragg reflector on sapphire by the insertion of GaN/AlGaN superlattice grown by metal-organic chemical vapor deposition.* Japanese Journal of Applied Physics Part 2-Letters, 2003. **42**(2B): p. L144-L146.

79. Waldrip, K.E., et al., *Stress engineering during metalorganic chemical vapor deposition of AlGaN/GaN distributed Bragg reflectors.* Applied Physics Letters, 2001. **78**(21): p. 3205-3207.

80. Carlin, J.F., et al., *Progresses in III-nitride distributed Bragg reflectors and microcavities using AlInN/GaN materials.* Physica Status Solidi B-Basic Solid State Physics, 2005. **242**(11): p. 2326-2344.

81. Kozuka, Y., et al., *Growths of AlInN single layers and distributed bragg reflectors for VCSELs.* MRS Online Proceedings Library Archive, 2015. **1736**.

82. Takeuchi, T., et al., *GaN-based vertical-cavity surface-emitting lasers with AlInN/GaN distributed Bragg reflectors.* Reports on Progress in Physics, 2018. **82**(1): p. 012502.

83. Griffin, P. and R. Oliver, *Porous nitride semiconductors reviewed.* Journal of Physics D: Applied Physics, 2020. **53**(38): p. 383002.

84. Zhu, T., et al., *Wafer-scale Fabrication of Non-Polar Mesoporous GaN Distributed Bragg Reflectors via Electrochemical Porosification.* Scientific Reports, 2017. **7**: p. 45344.

85. Zhang, C., et al., *Mesoporous GaN for Photonic Engineering-Highly Reflective GaN Mirrors as an Example.* Acs Photonics, 2015. **2**(7): p. 980-986.

86. Braun, M.M. and L. Pilon, *Effective optical properties of non-absorbing nanoporous thin films.* Thin Solid Films, 2006. **496**(2): p. 505-514.

87. Zhang, Y., et al., *A conductivity-based selective etching for next generation GaN devices.* Physica Status Solidi B-Basic Solid State Physics, 2010. **247**(7): p. 1713-1716.

88. Schwab, M.J., et al., *Aligned mesopore arrays in GaN by anodic etching and photoelectrochemical surface etching.* The Journal of Physical Chemistry C, 2013. **117**(33): p. 16890-16895.

89. Massabuau, F.C.-P., et al., *Dislocations as channels for the fabrication of sub-surface porous GaN by electrochemical etching.* APL Materials, 2020. **8**(3): p. 031115.

90. Chen, D., H. Xiao, and J. Han, *Nanopores in GaN by electrochemical anodization in hydrofluoric acid: Formation and mechanism.* Journal of Applied Physics, 2012. **112**(6).

91. Chen, D. and J. Han, *High reflectance membrane-based distributed Bragg reflectors for GaN photonics.* Applied Physics Letters, 2012. **101**(22).

92. Tao, R., et al., *Fabrication and optical properties of non-polar III-nitride air-gap distributed Bragg reflector microcavities.* Applied Physics Letters, 2013. **103**(20): p. 4.

93. Liu, F., et al., *High Purcell factor generation of indistinguishable on-chip single photons.* Nature nanotechnology, 2018. **13**(9): p. 835-840.

94. Haberer, E.D., et al., *Removal of thick (> 100 nm) InGaN layers for optical devices using band-gap-selective photoelectrochemical etching.* Applied Physics Letters, 2004. **85**(5): p. 762-764.

95. Debnath, R., et al., *Top-down fabrication of large-area GaN micro- and nanopillars.* Journal of Vacuum Science & Technology B, 2014. **32**(2).

96. El-Ella, H.A.R., et al., *Optical cavity efficacy and lasing of focused ion beam milled GaN/InGaN micropillars.* Journal of Applied Physics, 2012. **112**(11).

97. Wu, T.T., et al., *High quality factor nonpolar GaN photonic crystal nanocavities.* Applied Physics Letters, 2013. **102**(19): p. 4.

98. Niu, N., et al., *Ultra-low threshold gallium nitride photonic crystal nanobeam laser.* Applied Physics Letters, 2015. **106**(23).

99. Schneider, C., et al., *Quantum dot micropillar cavities with quality factors exceeding 250,000.* Applied Physics B-Lasers and Optics, 2016. **122**(1).

100. Nowak, A.K., et al., *Deterministic and electrically tunable bright single-photon source.* Nature Communications, 2014. **5**: p. 7.

101. Dousse, A., et al., *Controlled Light-Matter Coupling for a Single Quantum Dot Embedded in a Pillar Microcavity Using Far-Field Optical Lithography.* Physical Review Letters, 2008. **101**(26): p. 4.

102. Reitzenstein, S., et al., *Electrically Driven Quantum Dot Micropillar Light Sources.* Ieee Journal of Selected Topics in Quantum Electronics, 2011. **17**(6): p. 1670-1680.

103. Coulon, P.M., et al., *Dual-polarity GaN micropillars grown by metalorganic vapour phase epitaxy: Cross-correlation between structural and optical properties.* Journal of Applied Physics, 2014. **115**(15).

104. Krylyuk, S., et al., *Large-area GaN n-core/p-shell arrays fabricated using top-down etching and selective epitaxial overgrowth.* Applied Physics Letters, 2012. **101**(24): p. 4.

105. Tamboli, A.C., et al., *Room-temperature continuous-wave lasing in GaN/InGaN microdisks.* Nature Photonics, 2007. **1**(1): p. 61-64.

106. Aharonovich, I., et al., *Low threshold, room-temperature microdisk lasers in the blue spectral range.* Applied Physics Letters, 2013. **103**(2): p. 4.

107. Lu, T.-C., et al., *GaN-based two-dimensional surface-emitting photonic crystal lasers with AlN/GaN distributed Bragg reflector.* Applied Physics Letters, 2008. **92**(1).

108. Kao, T.S., et al. *Light emission characteristics of nonpolar a-plane GaN-based photonic crystal defect cavities*. in *High Contrast Metastructures IV*. 2015. Bellingham: SPIE-Int Soc Optical Engineering.

109. Stringfellow, G.B., *Organometallic vapor-phase epitaxy: theory and practice*. 1999: Elsevier.

110. Butler, H.S. and G.S. Kino, *Plasma sheath formation by radio-frequency fields.* Physics of Fluids, 1963. **6**(9): p. 1346-1355.

111. Paddock, S.W., *Confocal microscopy: methods and protocols*. Vol. 122. 1999: Springer Science & Business Media.

112. Kociak, M. and L.F. Zagonel, *Cathodoluminescence in the scanning transmission electron microscope.* Ultramicroscopy, 2017. **176**: p. 112-131.

113. Kawasaki, N., et al., *Extinction and Scattering Properties of High-Order Surface Plasmon Modes in Silver Nanoparticles Probed by Combined Spatially Resolved Electron Energy Loss Spectroscopy and Cathodoluminescence.* ACS Photonics, 2016. **3**(9): p. 1654-1661.

114. Zagonel, L.F., et al., *Nanometer Scale Spectral Imaging of Quantum Emitters in Nanowires and Its Correlation to Their Atomically Resolved Structure.* Nano Letters, 2011. **11**(2): p. 568-573.

115. Tizei, L. and M. Kociak, *Spatially resolved quantum nano-optics of single photons using an electron microscope.* Physical review letters, 2013. **110**(15): p. 153604.

116. Meuret, S., et al., *Photon bunching in cathodoluminescence.* Physical review letters, 2015. **114**(19): p. 197401.

117. Schmidt, G., et al., *Direct evidence of single quantum dot emission from GaN islands formed at threading dislocations using nanoscale cathodoluminescence: A source of single photons in the ultraviolet.* Applied Physics Letters, 2015. **106**(25): p. 252101.

118. Bourrellier, R., et al., *Bright UV single photon emission at point defects in h-BN.* Nano letters, 2016. **16**(7): p. 4317-4321.

119. Tararan, A., et al., *Cubic BN optical gap and intragap optically active defects.* arXiv preprint arXiv:1806.11446, 2018.

120. Meuret, S., et al., *Quantum nano optics of defect centers in diamond and h-BN with nano-cathodoluminescence*, in *2014 Conference on Lasers and Electro-Optics*. 2014.

121. Zhou, X., et al., *Nanoscale optical properties of indium gallium nitride/gallium nitride nanodisk-in-rod heterostructures.* ACS nano, 2015. **9**(3): p. 2868-2875.

122. Griffiths, J.T., et al., *Nanocathodoluminescence Reveals Mitigation of the Stark Shift in InGaN Quantum Wells by Si Doping.* Nano Letters, 2015. **15**(11): p. 7639-7643.

123. Gačević, Z.a., et al., *Emission of linearly polarized single photons from quantum dots contained in nonpolar, semipolar, and polar sections of pencil-like InGaN/GaN nanowires.* ACS Photonics, 2017. **4**(3): p. 657-664.

124. Griffiths, J.T., et al., *Nano-cathodoluminescence reveals the effect of electron damage on the optical properties of nitride optoelectronics and the damage threshold.* Journal of Applied Physics, 2016. **120**(16).

125. Zagonel, L.F., et al., *Visualizing highly localized luminescence in GaN/AlN heterostructures in nanowires.* Nanotechnology, 2012. **23**(45): p. 455205.

126. Meuret, S., et al., *Lifetime measurements well below the optical diffraction limit.* ACS photonics, 2016. **3**(7): p. 1157-1163.

127. Tizei, L.H., et al., *A polarity-driven nanometric luminescence asymmetry in AlN/GaN heterostructures.* Applied Physics Letters, 2014. **105**(14): p. 143106.

128. Pierret, A., et al., *Structural and optical properties of Alx Ga1–xN nanowires.* physica status solidi (RRL)–Rapid Research Letters, 2013. **7**(10): p. 868-873.

129. Pierret, A., et al., *Probing alloy composition gradient and nanometer-scale carrier localization in single AlGaN nanowires by nanocathodoluminescence.* Nanotechnology, 2013. **24**(30): p. 305703.

130. O'Neill, J., et al., *Electron-beam-induced segregation in InGaN/GaN multiple-quantum wells.* Applied physics letters, 2003. **83**(10): p. 1965-1967.

131. Rosenauer, A., et al., *Composition mapping in InGaN by scanning transmission electron microscopy.* Ultramicroscopy, 2011. **111**(8): p. 1316-1327.

132. Koukoula, T., et al., *Structure and strain state of polar and semipolar InGaN quantum dots.* Applied Surface Science, 2012. **260**: p. 7-12.

133. Widmann, F., et al., *Improved quality GaN grown by molecular beam epitaxy using In as a surfactant.* Applied Physics Letters, 1998. **73**(18): p. 2642-2644.

134. Tessarek, C., et al., *Strong phase separation of strained In x Ga 1− x N layers due to spinodal and binodal decomposition: Formation of stable quantum dots.* Physical Review B, 2011. **83**(11): p. 115316.

135. https://scipy.org/, *SciPy*.

136. Mirzal, A., *NMF versus ICA for blind source separation.* Advances in Data Analysis and Classification, 2017. **11**(1): p. 25-48.

137. https://scikit-learn.org/, *scikit-learn*.

138. Févotte, C. and J. Idier, *Algorithms for nonnegative matrix factorization with the β-divergence.* Neural computation, 2011. **23**(9): p. 2421-2456.

139. Springbett, H., et al., *Structure and composition of non-polar (11-20) InGaN nanorings grown by modified droplet epitaxy.* Physica Status Solidi B-Basic Solid State Physics, 2016. **253**(5): p. 840-844.

140. Springbett, H., *Microscopy and Spectroscopy of Materials for Blue Single Photon Sources (PhD Thesis)*. 2018, University of Cambridge.

141. Born, M. and E. Wolf, *Principles of optics: electromagnetic theory of propagation, interference and diffraction of light*. 2013: Elsevier.

142. Lin, C.-C. and C.-T. Lee, *GaN-based resonant-cavity light-emitting diodes with top and bottom dielectric distributed Bragg reflectors.* IEEE Photonics Technology Letters, 2010. **22**(17): p. 1291-1293.

143. Dai, J., et al., *Design and fabrication of UV band-pass filters based on SiO2/Si3N4 dielectric distributed bragg reflectors.* Applied Surface Science, 2016. **364**: p. 886-891.

144. Butte, R., et al., *Recent progress in the growth of highly reflective nitride-based distributed Bragg reflectors and their use in microcavities.* Japanese Journal of Applied Physics Part 1-Regular Papers Brief Communications & Review Papers, 2005. **44**(10): p. 7207-7216.

145. Butte, R., et al., *Current status of AlInN layers lattice-matched to GaN for photonics and electronics.* Journal of Physics D-Applied Physics, 2007. **40**(20): p. 6328-6344.

146. Byrnes, S.J., *Multilayer optical calculations.* arXiv preprint arXiv:1603.02720, 2016.

147. Pimputkar, S., et al., *Prospects for LED lighting.* Nature Photonics, 2009. **3**(4): p. 180.

148. Hammersley, S., et al., *The consequences of high injected carrier densities on carrier localization and efficiency droop in InGaN/GaN quantum well structures.* Journal of Applied Physics, 2012. **111**(8): p. 083512.

149. Wallace, M.J., et al., *Effect of the barrier growth mode on the luminescence and conductivity micron scale uniformity of InGaN light emitting diodes.* Journal of Applied Physics, 2015. **117**(11): p. 115705.

150. Verzellesi, G., et al., *Efficiency droop in InGaN/GaN blue light-emitting diodes: Physical mechanisms and remedies.* Journal of Applied Physics, 2013. **114**(7): p. 10_1.

151. Kim, H., et al., *Modeling of a GaN-based light-emitting diode for uniform current spreading.* Applied Physics Letters, 2000. **77**(12): p. 1903-1904.

152. Cao, X., et al., *Optimization of current spreading metal layer for GaN/InGaN-based light emitting diodes.* Solid-State Electronics, 2002. **46**(8): p. 1235-1239.

153. Sheu, J., et al., *High-transparency Ni/Au ohmic contact to p-type GaN.* Applied physics letters, 1999. **74**(16): p. 2340-2342.

154. Pan, S.-M., et al., *Enhanced output power of InGaN-GaN light-emitting diodes with high-transparency nickel-oxide-indium-tin-oxide ohmic contacts.* IEEE Photonics Technology Letters, 2003. **15**(5): p. 646-648.

155. Jo, G., et al., *Large-scale patterned multi-layer graphene films as transparent conducting electrodes for GaN light-emitting diodes.* Nanotechnology, 2010. **21**(17): p. 175201.

156. Li, C.-K. and Y.-R. Wu, *Study on the current spreading effect and light extraction enhancement of vertical GaN/InGaN LEDs.* IEEE Transactions on Electron Devices, 2012. **59**(2): p. 400-407.

157. Laubsch, A., et al., *High-Power and High-Efficiency InGaN-Based Light Emitters.* IEEE Transactions on Electron Devices, 2010. **57**(1): p. 79-87.

158. Mohammad, S.N., *Contact mechanisms and design principles for alloyed ohmic contacts to n-GaN.* Journal of applied physics, 2004. **95**(12): p. 7940-7953.

159. Motayed, A., et al., *Electrical, thermal, and microstructural characteristics of Ti/Al/Ti/Au multilayer Ohmic contacts to n-type GaN.* Journal of Applied Physics, 2003. **93**(2): p. 1087-1094.

160. Ruvimov, S., et al., *Microstructure of Ti/Al and Ti/Al/Ni/Au Ohmic contacts for n-GaN.* Applied Physics Letters, 1996. **69**(11): p. 1556-1558.

161. Lin, Y.-J., et al., *Schottky barrier height and nitrogen–vacancy-related defects in Ti alloyed Ohmic contacts to n-GaN.* Journal of applied physics, 2004. **95**(2): p. 571-575.

162. Wang, D.F., et al., *Low-resistance Ti/Al/Ti/Au multilayer ohmic contact to n-GaN.* Journal of Applied Physics, 2001. **89**(11): p. 6214-6217.

163. Fan, Z., et al., *Very low resistance multilayer Ohmic contact to n-GaN.* Applied Physics Letters, 1996. **68**(12): p. 1672-1674.

164. Hull, B., et al., *Influence of oxygen on the activation of p-type GaN.* Applied Physics Letters, 2000. **76**(16): p. 2271-2273.

165. Jang, J.-S. and T.-Y. Seong, *Electronic transport mechanisms of nonalloyed Pt Ohmic contacts to p-GaN.* Applied Physics Letters, 2000. **76**(19): p. 2743-2745.

166. Sarkar, B., et al., *On Ni/Au Alloyed Contacts to Mg-Doped GaN.* Journal of Electronic Materials, 2018. **47**(1): p. 305-311.

167. Chen, L.-C., et al., *Microstructural investigation of oxidized Ni/Au ohmic contact to p-type GaN.* Journal of applied physics, 1999. **86**(7): p. 3826-3832.

168. Jang, H.W., S.Y. Kim, and J.-L. Lee, *Mechanism for ohmic contact formation of oxidized Ni/Au on p-type GaN.* Journal of Applied Physics, 2003. **94**(3): p. 1748-1752.

169. Karpov, S., *ABC-model for interpretation of internal quantum efficiency and its droop in III-nitride LEDs: a review.* Optical and Quantum Electronics, 2015. **47**(6): p. 1293-1303.

170. Lee, G.W., J.-I. Shim, and D.-S. Shin, *On the ideality factor of the radiative recombination current in semiconductor light-emitting diodes.* Applied Physics Letters, 2016. **109**(3): p. 031104.

171. David, A. and M.J. Grundmann, *Droop in InGaN light-emitting diodes: A differential carrier lifetime analysis.* Applied Physics Letters, 2010. **96**(10): p. 103504.

172. Kim, M.-H., et al., *Origin of efficiency droop in GaN-based light-emitting diodes.* Applied Physics Letters, 2007. **91**(18): p. 183507.

173. Bertazzi, F., M. Goano, and E. Bellotti, *A numerical study of Auger recombination in bulk InGaN.* Applied Physics Letters, 2010. **97**(23): p. 231118.

174. Kioupakis, E., et al., *Indirect Auger recombination as a cause of efficiency droop in nitride light-emitting diodes.* Applied Physics Letters, 2011. **98**(16): p. 161107.

175. Laubsch, A., et al., *On the origin of IQE-'droop'in InGaN LEDs.* physica status solidi c, 2009. **6**(S2 2): p. S913-S916.

176. Ryu, H.-Y., D.-S. Shin, and J.-I. Shim, *Analysis of efficiency droop in nitride light-emitting diodes by the reduced effective volume of InGaN active material.* Applied Physics Letters, 2012. **100**(13): p. 131109.

177. Zhang, M., P. Bhattacharya, and W. Guo, *InGaN/GaN self-organized quantum dot green light emitting diodes with reduced efficiency droop.* Applied Physics Letters, 2010. **97**(1): p. 011103.

178. David, A. and M.J. Grundmann, *Influence of polarization fields on carrier lifetime and recombination rates in InGaN-based light-emitting diodes.* Applied Physics Letters, 2010. **97**(3): p. 033501.

179. Kioupakis, E., Q. Yan, and C.G. Van de Walle, *Interplay of polarization fields and Auger recombination in the efficiency droop of nitride light-emitting diodes.* Applied Physics Letters, 2012. **101**(23): p. 231107.

180. Davies, M., et al., *Comparative studies of efficiency droop in polar and non-polar InGaN quantum wells.* Applied Physics Letters, 2016. **108**(25): p. 252101.

181. Hader, J., J.V. Moloney, and S.W. Koch, *Density-activated defect recombination as a possible explanation for the efficiency droop in GaN-based diodes.* Applied Physics Letters, 2010. **96**(22): p. 221106.

182. Xia, C., et al., *Simulation of InGaN/GaN multiple quantum well light-emitting diodes with quantum dot model for electrical and optical effects.* Optical and quantum electronics, 2006. **38**(12-14): p. 1077-1089.

183. Cao, X., et al., *Diffusion and tunneling currents in GaN/InGaN multiple quantum well light-emitting diodes.* IEEE Electron Device Letters, 2002. **23**(9): p. 535-537.

184. Xie, J., et al., *On the efficiency droop in InGaN multiple quantum well blue light emitting diodes and its reduction with p-doped quantum well barriers.* Applied Physics Letters, 2008. **93**(12): p. 121107.

185. Meyaard, D.S., et al., *Asymmetry of carrier transport leading to efficiency droop in GaInN based light-emitting diodes.* Applied Physics Letters, 2011. **99**(25): p. 251115.

186. Lee, J., et al., *On carrier spillover in c-and m-plane InGaN light emitting diodes.* Applied Physics Letters, 2009. **95**(20): p. 201113.

187. Han, S.-H., et al., *Effect of electron blocking layer on efficiency droop in InGaN/GaN multiple quantum well light-emitting diodes.* Applied physics letters, 2009. **94**(23): p. 231123.

188. Wang, C., et al., *Hole injection and efficiency droop improvement in InGaN/GaN light-emitting diodes by band-engineered electron blocking layer.* Applied Physics Letters, 2010. **97**(26): p. 261103.

189. Malyutenko, V., S. Bolgov, and A. Podoltsev, *Current crowding effect on the ideality factor and efficiency droop in blue lateral InGaN/GaN light emitting diodes.* Applied Physics Letters, 2010. **97**(25): p. 251110.

190. Bogdanov, M.V., et al., *Current crowding effect on light extraction efficiency of thin-film LEDs.* Physica Status Solidi C, 2010. **7**(7-8): p. 2124-2126.

191. Lee, H., et al., *Effect of the surface texturing shapes fabricated using dry etching on the extraction efficiency of vertical light-emitting diodes.* Solid-State Electronics, 2008. **52**(8): p. 1193-1196.

192. Na, S.I., et al., *Surface texturing of p-GaN layer for efficient GaN LED by maskless selective etching.* physica status solidi (c), 2005. **2**(7): p. 2916-2919.

193. Ke, W.C., et al., *InGaN-Based Light-Emitting Diodes Grown on a Micro/Nanoscale Hybrid Patterned Sapphire Substrate.* Acs Applied Materials & Interfaces, 2016. **8**(50): p. 34520-34529.

194. Lee, Y.-J., et al., *Enhancing the output power of GaN-based LEDs grown on wet-etched patterned sapphire substrates.* IEEE Photonics Technology Letters, 2006. **18**(10): p. 1152-1154.

195. Yamada, M., et al., *InGaN-based near-ultraviolet and blue-light-emitting diodes with high external quantum efficiency using a patterned sapphire substrate and a mesh electrode.* Japanese Journal of Applied Physics, 2002. **41**(12B): p. L1431.

196. Nakada, N., et al., *Improved characteristics of InGaN multiple-quantum-well light-emitting diode by GaN/AlGaN distributed Bragg reflector grown on sapphire.* Applied Physics Letters, 2000. **76**(14): p. 1804-1806.

197. Zhao, Y.S., et al., *Efficiency enhancement of InGaN/GaN light-emitting diodes with a back-surface distributed bragg reflector.* Journal of Electronic Materials, 2003. **32**(12): p. 1523-1526.

198. Shiu, G.Y., et al., *InGaN Light-Emitting Diodes with an Embedded Nanoporous GaN Distributed Bragg Reflectors.* Scientific Reports, 2016. **6**: p. 29138.

199. Jang, L.-W., et al., *Electrical and structural properties of GaN films and GaN/InGaN light-emitting diodes grown on porous GaN templates fabricated by combined electrochemical and photoelectrochemical etching.* Journal of Alloys and Compounds, 2014. **589**: p. 507-512.

200. Soh, C., et al., *Nanopore morphology in porous GaN template and its effect on the LEDs emission.* Journal of Physics D: Applied Physics, 2013. **46**(36): p. 365102.

201. Shieh, B.C., et al., *InGaN light-emitting diodes with embedded nanoporous GaN distributed Bragg reflectors.* Applied Physics Express, 2015. **8**(8): p. 4.

202. Fan, F.H., et al., *Ultraviolet GaN Light-Emitting Diodes with Porous-AlGaN Reflectors.* Scientific Reports, 2017. **7**: p. 4968.

203. Wang, G.J., et al., *GaN/AlGaN ultraviolet light-emitting diode with an embedded porous-AlGaN distributed Bragg reflector.* Applied Physics Express, 2017. **10**(12): p. 122102.

204. Soh, C., et al., *Enhanced luminescence efficiency due to carrier localization in In Ga N/Ga N heterostructures grown on nanoporous GaN templates.* Applied Physics Letters, 2008. **93**(17): p. 173107.

205. Hartono, H., et al., *Reduction of threading dislocation density in GaN grown on strain relaxed nanoporous GaN template.* Applied physics letters, 2007. **90**(17): p. 171917.

206. Lee, K.J., et al., *Enhanced performance of InGaN/GaN multiple-quantum-well light-emitting diodes grown on nanoporous GaN layers.* Optics Express, 2014. **22**(13): p. A1164-A1173.

207. Lai, W.-C., et al., *GaN-Based Light-Emitting Diodes on Electrochemically Etched n-GaN Template.* IEEE Photonics Technology Letters, 2013. **25**(15): p. 1531-1534.

208. Zhang, C., et al., *A resonant-cavity blue-violet light-emitting diode with conductive nanoporous distributed Bragg reflector.* Physica Status Solidi a-Applications and Materials Science, 2017. **214**(8): p. 1600866.

209. Perovic, D.D., A. Howie, and C.J. Rossouw, *On the image contrast from dislocations in high-angle annular dark-field scanning transmission electron microscopy.* Philosophical Magazine Letters, 1993. **67**(4): p. 261-272.

210. Byrnes, S., *tmm (https://pypi.python.org/pypi/tmm)*.

211. https://numpy.org/, *NumPy*.

212. Schubert, E.F., *Light-emitting diodes.* Wiley Encyclopedia of Electrical and Electronics Engineering, 1999.

213. Han, D.-P., et al., *Analysis of nonradiative recombination mechanisms and their impacts on the device performance of InGaN/GaN light-emitting diodes.* Japanese Journal of Applied Physics, 2014. **54**(2S): p. 02BA01.

214. Feezell, D.F., et al., *Semipolar (20-2-1) InGaN/GaN Light-Emitting Diodes for High-Efficiency Solid-State Lighting.* Journal of Display Technology, 2013. **9**(4): p. 190-198.

215. Xu, J., et al., *Reduction in efficiency droop, forward voltage, ideality factor, and wavelength shift in polarization-matched GaInN/GaInN multi-quantum-well light-emitting diodes.* Applied Physics Letters, 2009. **94**(1): p. 011113.

216. Varshni, Y.P., *Temperature dependence of the energy gap in semiconductors.* Physica, 1967. **34**(1): p. 149-154.

217. Grigorescu, A. and C. Hagen, *Resists for sub-20-nm electron beam lithography with a focus on HSQ: state of the art.* Nanotechnology, 2009. **20**(29): p. 292001.

218. Reddy, N.P., et al., *Enhanced luminescence from GaN nanopillar arrays fabricated using a top-down process.* Nanotechnology, 2016. **27**(6).

219. Van de Ven, E.P., I.-W. Connick, and A.S. Harrus. *Advantages of dual frequency PECVD for deposition of ILD and passivation films*. in *Seventh International IEEE Conference on VLSI Multilevel Interconnection*. 1990. IEEE.

220. Danaie, K., et al., *Fabrication of UV-transparent SixOyNz membranes with a low frequency PECVD reactor.* Sensors and Actuators A: Physical, 2002. **99**(1-2): p. 78-81.

221. Cianci, E., et al., *Dual frequency PECVD silicon nitride for fabrication of CMUTs' membranes.* Sensors and Actuators A: Physical, 2006. **127**(1): p. 80-87.

222. Pant, B.D. and U.S. Tandon, *Etching of silicon nitride in CCl2F2, CHF3, SiF4, and SF6 reactive plasma: A comparative study.* Plasma Chemistry and Plasma Processing, 1999. **19**(4): p. 545-563.

223. Standaert, T., et al., *Role of fluorocarbon film formation in the etching of silicon, silicon dioxide, silicon nitride, and amorphous hydrogenated silicon carbide.* Journal of Vacuum Science & Technology A, 2004. **22**(1): p. 53-60.

224. Rueger, N.R., et al., *Role of steady state fluorocarbon films in the etching of silicon dioxide using CHF3 in an inductively coupled plasma reactor.* Journal of Vacuum Science & Technology a-Vacuum Surfaces and Films, 1997. **15**(4): p. 1881-1889.

225. Schaepkens, M., et al., *Study of the SiO2-to-Si3N4 etch selectivity mechanism in inductively coupled fluorocarbon plasmas and a comparison with the SiO2-to-Si mechanism.* Journal of Vacuum Science & Technology a-Vacuum Surfaces and Films, 1999. **17**(1): p. 26-37.

226. Kaspar, P., et al., *Silicon nitride hardmask fabrication using a cyclic CHF3-based reactive ion etching process for vertical profile nanostructures.* Journal of Vacuum Science & Technology B, 2010. **28**(6): p. 1179-1186.

227. Zhuang, D. and J. Edgar, *Wet etching of GaN, AlN, and SiC: a review.* Materials Science and Engineering: R: Reports, 2005. **48**(1): p. 1-46.

228. Stocker, D., E. Schubert, and J.M. Redwing, *Crystallographic wet chemical etching of GaN.* Applied Physics Letters, 1998. **73**(18): p. 2654-2656.

229. Li, D., et al., *Selective etching of GaN polar surface in potassium hydroxide solution studied by x-ray photoelectron spectroscopy.* Journal of Applied Physics, 2001. **90**(8): p. 4219-4223.

230. Chen, H.-S., et al., *Strain relaxation and quantum confinement in InGaN/GaN nanoposts.* Nanotechnology, 2006. **17**(5): p. 1454.

231. Holmes, M., et al., *Pure single-photon emission from an InGaN/GaN quantum dot.* APL Materials, 2021. **9**(6): p. 061106.

232. Wang, T., et al., *Deterministic optical polarisation in nitride quantum dots at thermoelectrically cooled temperatures.* Scientific Reports, 2017. **7**.

233. Wang, T., et al., *Experimental and theoretical analyses of strongly polarized photon emission from non-polar InGaN quantum dots.* arXiv preprint arXiv:1609.06885, 2016.

234. Patra, S.K., O. Marquardt, and S. Schulz, *Polar, semi-and non-polar nitride-based quantum dots: influence of substrate orientation and material parameter sets on electronic and optical properties.* Optical and Quantum Electronics, 2016. **48**(2): p. 151.

235. Springbett, H.P., et al., *Improvement of single photon emission from InGaN QDs embedded in porous micropillars.* Applied Physics Letters, 2018. **113**(10): p. 101107.

236. Robinson, J.W., et al., *Quantum-confined Stark effect in a single InGaN quantum dot under a lateral electric field.* Applied Physics Letters, 2005. **86**(21).

237. Yuan, Z.L., et al., *Electrically driven single-photon source.* Science, 2002. **295**(5552): p. 102-105.

238. Schliwinski, H.J., et al., *Thermal annealing effects on the mechanical properties of plasma-enhanced chemical vapor deposited silicon oxide films.* Journal of The Electrochemical Society, 1992. **139**(6): p. 1730-1735.

239. Wang, C., et al., *Temperature-dependent electroluminescence efficiency in blue InGaN–GaN light-emitting diodes with different well widths.* IEEE Photonics Technology Letters, 2010. **22**(4): p. 236-238.

240. Kocher, C.C., et al., *Highly polarized electrically driven single-photon emission from a non-polar InGaN quantum dot.* Applied Physics Letters, 2017. **111**(25).

241. Michler, P., et al., *Quantum correlation among photons from a single quantum dot at room temperature.* Nature, 2000. **406**(6799): p. 968-970.

242. Wang, T., et al., *Polarisation-controlled single photon emission at high temperatures from InGaN quantum dots.* Nanoscale, 2017. **9**(27): p. 9421-9427.

243. Robinson, J.W., *Time-integrated and time-resolved optical studies of InGaN quantum dots (PhD thesis)*. 2005.

244. Lai, J.H. and L. Shepherd, *An investigation of the effects of the molecular weight distribution on the sensitivity of positive electron resists.* Journal of Applied Polymer Science, 1976. **20**(9): p. 2367-2375.

245. Lide, D.R., *CRC Handbook of Chemistry and Physics*. 89th ed. 2008: CRC Press.

246. Guo, J., et al., *Schottky contact and the thermal stability of Ni on n-type GaN.* Journal of Applied Physics, 1996. **80**(3): p. 1623-1627.

247. Patra, S.K. and S. Schulz, *Electronic and optical properties of polar, semi-and non-polar InGaN QDs: the role of second-order piezoelectric effects.* Japanese Journal of Applied Physics, 2019. **58**(SC): p. SCCB38.

248. Mishkat-Ul-Masabih, S.M., et al., *Electrically injected nonpolar GaN-based VCSELs with lattice-matched nanoporous distributed Bragg reflector mirrors.* Applied Physics Express, 2019. **12**(3): p. 036504.